NASA/CR-1998-208704

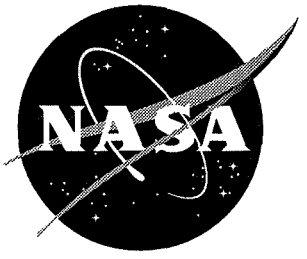

Boeing 18-Inch Fan Rig Broadband Noise Test

Ulrich W. Ganz, Paul D. Joppa, Timothy J. Patten, and Dnaiel F. Scharpf
Boeing Commercial Airplane Group, Seattle, Washington

National Aeronautics and
Space Administration

Langley Research Center
Hampton, Virginia 23681-2199

Prepared for Langley Research Center
under Contract NAS1-20090

September 1998

Available from the following:

NASA Center for AeroSpace Information (CASI)
7121 Standard Drive
Hanover, MD 21076-1320
(301) 621-0390

National Technical Information Service (NTIS)
5285 Port Royal Road
Springfield, VA 22161-2171
(703) 487-4650

Table of Contents

Acknowledgements

This test could not have taken place without the help of a large number of people. Of special note are John Premo who handled the far–field data acquisition and reduction, and Brian Arthur who organized and coordinated the myriad of tasks involved. Both were major contributors to the success of this test. We would also like to thank the contract monitors, Joe Posey and Dennis Huff at NASA.

Other major participants included Rick Gibbs and Ed Marzi, facilities and operations; Bert Johnson, Larry Yee, Gene Reindel, Guy Neubert, and Jim Underbrink, acoustic systems; Pete Landry and Jay Rogerson, aerothermal data systems; Mario Bubnich, Cecil Bugunovich, Bob Walker, Pat Connell, Tom Valenti, Leroy Moore, and Scott Nguyen, lab instrumentation and systems; Richard Hearsey, fan aerodynamic analysis; Jay Huffington, model designer; and Warren Davis, Noel Brandon, Meg Murch, Larry Clark, Les Armstrong, Mike Carrigan, and Dick Jones, model makers and shop.

Finally, the test would not have been successful without the important discussions and feedback provided by the other partners in the AST noise initiative, especially NASA Lewis Research Center (Jim Dittmar), NASA Langley Research Center (Carl Gerhold, Feri Farassat), General Electric Aero Engines (Phil Gliebe, Ramani Mani), Pratt and Whitney (Doug Mathews, Don Hanson), Stewart Glegg at Florida Atlantic University, plus many others too numerous to list but too essential to leave out.

Summary

In an increasingly global economy, the benefit to society of rapid, inexpensive transportation is largely undisputed. This has resulted in an escalating need for commercial airplanes throughout the world. Environmental concerns, especially noise in the community, limit the expansion of the world commercial aircraft fleet; for this reason, the industry is motivated to reduce aircraft noise in the community. Airplane community noise continues to be dominated by engine noise. For modern high-bypass ratio engines, the most important source of engine noise is the fan. Recently fan broadband noise has been exposed as a significant contributor. As a consequence, increasing amounts of research effort are being directed to the study of fan broadband noise and the mechanisms by which it is generated.

The test that is the subject of this Report was one of those efforts. This work has been funded by NASA as part of the Advanced Subsonic Technology (AST) initiative. The purposes of the test were to identify and quantify the mechanisms by which fan broadband noise is produced, and to assess the validity of such theoretical models of those mechanisms as may be available. To accomplish these purposes, the test was conducted with the Boeing 18-inch fan rig in the Boeing Low-Speed Aeroacoustic Facility (LSAF). The rig was designed to be particularly clean and geometrically simple to facilitate theoretical modeling and to minimize sources of interfering noise. The inlet is cylindrical and is equipped with a boundary layer suction system. The fan is typical of modern high-bypass ratio designs but is capable of operating with or without fan exit guide vanes (stators), and there is only a single flow stream. Fan loading and tip clearance are adjustable. Instrumentation included measurements of fan performance, the unsteady flow field incident on the fan and stators, and far-field and in-duct acoustic fields.

The test was conducted in two major segments. Between the segments, a meeting of interested AST partners took place to evaluate and re-direct the test plan. Changes in the test plan at this time resulted in better quality data. Where changes occurred in the test plan, only the more accurate or relevant data are reported here. For the most part, only typical results, illustrative of a particular result are presented, as the total set of data is very large.

Before testing began, the various noise floor sources were evaluated. While background noise levels from the LSAF free–jet were well below the fan broadband levels and therefore did not contaminate the fan noise signature, it was concluded that measurements at frequencies below 4 kHz were contaminated by the noise generated by the fan exhaust impinging on the fan-rig strut.

Both steady and unsteady characteristics of the inlet boundary layer were measured. It was concluded that the characteristics of the inlet boundary layer turbulence were similar to those of a flat plate boundary layer. There were some differences in the mean velocity profiles, the turbulence intensity profiles and the streamwise integral length scale distributions between the measured data and the flat plate data in zero pressure gradient, thought to be due to the favorable pressure gradients in the inlet in particular close to the fan face. The boundary layer suction provided displacement thickness near zero percent of the full boundary layer value for the maximum suction conditions. In unsteady flow measurements of this type, significant noise floors usually contaminate the cross-wire signals at high velocities. They were successfully minimized by sensor modifications and extraction of the pulse-synchronized average signal.

Unsteady flow measurements in the aft fan duct, at the axial position of the stators, showed the streamwise velocity deficit and the secondary flows in the rotor wakes are the dominating features of the unsteady flow for all conditions. The highest turbulence intensities occur in a region close to

the outer wall. The radial extent of this region is strongly affected by fan tip clearance. The lowest turbulence intensities occur in the midspan region because of the clean flow between the wakes. The turbulence in the hub wall region increases as fan loading is reduced. In spite of the complexity of the rotor wakes they exhibit remarkable similarities with two-dimensional wakes. Von Karman spectra approximate the spectral distributions of the turbulence quite well.

The acoustic results were manipulated to estimate the noise generated by different sources. Significant fan broadband noise was found to come from the rotor self-noise as measured with clean inflow and no boundary layer. The rotor tip clearance affected rotor self-noise somewhat. The interaction of the rotor with inlet boundary layer turbulence is also a significant source, and is strongly affected by rotor tip clearance. High level noise can be generated by a high-order nonuniformity rotating at a fraction of the fan speed, at least when tip clearance and loading are both large. Stator-generated noise is the loudest of the significant sources, by a small margin, at least on this rig. Stator noise is significantly affected by propagation through the fan.

Aerothermal measurements and analysis showed that stator and rotor incidence were significantly impacted by loading variations. Stator incidence is not influenced by inlet boundary layer size. Stator tip incidence was significantly impacted by clearance changes. Rotor tip incidence was significantly impacted by inlet boundary layer size. Data analysis with accurate radial mixing is necessary for accurate stator leading edge solutions. Accurate data analysis required good measurements for use with blockage calculation and well calibrated rotor exit rake instrumentation.

1 Introduction

In an increasingly global economy, the benefit to society of rapid, inexpensive transportation anywhere in the world is largely undisputed. This has resulted in an escalating need for commercial airplanes throughout the world. The need is expected to continue to grow into the foreseeable future. However, environmental concerns, especially noise in the community, limit the expansion of the world commercial aircraft fleet through limitations on airport growth imposed by the communities in which they are located. For this reason, the industry is motivated to reduce aircraft noise in the community.

Airplane community noise continues to be dominated by engine noise. For modern high-bypass ratio engines, the most important source of engine noise is the fan. The problem of fan tone noise and its reduction has been studied for many years, with some success. This has resulted in fan broadband noise being exposed as a significant contributor. In recent years, larger engines have become available, and there is a trend to fewer blades with wider chords. Both factors have resulted in lower frequency tones that have less impact, and consequently an increase in the relative importance of fan broadband noise. As a consequence, increasing amounts of research effort are being directed to the study of fan broadband noise and the mechanisms by which it is generated.

The test that is the subject of this Report was one of those efforts. This work has been funded by NASA as part of the Advanced Subsonic Technology (AST) initiative. The purposes of the test were to identify and quantify the mechanisms by which fan broadband noise is produced, and to assess the validity of such theoretical models of those mechanisms as may be available. In particular, Dr. Ramani Mani (GE Corporate Research and Development) and Professor Stewart Glegg (Florida Atlantic University) have also been funded under the AST initiative to develop such models.

To accomplish these purposes, the test was conducted with the Boeing 18-inch fan rig in the Boeing Low-Speed Aeroacoustic Facility (LSAF), a free-jet wind tunnel located in an anechoic chamber. The rig was designed to be particularly clean and geometrically simple to facilitate theoretical modeling and to minimize sources of interfering noise. The inlet is cylindrical and is equipped with a boundary layer suction system. The fan is typical of modern high-bypass ratio designs but is capable of operating with or without fan exit guide vanes (stators), and there is only a single flow stream. Fan loading and tip clearance are adjustable. Instrumentation included measurements of fan performance, the unsteady flow field incident on the fan and stators, and far-field and in-duct acoustic fields.

The test was conducted in two major segments. Between the segments, a meeting of interested AST partners took place to evaluate and re-direct the test plan. Changes in the test plan at this time resulted in better quality data in some cases, and more relevant data in others. The purpose of this Report is to show the major results of the test. Where changes occurred in the test plan, only the more accurate or relevant data are here reported. A more detailed history of the test is contained in Appendix 1. For the most part, only typical results, illustrative of a particular result are presented, as the total set of data is very large.

2 Facility

2.1 Boeing Low-Speed Aeroacoustic Facility, LSAF

The Boeing Low Speed Aeroacoustic Facility, LSAF, is an in-draft, open-jet wind tunnel which has a nominal 2.74m x 3.66m (9ft. x 12ft.) nozzle which opens into a 19.8 m x 22.8 m x 9.1 m (65 ft. x 75ft. x 30ft.) anechoic chamber as shown in Fig. 1. A large collector which is fitted with a series of silencers 10.7 m (35ft.) downstream of the nozzle which diverts the flow out of the chamber.

The walls, floor, and ceiling of the chamber are treated with 0.46m (1.5 ft.) foam wedges which provide an absorption coefficient of at least 0.99 for frequencies above 500 Hz. At the time these tests were conducted, the Mach number range of the tunnel was M = 0.05 – 0.25. (A new nozzle insert was built in 1996 which increased the maximum Mach number to 0.32) Axial and lateral components of turbulence at a distance of 3m downstream from the nozzle exit-plane were 0.3% for M_∞=0.10 (Ref. 2).

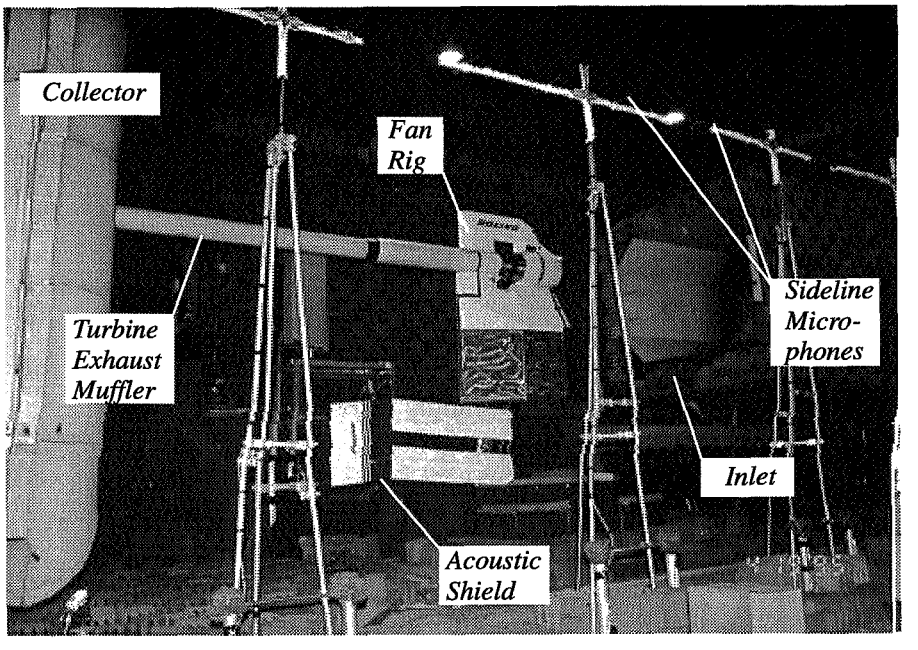

Fig. 1. The Boeing Low-Speed Aeroacoustic Facility.

LSAF Noise Floor Levels

The facility noise-floor spectrum illustrated in Fig. 2 is dominated by low frequencies which have been associated with the free-jet impingement on the flow collector, and silencers (Ref. 3). These levels are shown to be well below the noise floor of the fan-rig assembly and therefore have no adverse effect on the data acquired for this investigation.

Fan Rig Low-Frequency Noise Floor

Difficulty arose when discerning differences in the measured sideline SPL's below 4 kHz for a variety of model configurations as shown in Fig. 3. This noise will be shown to have been due to two sources: the fan exhaust impinging on the rig struts, and flow separation from the trailing edge of the translating centerbody.

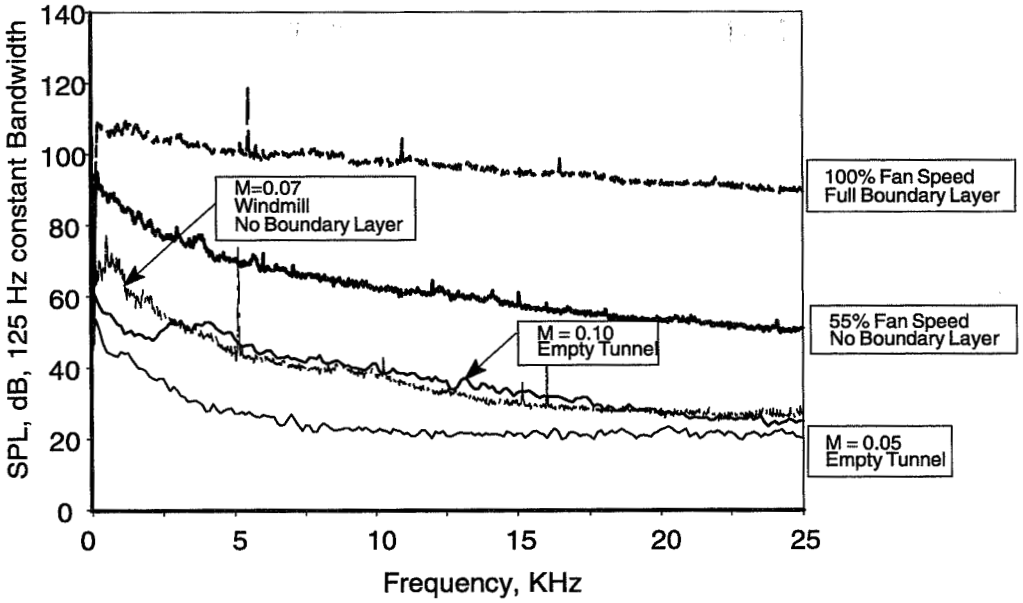

Fig. 2. SPL Measurements of LSAF Noise Floor at a 2.74m sideline, 2.74m downstream from the Nozzle Exit Plane. (Fan-rig data is corrected for bandwidth and distance.)

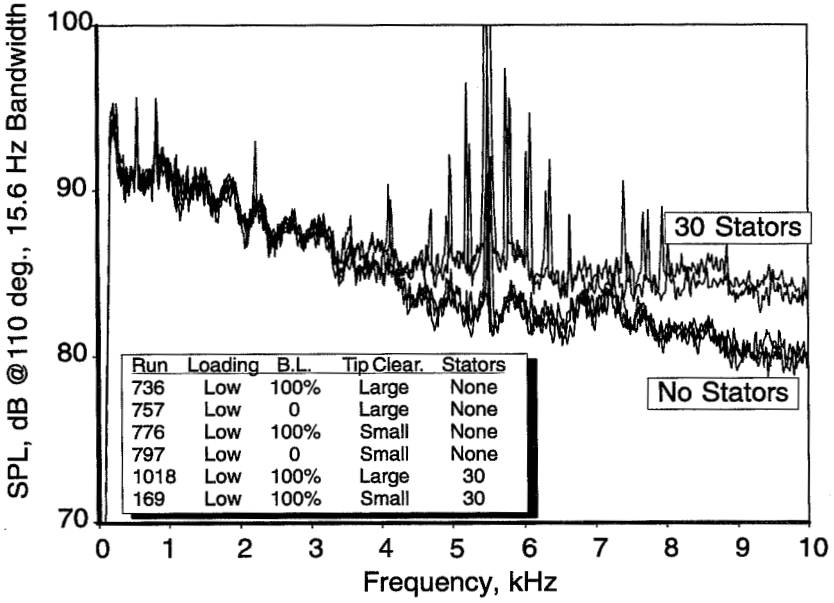

Fig. 3. Illustration of Low-Frequency Noise-Floor Contamination at a 5.49 m Sideline for a variety of Model Configurations at 100% Fan Speed.

Phased Array Noise-Source Location

A 42-element microphone phased array (Ref. 4, 5) was used in an effort to identify the source of the low-frequency noise which was contaminating the fan acoustic spectrum. Typical images are shown in Fig. 4 for frequencies of 2, and 4 kHz. The low frequency noise is centered at the upper strut, while the higher frequency noise appears to originate at the trailing edge of the translating centerbody.

Low Frequency Noise Source Identification

The noise level is expected to increase as M_{jet}^{6} , for the dipole-type noise due to the exhaust impinging on the strut, and M_{jet}^{8} for the quadrupole-type noise from the jet. Fig. 5 shows sound-power spectra for a range of fan speeds, in the forward and aft regions. From this data, the sound power level as a function of exhaust Mach number was plotted as shown in Fig. 6, where the Mach-number dependence can be determined from:

(1)

The frequencies of the sound-power spectra must be normalized as a Strouhal number in order to have appropriate scaling of the fluid dynamics. From these calculations, the dependance on fan-exhaust Mach number in the forward and aft regions are 5.2 and 6.1, respectively, for the low-frequencies. The value of 6.1 in the aft region clearly shows a dipole-type dependence on Mach number. The value of 5.2 in the forward region can be attributed to the fact that these measurements used an acoustic shield that prevented the jet/strut noise from propagating upstream; hence the deviation from the dipole-type dependence.

The Mach-number dependence in the higher frequencies, shows values of n=4 to 5.6, which would imply one of two things: 1) this is not a dipole-type source mechanism, or 2) the exhaust Mach number is not the appropriate scaling parameter for those frequencies. A more realistic value of n may be achieved by using a velocity that corresponds more closely to the actual source mechanisms at these frequencies.

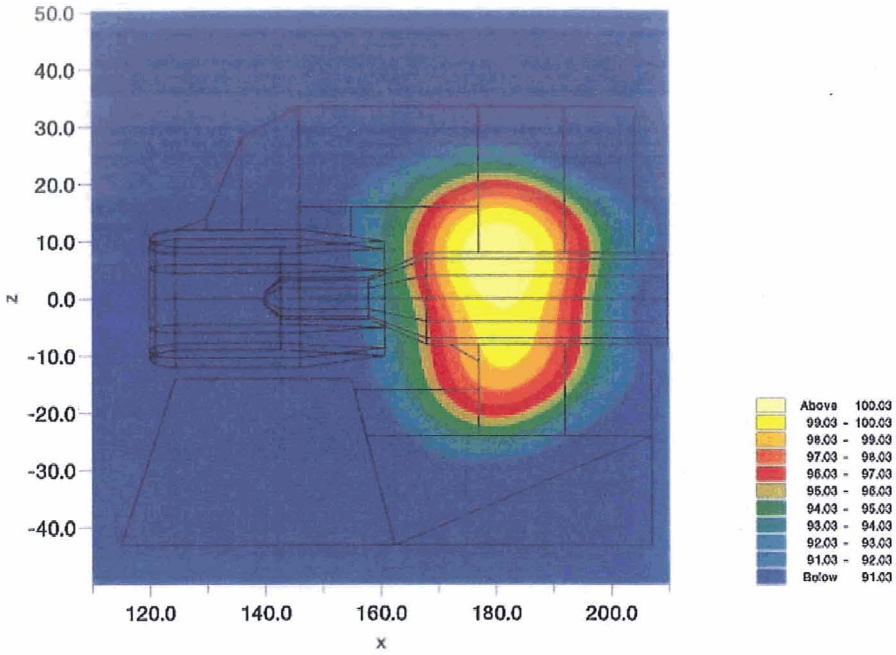

a) $f = 2$ kHz

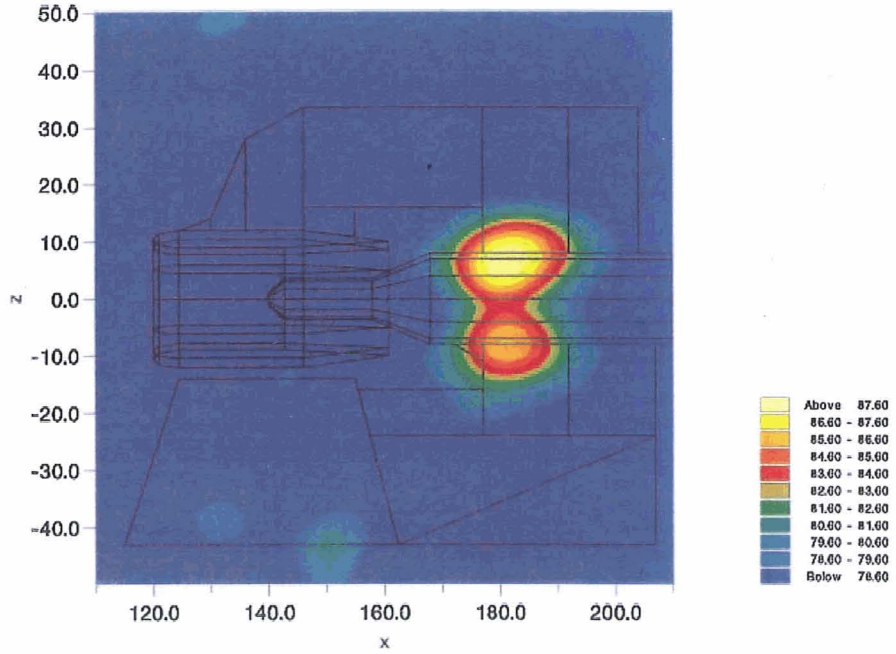

b) $f = 4$ kHz

Fig. 4. Phased-Array Source Image of the Fan Rig: Rotor-Alone, Full Boundary-Layer, 55%N1C, Low Loading; a) 2 kHz, b) 4 kHz

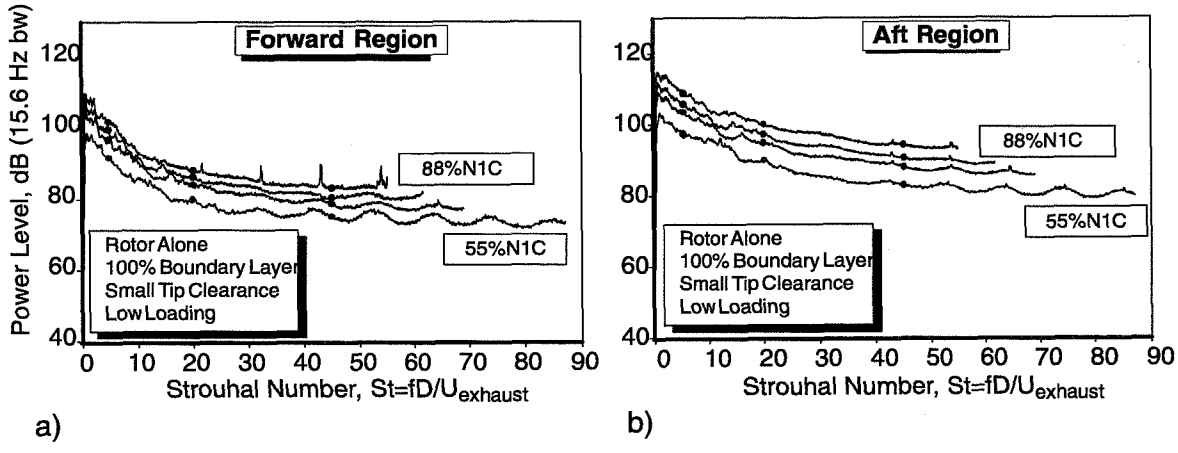

Fig. 5. Sound Power vs. Fan-Exhaust Mach Number; a) Forward Region, b) Aft Region.

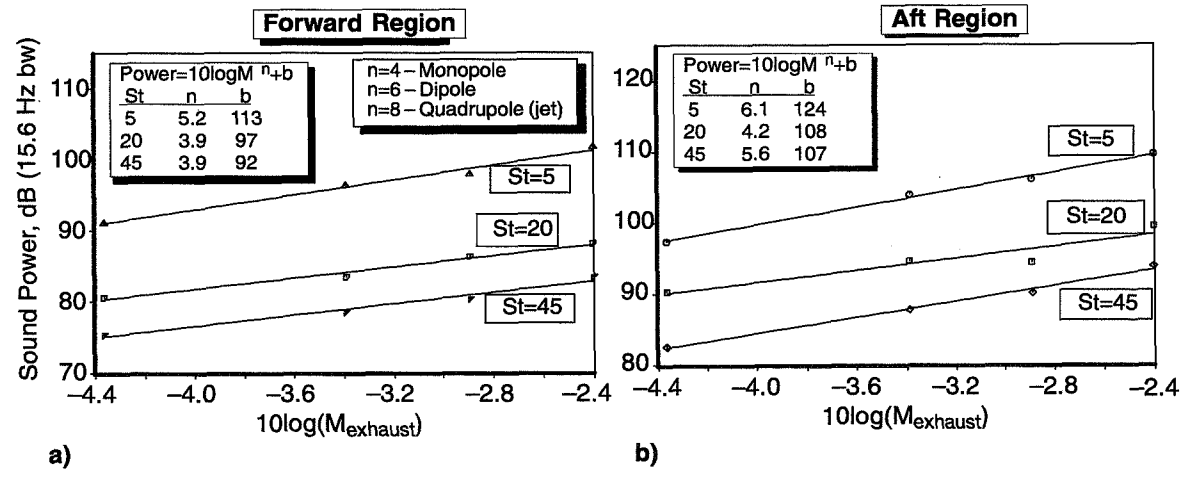

Fig. 6. Sound Power vs. Fan-Exhaust Mach Number; a) Forward Region, b) Aft Region.

Shear Layer Spectral Broadening Effects

Spectral broadening of an acoustic signature as it is passed through a wind tunnel shear layer has been shown to be a function of the freestream Mach number, shear-layer thickness, and the acoustic wavelength (Ref. 6,7). Scattering occurs at high frequencies when the acoustic wavelength is small compared to the shear-layer thickness. The energy at a particular frequency is scattered into other frequencies while the total energy is conserved. In terms of tonal noise, the peak level decreases, while the spectrum broadens at the tone frequency. For broadband noise, spectral broadening effects are minimal since attenuation at one frequency is compensated by the scattering from adjacent bands.

Fig. 7 shows the frequencies where spectral broadening begins based on the measurement angle in LSAF. The criteria for spectral broadening from references 6 and 7 are both shown. The amount of spectral broadening, (i.e., the spectral bandwidth, Δf, at a point which is 10 dB below the peak level), is shown in Fig. 8 for frequencies from 5 kHz to 25 kHz.

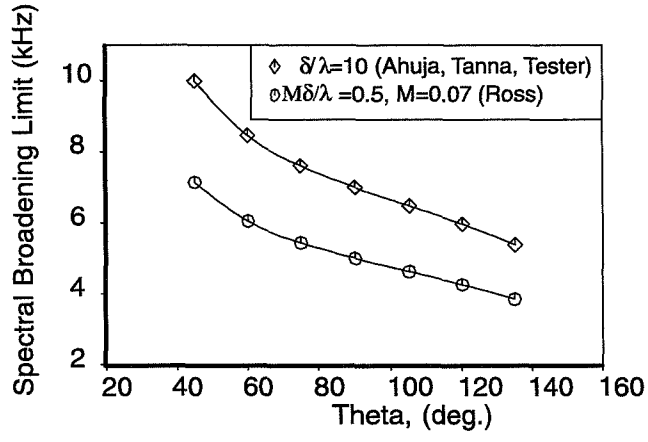

Fig. 7. Frequency Limit for the Onset of Spectral Broadening vs. Sideline Angle for LSAF.

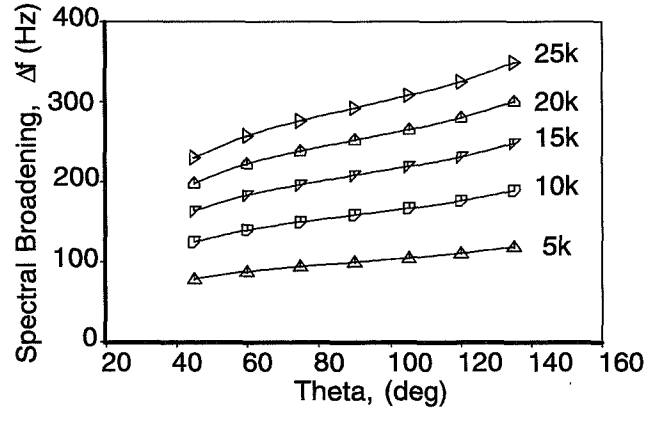

Fig. 8. Spectral Broadening, Δf, vs. LSAF Measurement Angle at M=0.07.

In an effort to examine the effects of spectral broadening, the rotor-alone case was operated at three Mach numbers as shown in Fig. 9. The tone at 3BPF was chosen since the scattering effects are greater at higher frequencies. The spectral broadening of the major tone (3BPF) is seen to be less than the predicted value of 160 Hz shown in Fig. 8 for all of the Mach numbers examined.

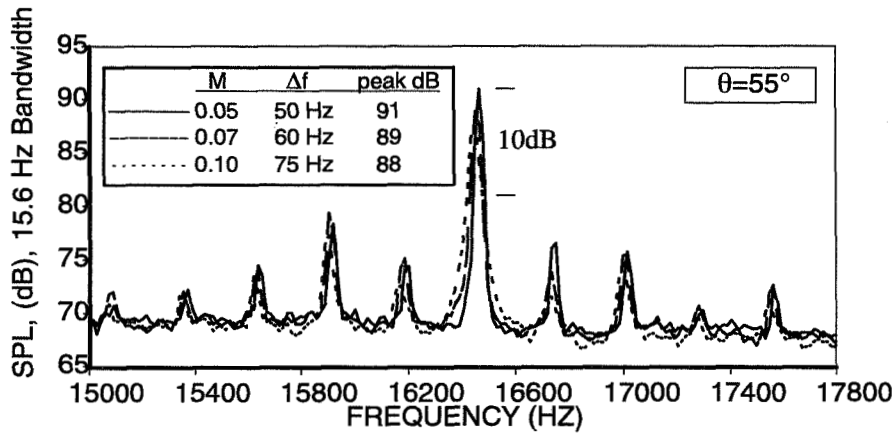

Fig. 9. Spectral Broadening of the 3BPF Rotor-Alone Tone Noise at Various Mach Numbers

Fig. 10 shows the sound power spectrum from a rotor-alone condition in which "haystacks" were seen to be generated about the base of the blade-passage harmonics. (This plot has been processed with the tone-removal algorithm of Section 4.4.) Note that the bandwidth of the tonal spreading is significantly higher than what would be expected due to spectral broadening from the shear layer. Because of this, these modulated spectral shapes are considered to be due to mechanisms other than spectral broadening due to the LSAF shear layer. This phenomenon will be discussed in Section 4.5 with regard to the rotor interaction with the inlet boundary layer.

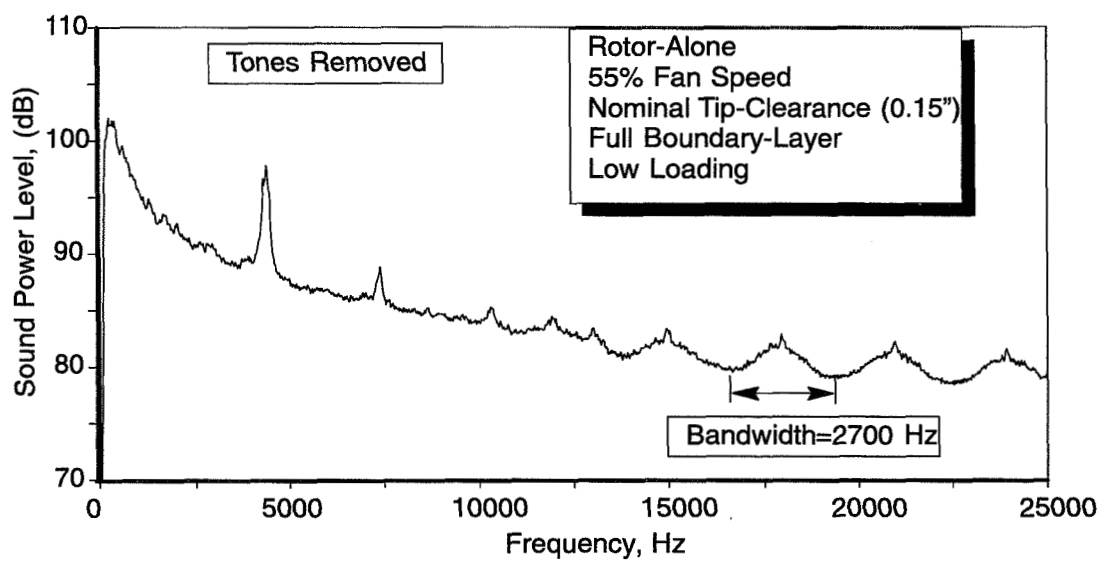

Fig. 10. Rotor-Alone Sound Power Spectrum Illustrating Haystacking effect not Attributed to Spectral Broadening from the shear Layer.

2.2 Boeing 18 inch Fan Rig

General rig configuration

Fig. 11 depicts the general configuration of the test rig. In the inlet, there are six axial locations where microphones can be installed in the six ribs of microphone ring arrays at any of 80 equi-spaced locations around the annulus. The most downstream of these is also the axial location where the boundary layer rakes are installed, as are the traversing inlet hotwire probe and traversing boundary layer total pressure probe.

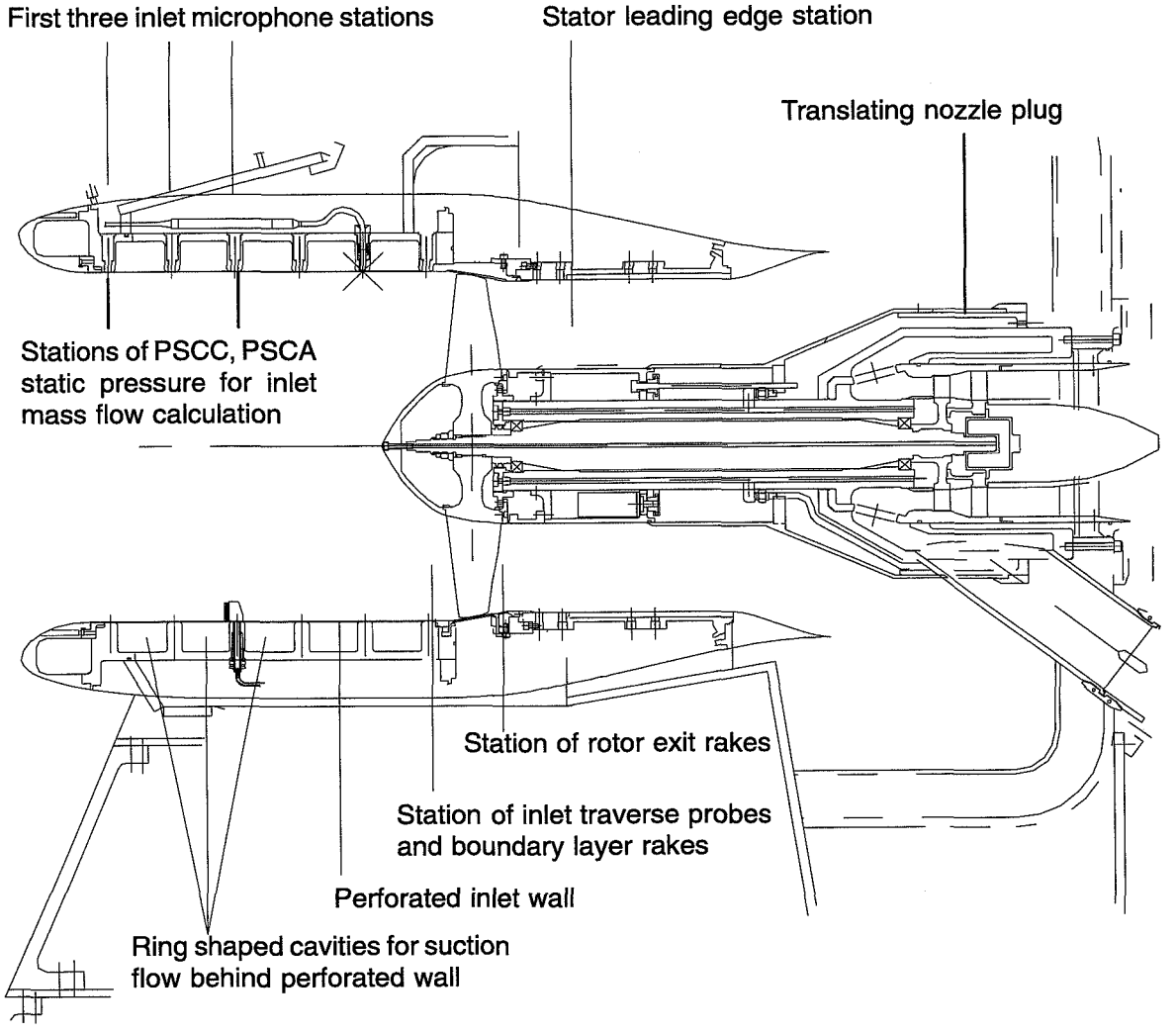

Fig. 11. Boeing 18 inch Fan Rig General Configuration

Inlet boundary-layer suction

The entire inlet surface from the first to last microphone location is a perforated wall through which the boundary-layer flows when the suction system is operating. The five ring shaped cavity regions

behind the perforated wall and between the axial microphone locations are the main collection channels for the boundary-layer suction flow. There is a manifold for these collection channels at the top and bottom of the rig. The suction flow from both the top and the bottom travels to the rear of the rig and down through a pipe located in the pedestal on which the rig is mounted. The pipe travels along the floor and walls of the test chamber and then exits the chamber. Outside the chamber, the pipe reaches the suction compressor which then exhausts to ambient outdoor conditions.

Near the beginning of the test, the boundary-layer suction system was evaluated at all fan speeds at one loading level. During this portion of the test, the four inlet boundary-layer rakes and a inlet traversing total pressure probe were installed close to the fan face. A full boundary-layer with no boundary-layer suction defines one extreme. "No boundary layer" defines the other extreme. The no boundary-layer level has zero boundary-layer thickness at all the fan speeds except the highest. At the highest fan speeds there is a portion of the boundary layer which is not removed. Data was acquired for the full boundary-layer, no boundary-layer and many levels of suction between these two extremes. The third level of boundary layer that would be used throughout the testing would be a partial boundary-layer. The partial boundary layer level is intended to have half the displacement thickness of the full boundary-layer. A more complete description of the boundary-layer bleed system and its evaluation is contained in section 2.3 of this report.

Loading variation

Downstream of the rotor at the rear of the mainstream aft duct, there is a translating nozzle plug mounted to the center body of the rig. The plug is shown in its most aft position in Fig. 11. This nozzle plug translates axially in order to adjust the fan loading. The forward sleeve of the plug slides under a sleeve which holds the stators and rotor exit hub instrumentation rakes. This stator mounting sleeve (not shown in Fig. 11) is attached to the non-rotating centerbody of the rig just aft of the rotor trailing edge. There are three main loading levels used for the test. At design fan speed, the loading was increased until the onset of stall. The loading was then decreased to a level slightly below the onset of stall. This nozzle plug setting was used at all fan speeds and defines the high loading line. The medium loading level was defined as a nozzle plug location which resulted in fan operation at design speed and design pressure ratio of 1.455. The lower loading line was consistent with some previous testing and also is the condition where the rotor nears its choke flow at design speed.

Tip-clearance variation

The fan tip-clearance can be varied by installing a shim on the shaft on the rear side of the rotor blisk. For this test, there were three clearance levels. The small clearance configurations had a mid chord static clearance of 0.050cm (0.020in), medium clearance had 0.089cm (0.035in) and large clearance had 0.127cm (0.050in). Clearance measurements were taken during rig operation in an attempt to measure actual running clearances. There were three clearance probes in the rubstrip over the rotor tip at mid chord. Each of these three capacitance probes was individually calibrated on the rotating rotor with another probe which was not installed during actual test operation. The three probes were only calibrated for the small clearance configuration and therefore could not be used to measure running clearance for the medium or large clearance cases. For all fan speeds at the small clearance, the three probes measured approximately 0.050cm, 0.050cm and 0.076cm (0.030in). This results in the small clearance configuration having an average running clearance of 0.064cm (0.025in), for medium clearance the average was 0.102cm (0.040in) and for large clearance the average was 0.140cm (0.055in). The static-to-running correlation for the small clearance was applied to both the medium and the large clearance. The ratio of clearance to mid chord blade height was 0.5% for the small, 0.8% for the medium and 1.1% for the large. This range of clearance to mid-chord blade

height is consistent with typical high bypass engine fan operation. The measurements indicate an asymmetric clearance variation which is not unexpected since this rotor is cantilevered a significant distance. The increase of clearance from static to running operation is influenced by the axial location of the tip clearance probes. As the rotor untwists as it runs, the blade location that is actually measured by the clearance probe is from a more aft static position which has a lower tip radius due to the radial slope of the rotor tip from leading edge to trailing edge. The radial growth due to centrifugal load appears to be countered by the untwist axial motion of the blade.

Blunt spinner

The spinner is quite blunt compared to conventional designs which are more conical. The reason the spinner is blunt is due to the initial design and test plans for the rig. Originally, there was a plan to attempt some laser flow-field measurements from a location in front of the rig, but some distance away from the line of rotation. In order to allow a larger portion of the blade span to be examined, a shorter spinner was designed.

Rotating portion of the fan rig

The rotor, spinner hub forward of the rotor, and a small ring attached to the rear of the rotor disk are the rotating portions of the flow path.

Fan rotor design

The fan rotor was designed using a U. S. Air Force program, UD0300M (Ref. 1). The design is intended to represent a conventional transonic wide chord fan. The following table summarizes the major design characteristics of this fan rotor.

Table 1.Rotor Design Parameters

Design Parameter	Value
Stage Pressure Ratio	1.455
Corrected Flow	24.81kg/s (54.7lb/s)
Flow per Rotor Inlet Area	180.3kg/s/m^2 (36.9lb/s/m^2)
Tip Speed	396m/s (1300ft/s)
Tip Relative Mach Number	1.29
Number of Blades	20
Hub/Tip Ratio	0.402
Aspect Ratio	1.65
Diameter	0.457m (18.0in)
Tip Solidity	1.15
Hub Solidity	2.46
Tip Max Thickness/Chord	0.025
Hub Max Thickness/Chord	0.100
Thickness–Leading/Trailing Edge	0.038cm (0.015in)

The flow per rotor inlet area is low relative to conventional wide chord fans. However, the higher design tip-speed generates a tip relative Mach number that is typical. The flow per rotor inlet area

needed to be low for operation without stators. Without stators, there is no increase of static pressure in the aft duct, and at low fan speeds a higher design flow rate could have resulted in an adverse pressure gradient on the outer diameter of the flow path where the fan aft duct exhausts to ambient. The possibility of such an adverse pressure gradient was determined to be unacceptable for this test since a large amount of test data would be collected at low fan speed.

Rotor geometry

The fan rotor design code provides coordinates that define non–standard airfoil sections at specified spanwise locations. Fig. 12 shows several design airfoil sections from hub to tip. The coordinates are for the fan at its design speed. In order to manufacture the blades, the design speed coordinates have been adjusted to generate manufacturing coordinates. This adjustment has been accomplished using tools employed by in–house engineers knowledgeable in rotating turbomachinery mechanical methods.

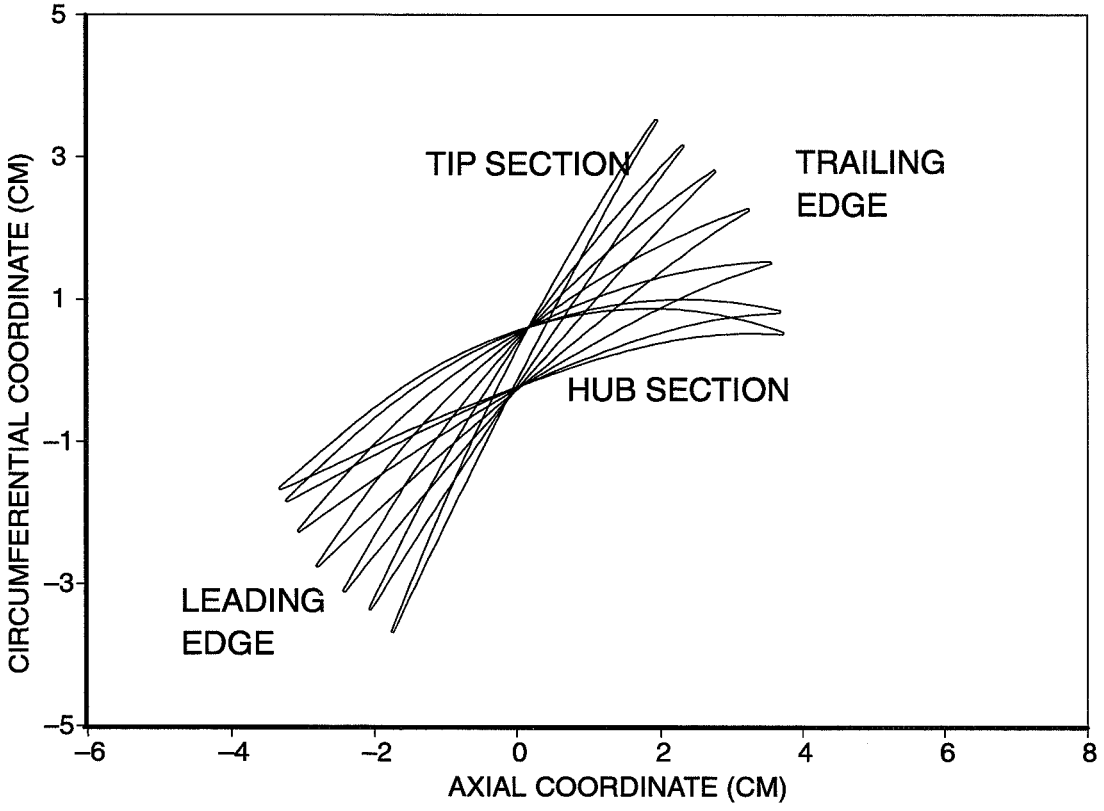

Fig. 12. Rotor Design Airfoil Coordinates

In order to provide the most symmetric and consistent relationship between the relative locations of the 20 blades to one another, the blade design is in the form of a blisk, an integrated set of blades and disk. The blisk was manufactured by an external supplier with experience in this field. As part of the blisk inspection, the angular position of each blade tip was evaluated and the largest error of circumferential position is 0 degrees 2 minutes 0 seconds.

The blisk inspection also included verification that the blade airfoil sections were within specified tolerances. The radial tolerance for an airfoil section was ±0.0254cm (0.010in). The airfoil rota-

tional tolerance was 0.25 of a degree. Axial chord tolerance was ±0.0127cm (0.005in). Airfoil surface location tolerance was ±0.00762cm (0.003in). Airfoil surface location tolerance within 0.635cm (0.25in) of the leading or trailing edges was ±0.00254cm (0.001in).

The inspection included evaluating one blade at all twelve inspection sections and the remainder of the blades at a hub, mid and tip section. The inspection was done by using a ten-times size plot of the specified airfoil surface projected onto a screen. The actual blade surface was traced and projected on the screen where it was visually compared with the inspection plot.

In general, the airfoils were extremely accurate. Only a few of the surface definitions were not within specifications and those were no more than a few thousandths of a centimeter out of specification.

Stator geometry, different sets, different axial positions

The stators were designed to do as much turning as possible at reasonable loading levels. The stators are double circular arc airfoils. Stator noise generation due to excessively high stator loading was to be avoided in the acoustic testing. Consequently, the stators do not remove all of the swirl from the flow. The stator exit swirl-angle varies from 35° at the hub to 10° at the tip. The camber varies from 10° at the hub to 32° at the tip. The leading edge and trailing edge thickness are 0.050cm (0.020in). The maximum thickness-to-chord ratio varies from 5% at the hub to 7% at the tip. There is no area contraction across the stator vanes as would be expected. This was mainly due to the complexities that would be introduced to the existing aft duct geometry in order to integrate such a contraction with the translating nozzle plug and the aft portion of the nacelle.

There are three sets of stators all with the same design specifications except that there are three chord values. The nominal set of 30 has a chord of 4.45cm (1.75in) and a maximum count of 60. The small set of 60 has a chord of 2.22cm (0.875in) and a maximum count of 60. The large set of 15 has a chord of 8.89cm (3.5in) and a maximum count of 30. The nominal set at 30 count, small set at 60 count and large set at 15 count have the design solidity. Solidity can be doubled with either the nominal or large set. The design solidity varies from 1.9 at the hub to 1.0 at the tip.

The stators can be mounted in two axial locations and Fig. 11 indicates the leading edge station in the forward position. All testing occurred with the stators in the forward position. The aft duct hot-wire instrumentation traversed at an axial location near the leading edge of the nominal-size stator vanes in the forward position.

Operation without stators

For the segments of the test when there were no stators installed, the hub sleeve downstream of the rotor was still installed. This sleeve over the centerbody supports the stators when they are installed. In order to keep the rotor conditions consistent for the cases with and without stators, the sleeve remained installed for all testing.

Potential for laser flow field measurement

The final design of the rig and its mounting pedestal allowed for laser measurements of the rotor flow field. Space was allowed in the base of the rig mounting pedestal for installation of the necessary instrumentation to take laser measurements through a window mounted over the rotor tip. No laser data acquisition has occurred on the rig.

2.3 Inlet Boundary-Layer Suction System

One of the unique features of the 18 inch Boeing fan rig is its capability to remove the inlet boundary layer by suction. The suction flow system consists of the following principal components:

- Inlet surface facesheet
- Suction flow collection and metering system
- Suction pump

Removal of the inlet boundary-layer occurs over the full length of the inlet from the downstream end of the bellmouth lip to the interface with the rubstrip. The inlet surface is a porous facesheet with a thickness of 1 mm and an open area ratio of 0.01. The holes in the facesheet have a diameter of 0.12 mm at the inner and 0.25 mm at the outer surface. The facesheet is supported by 6 ribs which are part of the outer barrel that forms the outer wall of the cavities that confine the suction bleed flow. The 5 ring shaped cavities drain the suction flow into the pedestal that supports the fan rig and the strut above the inlet.

The plenum inside the fan support-pedestal is connected via a 0.20 m (8 inch) diameter pipe to the suction pump. This pipe system includes a straight and a curved pipe section that were calibrated to provide massflow rates based on local static and total pressure and total temperature.

The suction pump is an eight stage radial compressor. The suction flow is controlled with the rotational speed of the compressor and a valve that controls induced flow at the upstream end of the compressor. The function of this valve is to provide stall-free operation of the pump when the suction requirements fall outside the operating envelope of the pump. This valve was closed for all conditions with complete removal of the inlet boundary layer. However for conditions with partial removal of the boundary layer the required suction massflow rates were sufficiently small that it was necessary to open the valve to prevent unstable operating conditions in the suction pump.

In order to eliminate reverse bleed flow during conditions without suction, a shutoff valve was incorporated in the pipe system that was closed for all conditions without suction. The axial pressure gradients in the inlet are minimal because of its cylindrical cross-section. However some pressure gradients are present close to the hilight because of the strong curvature in the flow around the inlet lip and close to the fan face because of the acceleration of the flow around the spinner. These pressure gradients will cause some flow through the facesheet, from the inlet into the cavity in areas of high inlet surface pressure and vice versa. This will result in some recirculation of the boundary layer from high to low pressure areas. Comparison of predicted and measured boundary layer profiles and displacement thickness show close agreement. This indicates that the development of the boundary layer over the porous inlet surface for conditions without suction is not significantly affected by the small amounts of recirculation through the facesheet.

The suction pump and its exhaust are located outside of the anechoic chamber. Far field acoustic measurements without and with maximum suction and the fan windmilling indicate that the noise of the suction system does not contaminate the far field noise data. This is also demonstrated by the data shown in figure 2. It shows that with no boundary layer (maximum suction) the far field noise increases by more than 15 db between conditions with the fan windmilling and 55% corrected fan speed. This confirms that the noise floor due to the suction system is well below the fan noise even at low corrected fan speeds.

Three inlet boundary-layer conditions were evaluated during the test, namely the full boundary-layer, the half boundary-layer and no boundary layer. For the full boundary-layer conditions the shutoff

valve in the suction system was closed. For the no boundary-layer conditions the suction pump was operated at its maximum rotor speed independent of fan operating conditions. Half boundary-layer conditions are defined as conditions with the inlet boundary-layer displacement thickness one half the size of its value for the full boundary-layer. The suction flow requirements for the half boundary-layer conditions were established during the evaluation of the inlet boundary-layer profile.

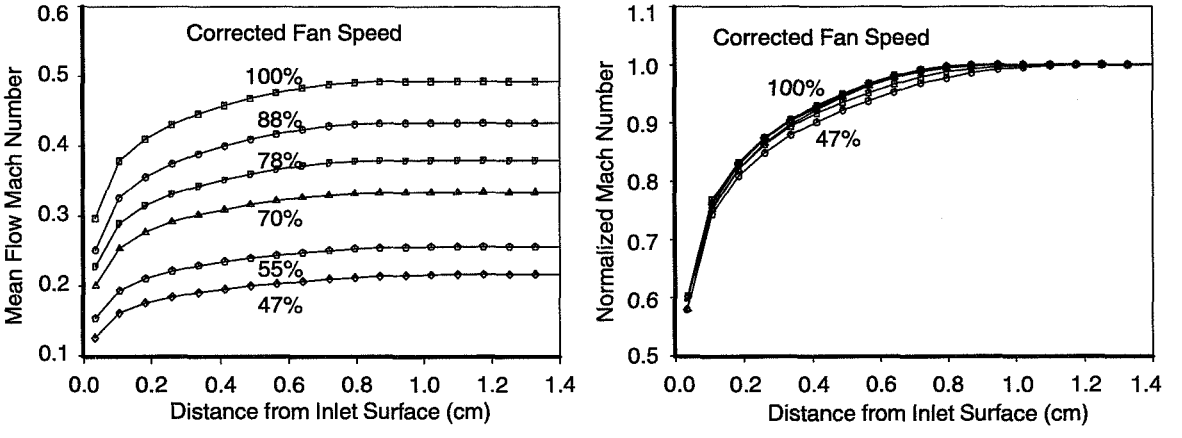

Fig. 13. Inlet Boundary-Layer Mach Number Profiles

The inlet boundary-layer was initially evaluated with a radially traversing total pressure probe. Because of its shape it is called a fishhook probe. It allowed measurements right up against the inlet surface. It was inserted in one of the microphone ports near the bottom of the inlet in the ring array closest to the fan face. Its static pressure port was located 38 mm upstream of the fan face. The probe was traversed in 0.8 mm increments from the inlet surface to a maximum insertion depth of 17 mm. The measured total-pressure profiles have been used together with the local static pressure and the total temperature to compute the Mach number and velocity profiles. The inlet boundary layer thickness was defined as the distance from the inlet surface where the velocity reaches 99.5 percent of its freestream value. The boundary layer profile was integrated to determine its displacement and its momentum thickness.

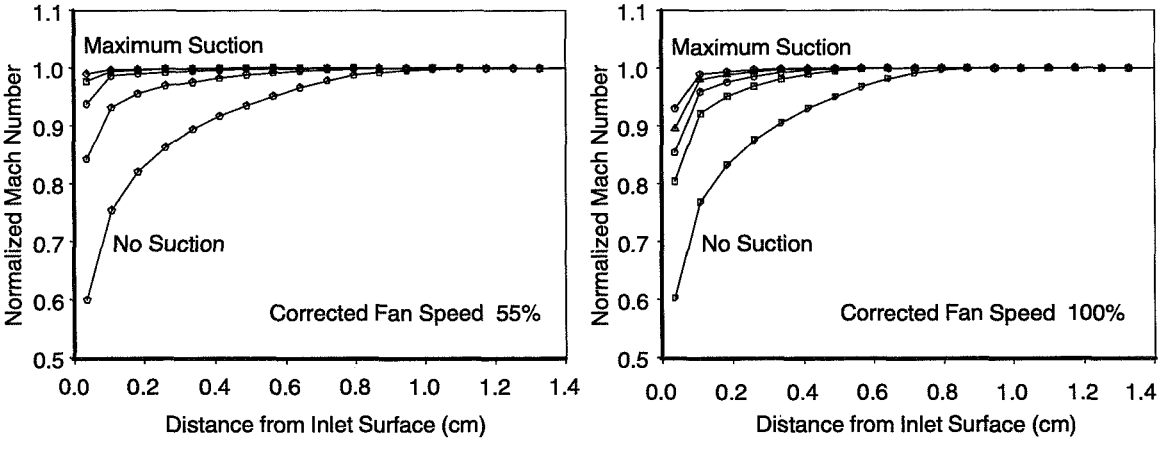

Fig. 14. Inlet Boundary-Layer

Mach number profiles based on the total pressure profiles measured with the fishhook probe are shown in Fig. 13. The results indicate that the boundary-layer thickness slightly decreases with increasing inlet mass flow rate. This trend for the boundary-layer thickness is comparable to what is expected for a flat plate boundary-layer because of the increase in the Reynolds number.

Boundary-layer profiles for different suction levels and two different fan speeds are shown in Fig. 14. With increasing suction level the boundary layer shrinks in size. At the low fan speeds the maximum suction level leads to near-elimination of the boundary layer. At high inlet mass-flow rates, at corrected fan speeds above 80% the velocity defect of the inlet boundary-layer is still quite apparent even at the highest suction flow rates.

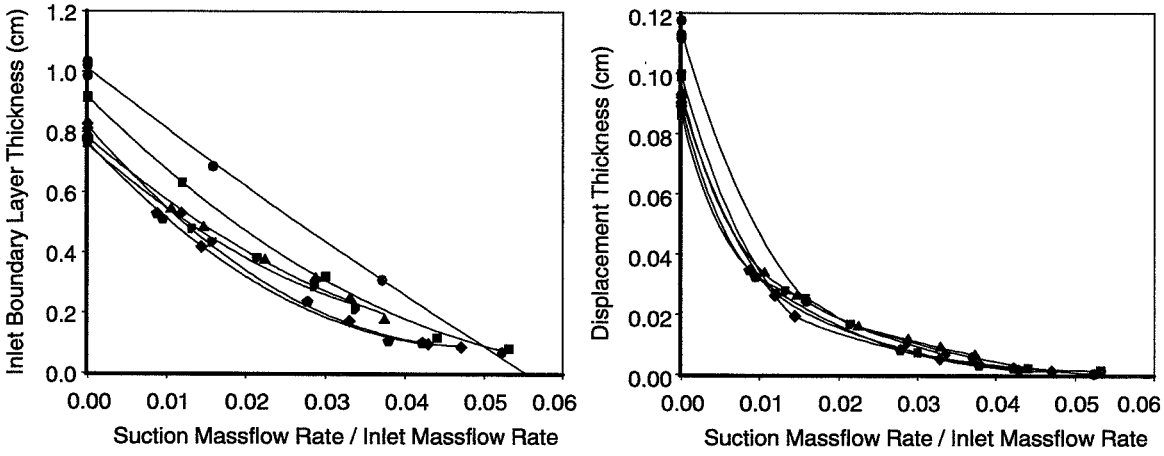

Fig. 15. Inlet Boundary-Layer Thickness

The variation of the inlet boundary-layer thickness and the displacement thickness with the ratio of the suction mass-flow rate to the inlet mass-flow rate is illustrated in Fig. 15. The results indicate that the range of suction rates evaluated covered a range of zero to six percent of the inlet massflow rate. The displacement thickness is decreasing much more rapidly with suction than the boundary layer thickness. This reflects the fact that the boundary-layer profile becomes more full with increased suction flows, as shown in Fig. 14. The lines are curve fits to the measured data points and represent data for different corrected fan speeds. The uppermost lines represent low speeds and the group of lower lines is made up of the higher fan-speed data. The massflow rate of the flow in the boundary layer without suction is about .9 percent of the inlet massflow rate. The suction massflow rates required to reduce the displacement thickness to 10 percent of its value without suction are therefore in the order of 3 times as large as the massflow rate in the boundary layer without suction. This is an indication that a more effective boundary layer control system would apply higher suction rates over a shorter axial segment of the inlet closer to the fan face.

One of the parameters most sensitive to the suction flow-rate was the pressure drop across the inlet face sheet. The variation of the inlet boundary-layer displacement thickness with this parameter is illustrated in the left half of Fig. 16. Each line is a curve fit for the data acquired at a particular corrected fan speed. Data at a pressure drop of zero represent the conditions without suction, the full boundary-layer thickness. The region of interest for the control of the half boundary-layer conditions is the area where the displacement thickness is one half of its value for the full boundary-layer. Unfortunately the data base does not include any data in that area. Curve fits were therefore used to develop a correlation between the pressure drop across the inlet facesheet and the corrected inlet

mass-flow rate for the half boundary-layer conditions. This correlation which is shown in the right half of Fig. 16, was then used during the test to set the rotor speed of the vacuum pump and the control valve at the entrance of the vacuum pump to provide adequate suction flows for the conditions with the half boundary-layer. Due to the shortcomings of the data base used in the development of this schedule, the displacement thickness of the half boundary layer conditions may deviate substantially from the desired values.

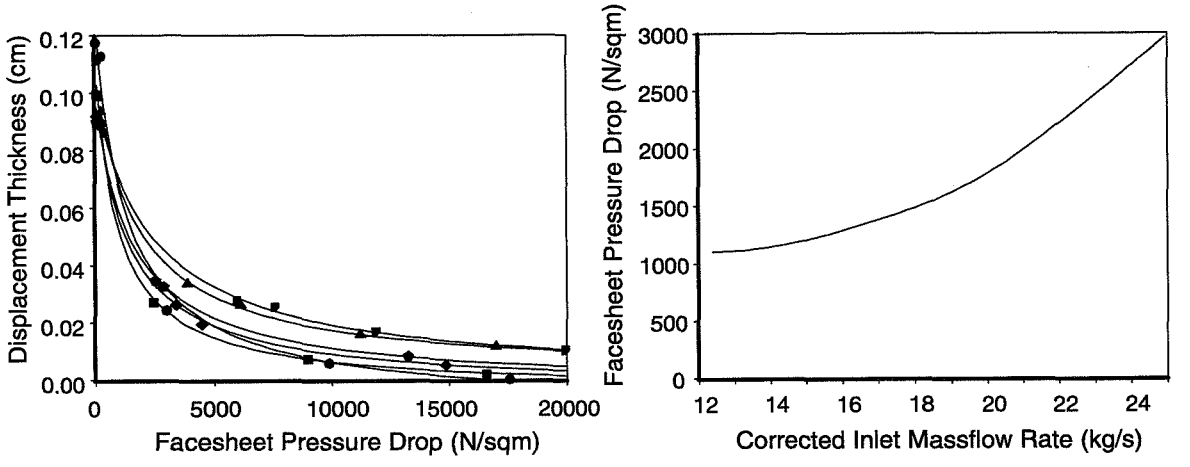

Fig. 16. Suction Flow Control Schedule for Half Boundary-Layer Conditions

3 Instrumentation

3.1 Performance Instrumentation

Rotor mass flow static pressures

There are eight static pressures (PSCC) located just upstream of the perforated inlet and equi-spaced around the annulus as depicted in Fig. 17. There is a similar set (PSCA) located in the fourth axial location of microphones from the inlet. The PSCA statics were used to calibrate the inlet mass flow before any testing of the rig. For the calibration test the inlet and a centerbody without rotor were installed in a wind tunnel. The wind tunnel can operate at varying freestream velocities and varying mass flows through the inlet. The mass flow through the inlet continued through a closed circuit and through a venturi measuring device. The calibration was done by a group experienced in inlet flow calibration and in their facilities typically used for this type of calibration. The accuracy quoted for this test is within $\pm 0.5\%$ of mass flow. The perforated inlet was sealed and tested for leaks prior to the inlet flow calibration test.

During the actual test of the fan rig for cases without boundary-layer suction, a correlation was developed between the calibrated PSCA statics and the PSCC statics upstream of the perforated inlet. For cases with boundary-layer suction, the PSCC statics were used to determine inlet flow and the rotor flow was calculated by subtracting the suction flow from the inlet flow.

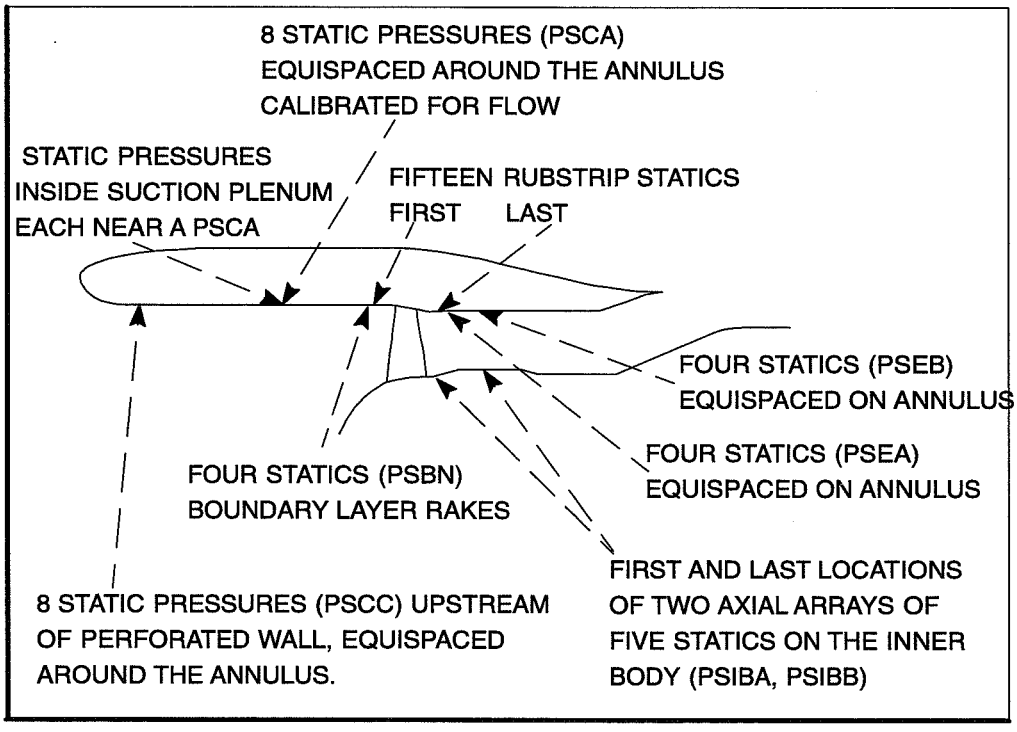

Fig. 17. Static Pressure Ports in the Mainstream Flow Path

Inlet suction mass flow static pressures

There are three statics in one of the ring-shaped suction cavities. Each of the three is located near a PSCA port. A pressure differential across the perforated sheet was calculated and correlated with

the mass flow through the suction system. The suction system itself had three sets of instrumentation at different locations in the suction pipe, each calibrated for mass flow. There was good consistency between the three sets, but one of the sets had better results at the lowest suction rates and therefore its data is used and correlated with the pressure differential across the perforated wall.

Inlet boundary-layer rake static pressures

There are four statics (PSBN), one for each of the inlet boundary-layer rakes at the axial location of the aft-most inlet microphone array. These statics were used along with the boundary-layer rake data to calculate boundary-layer velocity profiles.

Rotor rubstrip case static pressures

There is an axial array of fifteen statics (PSRS) that begins upstream of the rotor leading edge and ends downstream of the rotor trailing edge. These statics are mainly used as part of the rotor exit blockage evaluation which will be described in a later section.

Aft duct case static pressures

At two axial locations in the rotor aft duct, there is a set (PSEA, PSEB) of four statics equi-spaced on the case about the annulus. These are also part of the blockage evaluation.

Aft duct hub static pressures

At two annular locations in the rotor aft duct, there is a set (PSIBA, PSIBB) of five statics on the inner flow path wall covering an axial distance from near the rotor trailing edge to the cylindrical portion of the aft duct upstream of the stator leading edge. These are indirectly used in the blockage evaluation.

Inlet boundary-layer total-pressure rakes

The traversing total pressure probe and details of its use are described in another section of this document.

The four boundary layer rakes were installed during portions of the performance data acquisition. The main functions of these rakes were to confirm the measurements made by the traversing probe and to measure the symmetry of the boundary layer around the annulus. These rakes were mounted 38 mm upstream of the fan tip leading edge and the probe tips were 1.6cm forward of the mounting. At this inlet location the case wall radius is 0.23 m (9.063in). Each probe had sixteen chamfered pitot heads which covered a radial range from 0.229 m (9.018in) to 0.206 m (8.118in). The spacing between each head was 1.52 mm (0.060in).

The traverse probe data and the data from these rakes was consistent. Since the traverse probe was able to get closer to the wall and take data at smaller radial increments to better measure the boundary layer, it has been used to define the boundary-layer profiles.

The rake data indicated that the boundary layer was very uniform around the annulus.

Rotor trailing edge total pressure and temperature rakes

Fig. 11 indicates the location of the total pressure and temperature rakes downstream of the rotor. There are two rakes mounted on the inner wall and two on the outer wall. Each of the four rakes has both total pressure and total temperature probes. On each rake, the total pressure and temperature probes are in a pair at a specified radius. There are four, five or six pairs on the different rakes. The radial locations alternate between the rakes in order to allow an appropriate distance between

adjacent probes on each rake. The head of the probes at all radii are about 1.27cm (0.50in) downstream of the trailing edge of the rotor blades.

There are twenty pairs of probes spanning the radial distance across the aft-duct annulus. The inner and outer wall radii at the probe-head location are 0.102 m (4.00in) and 0.220 m (8.67in), respectively. There are probe heads at eight radial locations between 0.198 m (7.79in) and the outer wall. There are probe heads at seven radial locations between 0.127 m (4.99in) and the inner wall. The remaining five radial locations are between 0.132 m (5.20in) and 0.188 m (7.39in). The intent was to put as many radial probe locations near the end walls as would be reasonable without having too many rakes. The actual radial location of each total pressure and temperature probe head was measured once the rakes were installed in the rig. The radial locations are accurate to within ± 0.025cm (0.010in).

The total pressure probes are Kiel-type probes manufactured by United Sensor. The sensor head shroud diameter is 0.158cm (0.0625in). The Kiel probe is able to accurately capture total pressure within an angle of 35 degrees from its center line. Each total temperature probe is an aspirated, chamfered cylinder with an outer diameter of 0.158cm (0.0625in) diameter. The total temperature probes are made of thermocouple wire that was purchased from a vendor and was manufactured and calibrated to an accuracy of ± 1.0 °F. The wire was re-calibrated in–house to an accuracy of ± 0.25 °F prior to the wire installation in the in-house chamfered probes. The thermocouple wires were not able to be recalibrated after manufacture of the probe. The in–house manufactured temperature probe is able to accurately capture total temperature within an angle of 15°–20° from its center line. The total pressure and total temperature sensors in a pair are separated from each other by 4.76 mm (0.188in). Sensors on a rake at adjacent radii were no closer than 5.1 mm (0.20in). Each of the four rakes has a maximum width of 9.53 mm (0.375in). The rakes are angled at forty degrees for the inner and for the outer. The angle range that the inner rakes experience is from about fifty degrees at the hub to 35° at mid span. The angle range that the outer rakes experience is from about 35° at mid span to sixty degrees at the tip. None of the rake instrumentation was recalibrated during or after the test. The total-pressure probes measured a pressure difference relative to a reference pressure measurement. The total temperature probes measured a temperature difference relative to a freestream total temperature measurement mounted on the outer side of the nacelle.

3.2 Performance Instrumentation During Acoustic Test

During the acoustic portion of the test, the intrusive performance instrumentation was removed. This instrumentation includes the four inlet boundary-layer rakes, the inlet traverse probes, the fan rotor exit rakes and the fan aft-duct hotwire traverse probe.

3.3 Hotwire Instrumentation

The velocity fields in the inlet and the fan duct have been evaluated with hotwire anemometers. The primary purpose of these measurements is to define the unsteady velocity components incident on the rotor and stator blades, but the measurements also provided the mean flow velocity and flow angle. The inlet flow data was acquired at an axial position as close as possible to the fan face. In the fan duct the sensor elements of the hotwire were positioned near the plane of the leading edge of the smallest stators. The inlet flow measurements were concentrated in the inlet boundary layer region but extended to radial positions 0.102 m (4 in.) from the inlet surface. The fan-duct measurements covered the full radial extent from the hub to the outer wall. For some conditions concerned with variations in the inlet boundary-layer thickness or the tip clearance relative to the baseline configuration that were expected to cause differences primarily in the flow close to the outer wall, the data was restricted to a limited radial extent covering the outer wall region.

In order to define the unsteady velocity fields incident on the rotor and the stators as completely as possible, all 3 unsteady velocity components were measured. The measurements were conducted with cross-wire probes, which measure the streamwise and only one transverse component simultaneously. Two different probes were used to acquire the two transverse components (circumferential and radial). The data acquisition system allowed only for the acquisition of data from one sensor at any one time and therefore the data for the two transverse components were acquired in two different data sets. However each data set includes the time history of a synchronizing pulse. This pulse makes it feasible to create pulse–synchronized averages and to combine such averages from different data sets.

The mean flow angle relative to the probes has been minimized by lining up the probes with the local mean flow. For the measurements in the inlet the probes have been lined up parallel to the inlet axis. In the fan duct the probes are oriented normal to a radial line and offset by an angle of 30 degrees relative to the fan axis.

A preliminary evaluation of hotwire and hotfilm sensors indicated that the hot films had a limited frequency response and that the high-frequency content of their signals is contaminated by self–noise. Based on this evaluation and Reference 8 it was also learned that the noise floor of hotwires can be reduced and their durability can be improved by stiffening the prongs that support the sensing elements without affecting the steady state or dynamic response significantly. By applying epoxy to the base of the support prongs the reliable operating range of the hotwire sensors has been extended to 250 m/s. Based on these results the following sensors were selected and appropriately modified for the measurements:

- Inlet, streamwise and transverse velocity component — TSI 1249BA–T1.5
  streamwise and radial velocity component — TSI 1246–T1.5
- Fan duct, streamwise and transverse velocity component — TSI 1246P–T1.5
  streamwise and radial velocity component — TSI 1246–T1.5

Hotwire sensors have unfortunately highly non-linear operating characteristics. This requires that velocity and flow angles are computed based on calibration characteristics that differ from sensor to sensor. The steady state calibration characteristics were determined for each sensor by evaluating their signals in the flow of a calibration device. This evaluation covered 17 velocities from 15 to 260 m/s and 13 angles from –30 to 30 degrees, a total of 221 points. Cables and anemometry control units are matched between the calibration and the actual test setup. The calibration characteristics may

change during operation if the wires are stretched due to excessive steady or dynamic loads resulting from vibration of the support structure or if minute particles are deposited on the wire.

The hotwire is not only sensitive to changes in velocity, but also to pressure and temperature variations. To minimize the effects of fluctuating temperature on the hotwire signal, the wires were operated at a high temperature (250 deg. C.). The effects of local total temperature and static pressure on the steady-state results are minimized by accounting for them in the data analysis. For the inlet measurements the pressure at the sensor was assumed to be equal to the inlet surface-pressure measured at the axial position of the hotwire sensor and the total temperature was assumed to be equal to that measured in the freejet flow. For the fan duct measurements the local static pressure was computed based on the local surface pressures measured on the hub and the outer duct wall and using the assumption of constant swirl velocity independent of radius. The pressure profiles predicted by this method closely matched those predicted with the PERCH code. The local total-temperature was measured by a thermocouple riding beside the cross-wire probe at the same radial position on the same traversing mechanism.

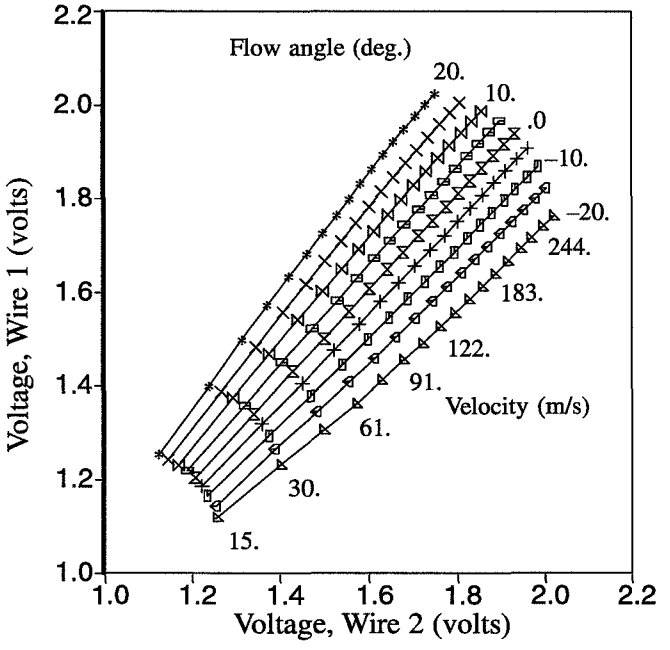

Fig. 18. Cross–wire calibration characteristics

The cross-wire signals were filtered for anti-aliasing by a Krohn-Hite 4-pole lowpass filter at 50 kHz. The synchronizing pulse signal and the voltages from the 2 wires were then sampled at a rate of 100 kHz and converted into 16-bit digital signals. The sample length for each data point was one second. The digitized data was then transferred to disk for post–test analysis. The data acquisition and analysis procedure is outlined in Fig. 19.

Data analysis occurred in two steps, both of them off-line. In the first step the time histories of the cross-wire voltages were transformed into time histories of instantaneous velocity and flow angle, by using the sensor calibration characteristics and the values of local static pressure and total temperature. The data is corrected to first order for deviations in the mean fluid properties between the test and the calibration conditions. The corrections attempt to account for changes in the fluid density, molecular viscosity and fluid thermal-conductivity. The corrective terms are based on the local total

temperature and the local static pressure in the fluid during the calibration and the actual test conditions.

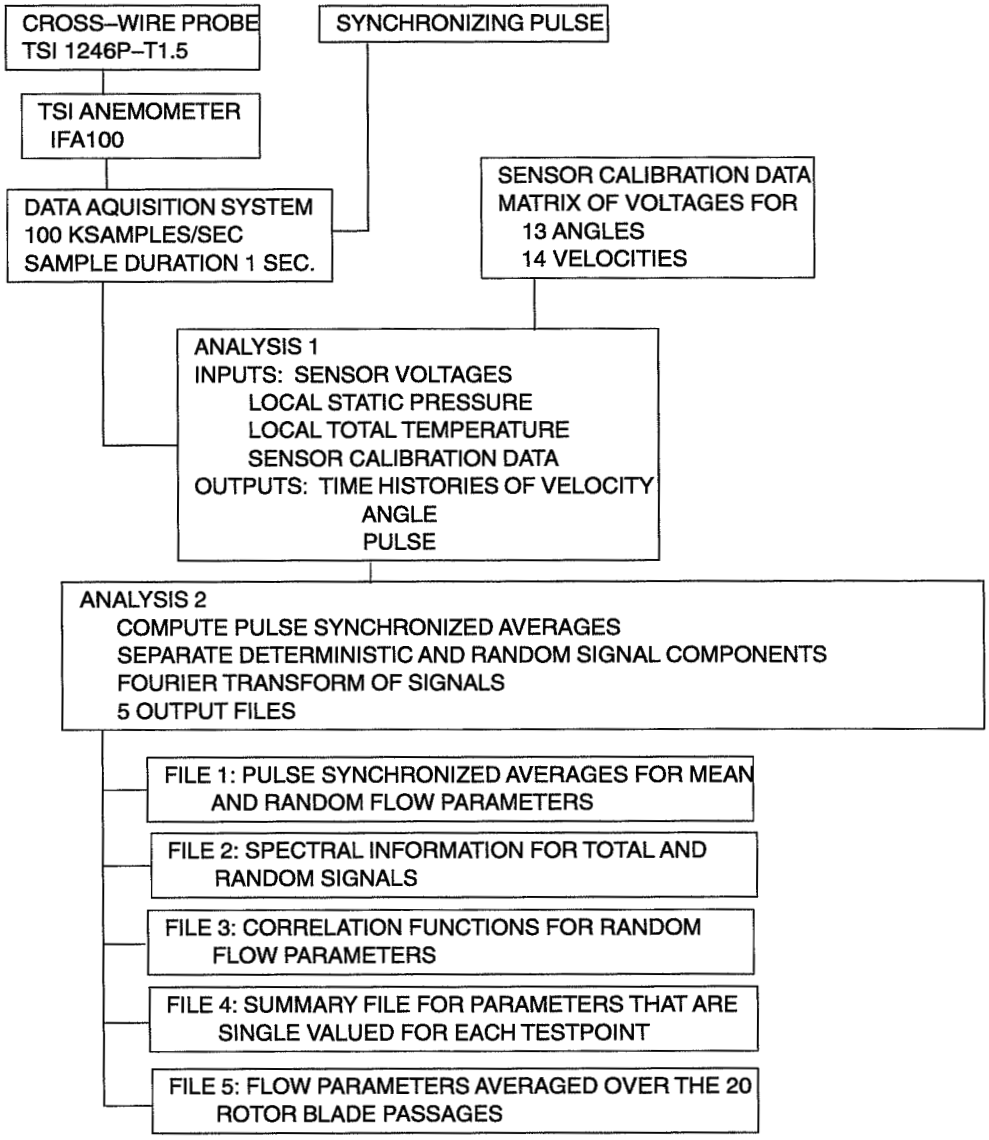

Fig. 19. Hotwire Data Acquisition and Analysis System

The second analysis makes use of the time histories of the synchronizing pulse, the velocity and the flow angle. The hotwire data is resampled to provide 720 points per rotor rotation based on the synchronizing pulse signal. The data is then averaged over all the rotations contained in the sample to provide the pulse-synchronized averages. These averages are then subtracted from the original signals to provide the random signal components. The statistical properties of the random signals (turbulence intensities, integral length-scales, spectra, correlation coefficients) are then computed. Additional averages are produced by averaging over all blade passages. A simple transform based

on the local wheel speed of the rotor is used to compute some flow parameters in the rotor-bound coordinate system.

Typical results that demonstrate the pulse synchronized averaging process are shown in Fig. 69. They illustrate the excellent repeatability of the pulse signal and the large amount of random fluctuations in the velocity and flow-angle signals within the rotor wakes.

3.4 Primary Acoustic Far Field Instrumentation

The primary acoustic results from this test were acquired from microphones located outside the wind tunnel free-jet shear layer. An array of 24 microphones was located in the horizontal plane of the model axis, on a 5.486 m (18 ft.) sideline relative to the model. The reference point was the center of the inlet in the hilight plane. The directivity angles to the model axis were 40°, 42.5°, 45°, 47.5°, 50°, 55°, 60°, ..., 135°, 140°, and 145°, 0° being directly upstream. A sketch of the layout, from above, is shown in Fig. 20.

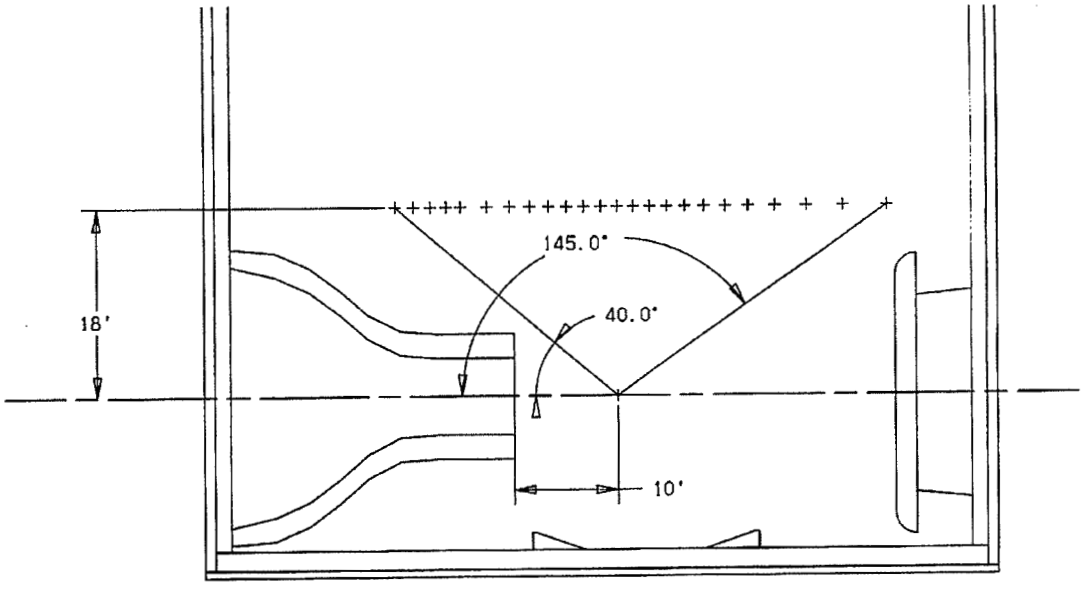

Fig. 20. Plan view of sideline microphone arrangement

The microphones used were 1/4-inch condenser microphones, B&K model 4135. They were mounted in holders and installed on poles holding 4 or 5 units, as shown in Fig. 21.

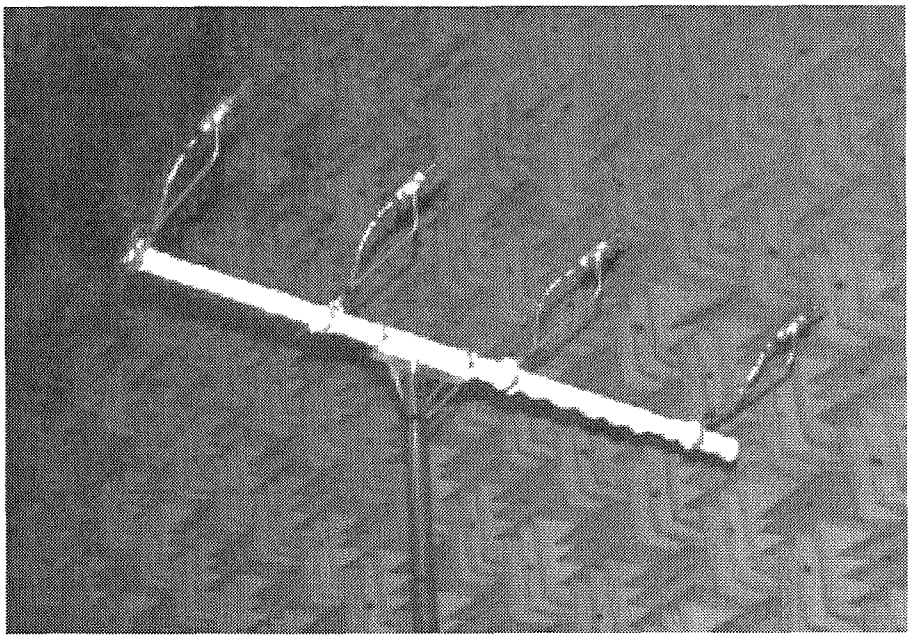

Fig. 21. Sideline microphone mounting system

The microphones were oriented with the normal to the diaphragm directed at the reference point. The poles were a new design, of greater rigidity than the previous units which were prone to moving during wind-tunnel operation. Because of the larger dimensions, a small experimental program was initiated to evaluate possible reflections and scattering from the stands. Two significant sources were found. The first was a reflection from the crossbar, which was reduced about 8dB by covering the bar with 9.5 mm (3/8 in.) Nomex felt. The effect is seen in Fig. 22, where the small ripples are significantly reduced. (The figure shows the measured spectrum of a broadband sound source.)

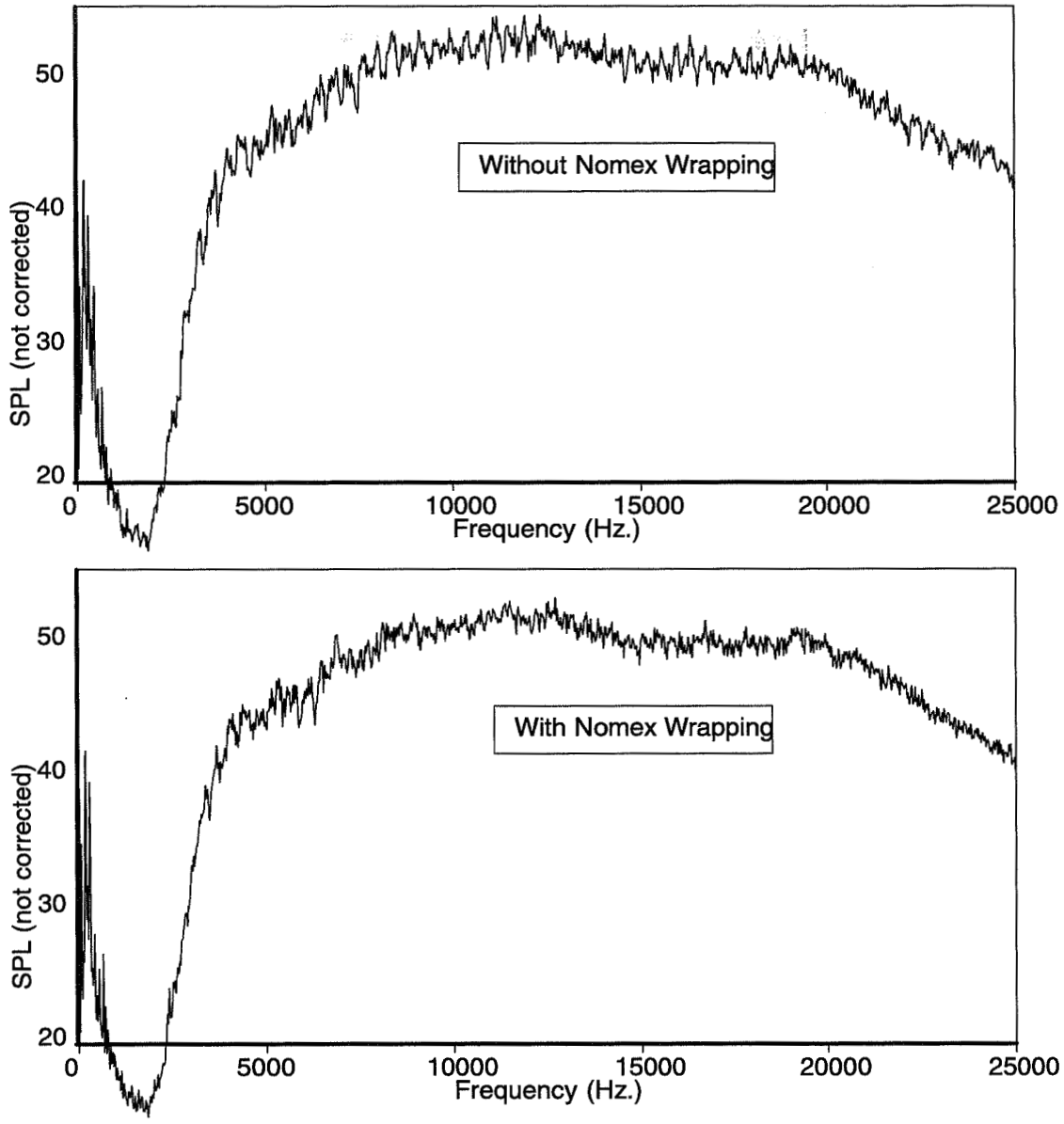

Fig. 22. Effect of wrapping crossbar with 3/8 inch Nomez felt

The second source of scattering of reflections was the microphone mount itself. The microphones were embedded in a plug of flexible foam about 38 mm (1.5 in.) in diameter and 75–100 mm (3–4 in.) long. This plug was inserted into a thin-wall metal tube of the same diameter. By carving the front of the plug to a conical shape, scattering at the microphone diaphragm was significantly reduced. The effect of this change is seen in Fig. 23.

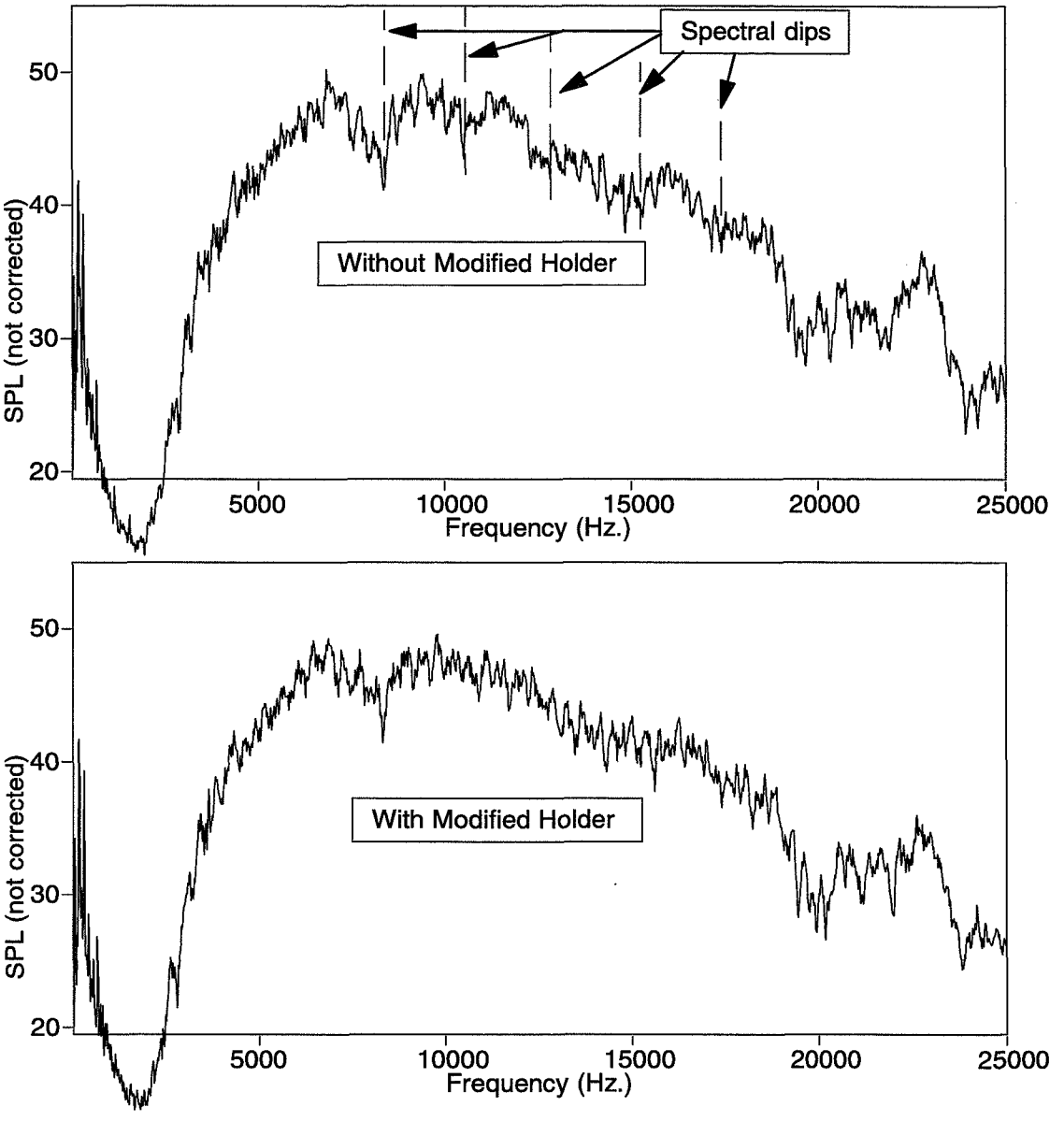

Fig. 23. Effect of tapering the microphone holder foam plug

Final microphone positioning was done with a laser positioning system; the accuracy and repeatability of position are estimated to be 6 mm (1/4 in.). The poles were hinged and counterweighted to allow the microphones to be rotated down for pistonphone calibration checks, which were performed at the beginning and at the end of every day of acoustic testing.

An acoustic shield, approximately 1.22 m (48 in.) long and .914 m (36 in.) high, can be located so as to shield the microphone array from noise radiated from the aft duct, thus improving the ability to accurately measure inlet-radiated noise (see Fig. 24). The shield can be rotated out of the way for measurement of aft-radiated noise. This rotation is fairly rapid (less than one minute) so that data could be acquired for every condition from 40° to 105° with the shield up for inlet measurements and from 70° to 145° with the shield down for aft-duct measurements.

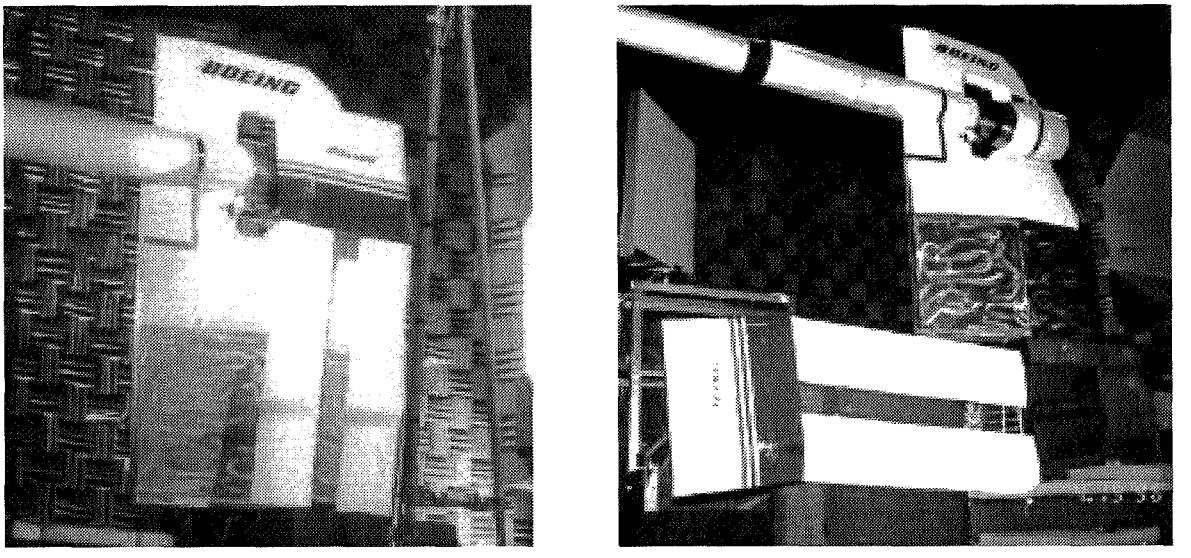

Fig. 24. Acoustic shield, up (l) and down (r) positions

Narrowband spectra were acquired from these microphones in groups of four through a digital data system based around an array processor, in the form of Hanning-windowed FFT records of 1600 points over a range of 0 to 25kHz, giving a bin spacing of 15.625Hz. Spectra were averaged over 125 samples. This bin spacing was chosen to allow a minimum of eight bins between rotor shaft harmonic tones (buzzsaw noise) so that the underlying broadband could be extracted. (Note that the in-duct measurements are very similar but not exactly the same, with 16 Hz bin spacing over 0 to 25.6kHz.) All acoustic data was corrected for level (based on twice-daily pistonphone calibrations) and frequency response (based on electrostatic calibrations, which are assumed to be stable as long as the diaphragm tension and hence the level sensitivity do not change).

3.5 Azimuthal Array

For a few conditions, an axially traversing azimuthal array of microphones was used to examine the radiated sound field more completely. In particular there was some desire to confirm that there was not a great deal of azimuthal asymmetry (see Ref. 11) The array consisted of 24 microphones equally spaced at 5° intervals located on a plane normal to the model axis, at a radius of 14 feet, at angles of approximately 40°–160° from vertical (12 o'clock). The plane of microphones traversed parallel to the model axis over a directivity angle range of 53°–145° from directly upstream. A sketch of the array layout is shown in Fig. 25.

The signals from these microphones were recorded on the high-capacity digital data system used for mode measurements (see below). This is not the data system used above for the sideline array, because it was desired to use the data for modal analysis so simultaneous recording of all signals was needed. (The modal analysis was not a success.) The signals were calibrated for sensitivity using daily pistonphone checks, but were not calibrated for frequency response.

Early results confirmed that the broadband noise was essentially axisymmetric, but the time required to acquire a full set of data for one condition was excessive. Consequently use of this array was abandoned early in the test.

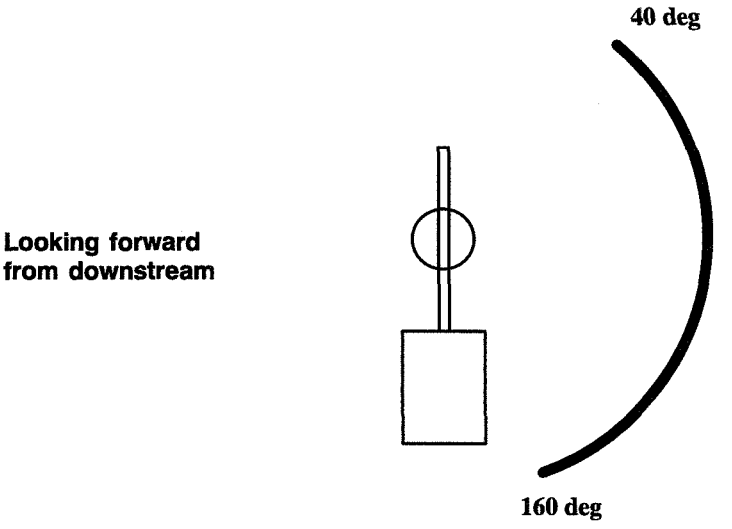

Fig. 25. Sketch of azimuthal array arrangement. The array traverses axially (not shown)

3.6 Acoustic In-Duct Instrumentation

The in-duct microphones used were 6.35 mm (1/4 in.) condenser microphones, B&K model 4136. These units were connected to preamplifiers using short flexible cables ("goosenecks") with the preamplifier assemblies mounted inside the nacelle walls. Fig. 26 illustrates the arrangement for a circumferential row of microphones in the inlet near the highlight plane. The microphone buttons are mounted in an insulated holder which can be quickly installed or removed from the duct, to facilitate replacement of units which might fail or exhibit calibration changes during testing. This is particularly important for uniformly-spaced mode-measurement arrays because degradation of a single unit can severely degrade the quality of the results.

In spite of this arrangement, it was found that replacement of questionable microphones consumed a large quantity of test time. The flexible cables between the buttons and the preamplifier in particular were found to be fragile and failed frequently.

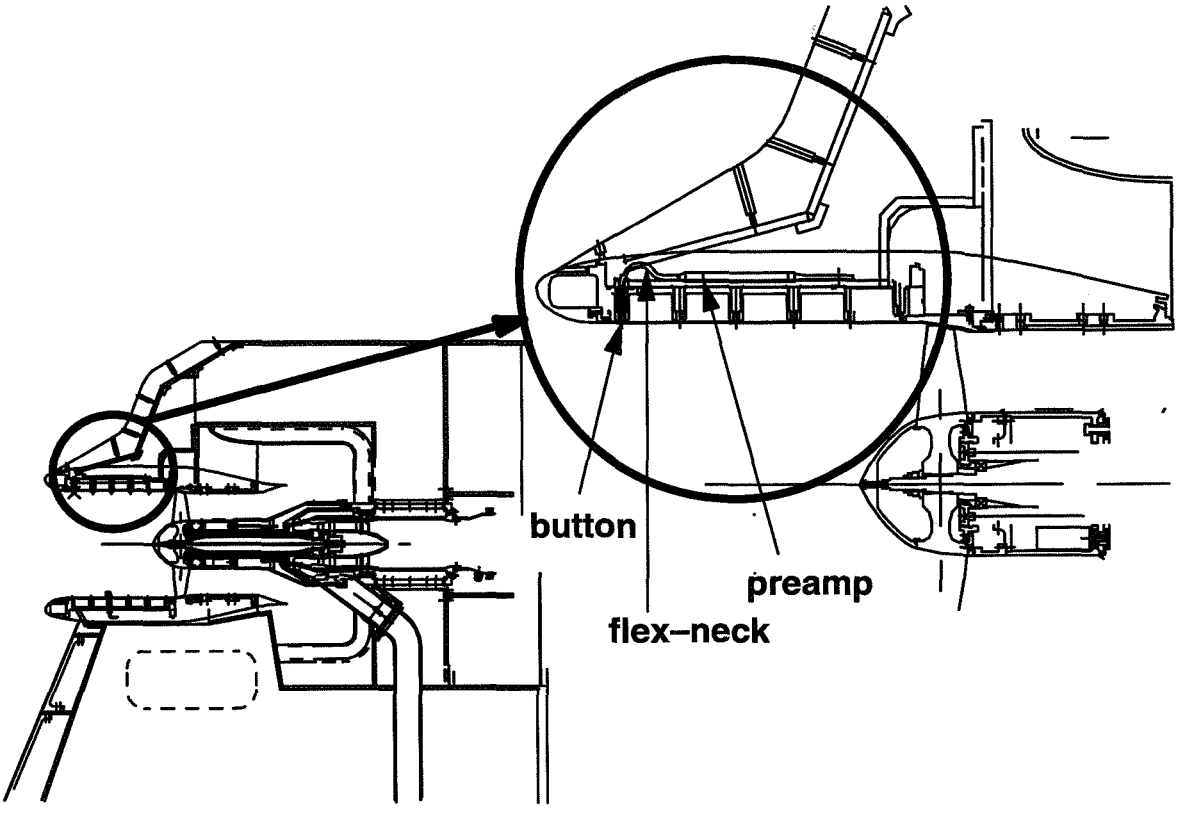

Fig. 26. Microphone installation in fan rig duct

Calibration

Accurate phase calibration of a large number of microphones at high frequencies is difficult to do. For this test, we used a traveling-wave tube technique to obtain calibration data at reasonable intervals. However, the method has some limitations (data scatter and convergence failure, primarily).

A preliminary assessment of calibration needs was based on the simple notion that a 40dB signal-to-noise ratio would be desirable, and would require one percent calibration accuracy (about 0.1dB amplitude and 0.6 degrees phase). The wave tube technique is capable of approaching this accuracy, and has been used before. However, a more careful analysis (see Quazi, Ref. 9) shows that there is considerably greater latitude, at least if non-exotic wavenumber decomposition algorithms are used. In practice, it was found that satisfactory results were obtained by choosing reasonably well-matched microphone buttons, limiting the frequency band to less than 25kHz for 6.35 mm (1/4 in.) pressure type units, and adjusting the gain for each channel to compensate for the mid-frequency sensitivity. Consequently no results to date have needed the calibrations, although there is likely some sacrifice of S/N ratio especially at the higher frequencies. If higher performance is needed in the future, or if more sophisticated high-resolution algorithms are to be used, the data are available in the archive and the calibrations can be applied.

Assessment of flow noise

Previous experience with this kind of mode measurement had provided some confidence that flow noise would not be a problem, at least in the inlet. In the present instance, the inlet array was located fairly close to the highlight plane, and some anomalous narrowband noises were seen in initial ex-

periments. Since the microphones were located near the laminar–turbulent transition, it was speculated that fluid instabilities in the transition region were responsible for the problem. A trip strip of 0.010-inch dots was installed about 1 inch upstream of the microphones which largely eliminated the problem.

In the aft duct, there is a substantial turbulence intensity near the wall from several sources (see the discussion under unsteady flow measurement results). There was a substantial pressure fluctuation also, as seen in the mode results. The available signal-to-noise ratio was degraded especially at low frequencies, but the main features were still clearly visible. See the acoustic results section for more details.

Array span/resolution tradeoff

The mode measurement system is designed to evaluate sound pressure as a function of azimuthal wavenumber or spinning mode order. Duct modes have both radial and azimuthal structure, but it is impractical to measure individual modes with a 1-dimensional array. A radial array would protrude into the flow, and necessarily alter the noise generation mechanisms. Any 2-dimensional array, circumferential–radial or circumferential–axial, would require very many sensors, on the order of a thousand for practical results. There are ways around these limitations where steady tones are concerned; the main trick being coherent signal averaging to extract complex pressure-amplitude relative to a rotor-locked reference time signal. This permits a single moveable microphone to acquire data from many different locations at different times, relying on the stationary nature of the signals to combine these samples meaningfully. However, this does not work for broadband noise as the sources are not steady. Consequently, for this test only the azimuthal variation was measured.

The acoustic modes in a cylindrical duct vary harmonically in the azimuthal direction, so a circular array at a fixed axial station is suitable for measuring them. If the relative phases of the radial orders within a given spinning order are fixed, as is the case with tone noise and might be the case if the source of broadband noise were sufficiently constrained to a single radius, then the radial modes can interfere with each other and a single axial station might not be representative of the true average intensity of a given spinning order. This is a limitation of this method. At high spinning orders, where only one radial order can propagate, this problem is not present.

Two axial locations were chosen, one in the inlet as far upstream as practical and another downstream of the rotor but upstream of the stator location. A maximum of 40 channels per array was used.

For fixed microphone locations, there is a tradeoff between modal resolution and aliasing. Ideally, a full-circle array of very many equally-spaced sensors would be used; this would give independent measurement of the level in each spinning order, up to a spinning order whose magnitude was equal to half the number of sensors. Unfortunately such an arrangement requires a prohibitive number of microphones if aliasing is to be prevented at high frequencies. To keep the channel count practical, compromises were made on both fronts. Several arrays were tried early in the test, but the bulk of the mode data was based on a single inlet and a single aft array.

The inlet array used 40 microphones covering a half circle, which gave a resolution (bin spacing) of two spinning orders with the discrete Fourier transform beamforming used here. This is the array illustrated in Fig. 26. This allowed alias-free results for spinning orders as high as ± 40. These spinning orders are not cut on below about 8kHz, a frequency a little over twice the blade passage frequency. Above that frequency, aliasing is tolerated; fortunately in this case the modal structure could be sensibly interpreted in that region. The aliasing is illustrated in Fig. 27, where a region of spinning order/frequency space is indicated which is unambiguous below the 8kHz frequency.

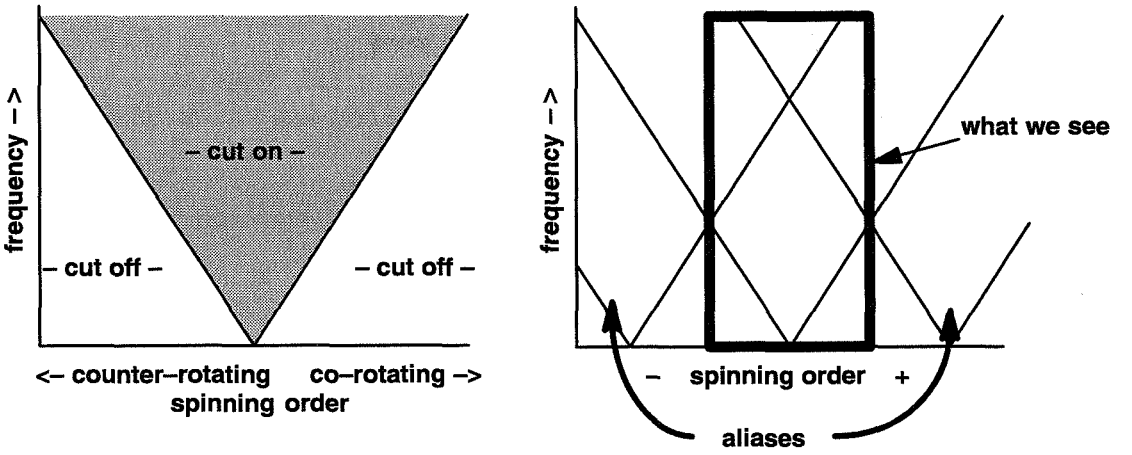

Fig. 27. Acoustic cut-on and aliasing for inlet array

Downstream of the fan it was not possible to cover a full 180 degrees of circumference. As the rig was drilled with a hole spacing of 360/80 = 4.5 degrees, and an integer fraction of a full circle was desired so that the bin centers would be on whole mode orders, a quarter-circle array was chosen. It was not possible to install microphones any closer than 4.5 degrees, so only 20 microphones were needed. This allowed for the possibility of using two arrays very close together (0.6 inch) in the hopes that they could be used as a kind of multi-modal intensity probe to separate upstream from downstream acoustic modes. (This did not prove to be very practical, and further discussion is not included in this report.) These arrays have half the resolution of the inlet array, but the same aliasing.

Data acquisition

The microphone signals are routed to a digital data system which records the data for later analysis. The system is based on an HP9000/385 host computer with HP3565 front end. It can acquire up to 54 channels, of which 40 were used at one time for this test. This system calculates and records the cross-spectra of each channel referred to channel 1. The data are not ensemble averaged, but 16 instances are recorded for each condition for later averaging. The reasons for this approach are more fully discussed in Ref. 10. From this information, in-duct wall pressure spectra and modal distribution as a function of frequency can be calculated, as is more fully described in Sec. 4.5.

3.7 Rubstrip Unsteady Pressure Instrumentation

An array of 16 unsteady pressure transducers was mounted in the surface of the rotor rubstrip and complemented with an additional transducer in the circular mode measurement ring closest to the fan face. The purpose of this array was to provide information about the unsteady surface pressure field in the fan tip region. It was assumed that data from this array in conjunction with some CFD predictions could at some point in the future provide detailed information about the complex rotor tip flows and the the acoustic pressure field emanating from this region.

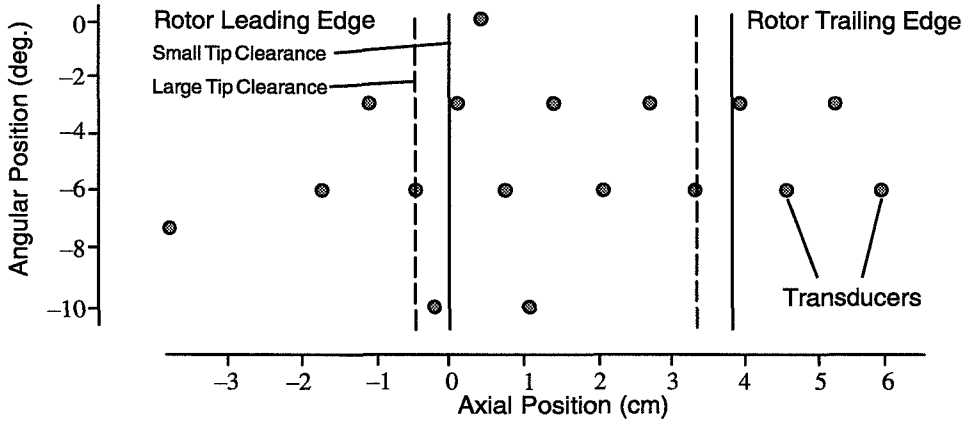

Fig. 28. Array of Unsteady Pressure Transducers in Rotor Rubstrip

The array consisted of thin film pressure transducers (Kulite XCS–093–25D) and their arrangement in the rubstrip is shown in Fig. 28. The transducers were recessed .8 mm from the surface to prevent damage to the transducers and the rotor in the case of a fan tip rub. The decision to incorporate this array into the instrumentation of this test was made late in the planning phase of the test. It was therefore necessary to use readily available transducers that had been used previously in many full-scale tests within the Boeing Company.

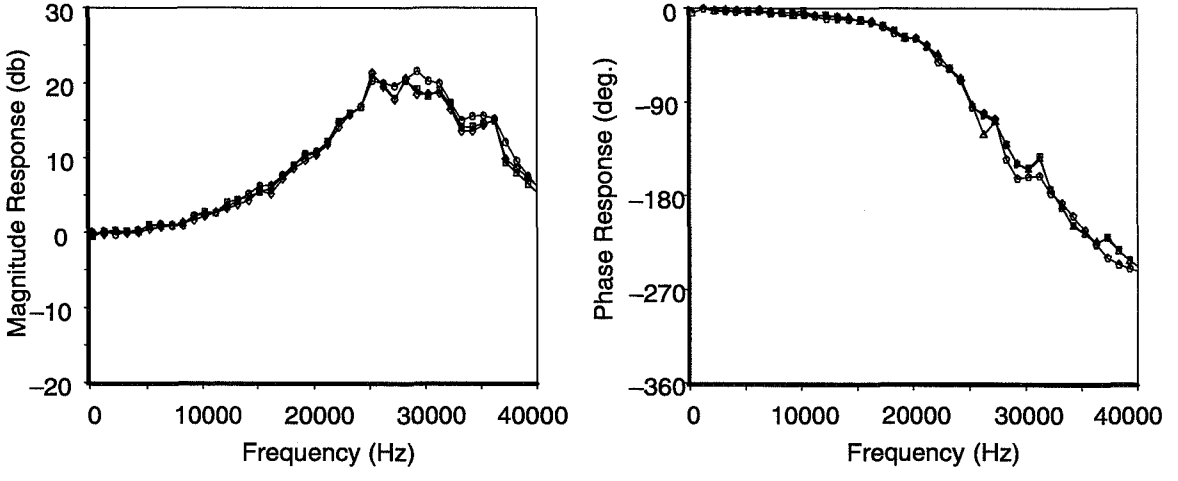

Fig. 29. Typical Frequency Response for Rubstrip Unsteady Pressure Transducers

The sensing element of the transducers is protected with a screen, a very thin perforated plate. The cavity between the sensing element and the protective screen has a significant effect on the high fre-

quency response of the transducers. Its effect is small over the frequency range of typical full scale testing, but becomes very significant for the model-scale frequency range. Calibration characteristics for the individual transducers have been acquired with the calibration procedure used for the microphones of the mode measurement system. Typical response functions for one of the transducers based on three different calibrations are shown in Fig. 29.

Data of the transducer array and the synchronizing pulse was acquired simultaneously at a rate of about 130,000 samples per second. Total sample length was in the order of 1 second for each condition. During the data acquisition process the data was averaged in the pulse-synchronized mode, separated into average and random signal content and transferred to disk. In this process only the low-frequency correction based on the piston–phone calibration was applied to the data. The data acquisition and analysis procedure is described in Fig. 30.

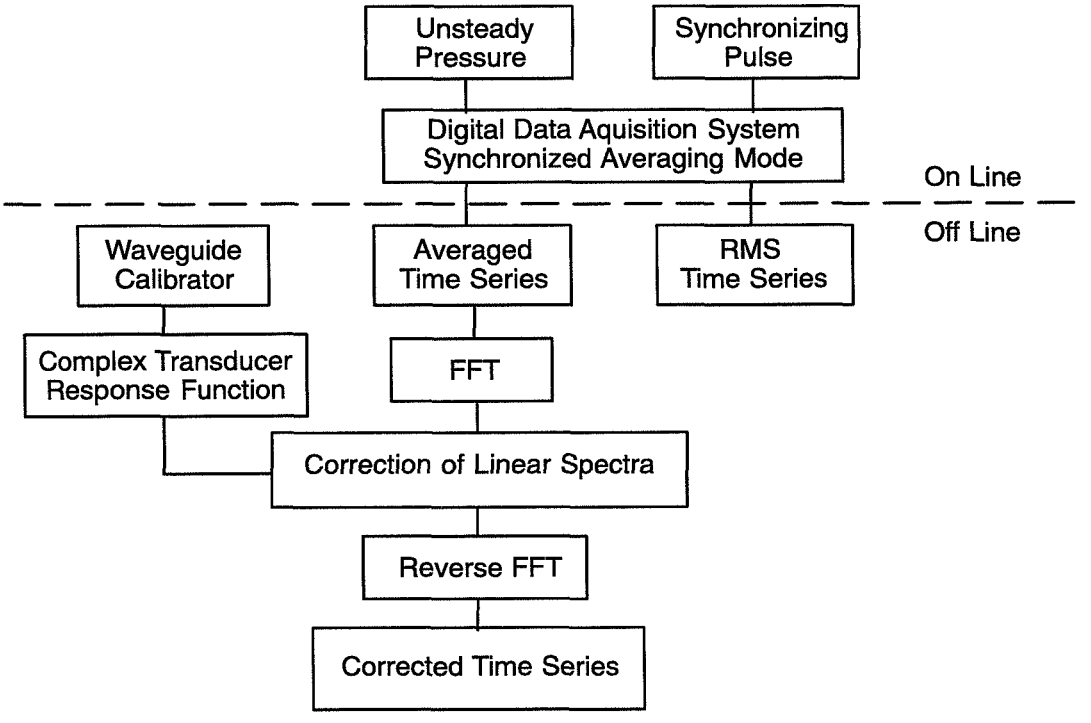

Fig. 30. Rubstrip Unsteady Pressure Data Acquisition and Analysis Procedure

During the data analysis process the pulse-synchronized average time series of each transducer is Fourier transformed and then corrected by using the complex transducer response function of the individual sensor. A reverse Fourier transform then provides the corrected time series. The RMS time series cannot be corrected.

4 Results

4.1 Performance Measurements

Data analysis with PERCH

The data acquired by the performance instrumentation is used as input and analyzed using a U. S. Air Force computer program, PERCH, written by Medlock (Ref. 12). PERCH employs a streamline curvature method to calculate an inviscid, axisymmetric flow field solution consistent with the input data. The flow field grid defined by streamlines and pseudo-axial stations is shown in Fig. 31.

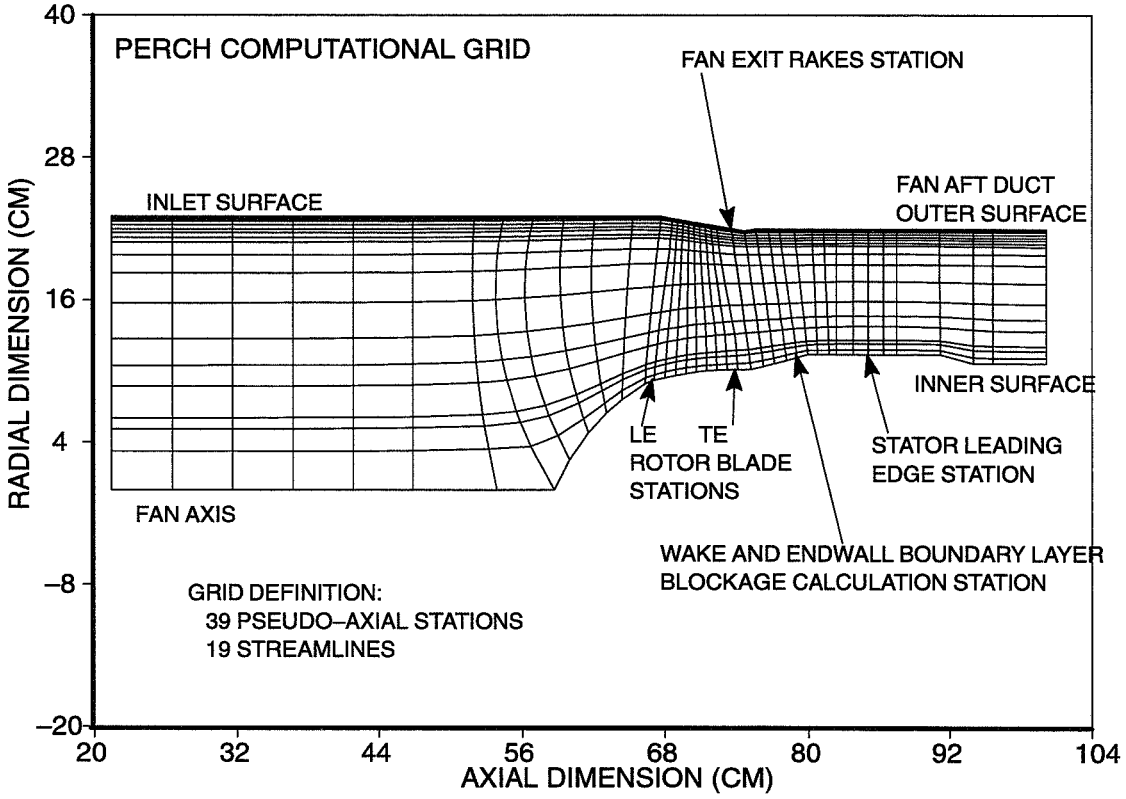

Fig. 31. PERCH Code Computational Grid

There are several data inputs to PERCH. The flow path geometry is defined by specifying the coordinates for each pseudo-axial station. The rotor-blade stations from leading edge to trailing edge are not directly specified. The rotor geometry is input as airfoil surface coordinates at several radial stations. The rotor-blade stations are generated based on the airfoil surface data and a specified station definition as a fraction of the distance from the leading edge to the trailing edge. The streamline definition has been specified such that the density of rotor exit-rake data is properly captured. Therefore, the outer streamlines are especially dense and to some degree the inner are as well. There is no stator geometry input since there was no stator exit instrumentation for the test.

For cases with no inlet boundary-layer suction, the inlet mass flow and rotor mass flow are the same. The mass flow is calculated from the measured PSCA static pressures which were used in calibrating the inlet for mass flow. For cases with inlet boundary-layer suction, the PSCA static pressures are not useful since their location is in the midst of the boundary-layer suction region of the inlet. The

inlet mass flow is calculated from the measured PSCC static pressures upstream of the perforated inlet which have been correlated with the PSCA static pressures for a large number of cases without boundary-layer suction. The inlet boundary-layer suction mass flow is calculated from the measured pressure drop across the perforated inlet wall in conjunction with the correlation between this pressure drop and the mass flow through the suction system. The rotor mass flow used for cases with boundary-layer suction is the inlet mass flow minus the boundary-layer suction mass flow. The rotor mass flow is input since it would be quite difficult to input the whole inlet mass flow and then accurately account for any inlet boundary-layer suction mass flow as a bleed amount between all of the stations in the inlet grid. Prior to the actual acoustic testing, the rig inlet was calibrated for mass flow as described in a previous section of this report. The input rotor mass flow is accurate to within $\pm 0.50\%$.

The fan mechanical rotational speed, freestream total pressure and temperature are input. For each combination of fan speed and boundary-layer size (full, partial and no boundary layer), a normalized inlet boundary-layer total-pressure profile has been developed from the inlet boundary-layer total-pressure traverse probe. From this profile and the freestream total-pressure, a total-pressure profile is used as input. The rotor exit rakes record an average total pressure and total temperature measurement at twenty radial locations. These measurements are input at the appropriate radial position at a pseudo-axial station, Fig. 31, where the probe heads were located.

The final data used as input are static pressures on the outer wall from the inlet to downstream of the rotor which are used for calculating an area blockage term which is intended to capture blockage caused by the wakes and endwall boundary layers. PERCH can calculate a flow field solution without determining blockage if no measured static pressure is specified for the blockage calculation. Based on methods typically employed by users of this code, the preferred method of calculating blockage is to use the measured case static pressure distribution from the leading edge of the rotor to the aft duct downstream of the rotor. The calculation of blockage can be specified at any of the computing stations. If the measured static pressure is lower than the no-blockage solution static pressure then the new solution uses the measured static pressure as the new-case static pressure at the blockage station. The use of the lower measured static pressure creates a new solution with increased velocities at the constant total pressure. An area blockage term is determined by comparing the solutions with and without use of the measured case static pressure and calculating an equivalent blockage value. The suggested method is to have blockage calculated at the leading edge station and a station aft of the rotor and then interpolate the blockage at stations between these two. The blockage calculated at the aft-blockage computing station is the blockage used for all stations further downstream. This recommended method has been employed for all the analyses.

There are a few stations downstream of the rotor where the blockage could be calculated. In determining which station to use, blockage was calculated at each of these potential stations. Most of the available stations just downstream of the rotor define corner points of the computational grid on either the outer or inner wall. These stations all had case pressures that were affected by the curvature of the endwall streamline which defined a corner. Because of this, none of these stations gave reasonable blockage values. Of the remaining stations, the blockage ranged from 5% to 11%. The station that has been chosen for blockage calculations is the one where the blockage is in the 7–8% range. This station has been chosen because the 7–8% is in the middle of the 5–11% range and 7–8% is reasonable relative to other published fan rotor results which used downstream rakes to measure stagnation pressure and temperature. An additional method to validate the calculated blockage is to compare the hub static pressure from the solution with the sets of measured hub static pressures

just downstream of the rotor. The hub static pressures of the solution agreed well with the measurements.

Rotor inlet conditions

The fan rig was operated under a wide variety of operating conditions and configurations. For each combination of loading and fan speed, there are three levels of inlet boundary-layer thickness, three levels of clearance and three stator configurations. The exit nozzle plug could be positioned in order to have the same rotor mass flow for each combination of boundary-layer thickness, clearance and stator configuration. Determining and using all of those combinations would result in an inefficient use of test time. Therefore, for each stator configuration a new set of three nozzle plug (loading) positions was determined in order to keep the rotor mass flow the same as rotor alone operation, but new nozzle plug settings were not determined for the clearance and boundary-layer variations. Fig. 32 shows an example of the success that was achieved in choosing a set of three new nozzle settings for the 30-nominal stator configuration in order to match the rotor-alone mass flow.

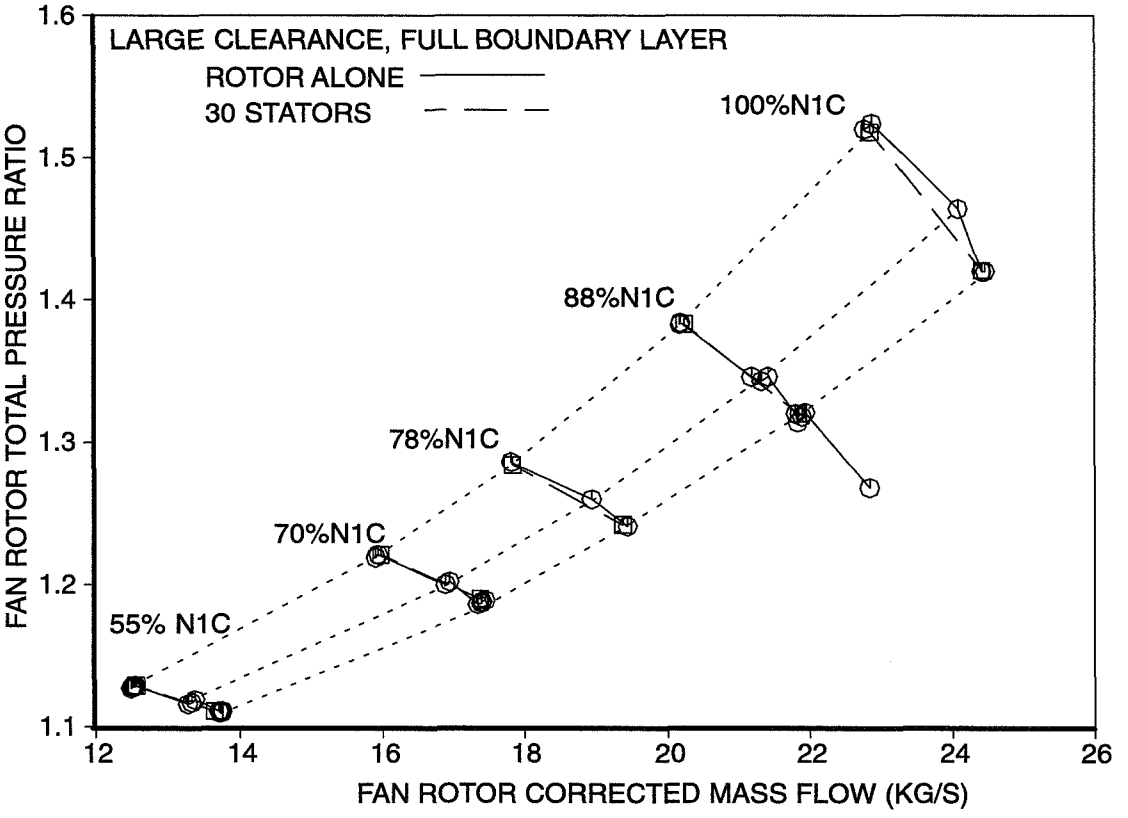

Fig. 32. Matching Rotor Mass Flow for Rotor-Alone and Stator Configurations

For rotor-alone, there was one set of three nozzle positions that was used for all variations of clearance and boundary layer. For each of the rotor/stator configurations, there was another set of three nozzle positions that was used for all variations of clearance and boundary layer. The 30 nominal and 15 large-chord stator sets had the same nozzle positions and the 60 small-stator set had a slightly different low-loading nozzle position.

Rotor-alone map – clearance variation

Fig. 33 shows the effect of clearance variation. The configuration is rotor-alone and full boundary-layer thickness. The exit nozzle plug position is the same for both clearances. The effect of clearance variation is most significant at high speed and high loading since the pressure differential from suction side to pressure side is largest at these conditions. For almost every operating point on the map there is a noticeable increase in both flow and pressure ratio as the clearance is reduced.

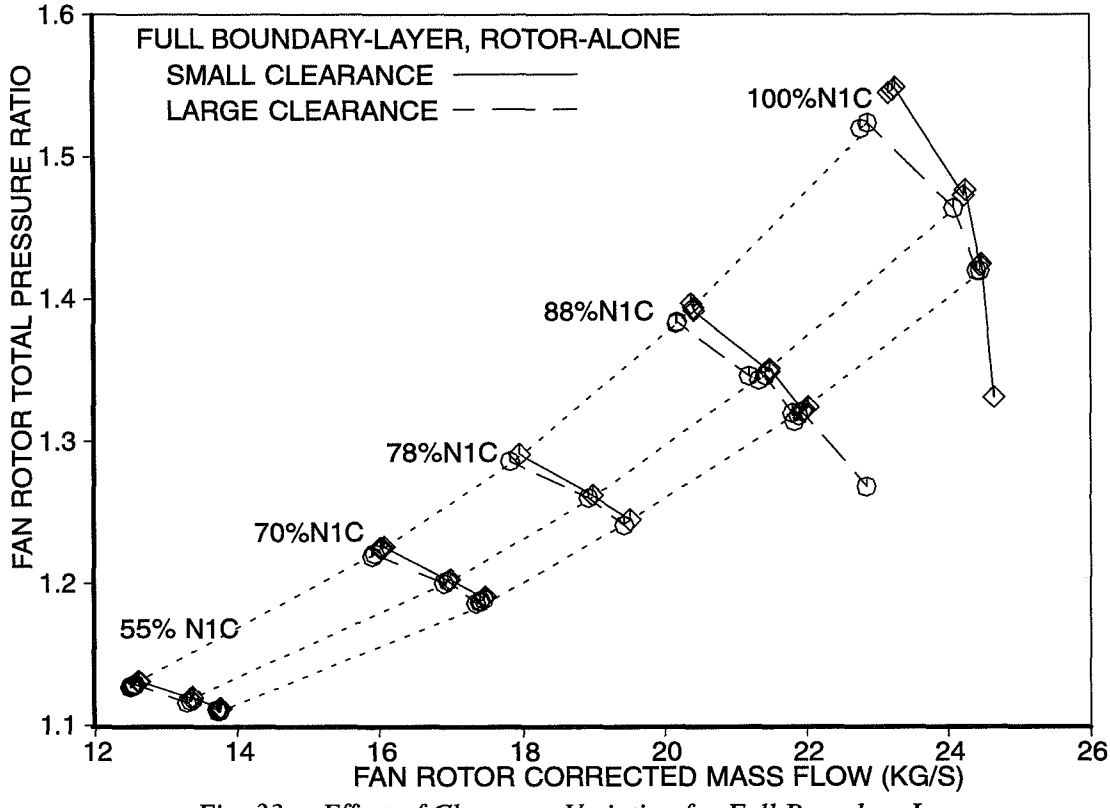

Fig. 33. Effect of Clearance Variation for Full Boundary Layer

Fig. 34 shows the efficiency change for the clearance variation. The expectation would be that the small clearance would have higher efficiency especially for the operating points at higher speeds and higher loading where the effect is most significant. At the higher speeds and high loading the efficiency is higher. As the speed or loading decreases, the effect is less noticeable and the differences appear to be within the scatter of the data. The data scatter is large. For example, consider the 88% and 100% speed and highest loading operating points for small clearance. At 100% speed, there are data for three different runs and the efficiency range is 91% to 92%. For 88% speed, the range of efficiency is 92% to 95%. These points are meant to be the same operating point, but it is apparent that the mass flow, pressure ratio and temperature ratio are slightly different. As indicated in a previous section, none of the rotor exit rake instrumentation was recalibrated after the initial calibration. It is certainly possible that the calibrations changed over the period of the test, especially for the total temperature probes which have a significant impact on the efficiency. This does not explain all of the difference since there is variation between test points taken at the same condition within a few days of each other. A detailed evaluation of the data scatter has not occurred, but presentation of the data occurs here nonetheless.

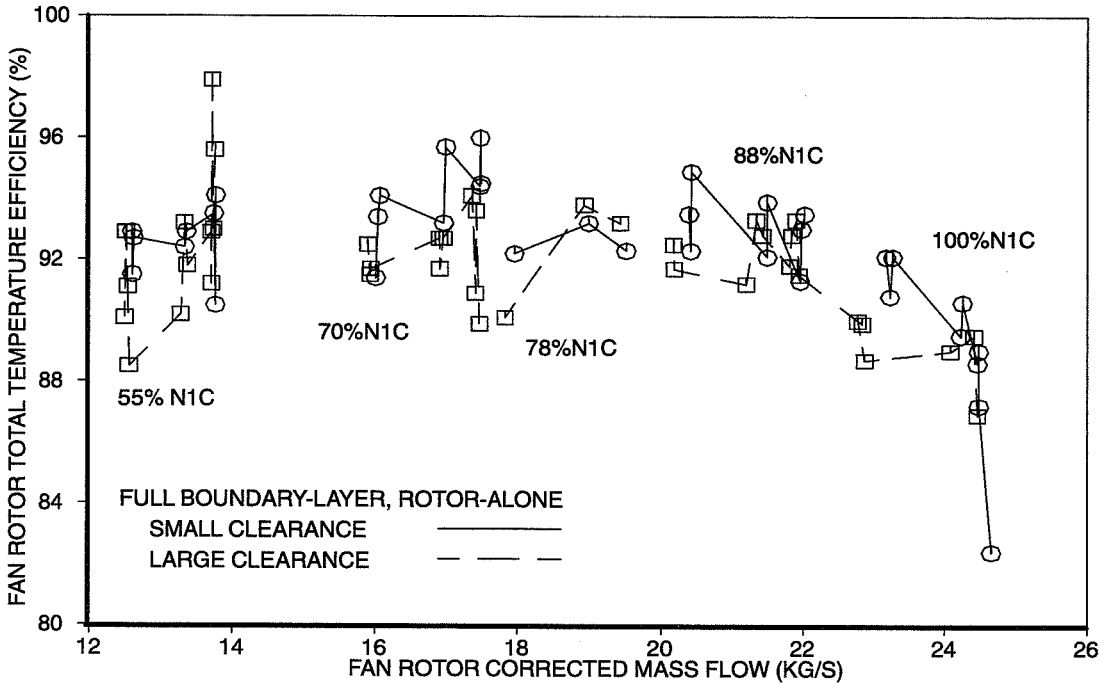

Fig. 34. Effect of Clearance Variation on Efficiency for Full Boundary-Layer

Fig. 35 and Fig. 36 show the effect of clearance variation for the case of no boundary-layer and rotor-alone. As with the full boundary-layer case, the most significant changes occur at high loading and high fan speed.

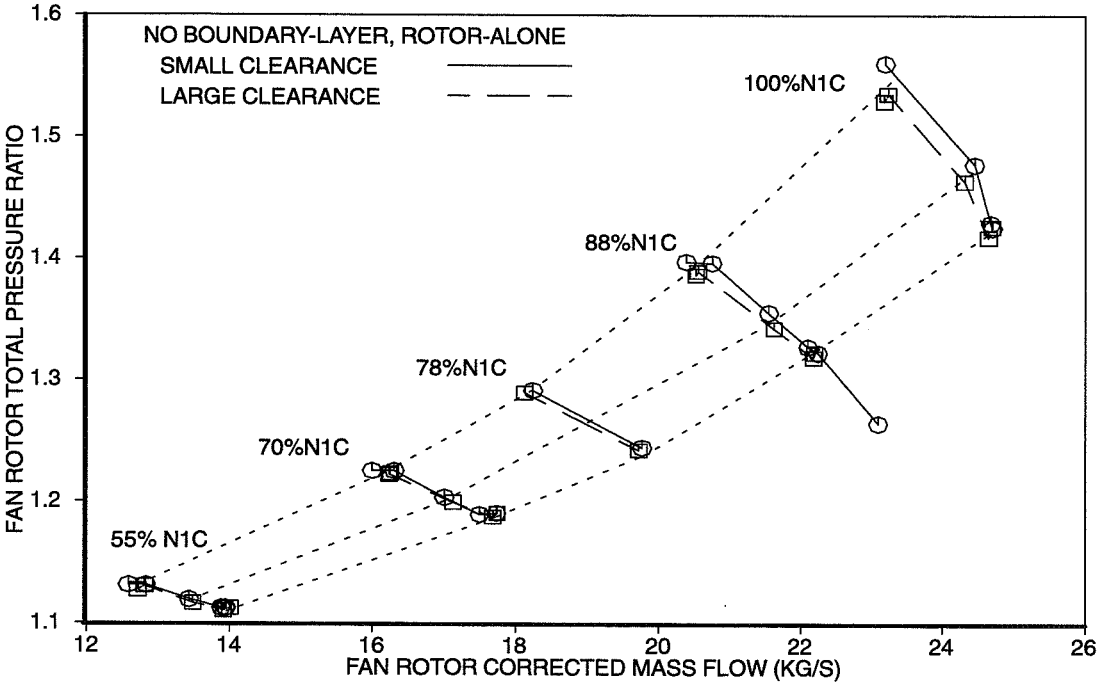

Fig. 35. Effect of Clearance Variation for No Boundary-Layer

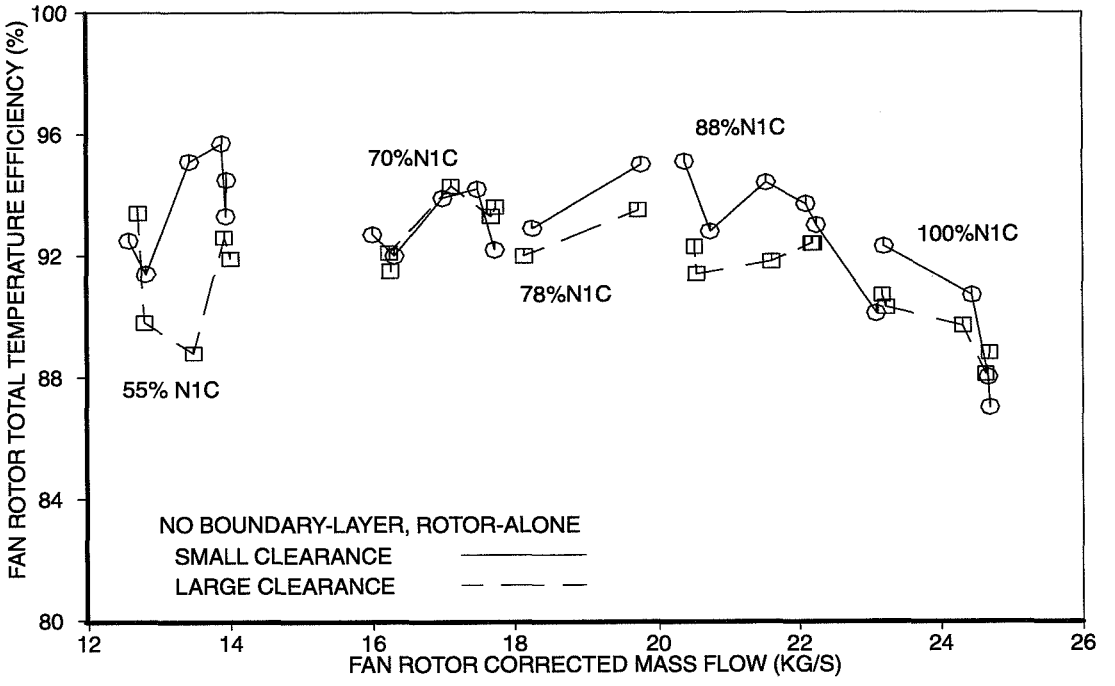

Fig. 36. Effect of Clearance Variation on Efficiency for No Boundary Layer

Rotor-alone map – boundary layer variation

Fig. 37 and Fig. 38 show the effect of boundary-layer variation. The configuration is rotor-alone and large clearance. The exit nozzle plug position is the same for both boundary layer sizes. For almost every operating point on the map there is a noticeable increase in flow, but pressure ratio and efficiency do not show much change except at 100% fan speed and the highest loading. Whereas the clearance changes showed pressure ratio and efficiency changes, variations in boundary layer size do not have the same significant impact. This appears to indicate that for large clearance, the reduced boundary-layer creates a larger effective nozzle area for the same geometric area and therefore a larger mass flow at constant fan speed. However, the performance of the fan, in terms of pressure ratio and efficiency seems dominated by the large clearance effect.

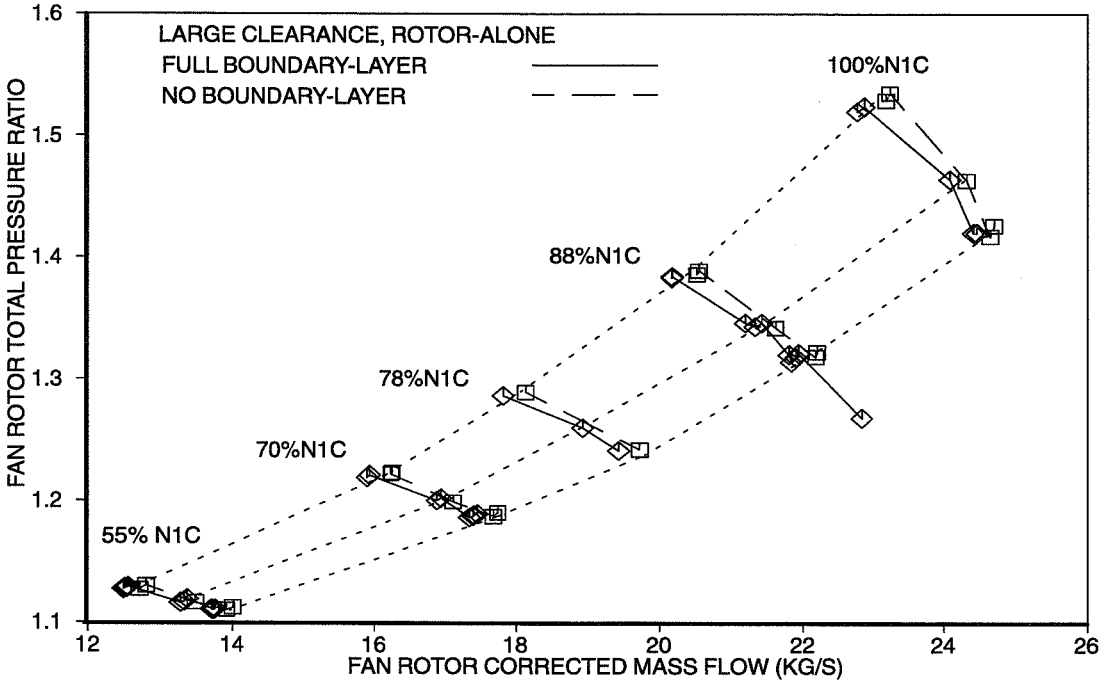

Fig. 37. Effect of Boundary-Layer Variation for Large Clearance

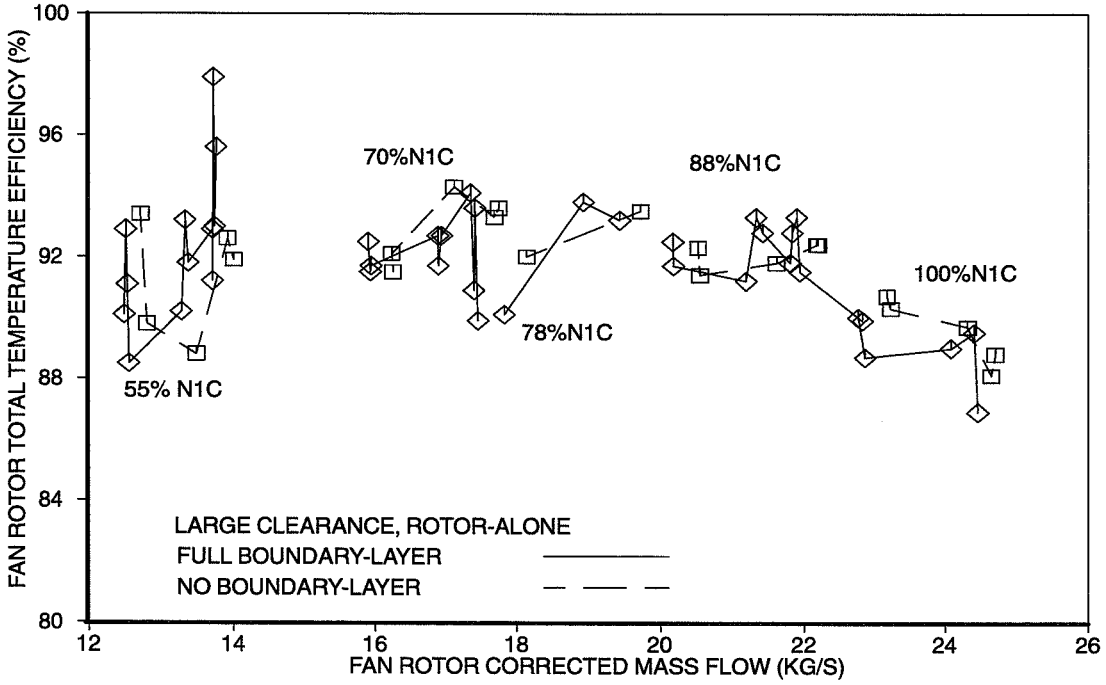

Fig. 38. Effect of Boundary-Layer Variation on Efficiency for Large Clearance

Fig. 39 and Fig. 40 show the effect of boundary-layer variation for the small clearance configuration. The efficiency may improve slightly for small clearance than it does for large, but the differ-

ence is certainly within the scatter of the data. As with the large clearance, the small clearance effect seems to be more dominant on the rotor performance than the variation of boundary layer.

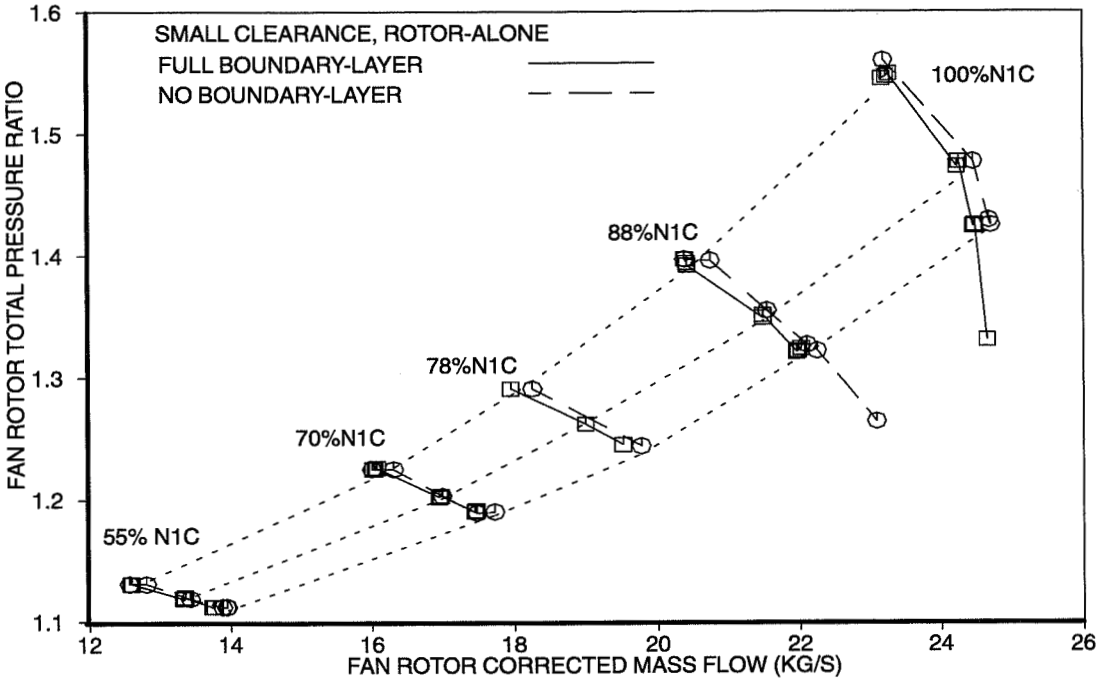

Fig. 39. Effect of Boundary-Layer Variation for Small Clearance

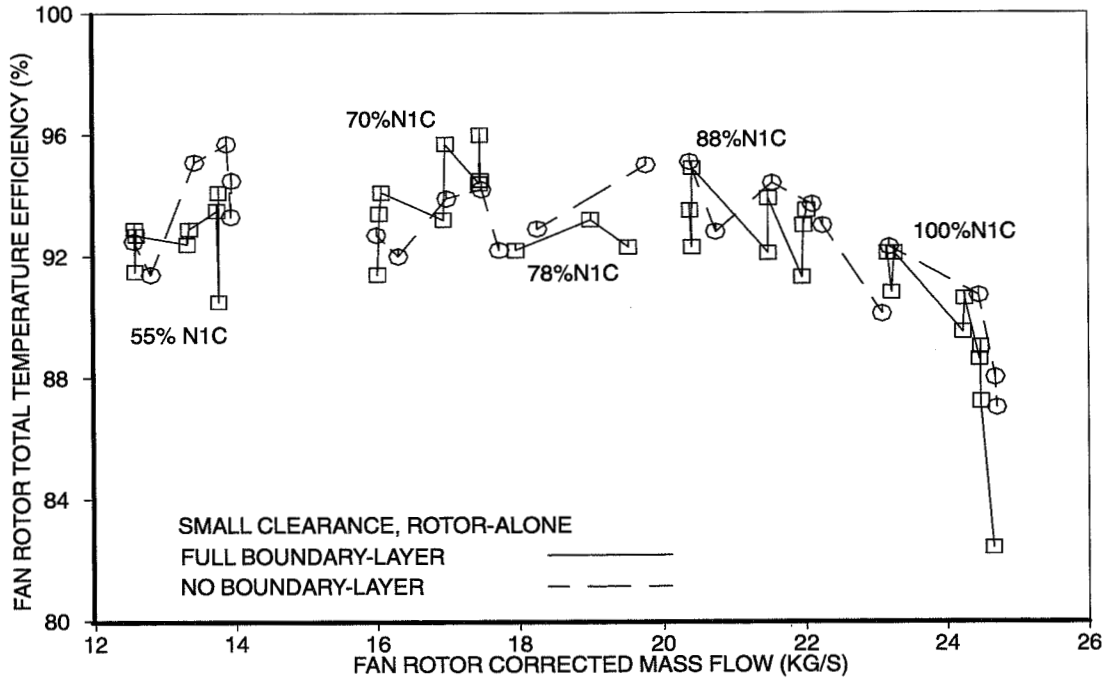

Fig. 40. Effect of Boundary-Layer Variation on Efficiency for Small Clearance

The lack of efficiency improvement for boundary-layer reduction may indicate that the clearance flow-field dominates the fan-tip performance. In spite of the data scatter, the effect of reduced boundary-layer size appears to improve the small-clearance case more than the large-clearance case. This may indicate that for very low clearances, a reduced boundary-layer would improve performance. However, once the clearance gets to a certain level, reducing the boundary layer size will not affect fan performance.

Rotor and stator incidence – loading variation

On of the major variations of the test was the variation of fan loading. As previously indicated, there were three primary loading levels used for the test. Fig. 41 shows the change in the radial profile of rotor incidence for the three loading levels for full boundary layer and small clearance at 55%, 78% and 100% fan speeds. The high loading incidence is about three degrees greater than low loading. The full boundary-layer results in incidence levels of 20 to 25 degrees at the tip.

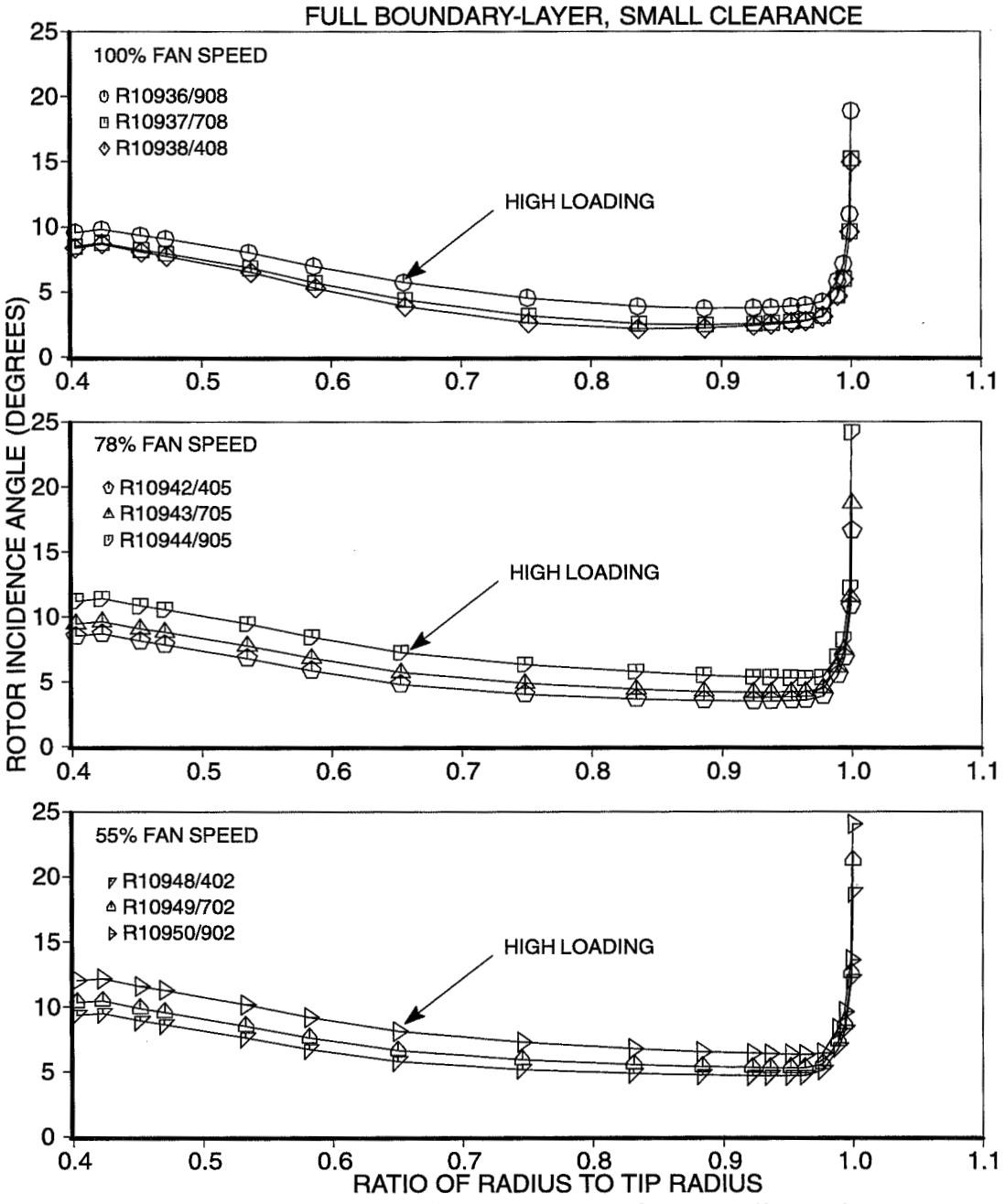

Fig. 41. Effect of Fan Loading on Rotor Incidence – Full Boundary-Layer

Fig. 42 shows the stator incidence changes with loading for the same configuration as Fig. 41. The stator incidence is about ten degrees higher for the high-loading versus low-loading and the tip incidence is 20 to 30 degrees for 100% speed and about 10 degrees for lower speeds.

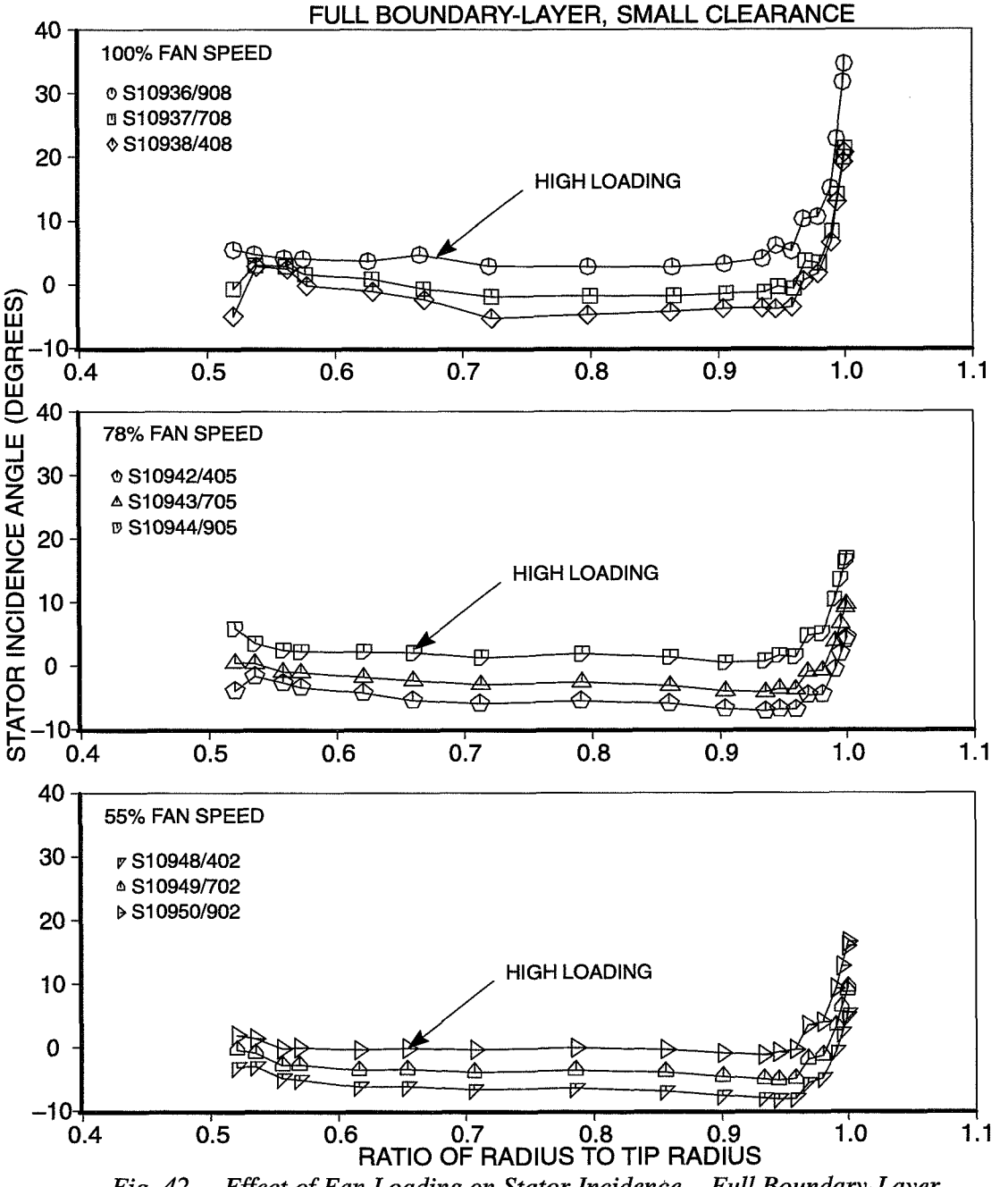

Fig. 42. Effect of Fan Loading on Stator Incidence – Full Boundary-Layer

Fig. 43 shows the change in the radial profile of rotor incidence for high- and low-loading levels for no boundary-layer and small clearance at 55%, 78% and 100% fan speeds. The high-loading incidence is about three degrees greater than low loading. The no boundary-layer results in incidence levels of 5 to 10 degrees at the tip, significantly less than full boundary-layer. It is apparent that the boundary layer has not been thoroughly removed at the high fan speed.

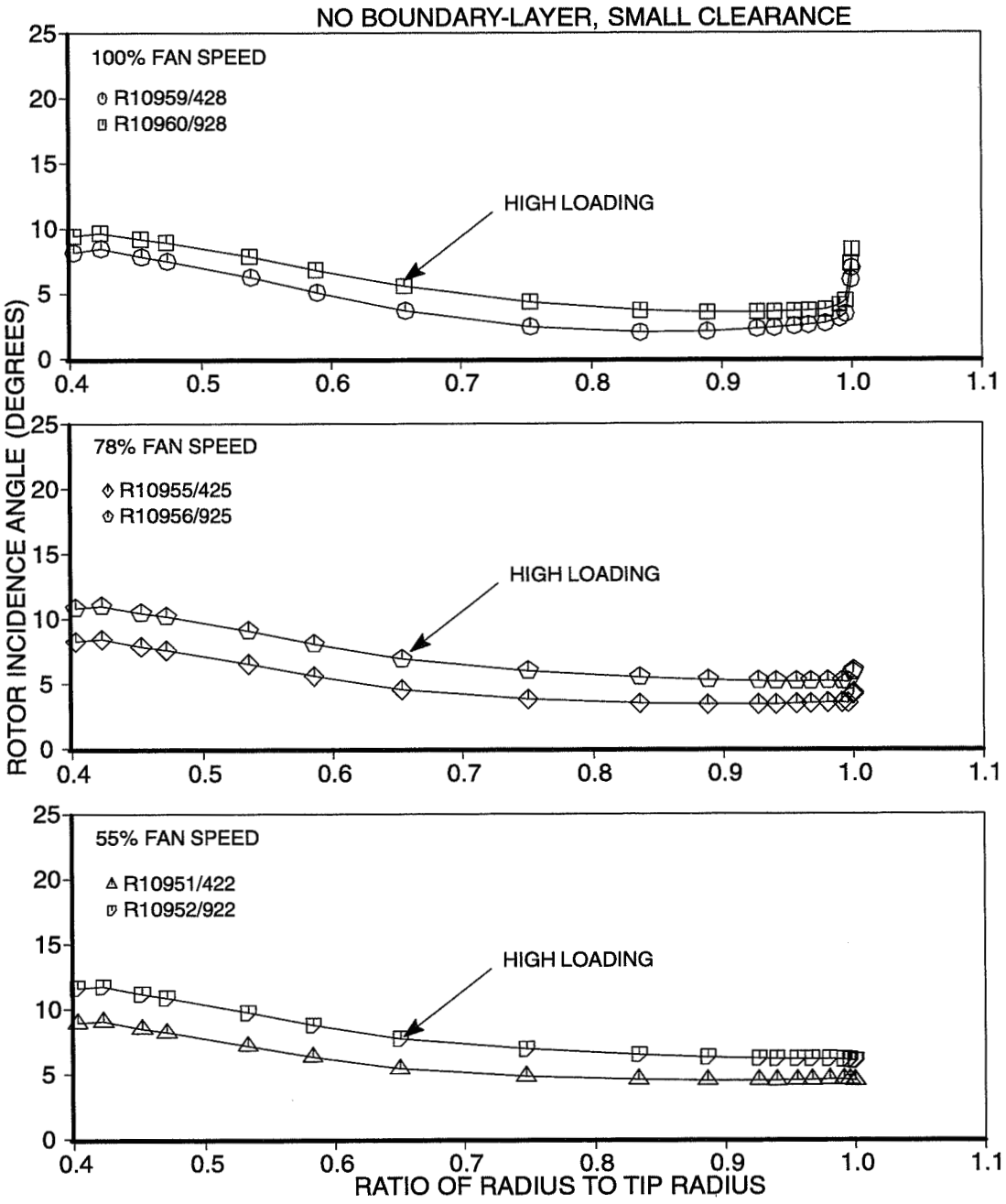

Fig. 43. Effect of Fan Loading on Rotor Incidence – No Boundary-Layer

Fig. 44 shows the stator incidence changes with loading for the same configuration as Fig. 43. The stator incidence is about ten degrees higher for the high-loading versus low-loading and the tip incidence is 20 to 30 degrees for 100% speed and about 10 degrees for lower speeds, as it was for the full boundary layer configuration. The change of boundary-layer size does not impact the stator incidence significantly. This comparison is for small-clearance and the large-clearance shows the same result.

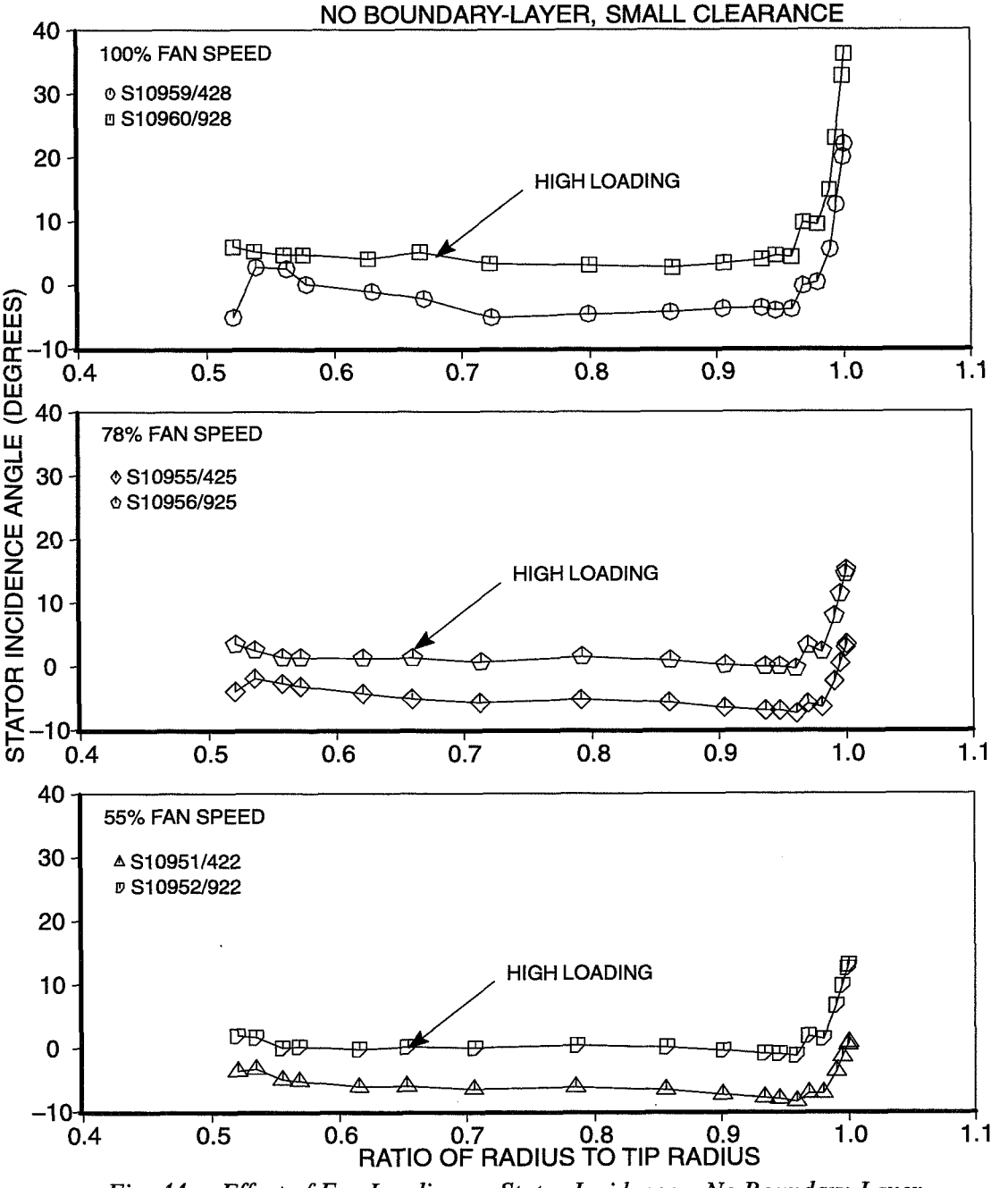

Fig. 44. Effect of Fan Loading on Stator Incidence – No Boundary-Layer

Rotor and stator incidence – boundary layer variation

Another major variation of the test was the different boundary-layer sizes. All of this data is for cases of full or no boundary layer. Very little partial boundary-layer data was acquired. Fig. 45 shows the variation of rotor incidence for full and no boundary-layer at large clearance and high loading. The tip incidence reduces significantly while there is not much change at other radii.

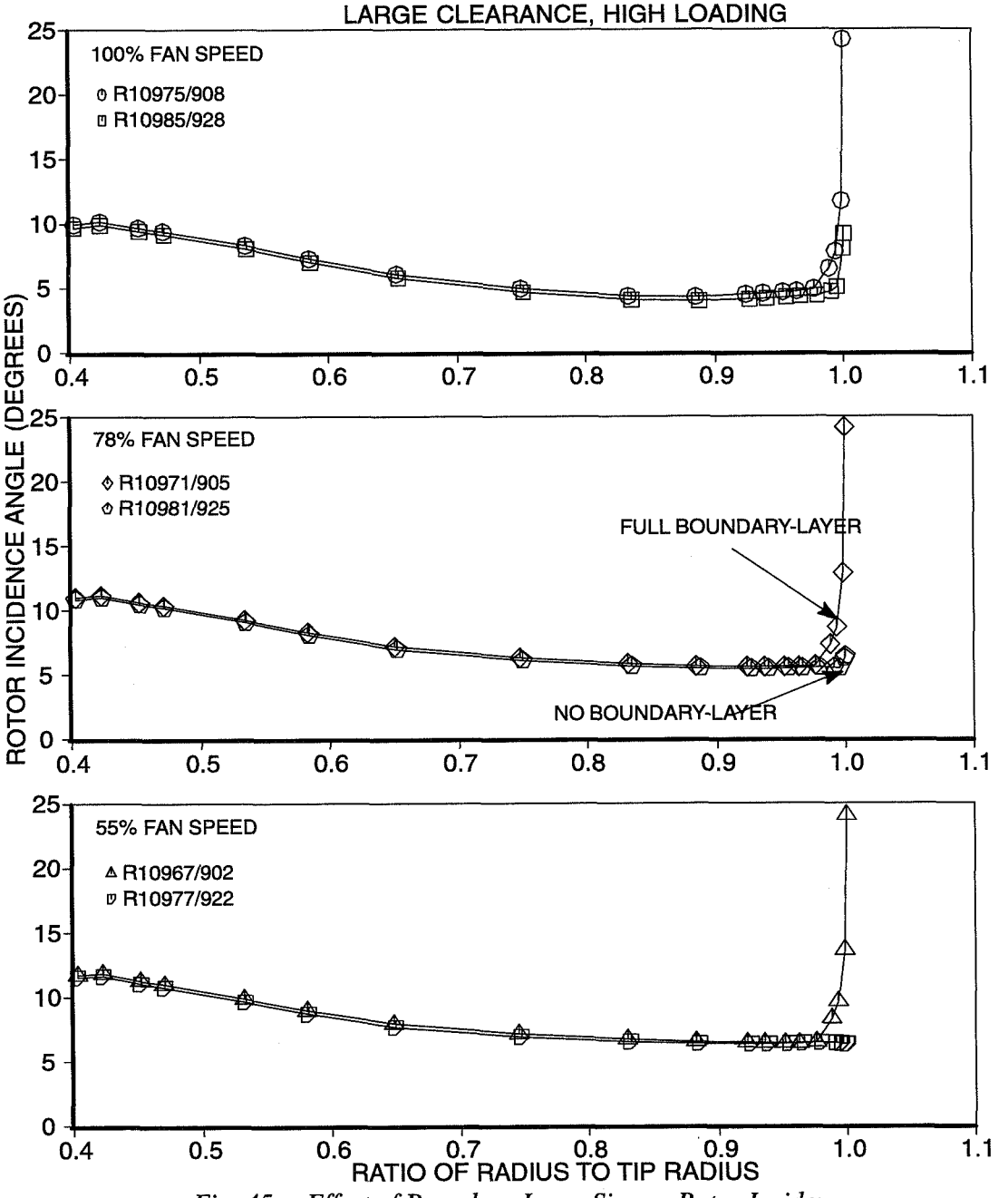

Fig. 45. Effect of Boundary-Layer Size on Rotor Incidence

Fig. 46 shows the change in stator incidence with boundary layer at large clearance. There is not a very large change of stator incidence with a change of boundary layer size for large clearance as was also apparent in the previous section for small-clearance. This indicates that the tip-clearance effects are more dominant on the flow field than the inlet boundary-layer size.

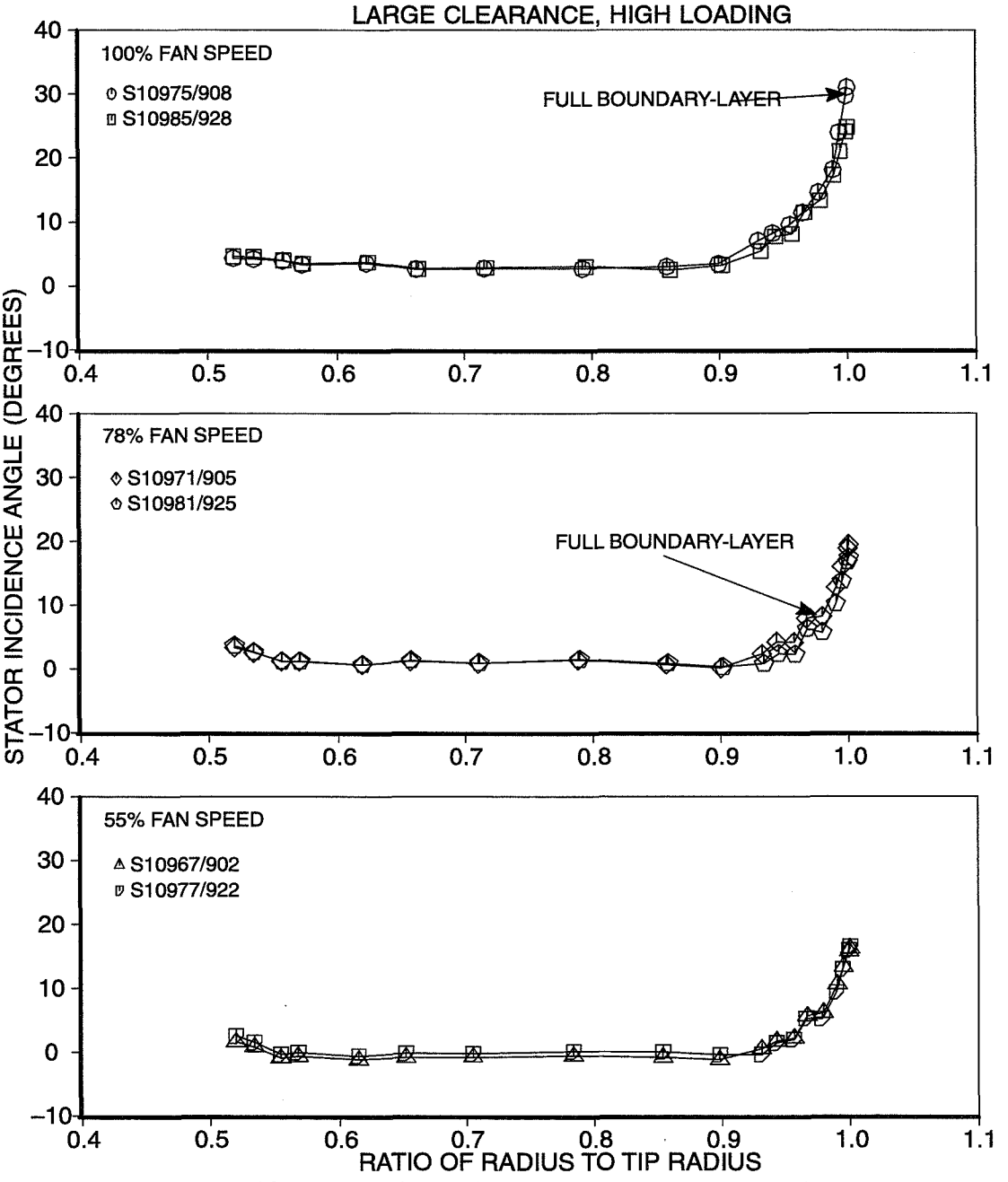

Fig. 46. Effect of Boundary-Layer Size on Stator Incidence

Rotor and stator incidence – clearance variation

The third major variable in the test was tip clearance. Fig. 47 indicates the change in rotor incidence for the change from small- to large-clearance for full boundary-layer. The changes are very small and due to the fact that the rotor mass flow is reduced for large-clearance and thus the incidence increases slightly.

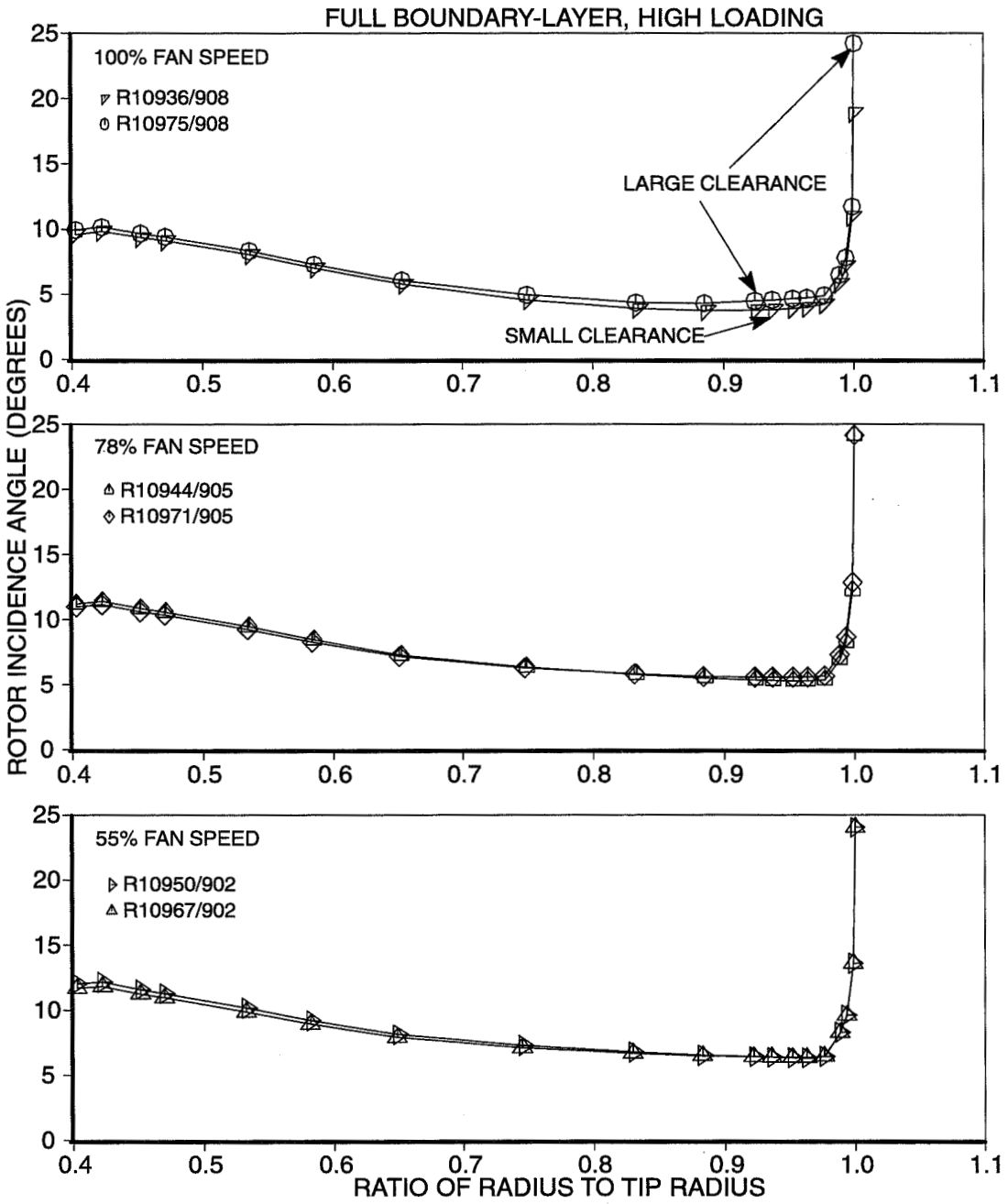

Fig. 47. Effect of Clearance on Rotor Incidence – Full Boundary-Layer

Fig. 48 shows the change in stator incidence with clearance change at full boundary-layer. There is a significant change in stator incidence near the tip with a change of clearance.

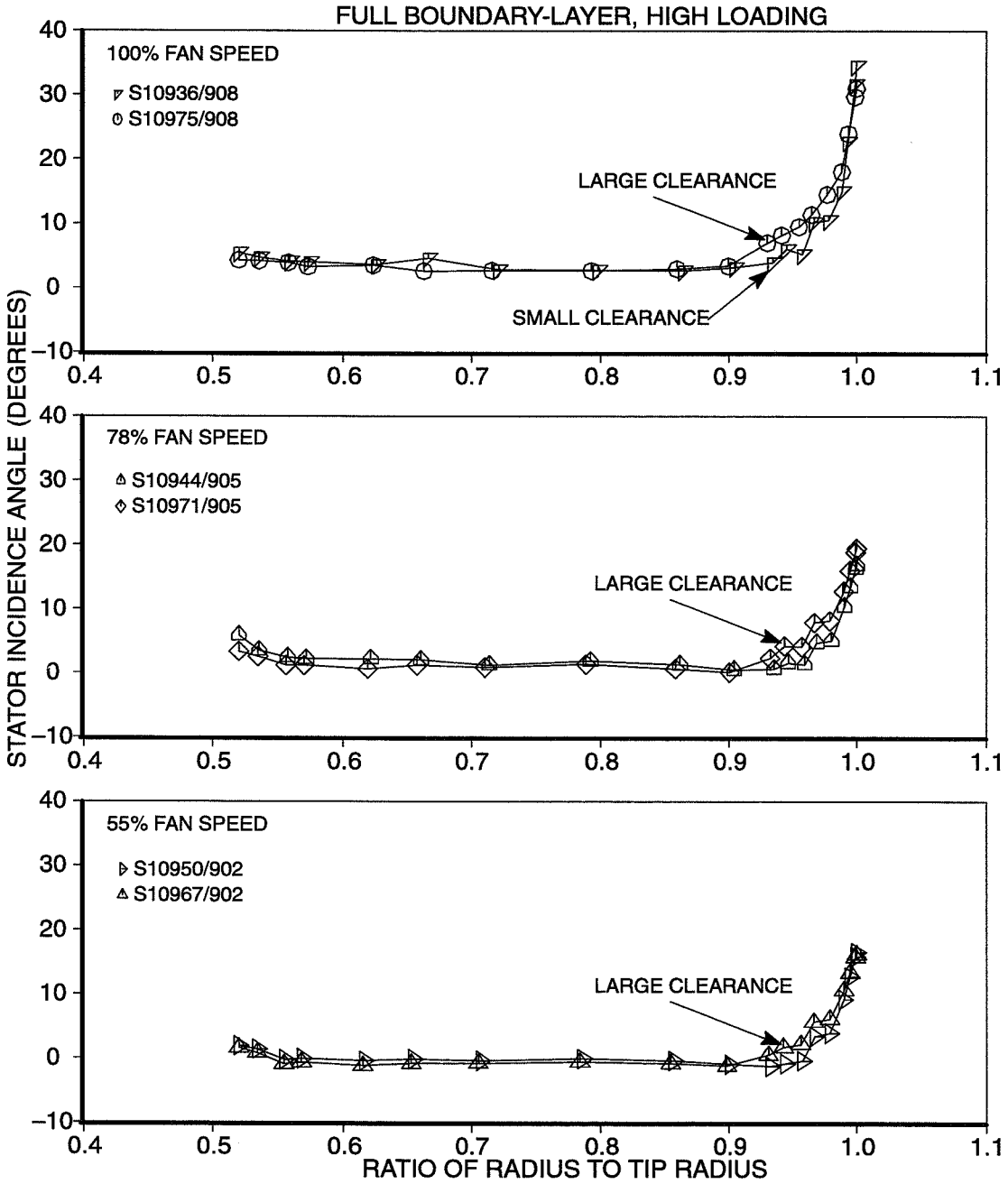

Fig. 48. Effect of Clearance on Stator Incidence – Full Boundary-Layer

Fig. 49 indicates the change in rotor incidence for the change from small- to large-clearance for the no boundary-layer configuration. The changes are very small and due to the fact that the rotor mass flow is reduced for large-clearance and thus the incidence increases slightly.

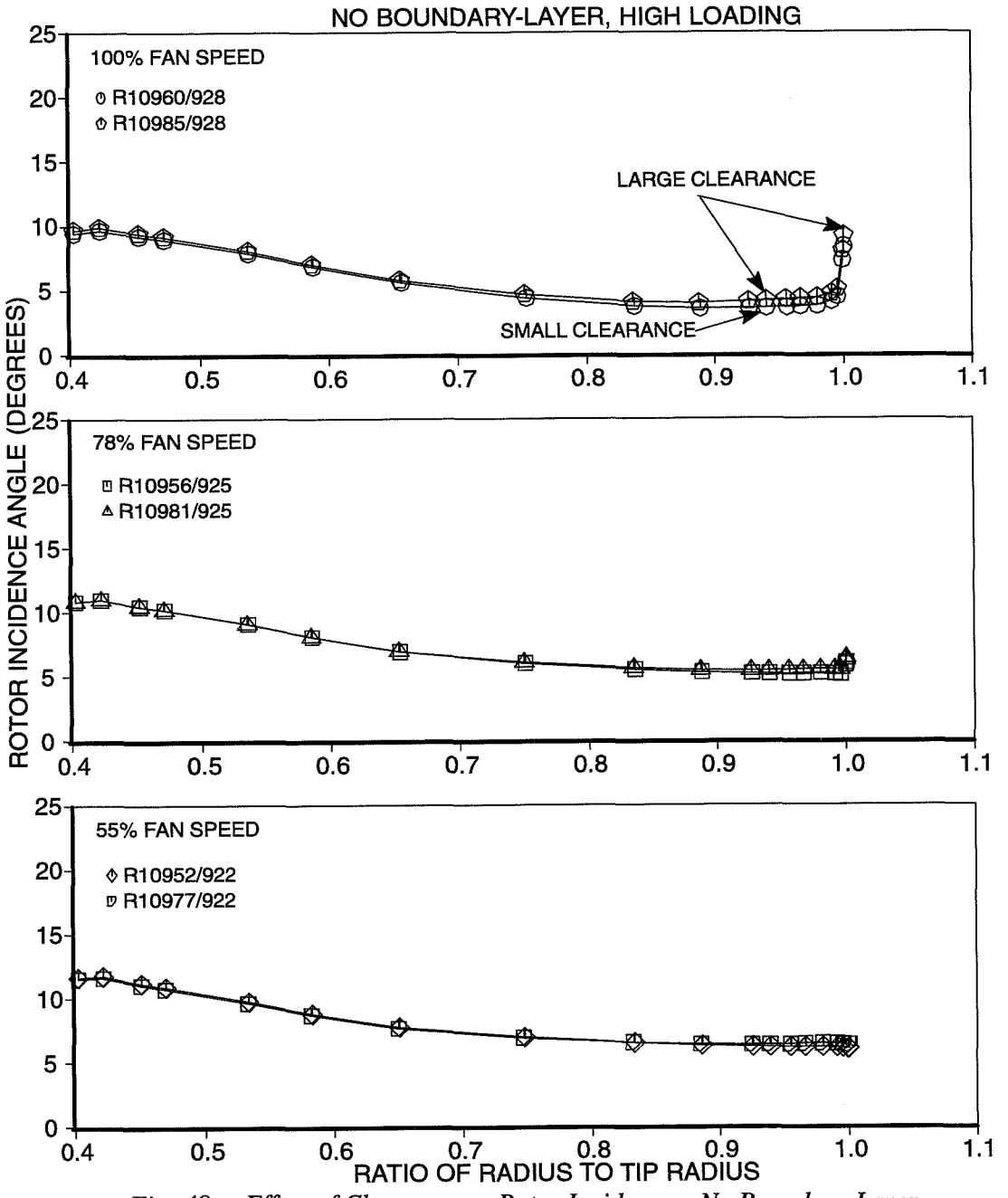

Fig. 49. Effect of Clearance on Rotor Incidence – No Boundary-Layer

Fig. 50 shows the change in stator incidence with clearance change at no boundary-layer. There is a significant change in stator incidence near the tip with a change of clearance. As with the full boundary-layer case, the change from small- to large-clearance increases the stator incidence over most of the tip region. However, in both boundary layer cases, the incidence right at the tip is actually higher for the small clearance. This brings up an important note about the stator incidence angles calculated in the analysis method for this report. The analysis method does not include any radial mixing as the flow travels downstream from the rotor trailing edge. The values of total pressure and

angular momentum (total temperature) at the rotor trailing edge are held constant on streamlines. The stator incidence angle plotted is based on the flow angle at the stator leading-edge station with no radial mixing. The higher stator incidence at the tip for the small clearance is likely due to the fact that at the rotor trailing edge, the small clearance when compared to the large clearance, has a lower-speed core flow near the tip.

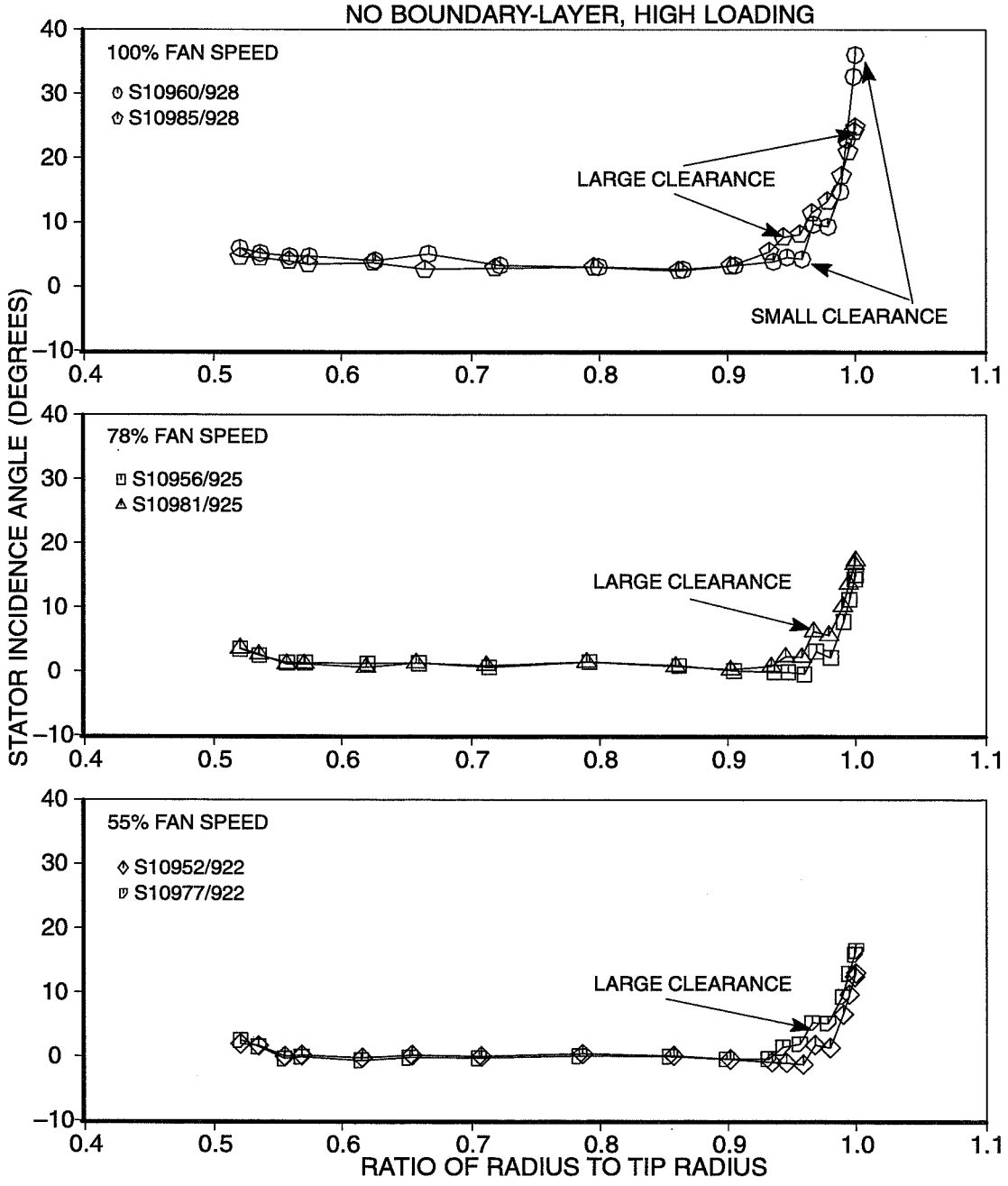

Fig. 50. Effect of Clearance on Stator Incidence – No Boundary-Layer

Detailed analysis results – medium loading for 55, 70, 88 and 100% fan speeds

Fig. 51 to Fig. 58 provide radial profiles of several rotor and stator parameters for the medium loading condition at 55, 70, 88 and 100% fan speeds. This data is from a configuration of rotor-alone, small clearance, and full boundary-layer.

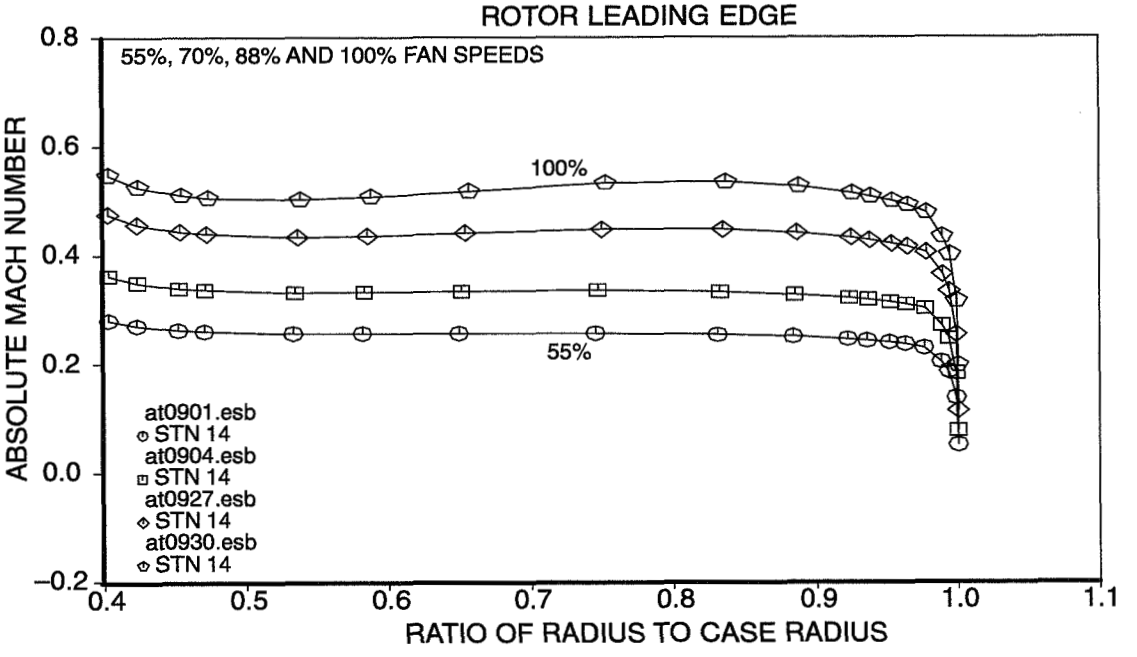

Fig. 51. Absolute Mach Number at Rotor Leading Edge

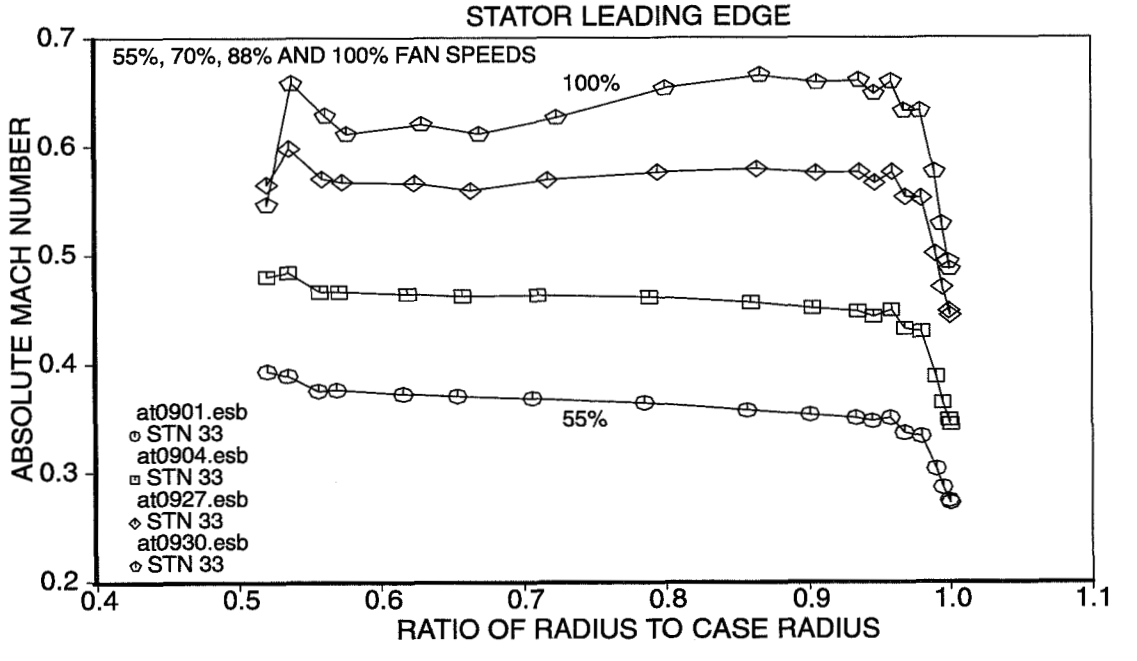

Fig. 52. Absolute Mach Number at Stator Leading Edge

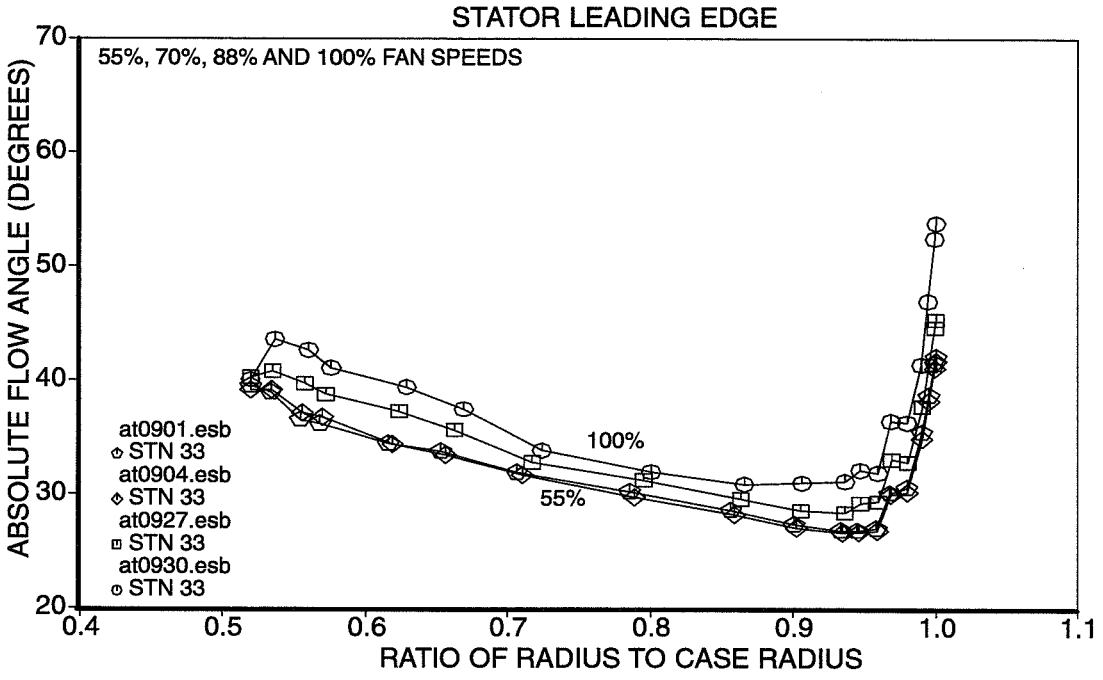

Fig. 53. Stator Leading Edge Absolute Flow Angle

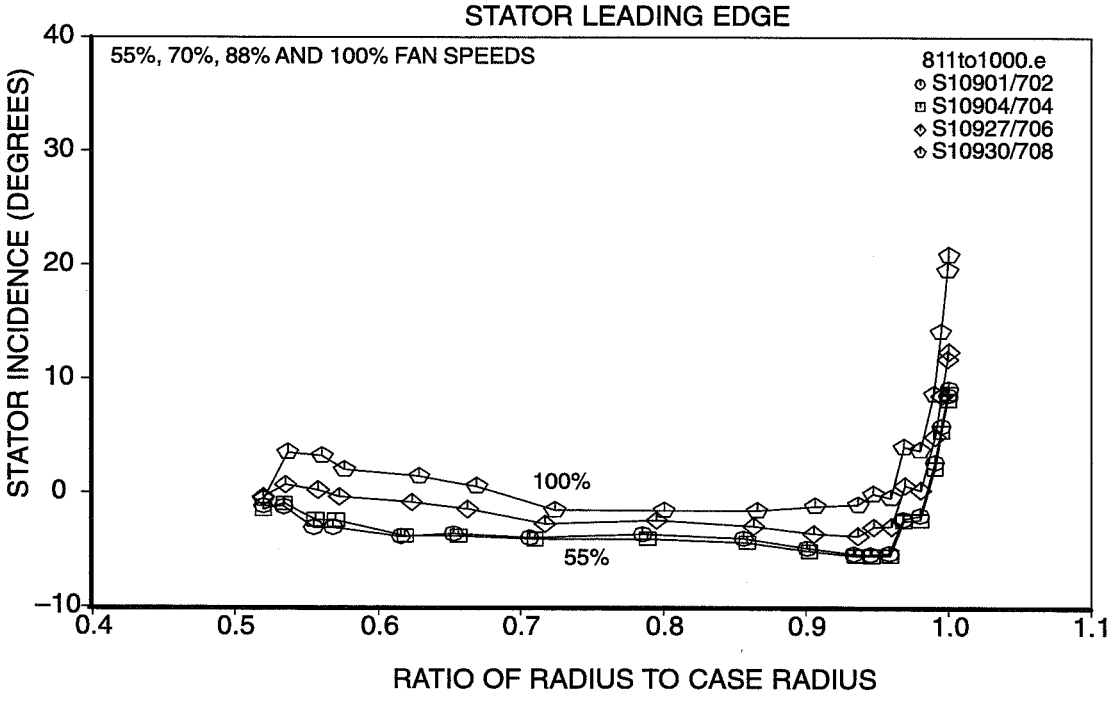

Fig. 54. Stator Incidence

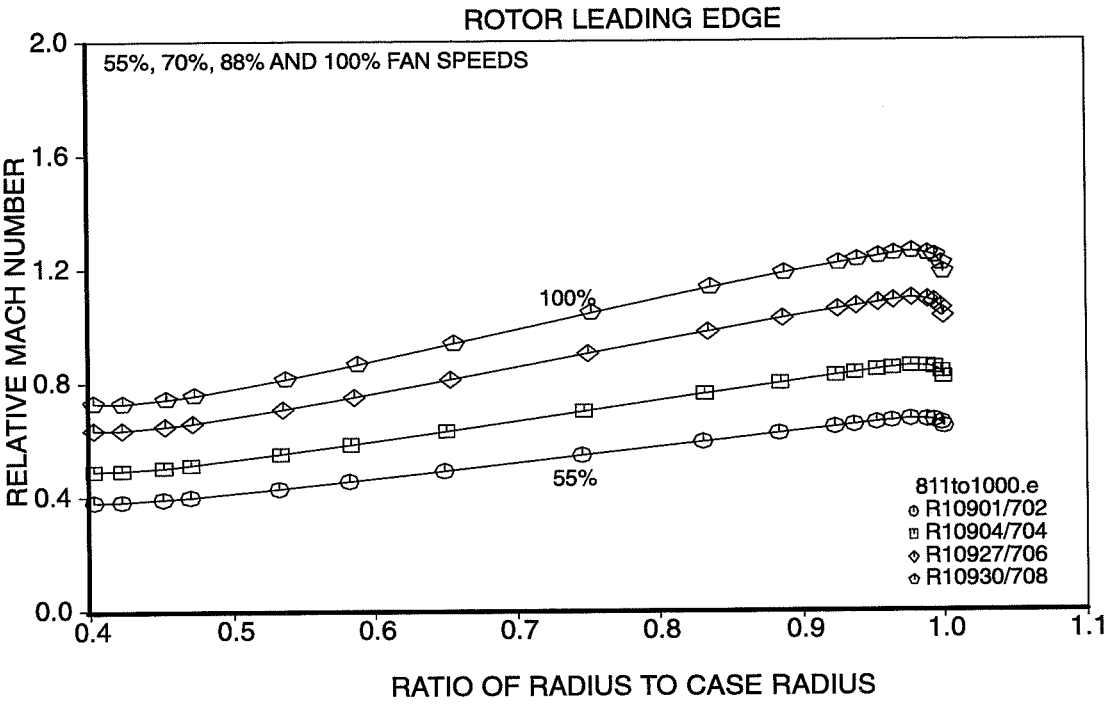

Fig. 55. Rotor Leading Edge Relative Mach Number

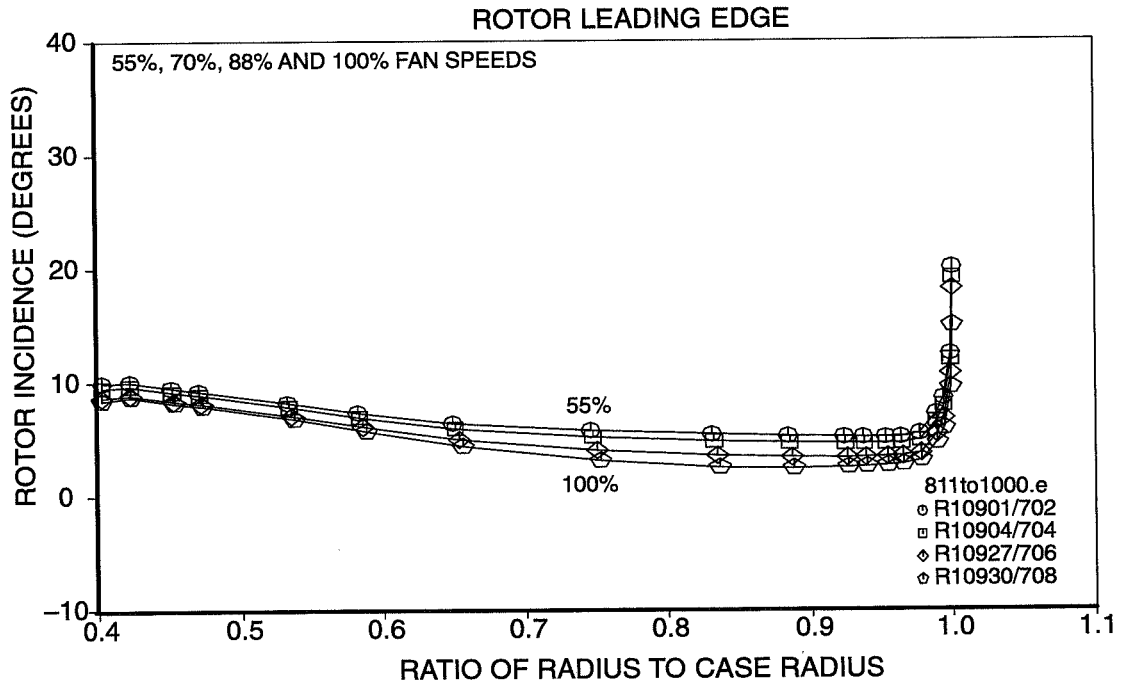

Fig. 56. Rotor Incidence

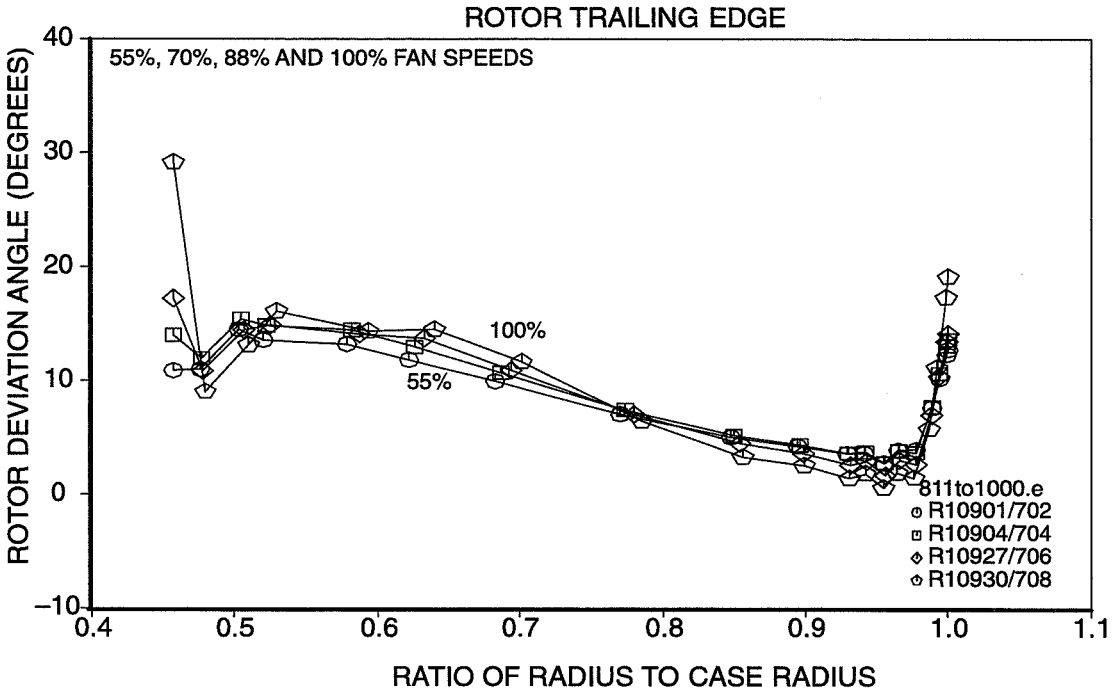

Fig. 57. Rotor Trailing Edge Deviation Angle

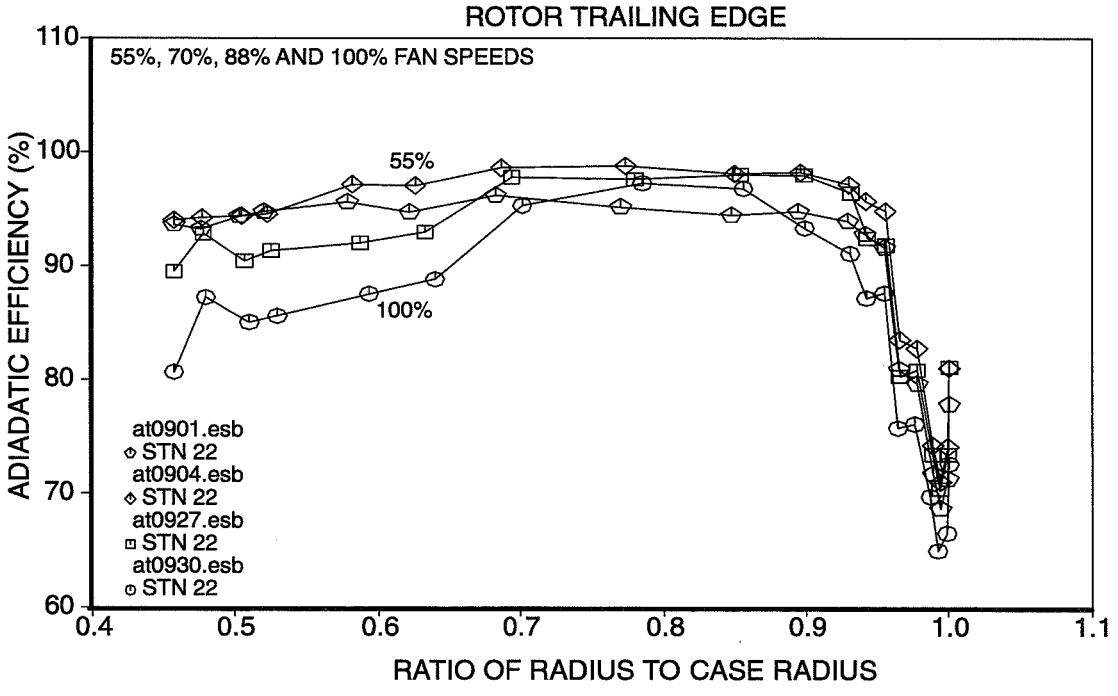

Fig. 58. Rotor Adiabatic Efficiency

4.2 Inlet Unsteady-Flow Measurements

The purpose of these measurements was to provide information about the unsteady flow properties close to the fan face. It was clear from the beginning that measurements at this location were going to be complicated by the high noise levels and the small size of the inlet boundary-layer.

The measurements are affected by at least 2 noise floors. The first one is due to the acoustic velocity fluctuations associated with the near field of the fan. This noise floor is composed of tone and broadband components. The tone components can be removed by subtracting the pulse-synchronized average signal from the raw signal. The broadband noise component of the acoustic velocity signal cannot be separated from the total signal, but it is expected to vary little through the boundary layer whereas the convected unsteady velocity field of the boundary layer varies significantly across the boundary layer. Thus where the composite unsteady velocity signal varies significantly across the boundary layer we expect it to be dominated by the unsteady velocity field of the boundary layer. The other noise floor is associated with the hotwire sensor. It most likely is associated with vibrations of the wire which are excited by vibrations of the wire support structure. Both noise floors become more significant with increasing mean-flow velocity and primarily affect the measurements close to the edge of the boundary layer or outside of it.

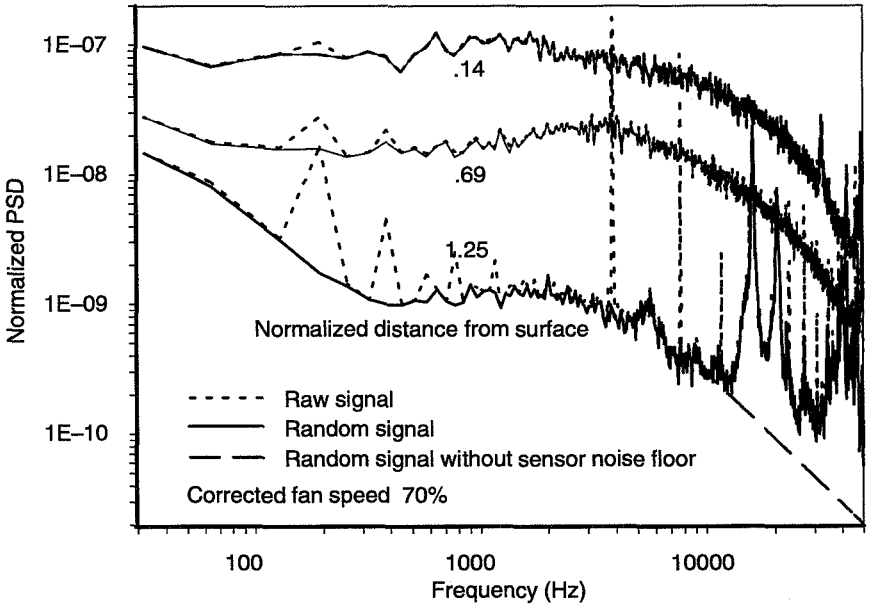

Fig. 59. Noise Floors in Power Spectral Density of Turbulence Velocity Components

The character of the noise floors is depicted in Fig. 59 for a corrected fan speed of 70%. It shows normalized power spectra for the transverse velocity component acquired at 3 different distances from the inlet wall, namely for the position closest to the wall, the center of the boundary layer and the edge of it. All spectral densities have been normalized with the same velocity scale, the mean flow velocity at the edge of the boundary layer. For each position 3 curves are shown, representing the raw signal, the random signal and an estimated cleaned-up random signal. The random signal results from subtracting the pulse-synchronized signal from the raw signal. It shows reduced levels at the harmonics of the fan rotational speed, in particular at the fan BPF and its harmonics.

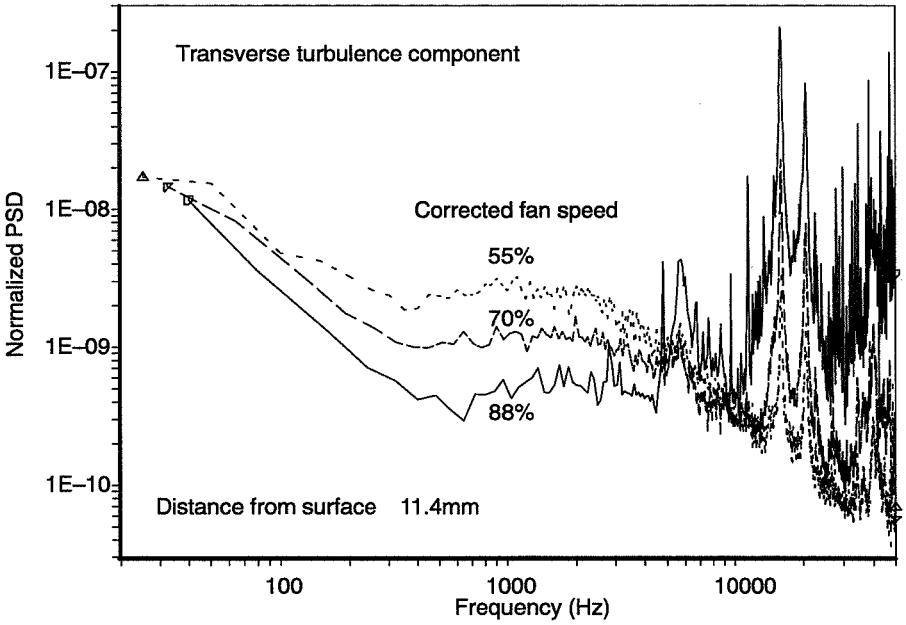

Fig. 60. Cross–Wire Self Noise Floor

The sensor self-noise floor is composed of high-frequency tones with broadband humps at their base (Fig. 60). The frequencies of these tones does not change with the mean-flow velocity, a good indication that they are associated with structural resonances in the sensor support structure. This noise floor only appears close to the edge and outside of the inlet boundary-layer and is only significant for the miniature sensor used in the inlet measurements. The cleaned-up signal is estimated by assuming a –5/3 roll off at high frequencies, representing the spectral shape of an inertial subrange. The intercept point between the actual and the cleaned-up spectrum is positioned such that as much as possible of the original spectrum is preserved without including the tones and skirts resulting from the sensor self-noise floor (Fig. 59).

Turbulence intensity profiles for the transverse component are shown in Fig. 61. They clearly indicate that the contribution of the noise floors becomes significant in the region close to the edge and outside of the boundary layer. The results also indicate that both noise floors become more signifi-

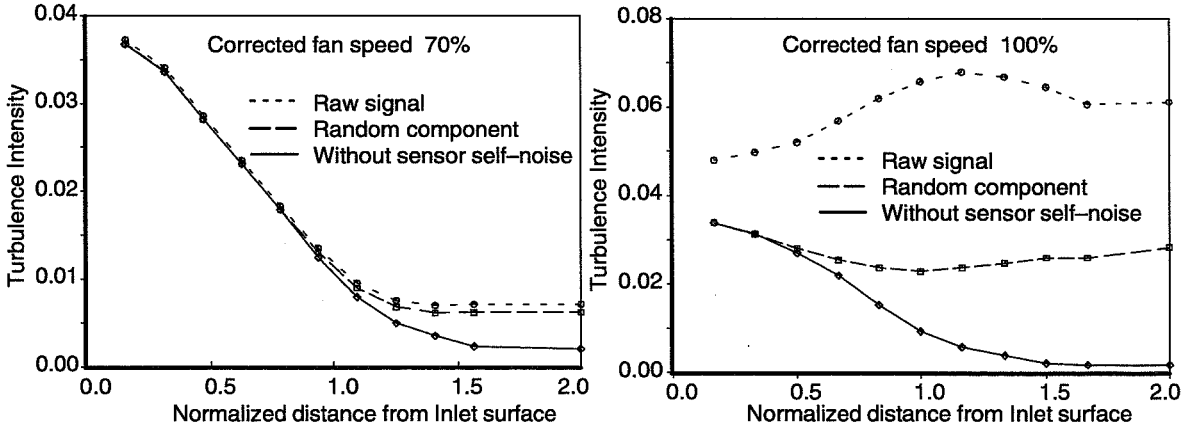

Fig. 61. Effect of Noise Floors on Intensity Profiles of Transverse Turbulence Component

cant at higher fan speeds. The abscissa represents the distance from the inlet surface to the center of the measurement volume of the cross-wire sensor normalized with the thickness of the boundary layer. The latter is based on the total pressure measurements with the fish-hook probe and is defined by the point of the boundary-layer profile where the mean flow velocity reaches a ratio of .995 of the velocity outside of the boundary layer. The measured inlet boundary-layer thicknesses are shown in Fig. 15. The turbulence intensity profiles indicate that low level, intermittent turbulent fluctuations extend significantly beyond that point. The significant noise-floor corrections required at the high fan speeds are due to the harmonic velocity field associated with the rotor bound velocity field and the high self-noise floor of the cross-wire probes.

The quality of the results is also affected by the small size of the boundary layer. The average boundary-layer thickness without suction is 8 to 10 mm. The measurement volume of the cross-wire probes is 1.5x1.5x1 mm. Therefore the properties of the unsteady velocity field cannot be regarded as homogeneous throughout the measurement volume.

Mean-flow velocity profiles based on the cross-wire measurements are shown in Fig. 62. Also included in this figure are the velocity profiles based on the total-pressure measurements and the profile for the flat plate boundary-layer in flow without pressure gradient (Ref. 13). The profiles based on the total pressure and the cross-wire measurements agree reasonably well. Part of the difference may be due to the spatial averaging in the cross-wire measurements, because of the large measurement volume of this probe. The measured profiles differ significantly from the profile of Reference 13. A favorable pressure gradient exists close to the fan face because of the cross-sectional area reduction caused by the spinner. A favorable pressure gradient is also present throughout most of the inlet because of the natural boundary-layer growth. It is assumed that these pressure gradients are the main cause for the differences between the measured velocity profiles and the one reported in Reference 13.

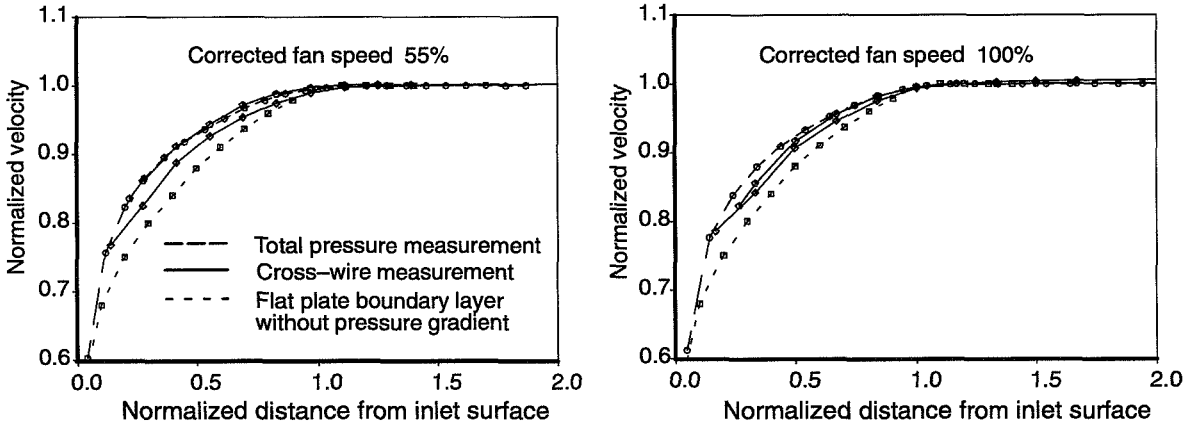

Fig. 62. Inlet Boundary Layer Mean Flow Velocity Profiles

Fig. 63 shows turbulence-intensity profiles for all three velocity components. The definition of the turbulence intensity as used in this figure is defined as the ratio between the local value of the rms of the velocity fluctuations normalized with the mean-flow velocity at the edge of the boundary layer. The rms values are based on the data corrected for both noise floors. The abscissa is again the distance from the inlet surface normalized with the boundary-layer thickness. The latter is based on the velocity profiles derived from the total-pressure profiles. The figure includes data acquired at

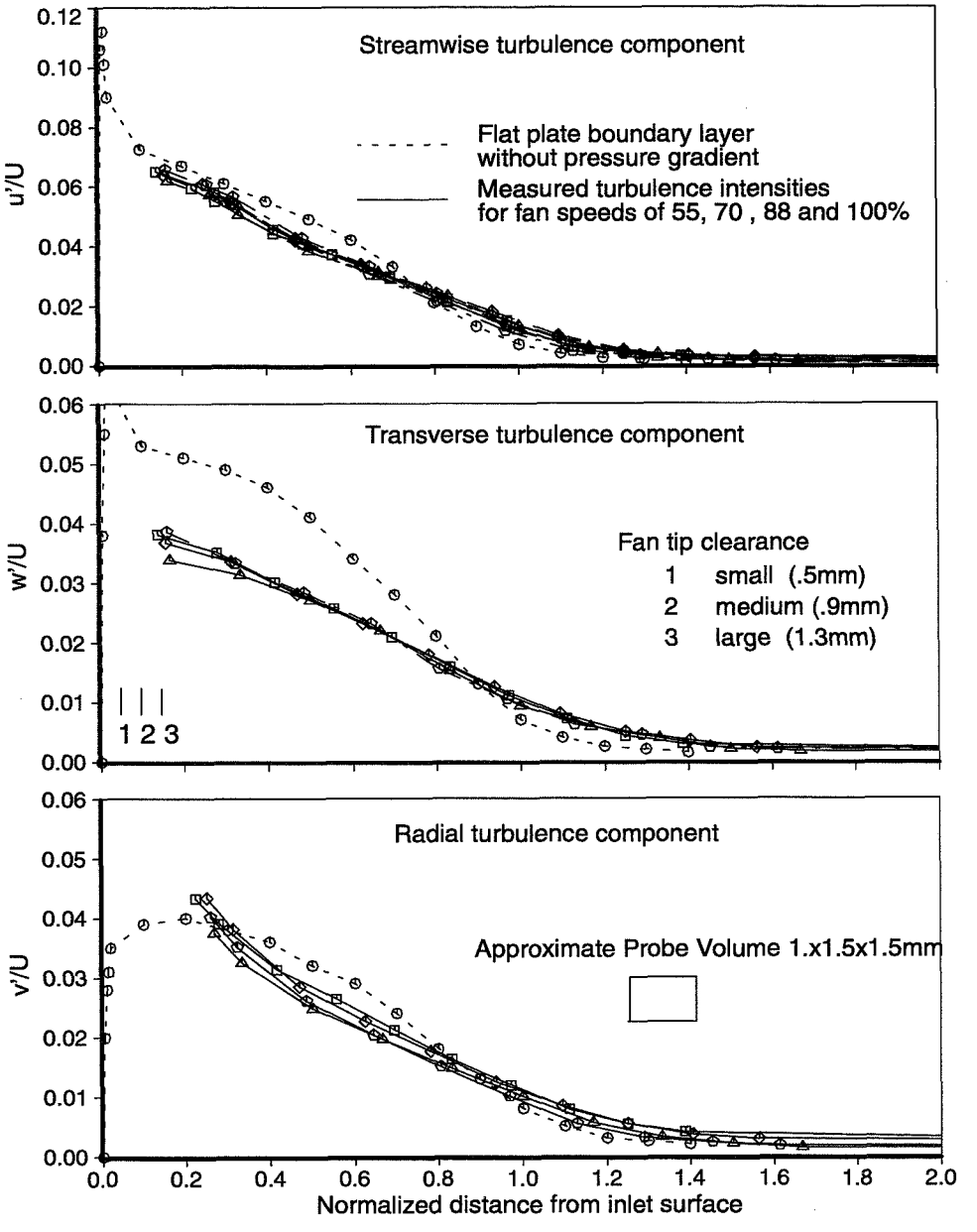

Fig. 63. Turbulence Intensity Profiles for the Inlet Boundary Layer

4 different fan speeds (55, 70, 88 and 100%). The profiles for the radial and the transverse turbulence components were measured with two different sensors. The profiles for the streamwise turbulence component includes eight data sets since it was measured with both sensors. These profiles are based on mean-flow velocities outside of the boundary layer that range from 80 to 160 m/s and collapse quite well. Also shown in this figure are the turbulence-intensity profiles for the boundary layer on a flat plate as reported in Reference 13. Both data sets have been normalized in the same fashion. The general character of the profiles is similar. However significant differences are apparent close to the wall and in particular in the transverse turbulence component. Some of the differences can be associated with the large size of the cross-wire probe relative to the boundary layer thickness and

the resulting amount of spatial averaging. The measurement volume of the cross-wire probe is depicted in the figure. The two data sets coincide in level where the curvature in the profiles is near zero, at a normalized wall distance of .9, where one would expect the effect of spatial averaging to be minimal. At points inboard and outboard of this position the data sets deviate in the proper direction based on the curvature of the profiles, but the differences are much larger than those expected based on the errors due to spatial averaging in the current data set. Other causes that may contribute to the differences between the two data sets are:

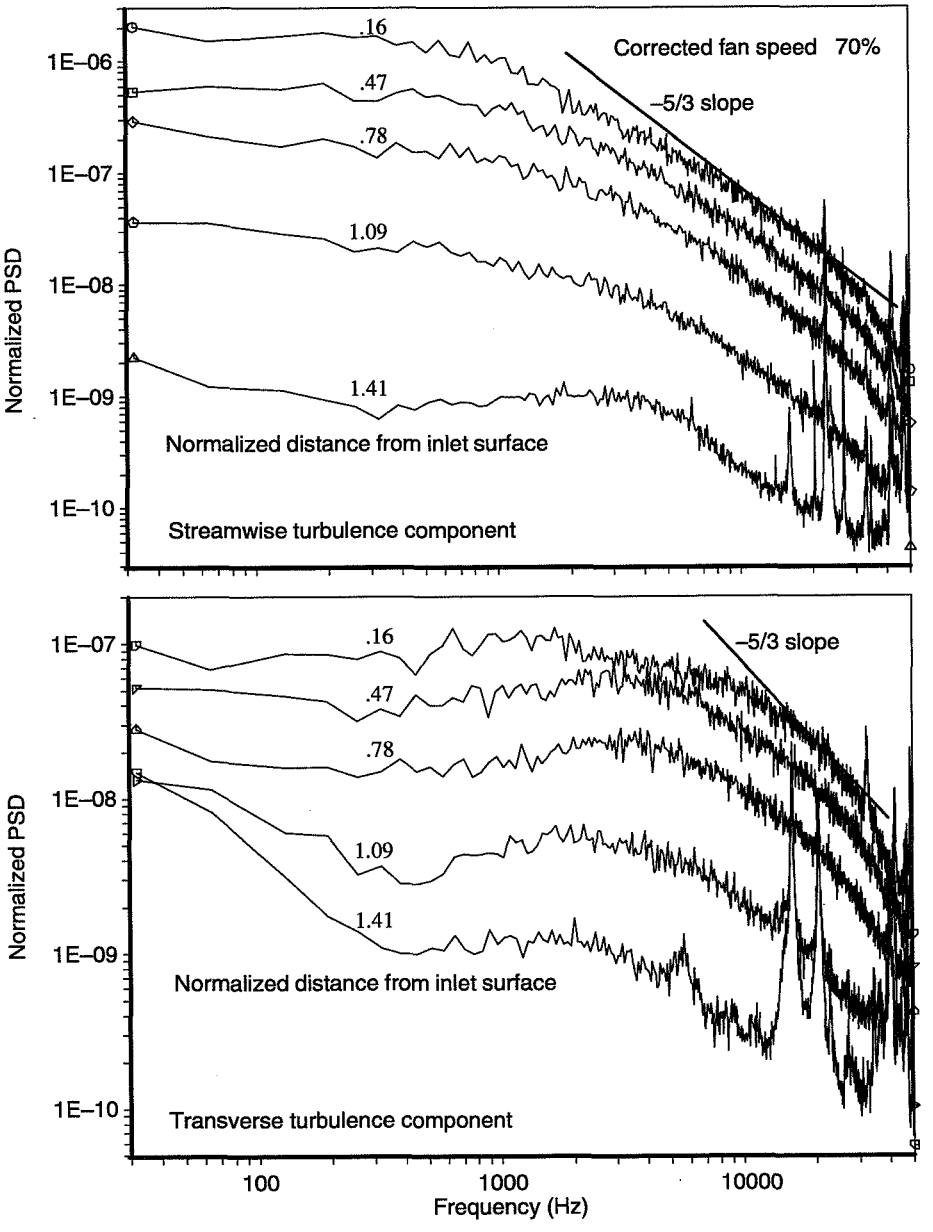

Fig. 64. Normalized Power Spectral Densities for Inlet Boundary-Layer Turbulence

- A favorable pressure gradient exists close to the fan face due to spinner blockage and in general due to boundary-layer growth along the inlet surface.
- Porous surface and axial variation of surface pressure will result in some local boundary-layer suction and blowing in conditions without forced suction.
- The intense sound pressure field throughout the inlet and in particular close to the fan face
- The transverse curvature of the inlet surface

The first one of these effects is the most likely to be responsible for the differences in the turbulence intensity profiles. Data presented in Reference 14 demonstrate the effect of adverse pressure gradients on the turbulence-intensity profiles of wall boundary-layers.

Normalized power spectral densities, PSD, for the streamwise and the transverse component of the inlet boundary-layer turbulence are shown in Fig. 64. Spectra for 5 different positions in the boundary layer are shown. The distance from the inlet surface normalized with the inlet boundary-layer thickness is indicated for each PSD and varies from .16 to 1.41. The results indicate that the spectrum level decreases continuously from a peak close to the inlet surface with increasing distance from the surface over the full frequency range. In the low-frequency range the spectrum level of the streamwise component is significantly higher than the level of the transverse component. In the high frequency range the spectrum level of the two components become similar with the transverse component slightly higher. This is illustrated in Fig. 65.

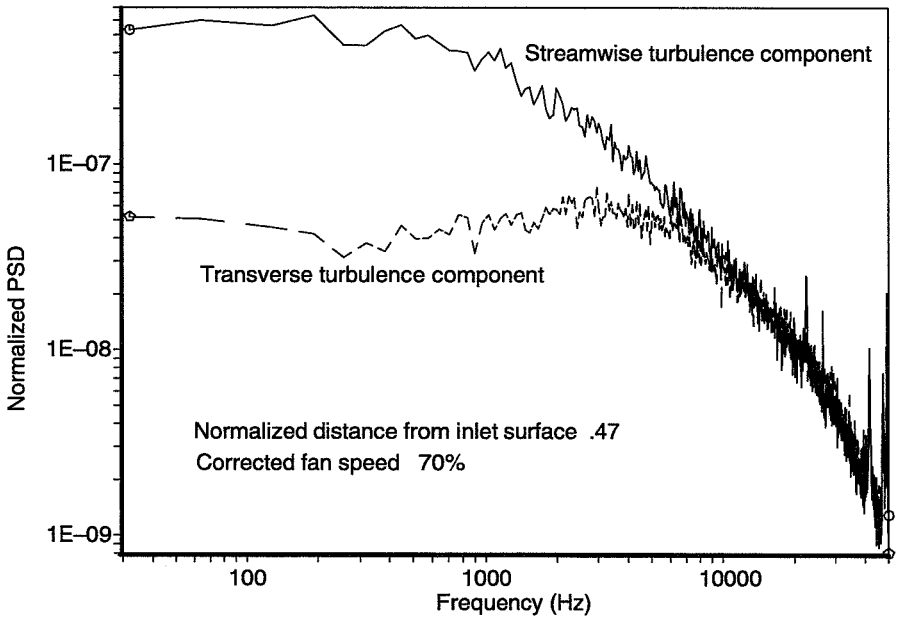

Fig. 65. Normalized Power Spectral Densities of Inlet Boundary-Layer Turbulence

The effect of suction on the inlet boundary-layer has also been evaluated with cross-wire measurements. Measured mean-flow velocity profiles based on different levels of suction and for two different corrected fan speeds are shown in Fig. 66. The length scale used to normalize the distance from

the inlet surface is the boundary-layer thickness for the no-suction condition and is again based on the total pressure measurements. The results indicate that the high suction levels nearly eliminate the boundary layer, especially at the lower corrected fan speed. The goal for the intermediate suction level was to achieve a displacement thickness of 50 percent of the boundary layer without suction. The actual thickness turned out somewhat smaller.

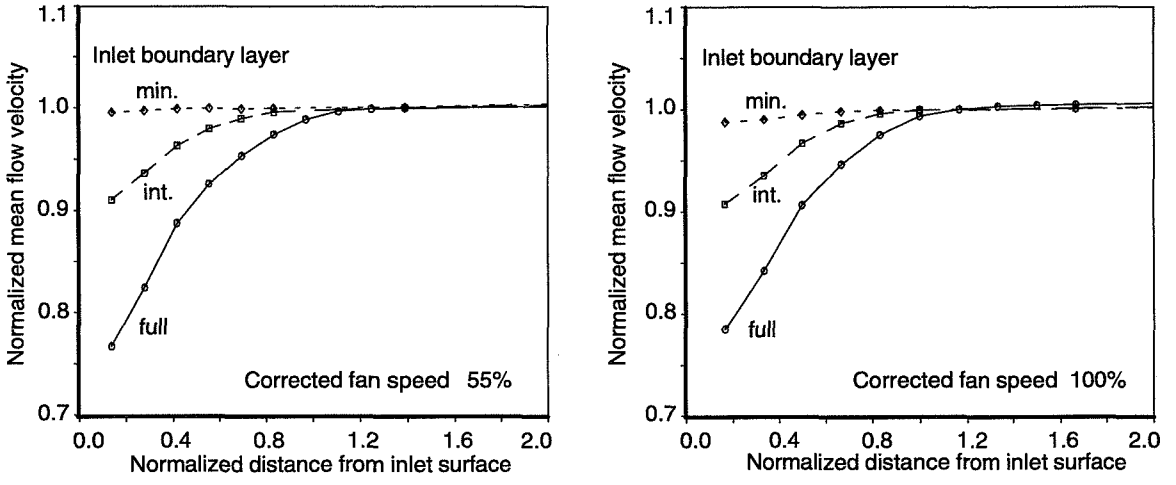

Fig. 66. Effect of Inlet Boundary-Layer Suction on Velocity Profiles

Profiles of the turbulence intensities across the inlet boundary-layer are shown in Fig. 67. The abscissa is defined as in Fig. 66. The turbulence intensities are based on the cleaned-up spectra. The low turbulence intensities, representative for the flow outside of the boundary layer extend closer to the wall for the condition with the high suction rate, but some turbulence still remains close to the wall. The turbulence intensities are reduced for the intermediate suction rate but remain significant. The turbulence-intensity profiles at other corrected fan speeds are very similar to those in Fig. 67.

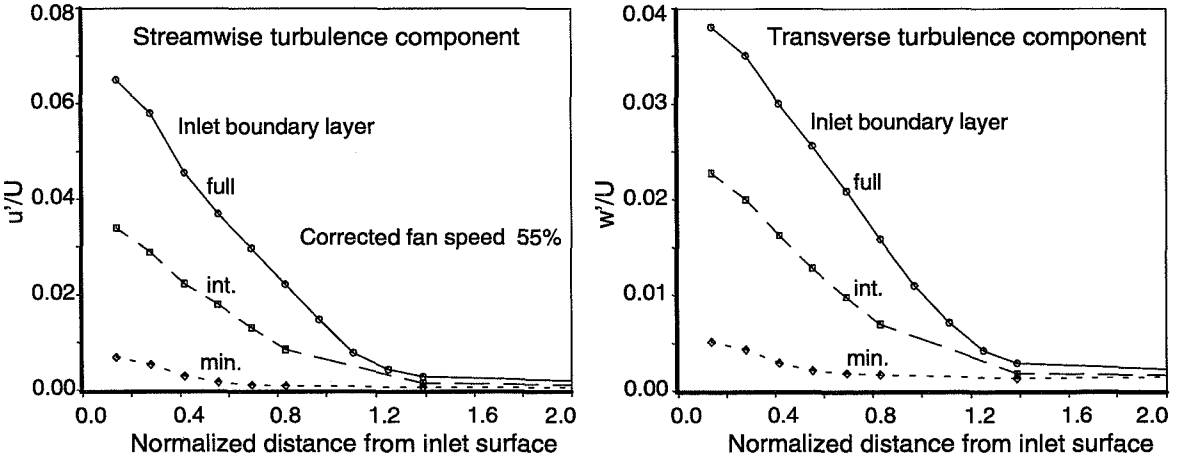

Fig. 67. Effect of Suction on Inlet Boundary-Layer Turbulence Intensity Profiles

Streamwise integral length scales of the inlet boundary-layer are shown in Fig. 68. The results for the transverse and the radial turbulence velocity components include four data sets, for four cor-

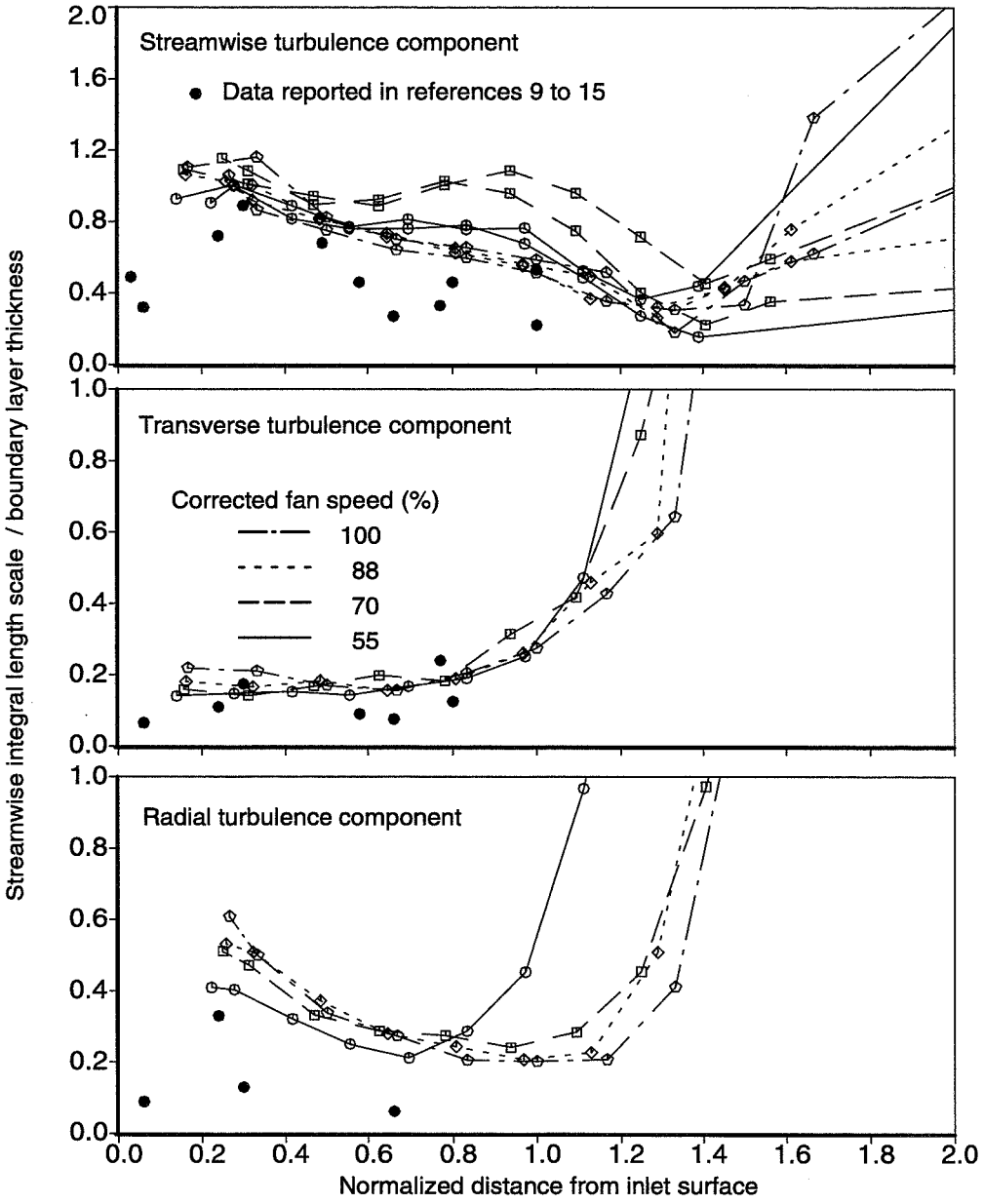

Fig. 68. Normalized Streamwise Integral Length Scales of Inlet Boundary Layer Turbulence

rected fan speeds ranging from 55 to 100%. Since the streamwise turbulence component was evaluated in conjunction with both other components, eight data sets are available for it. The streamwise length scales are related to the limit value of the power spectral density as the frequency goes towards zero:

$$\frac{L_{ux}}{\delta} = \lim_{f=0} PSD_{uu}(f) \frac{U_{\infty}}{4 \overline{u^2} \delta} \qquad (2)$$

with	L_{ux}	Streamwise integral length scale of velocity component u
	δ	Boundary layer thickness
	PSD_{uu} (f)	Power spectral density of velocity component u at frequency f
	U	Mean flow velocity
	$\overline{u^2}$	Variance of turbulence component u

The results for the various fan speeds, (i.e., mean flow velocities) collapse quite well for normalized distances less than 1. For normalized distances larger than 1 the results become dominated by a noise floor and do not represent the scales of inlet boundary-layer turbulence. There is evidence in the measured spectra that for such locations the low frequency content of the spectra is dominated by large scale disturbances that are present in the boundary layer as well as in the clean flow adjacent to it. These disturbances tend to hold up the low-frequency limit of the spectra, resulting in excessively large integral length-scales. Inside the boundary layer the length scales exhibit significant differences between the scales of the streamwise, on the one side, and those of the transverse and radial turbulence components. This seems to be typical for length-scale distributions in wall boundary layers. Also shown in Fig. 67 are integral length scales for flat plate boundary layers as reported in references 13 to 19. They show similar differences between the length scales of the streamwise and those of the other two velocity components. The scales measured in the inlet boundary-layer are in general larger than those reported for the flat plate boundary-layer. This difference may be associated with the effects of the flow contraction close to the fan face.

Since only single-point measurements have been made, no information is available on the transverse integral length-scales of the inlet boundary-layer turbulence.

The hotwire signal is not only affected by the fluctuating signals associated with the inlet boundary-layer, but also those resulting from the acoustic pressure field. The periodic signal components of the acoustic field are extracted from the total signal when the pulse-synchronized average signal is subtracted. It is not possible to separate the broadband acoustic signal from the composite random signal. However it may be assumed that the broadband acoustic signal is of nearly constant magnitude throughout the region that encompasses the outer edge of the inlet boundary-layer and the clean flow just outside of the latter. Thus the contribution of the broadband acoustic signal to the total signal must be smaller than the composite signal measured outside of the boundary layer.

4.3 Fan Duct Unsteady-Flow Measurements

The unsteady flow measurements in the fan duct were conducted with a single radially traversing cross-wire probe. The axial position of the probe was selected to coincide with the leading edge of the smallest stator set. However all measurements were made in the rotor-alone configuration, without stators. The flow in this area has a substantial amount of swirl and in order to keep all measurements within the probe calibration envelope the probe was rotated into the flow by an angle of 30°. The probe was mounted on a traversing mechanism that allowed it to traverse from the outer duct wall all the way to the hub surface. Hotwire data were obtained for 66 runs, each run consisting of 12, 14 or 24 test points at different radial positions in the duct, adding up to a total of 1260 test points. The matrix of configurations for which hotwire data was acquired is shown in Table 8.1. The majority of the data was acquired with a cross-wire probe (TSI 1246–T1.5) configured to measure the streamwise and the transverse velocity components. The transverse component is normal to the mean flow direction and normal to the radial direction. A more limited data set was acquired with a probe of the same type but configured to measure the streamwise and the radial velocity components. The data acquisition procedure was the same as for the inlet boundary-layer data, except for additional post test processing.

Typical results that demonstrate the pulse-synchronized averaging process are shown in Fig. 69. The first segment of this figure shows the synchronization pulse which was used to separate the harmonic and the random signal components. The synchronization pulse was also used to resample the data such that each data point corresponded to a particular position of the rotor. The resampling process provided 720 equispaced points per rotation. The 3 segments of the figure actually show 8 traces covering 8 different rotations. The eight traces for the pulse signal nearly coincide and demonstrate the excellent repeatability of this signal. The trailing edge of the pulse which is steeper than its leading edge was used to define the start and end of each rotation.

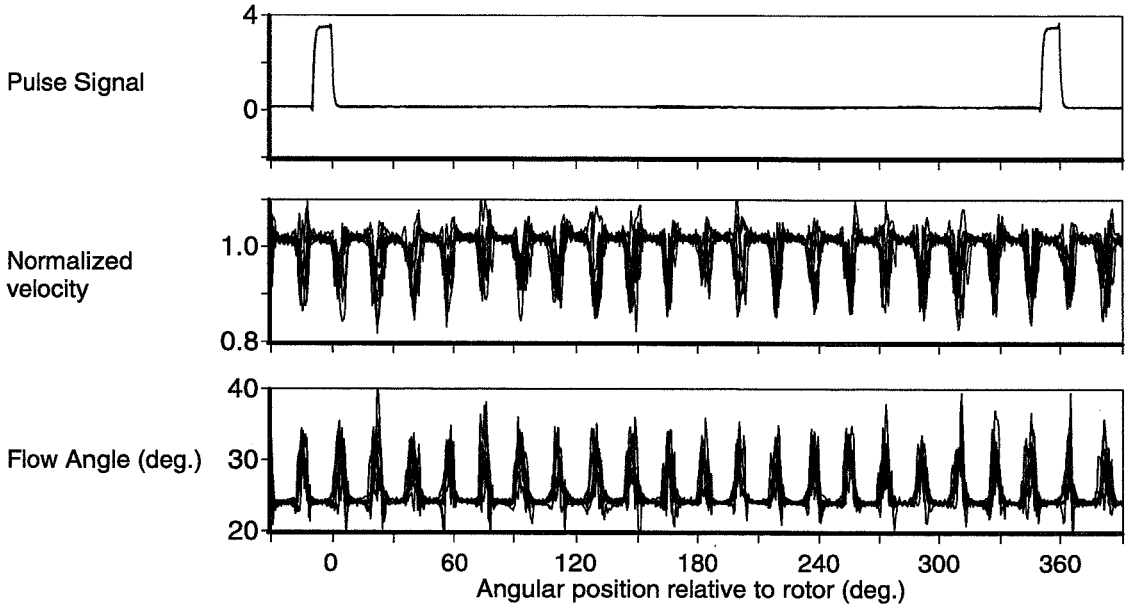

Fig. 69. Pulse-Synchronized Averaging Process 1

The traces of the velocity and the flow angle clearly demonstrate the effect of the wakes of the 20 rotor blades. Both signals show significant harmonic content but also exhibit large random fluctuations within the rotor wakes. The velocity signal has been normalized with the circumferential average of the velocity for this radial position and shows that each rotor wake results in a pulse-like decrease of the velocity. The flow angle signal indicates that each rotor wake results in a pulse-like increase of the flow angle.

The pulse-synchronized averaging process is used to separate the signal into a deterministic and a random signal. The deterministic signal contains the harmonic signal content and provides the locally averaged flow parameters at each point of the resampling process. Additional averaging provides circumferentially averaged flow parameters for each radial position and spatial averages based on averaging over the full annulus cross-section.

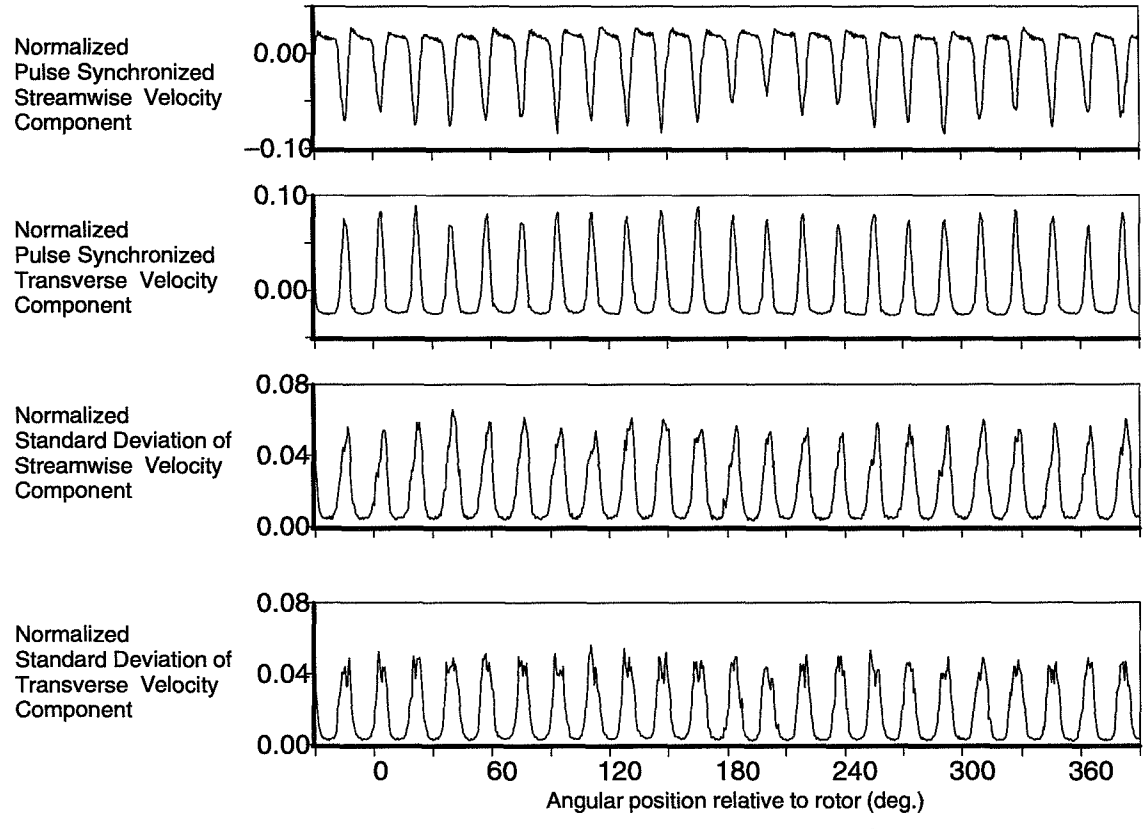

Fig. 70. Pulse-Synchronized Averaging Process 2

The pulse-synchronized average velocities and turbulence intensities corresponding to the raw signals of Fig. 69 are shown in Fig. 70. The first segment of this figure depicts the locally-averaged streamwise disturbance velocity normalized with the circumferentially-averaged velocity. The second segment presents the corresponding signal for the transverse velocity component. These components were obtained by decomposing the vector of the locally-averaged velocity into components parallel and normal to the circumferentially-averaged velocity and subtracting the latter from the streamwise component. The last two segments of Fig. 70 show the circumferential variation of the random signal content for the streamwise and the transverse velocity components. The local random signal was obtained by subtracting the local mean velocity vector from the instantaneous velocity

vector. The local standard deviation was then determined based on the local mean-square value resulting from summing over all rotations. The results indicate that the turbulence intensities, the standard deviations of the random velocity fluctuations normalized with the circumferentially-averaged velocity, are small between the rotor wakes (less than 1%) and reach levels in the order of 4 to 6 percent in the core of the wakes. The variation of the intensity for the transverse velocity component has an almost square-wave-like character similar to those observed in two-dimensional wakes. The intensity distribution for the streamwise turbulence component however is not symmetric relative to the wake center, its peak occurring on the trailing side of the wake.

The angular position is computed based on the pulse signal and is proportional to the product of time and angular velocity of the rotor. For a stationary observer the viscous material associated with the boundary layer from the pressure side of the rotor blade arrives first, before the flow coming off the suction side of the rotor blade. Thus in Fig. 70 the left side of a wake is associated with the pressure side and the right side with the suction-side flows of the rotor blade. The averages shown in Fig. 70 demonstrate that the harmonic as well as the random velocity fluctuations are very similar for all rotor blade wakes.

Pulse-synchronized average data

The regularity of the pulse-synchronized average flow is demonstrated in Fig. 71 which depicts the radial and circumferential variations of the harmonic content for the streamwise velocity component and the flow angle in the form of contour plots. In this figure the wakes appear again as regions of negative velocity disturbances and increased flow angles. Near the rotor-blade trailing edge the wakes would appear as nearly radial lines. Because of the radial variation of the rotor blade angle at the trailing edge, the wake lean increases with distance from the rotor trailing edge. The results indicate that at the cross-wire measurement position the wake lean between the hub and the tip covers about 1.5 rotor-blade spacings. In the hub region the wake leaves the rotor in a nearly axial direction and arrives at the measurement location nearly simultaneously. In the tip region the wake flow leaves the rotor at a large angle relative to the rotor axis and its arrival at a fixed angular position trails behind the arrival of the rotor blade. This rotor wake lean will increase with distance from the rotor trailing edge. It is an indication of the significant amount of shear between the different radial layers of the flow downstream of the rotor and the much higher angular velocities in the hub region. Based on the great similarity of the wakes from the various rotor blades, only a limited region of the total duct cross-section will be shown in most of the following plots.

The spatial variation of the three components of the pulse-synchronized average velocities is shown in Fig. 72. The velocity components are based on an orthogonal system lined up with the mean velocity at each radial position. The latter is determined by averaging the local mean flow vectors over all angular positions. The streamwise component does not include its dc content and all components have been normalized with the circumferentially averaged velocity at the respective radial position. The components are positive in the mean flow direction for the streamwise component, in the direction of rotor rotation for the transverse component and radially outwards for the radial component. The rotor wakes are of course not lined up with any axis of this coordinate system and their orientation relative to the axis changes with radial position. In this stationary framework the wakes appear as sheets of laterally traversing flow imbedded in a convecting medium. In two-dimensional airfoil wake flow one would expect an average flow disturbance only in the direction of the mean flow and no components in the spanwise and the normal direction. The rotor wake results however indicate that at a distance of about three rotor chords all components of the average unsteady velocity field are of the same order of magnitude. This average unsteady velocity field and in particular the trans-

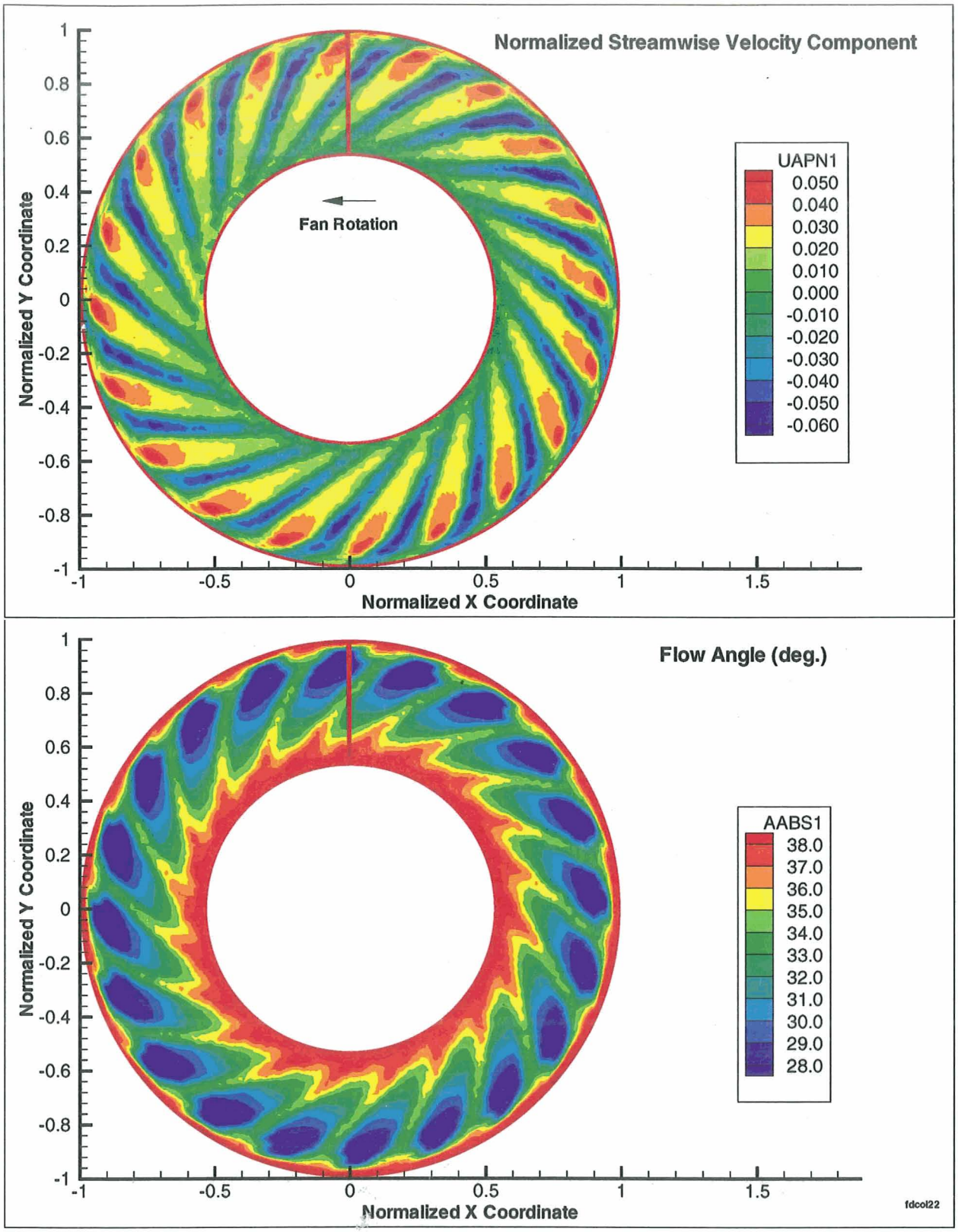

Figure 71. Pulse Synchronized Averge Velocity Field
Corrected Fan Speed 70%, High Fan Loading
Large Tip Clearance, Full Inlet Boundary Layer, Runs 920 and 885

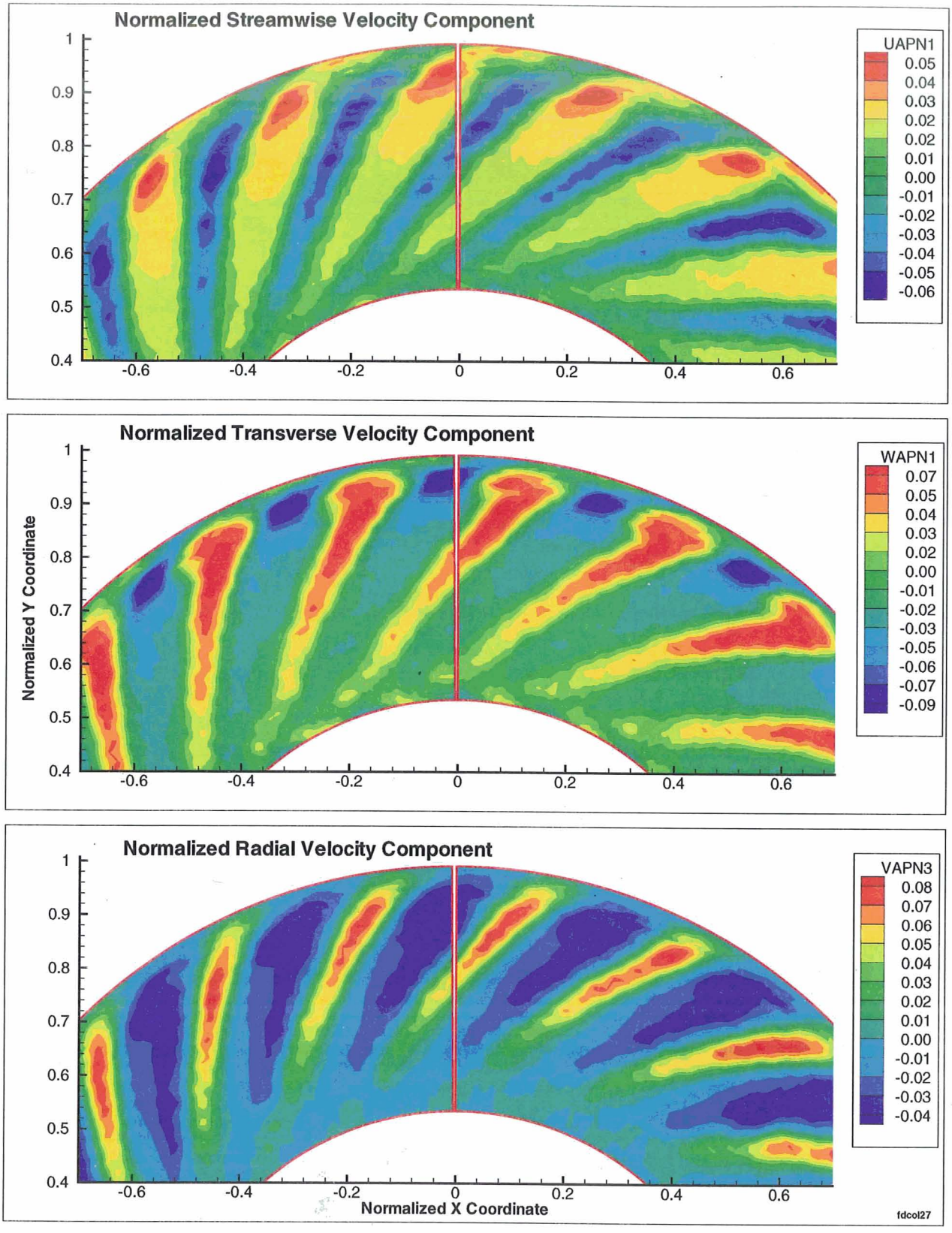

Figure 72. Pulse Synchronized Average Flow Parameters in Stationary Coordinate System Corrected Fan Speed 70%, Large Tip clearance, Full Inlet Boundary Layer, High Fan Loading, Runs 920 and 885

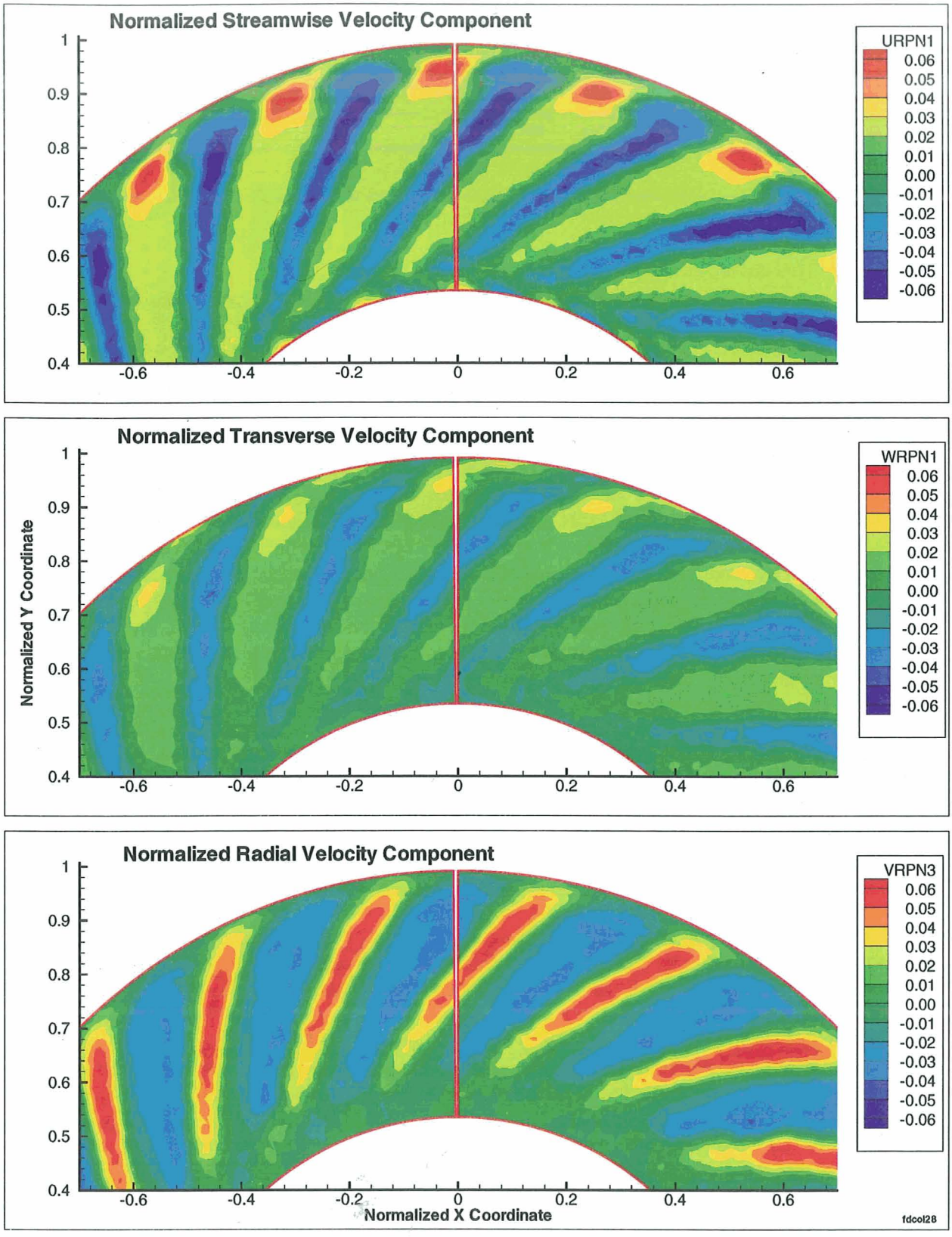

Figure 73. Pulse Synchronized Average Unsteady Velocities in Rotor Coordinate System Corrected Fan Speed 70%, Large Tip Clearance, Full Inlet Boundary Layer, High Fan Loading, Runs 920 and 885

verse component are key ingredients in the generation of fan tone noise. The highest levels of these harmonic velocity fluctuations occur close to the outer duct wall.

A simple transform can be used to define the corresponding velocities in the rotor-bound coordinate system by subtracting the local wheel speed vector from the instantaneous velocity vector. The resulting pulse-synchronized average velocity components are depicted in Fig. 73. The components are again based on an orthogonal coordinate system with the streamwise component lined up with the circumferentially averaged relative velocity at the respective radial position. The radial velocity component does not change in this transform. The velocity components are normalized with the circumferentially averaged relative velocity at the particular radial position. In this coordinate system the streamwise axis is lined up with the wake axis and in the situation of a two-dimensional wake the transverse and the radial components would be zero. The results do indeed indicate that the transverse unsteady velocity component is significantly smaller than the streamwise component. However the radial component is in general of the same order of magnitude as the streamwise component.

The information presented in the preceding figures can be condensed by displaying two of the components in the form of vectors. This representation is frequently used when the components are orthogonal and two vector components fall into the display surface. This is not the case with the current data set in either the stationary or the rotor bound coordinate system. The display surface is the duct cross-section at the location of the cross-wire, it only contains the radial velocity component, the streamwise and the transverse components are oblique to it. The local trace velocity in this plane was determined by projecting the locally averaged velocity vector onto the display surface, using the circumferentially-averaged velocity vector as the projection direction. The resulting velocity vectors are shown in Fig. 74 for the stationary and the rotor-bound coordinate system. The third velocity component shown in this figure in the form of color contours is the streamwise disturbance velocity component with the same definition as for the data shown in Fig. 72 and Fig. 73. The three velocity vector components are not orthogonal and do not represent the complete harmonic velocity field, but they provide a good representation of the secondary flows in the flow field downstream of the fan. All three velocity components have been normalized with mean velocities. In the stationary system, the upper segment of the figure, the circumferentially averaged mean velocity is the normalizing velocity. In the rotor-bound system, the lower segment, the circumferentially averaged relative velocity is the normalizing parameter.

Both segments of Fig. 74 demonstrate well defined relationships between the velocity components. The radial velocity component is positive, outward bound in the wake region where the streamwise disturbance is negative (blue regions). Inbetween the wakes (red and yellow regions) the secondary flows are directed inboard. In the rotor-bound system the secondary flows are lined up with the wakes and the vectors indicate that the transverse and radial velocity components are associated with the outward migration of the wake material. This migration comes about because of the imbalance between the radial pressure gradient and the centrifugal forces acting on the wake material. The radial pressure gradient is controlled by the average angular momentum of the local flow field. In areas where the angular velocity is above average (wakes) the flow will migrate outboard and in the flow segments with below-average angular momentum (inbetween wakes) the flow will tend to migrate inboard. The radial velocities are small in the hub region and tend to increase with radial position. This may be due to the radial variation in the difference of angular velocity between the wake flow and the flow segments between the wakes. In the hub region the flow angle in the rotor bound system is close to zero, the relative velocity is nearly axial. In this situation the absolute angular velocity

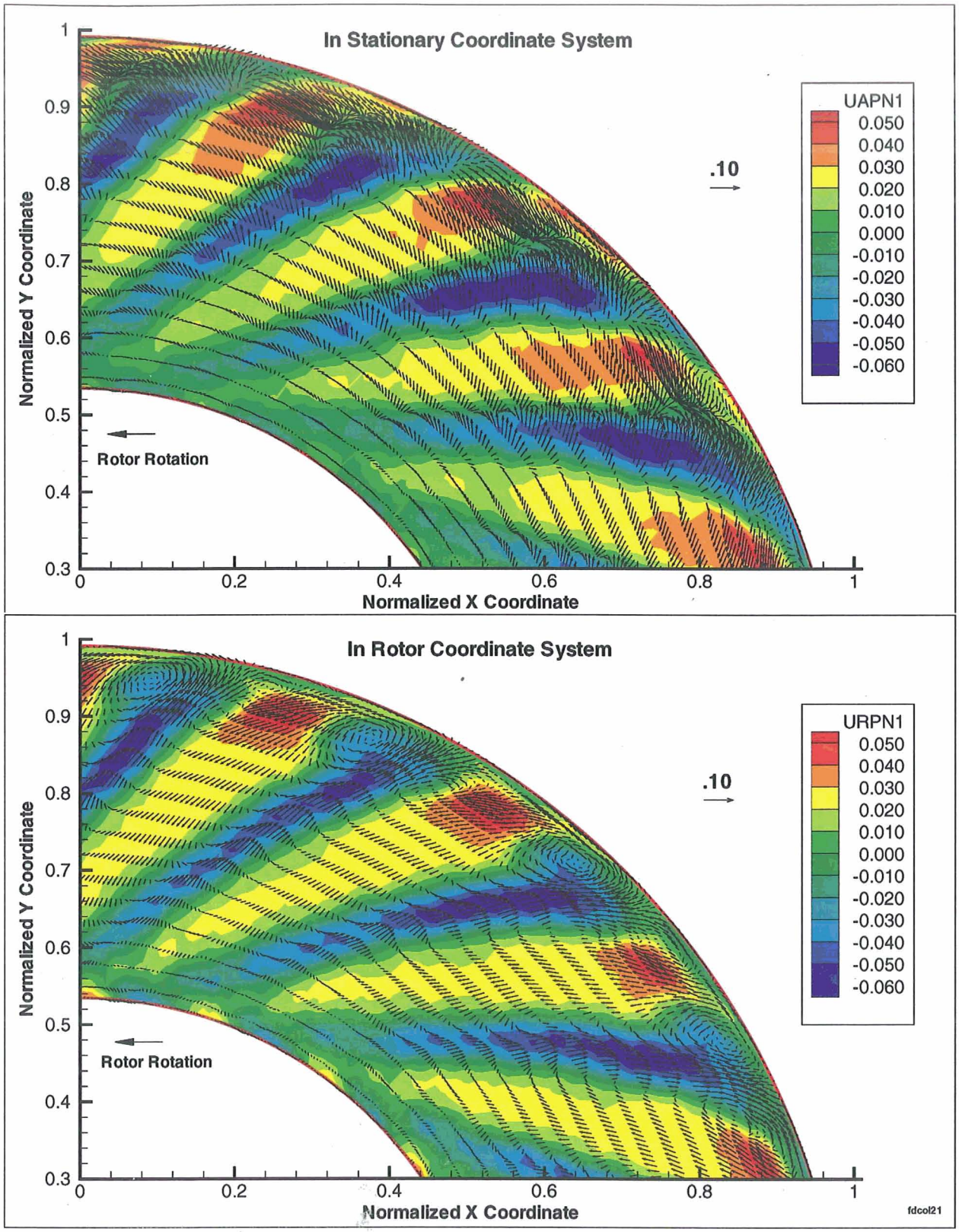

Figure 74. Normalized Pulse Synchronized Averge Velocity Field
Corrected Fan Speed 70%, High Fan Loading
Large Tip Clearance, Full Inlet Boundary Layer, Runs 920 and 885

is the same for wake and non-wake material and no radial exchange will take place. The flow angle in the rotor-bound system typically increases with radial position. The difference in angular velocity between wake and non–wake material increases with this angle and therefore results in higher radial velocities in the outer region of the annulus.

The generation of fan tone noise due to rotor wake / stator interaction depends to a large extent on the transverse component of the harmonic velocity field. This velocity field is represented by the vector field shown in the upper segment of Fig. 74. Fan tone-noise generation can be reduced by orienting the stator leading edge such that the unsteady velocity component perpendicular to the stator leading edge is minimized. The current data set indicates that this could be achieved by leaning the stator tips in the direction of rotor rotation, opposite to the lean of the rotor wakes.

Rotor wake lean will decrease the phase velocity of the wake disturbance along a radial line fixed in space, representing the leading edge of a stator. It also will decrease the wavelengths along the stator leading edge for the harmonic velocity disturbance associated with the rotor wake. Both of these effects will tend to reduce the generation of fan tone noise due to the interaction of rotor wakes with stators. These effects can be enhanced by leaning the stators in the opposite direction from the rotor wake lean, with the stator tip moved in the direction of rotor rotation relative to the stator hub.

Fig. 75 through Fig. 77 present results similar to those shown in the bottom half of Fig. 74. These results are representative for all acquired data sets. They are based on two corrected fan speeds (55 and 88%), the low and high fan-loading lines and the small and large fan tip-clearance. The velocity components have again been normalized with the circumferentially-averaged relative velocity. The data presented in these figures indicate the following:

- At all conditions the dominating features of the pulse synchronized velocity field are the streamwise velocity deficit and the secondary flows in the rotor wakes. There is no indication of vortex–like features in the secondary flows.
- Fan loading increases the wake width and the magnitude of the secondary flows.
- Wake material seems to accumulate at the leading edge of the rotor wake near the outer wall. Some vortical motion seems to occur in that area.
- The wake position in the measurement plane shifts in the direction of rotation for the conditions with small tip-clearance and for the higher fan-speed conditions indicating smaller deviation angles.

The results presented in Fig. 77 are limited to the outer segment of the annulus, because the data set for the radial velocity component is limited to only the 14 outermost radial positions.

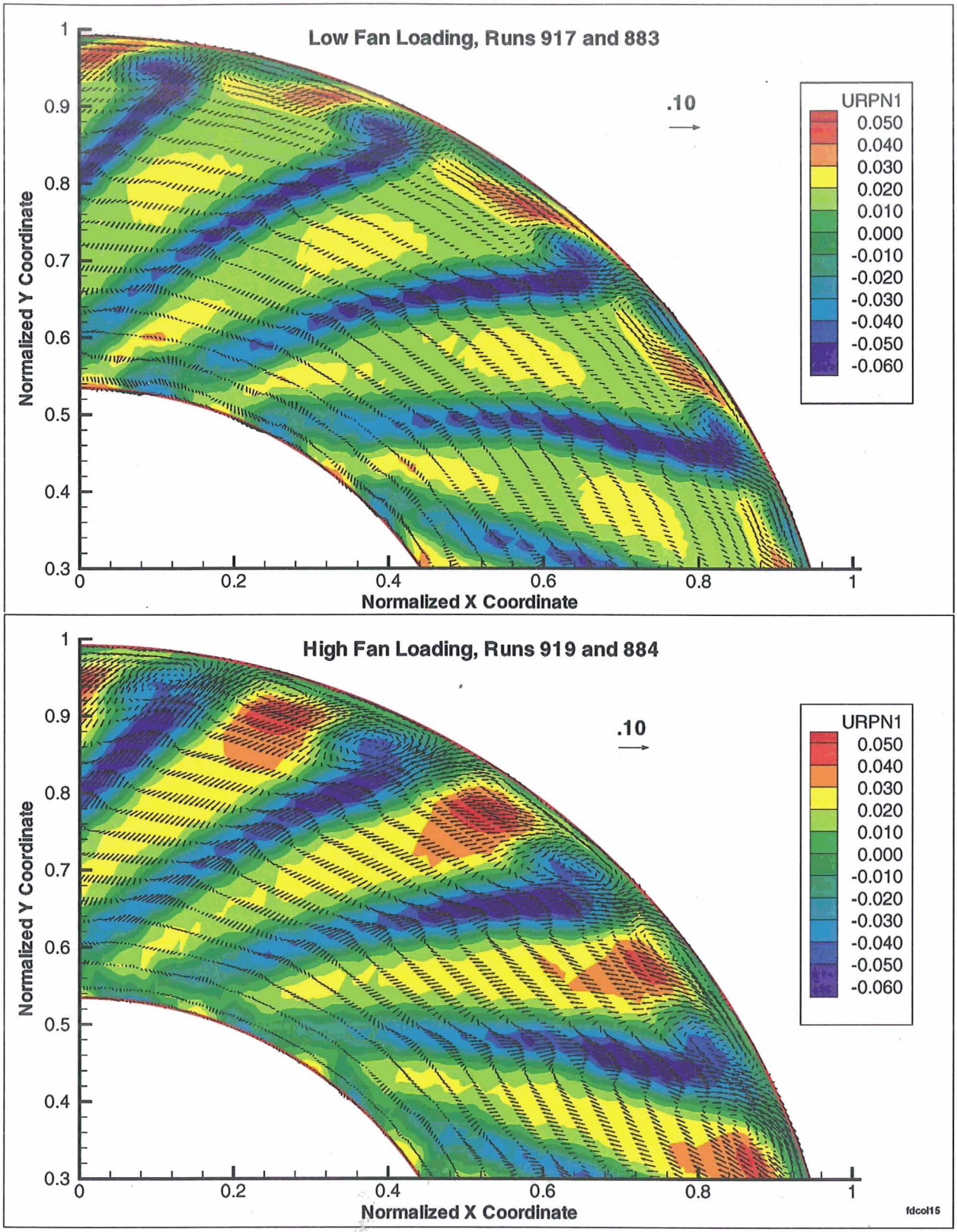

Figure 75. Pulse Synchronized Averge Velocity Field in Rotor Coordinate System Normalized with Local Relative Velocity, Corrected Fan Speed 55% Large Tip clearance , Full Inlet Boundary Layer

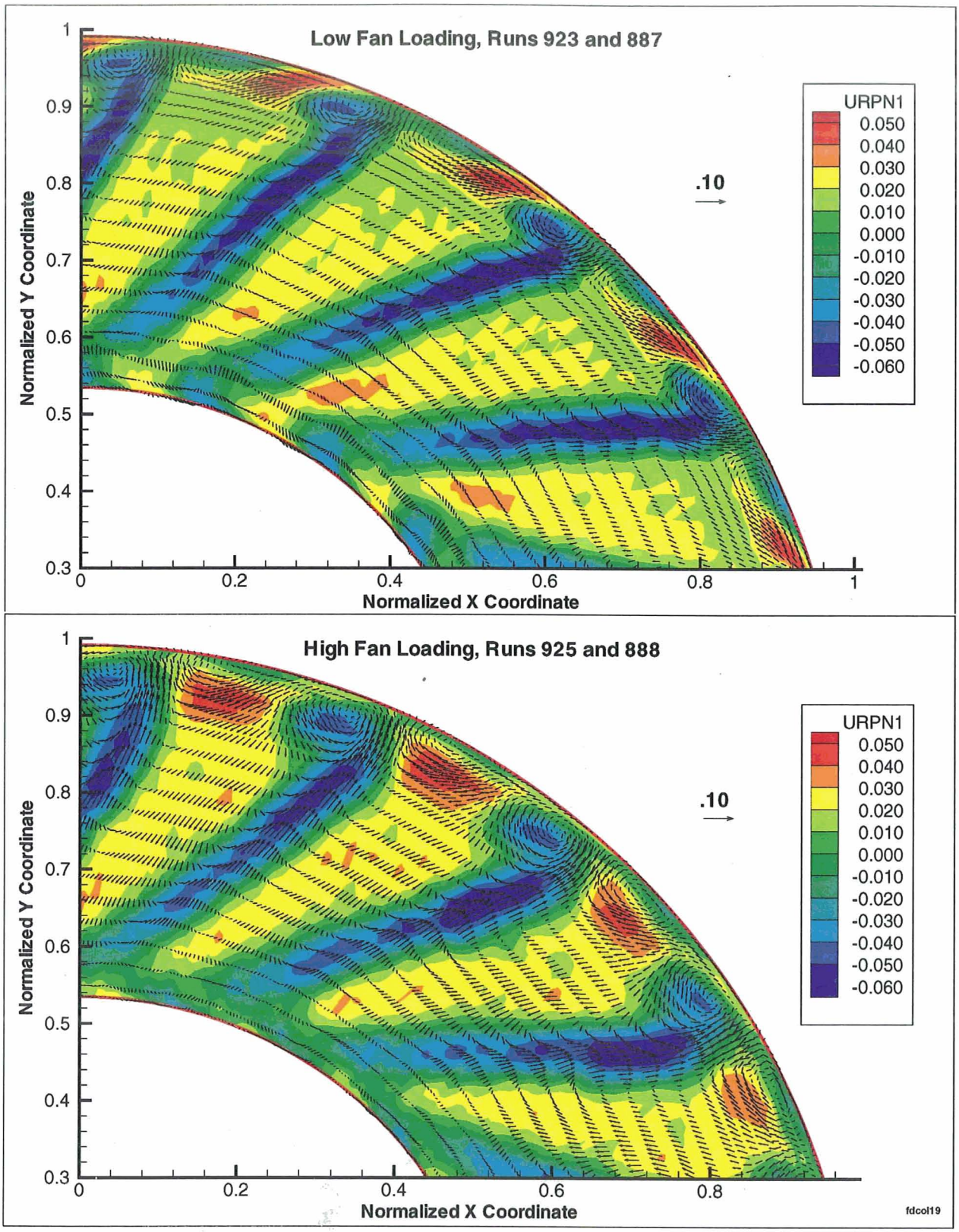

Figure 76. Pulse Synchronized Averge Velocity Field in Rotor Coordinate System Normalized with Local Relative Velocity, Corrected Fan Speed 88% Large Tip Clearance, Full Inlet Boundary Layer

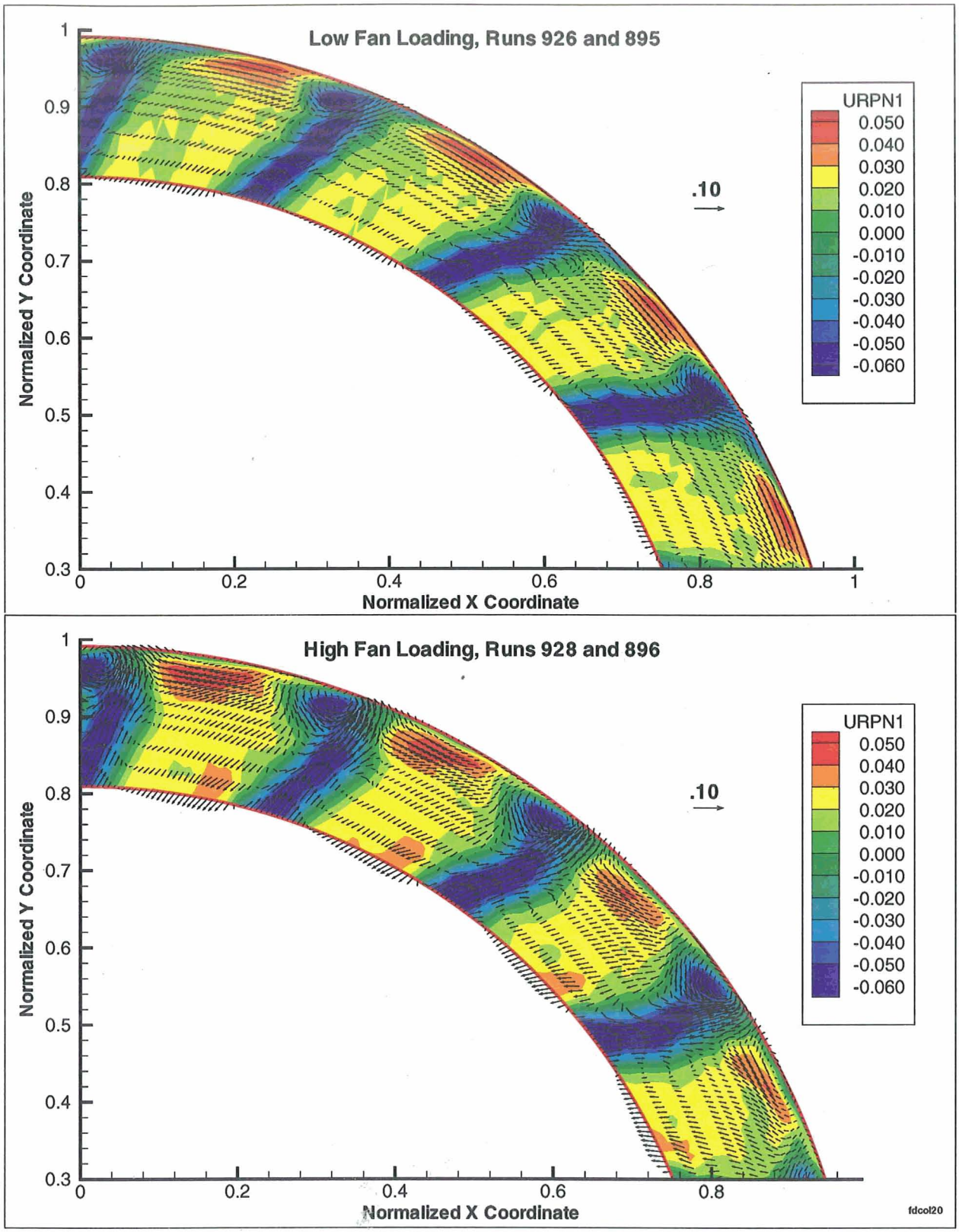

Figure 77. Pulse Synchronized Averge Velocity Field in Rotor Coordinate System Normalized with Local Relative Velocity, Corrected Fan Speed 88% Small Tip clearance, Full Inlet Boundary Layer

Turbulence

Fig. 78 through Fig. 81 present the spatial distributions of the turbulence intensities for the three components in the stationary coordinate system. The intensities are defined as the ratio of the local standard deviation of the random signals and the circumferentially-averaged mean velocity. The three components are orthogonal with the streamwise component lined up with the circumferentially averaged absolute velocity. Results are shown for a corrected fan speed of 70 percent. Fig. 78 and Fig. 79 show results at low and high fan-loading for the large fan tip-clearance configuration. Fig. 80 and Fig. 81 depict the corresponding results for the small tip-clearance. These results are representative for all fan speeds and show the following trends:

- The wake width and the width of the high turbulence intensity region along the outer wall increase with fan loading.
- For high fan-loading the peak turbulence intensities occur close to the outer duct wall. For low fan loadings the turbulence intensities in the hub region increase.
- The high-intensity region along the outer duct wall is strongly affected by the fan tip-clearance.
- A high-intensity region forms on the leading side of the wake at its intersection with the outer wall boundary-layer.
- In the wake region the streamwise turbulence intensity peaks close to the trailing edge of the wake, the radial component peaks close to its leading edge.

Radial profiles for the circumferentially averaged turbulence intensities are shown in Fig. 82. These intensities are defined as the ratio of the circumferential average of the standard deviation of the random velocity fluctuations and the local circumferential average of the velocity. The results include data for all three components and therefore are based on measurements with two different cross-wire probes. Each of the probes provides results for the streamwise turbulence component and both of them are shown. The results indicate the following:

- Except close to the walls the intensities of all turbulence components are about the same.
- The highest turbulence intensities occur close to the hub and outer walls.
- The lowest intensities occur in the midspan region, primarily because of the clean flow regions between the wakes which have low turbulence levels.
- The agreement between the intensities of the streamwise turbulence component measured with two different probes is very good.
- In the midspan region the turbulence intensities increase with loading. This is primarily due to an increase in the wake width.
- In the hub region the turbulence intensities increase with decreasing fan loading.
- The radial turbulence component is suppressed close to the walls.

The transverse turbulence component is expected to be the most important component in the generation of fan broadband noise by the stators. The effects of fan loading and tip-clearance on the circumferentially averaged turbulence intensity of the transverse component are shown in Fig. 83 for corrected fan speeds of 55, 70 and 88%. The data indicate the following:

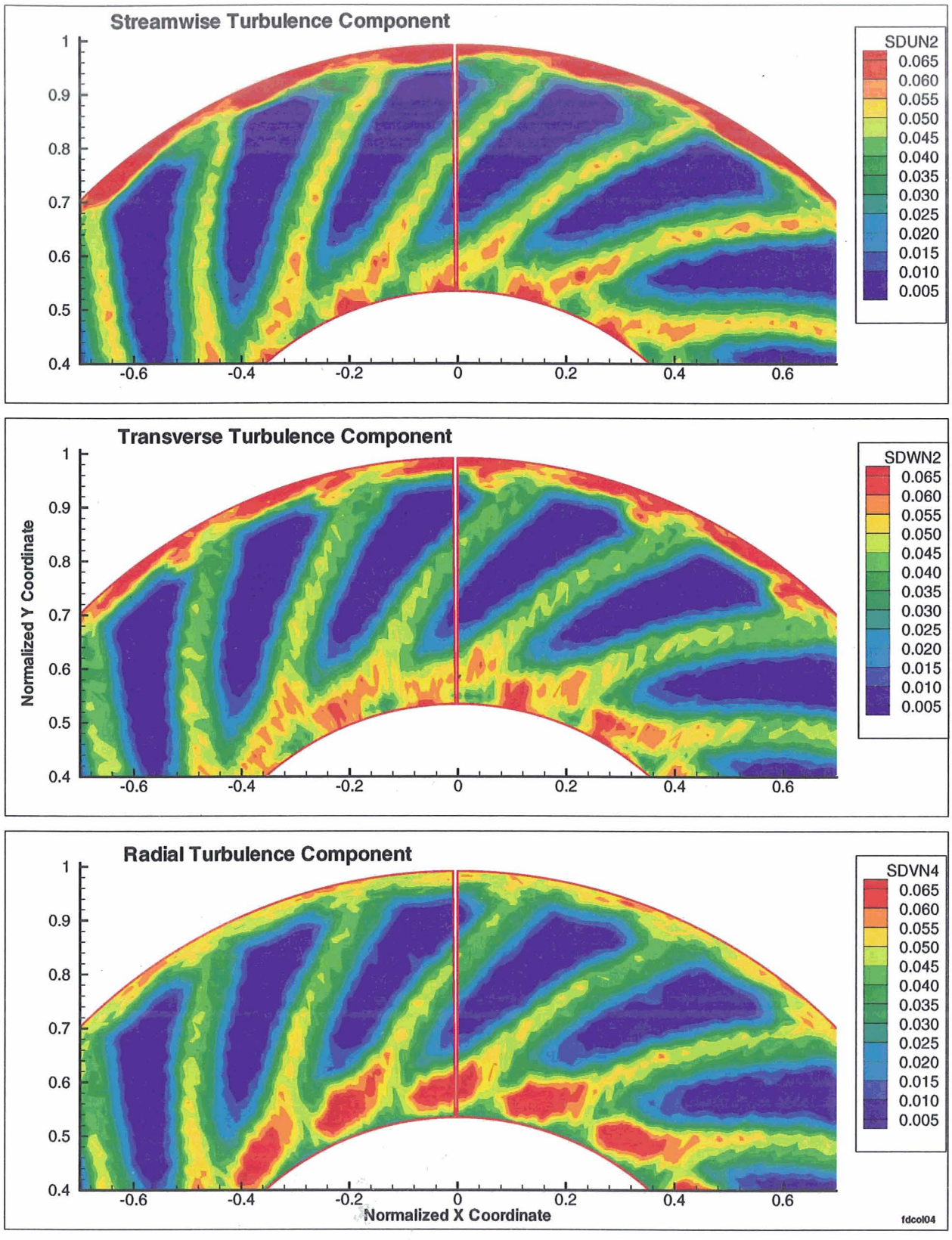

Figure 78. *Turbulence Intensities in Stationary Coordinate System Corrected Fan Speed 70%, Large Tip Clearance, Full Inlet Boundary Layer, Low Fan Loading, Runs 922 and 886*

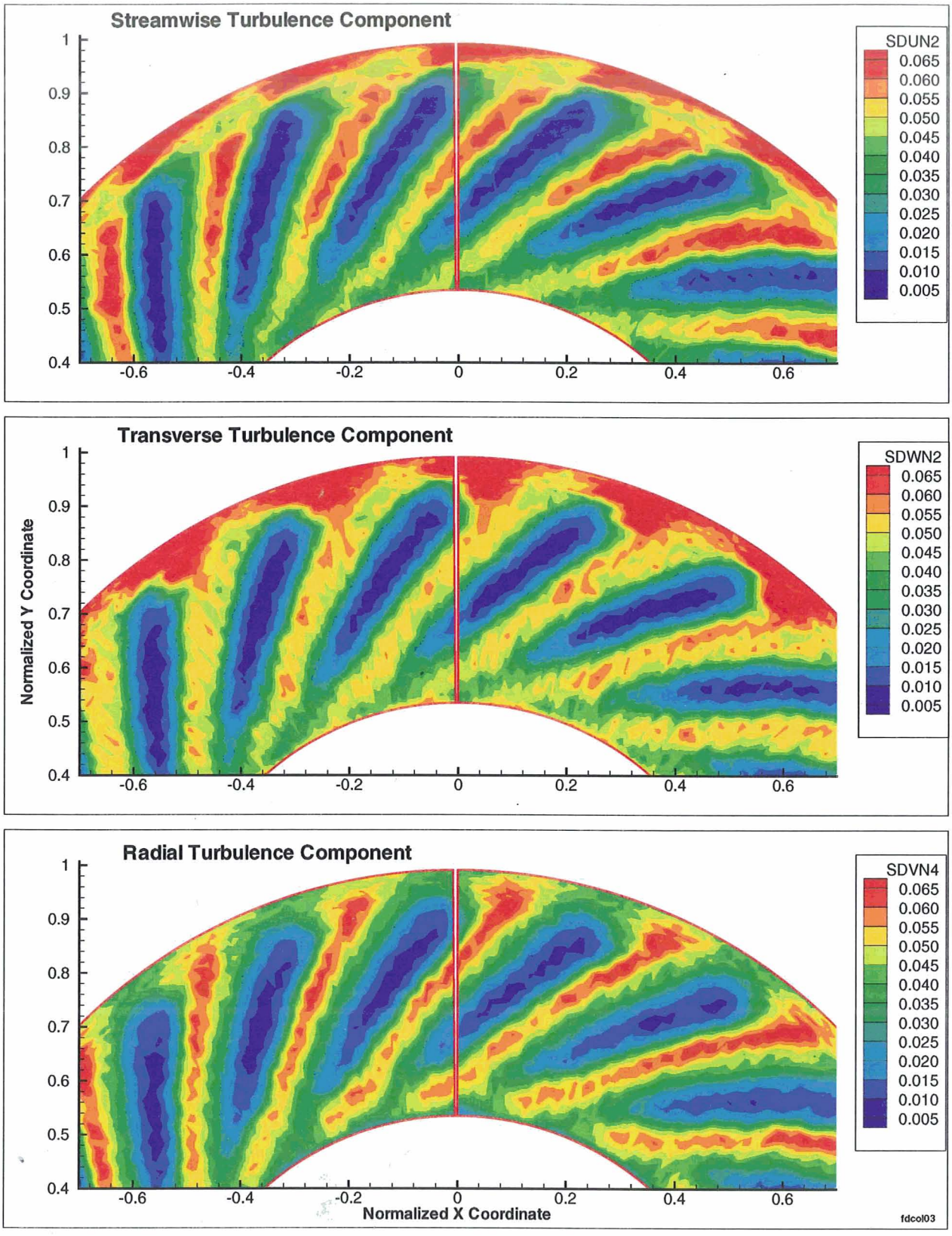

Figure 79. *Turbulence Intensities in Stationary Coordinate System Corrected Fan Speed 70%, Large Tip Clearance, Full Inlet Boundary Layer, High Fan Loading, Runs 920 and 885*

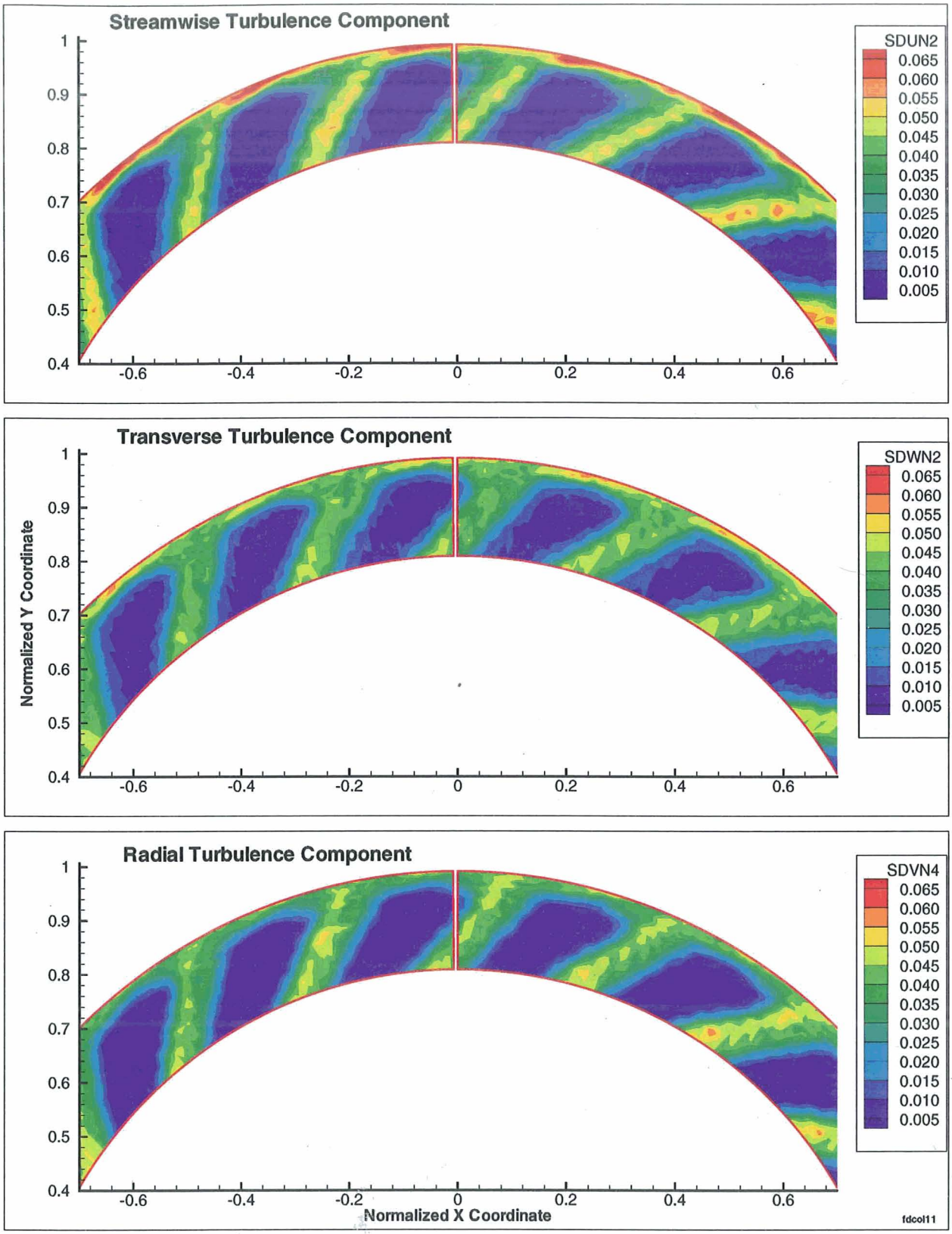

Figure 80. *Turbulence Intensities in Stationary Coordinate System Corrected Fan Speed 70%, Small Tip Clearance, Full Inlet Boundary Layer, Low Fan Loading, Runs 905 and 894*

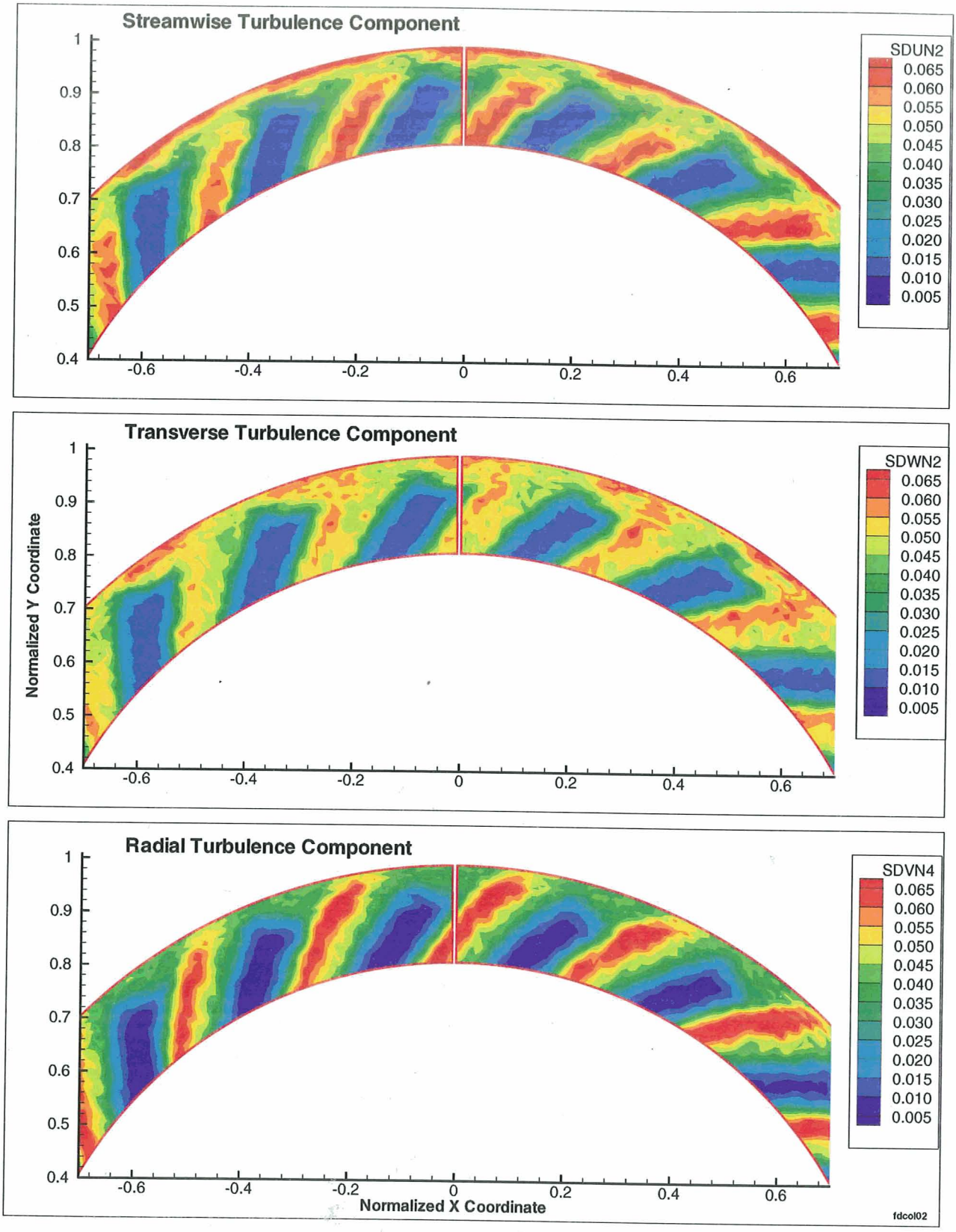

Figure 81. *Turbulence Intensities in Stationary Coordinate System Corrected Fan Speed 70%, Small Tip clearance, Full Inlet Boundary Layer, High Fan Loading, Runs 903 and 893*

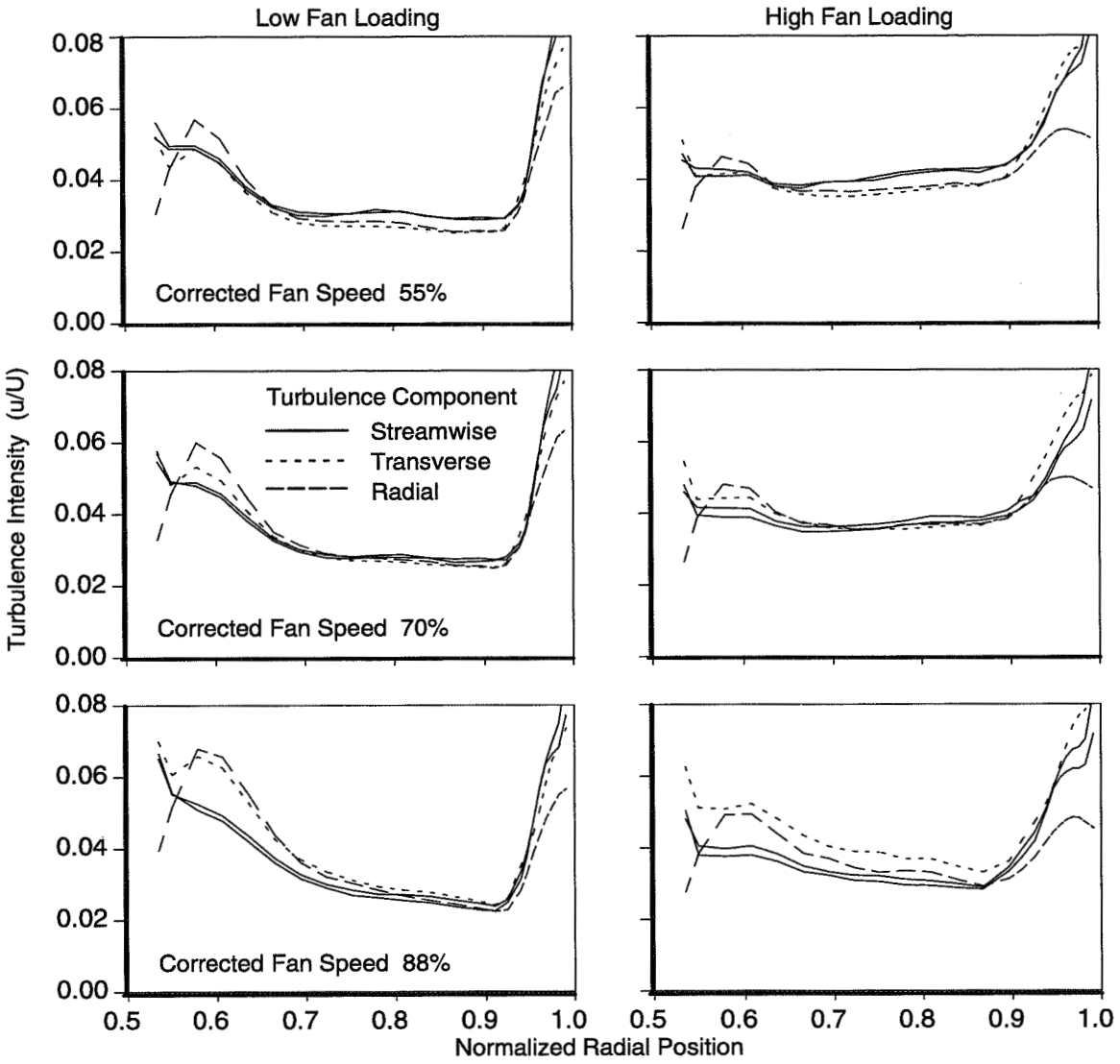

Fig. 82. Circumferentially-Averaged Intensities for all Turbulence Components

- The fan tip-clearance primarily affects the region close to the outer wall. The radial extent of this region and the turbulence intensities within this region increase with fan tip-clearance. This is an indication that the turbulence in this region is dominated by the effects of the rotor tip flows.
- Turbulence intensities increase in the tip region and decrease in the hub region with increasing fan loading.
- The minimal differences between the turbulence intensities in the hub and the midspan region for configurations with different fan tip clearances are an indication of the good repeatability of the turbulence measurements.

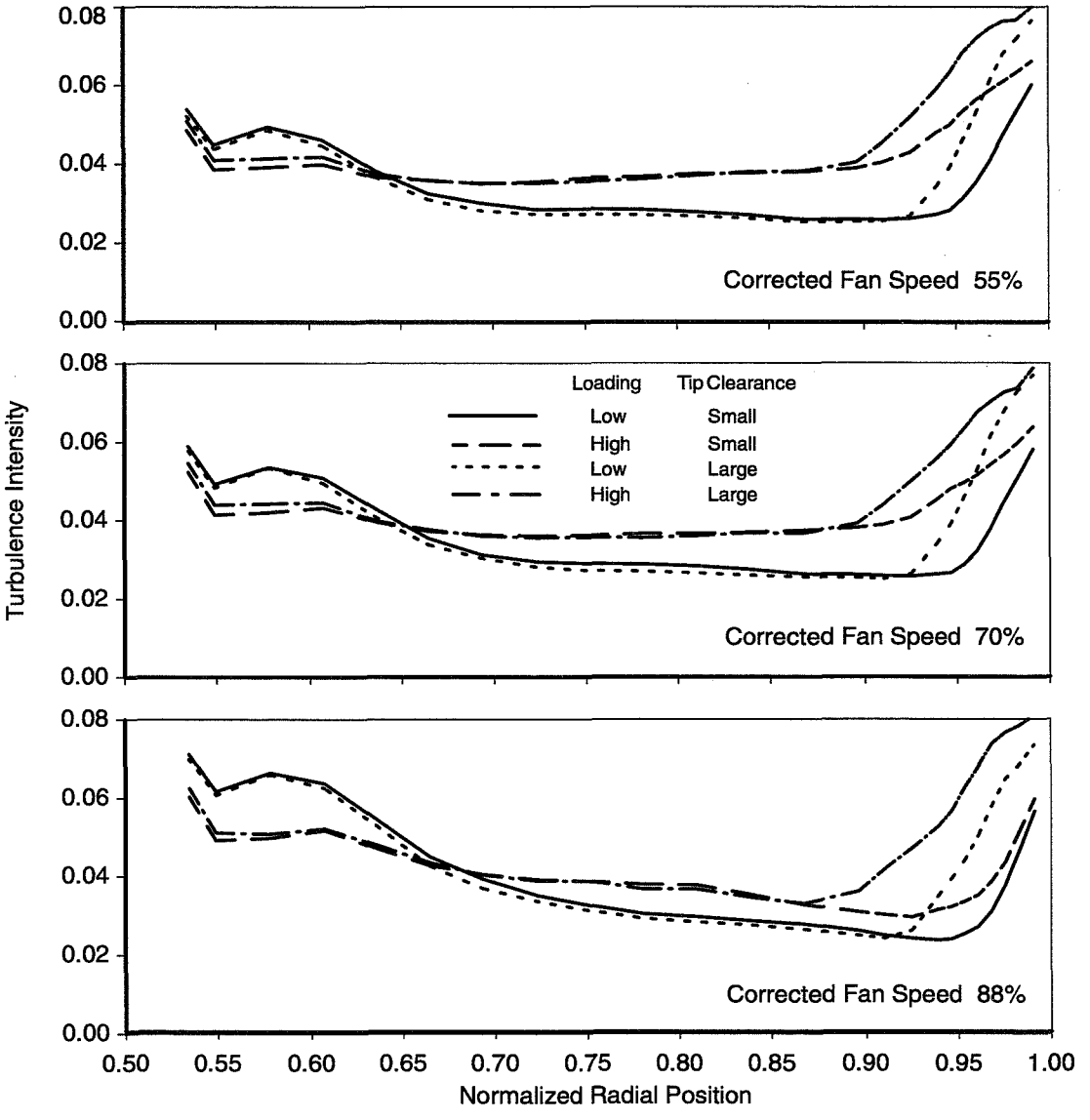

Fig. 83. Circumferentially Averaged Intensity for Transverse Turbulence Component

The effects of the inlet boundary layer on the circumferentially-averaged intensities of the transverse turbulence component are shown in Fig. 84 for corrected fan speeds of 55, 70 and 88%. The results for the 55% fan speed are nearly identical to those of the 70% speed. In anticipation that the inlet boundary layer would only affect the outer wall region of the flow, the data acquired for conditions with the inlet boundary-layer removed were limited to the outermost 40% of the span. For three of the four comparisons the differences between conditions with and without inlet boundary-layer are minimal. The small differences observed in the 70% speed condition at high fan loading extend into the midspan region and may be associated with a small fan-loading change. In general it is concluded that the effects of the inlet boundary-layer on the unsteady flow field downstream of the fan rotor are minimal.

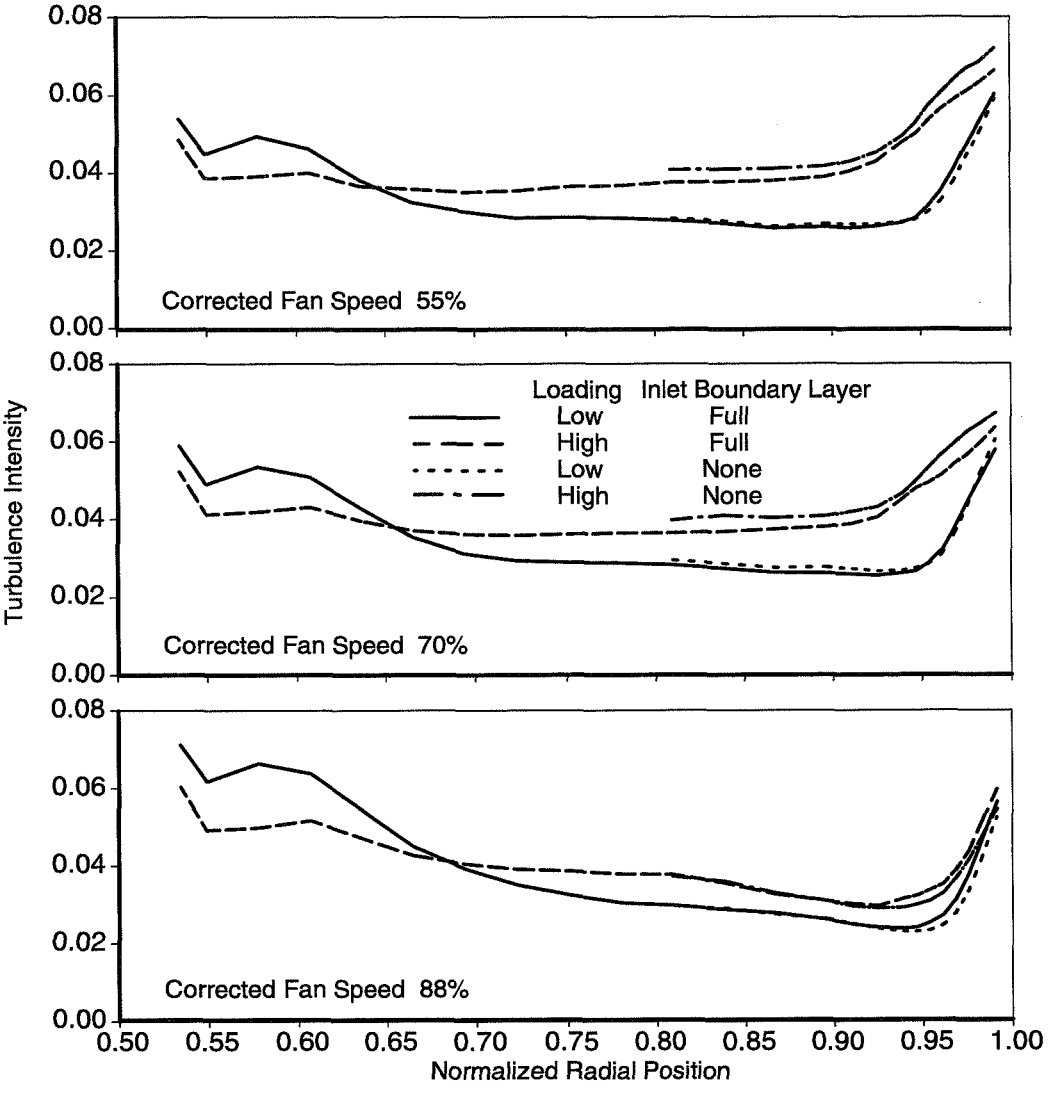

Fig. 84. Effect of Inlet Boundary Layer on Intensity Profiles of Transverse Turbulence Component

No attempts have been made to estimate the contribution of the broadband acoustic signals to the hotwire signal. It may however be assumed that the fan broadband noise at the location of the hotwire sensor is circumferentially homogeneous. Its maximum potential contribution to the hotwire signal would therefore be in the order of the noise floor between the rotor blade wakes, a low level if compared with the peak values of the random signal in the wakes. The effects of fluctuating temperature and density in the flow field convected past the hotwire sensor have not been assessed either. They are expected to primarily affect the measurement of the streamwise turbulence component.

Average Wake Properties

The data analysis process also includes averaging over all blade passages. This makes it possible to evaluate the variation of unsteady flow parameters over the average blade-passage. The data is ordered such that the maximum velocity defect for the relative velocity occurs at the zero degree angle and the blade passage extends from –9° to +9° at all radial positions. Unsteady flow parameters associated with the blade boundary-layer developing on the blade pressure-side appear at the negative angles, those associated with the suction-side blade boundary-layer appear at positive angles.

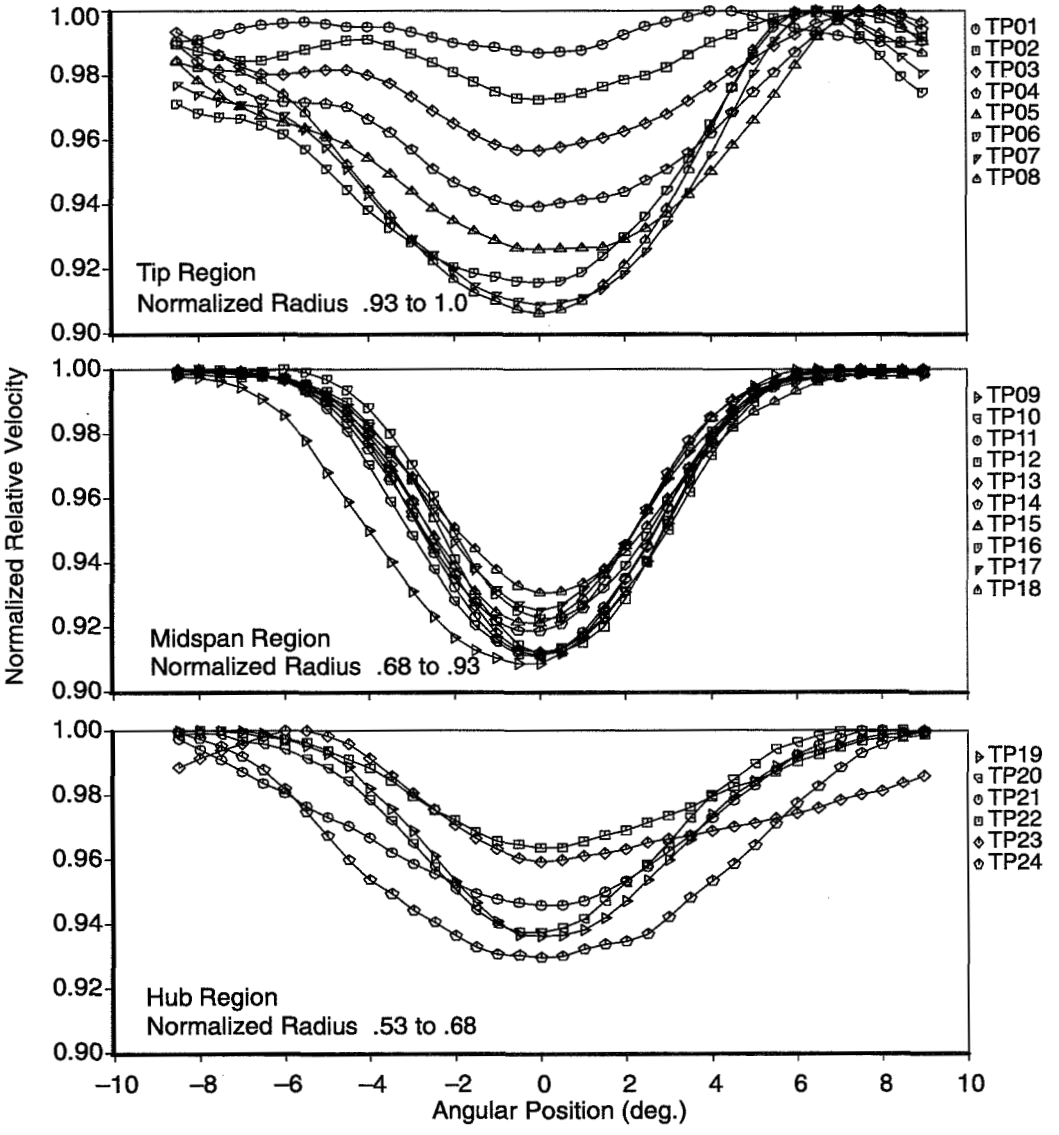

Fig. 85. Normalized Relative Velocity Profiles
Corrected Fan Speed 70%, Small Tip Clearance, High Fan Loading

Rotor relative velocities, computed based on the measured local average flow velocity and the local wheel speed of the rotor are shown in Fig. 85. The velocities have been normalized with the maxi-

mum relative velocity occurring at the particular radial location and are shown in 3 groups for different ranges of radial positions. The top group represents the tip region and is based on normalized radial positions from .93 to 1.0. The center group shows data for the midspan or wake region (normalized radii from .68 to .93) and the bottom group represents the hub region (normalized radii from .52 to .68). The last two digits of the symbol identifiers in the figure represent the test point number. The radial positions for the test points are identified in Table 8.2. The results indicate that in the midspan region the individual wakes are clearly separated by clean, non-viscous flow segments. In this region it is possible to define wake parameters such as the wake width. However in the tip region where the wakes merge with the wall boundary-layer and in the hub region where they merge among themselves as well as with the hub wall boundary-layer it becomes difficult to define some of the wake parameters.

Wake profiles for the maximum and minimum fan-loading conditions at a fan speed of 70% with the small tip-clearance are shown in Fig. 86. The results indicate that fan loading primarily affects the wake width and not the maximum wake defect.

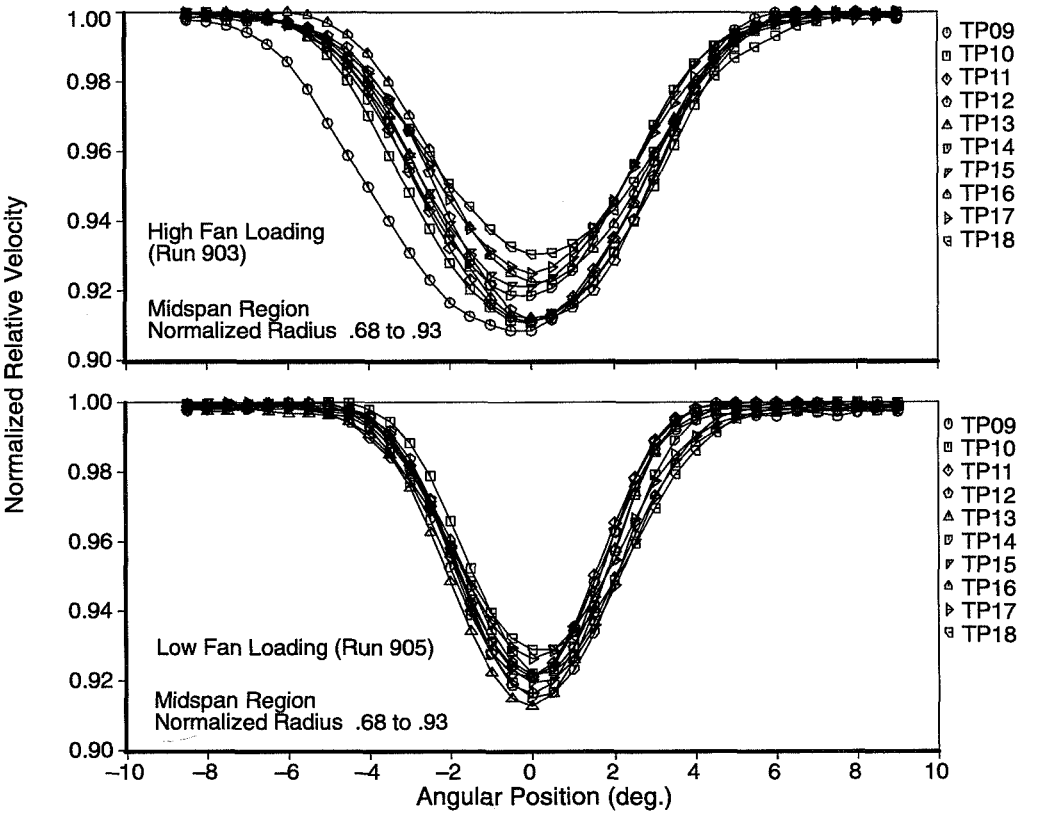

Fig. 86. Effect of Fan Loading on Normalized Relative Velocity Profiles Corrected Fan Speed 70%, Small Tip Clearance

Improved collapse of the wake shapes obtained at different radii is achieved by normalizing the wake velocity defect by its maximum and the angular coordinate by the wake width. This is demonstrated in the top half of Fig. 87, which shows the wake velocity-defect profiles at all the radii of the midspan region for all three fan loadings at a corrected fan speed of 70%. The maximum wake defect is defined as the difference between the maximum and the minimum relative velocity and the local wake-width is defined as the distance between the points where the velocity defect is 50% of its max-

imum value. The profiles of the wakes measured in the midspan region are almost perfectly symmetric. The bottom half of this figure shows the midspan velocity-defect profiles for the high loading conditions at 55, 70 and 88% corrected fan speed. Again the data collapse reasonably well. At the axial location of the cross-wire relative to the rotor blades, the wake shape is dominated by the viscous flow effects. The larger scale flow effects appearing as wake-to-wake ramp functions reported in rotor wake models of References 20 and 21 do not appear in the present data set.

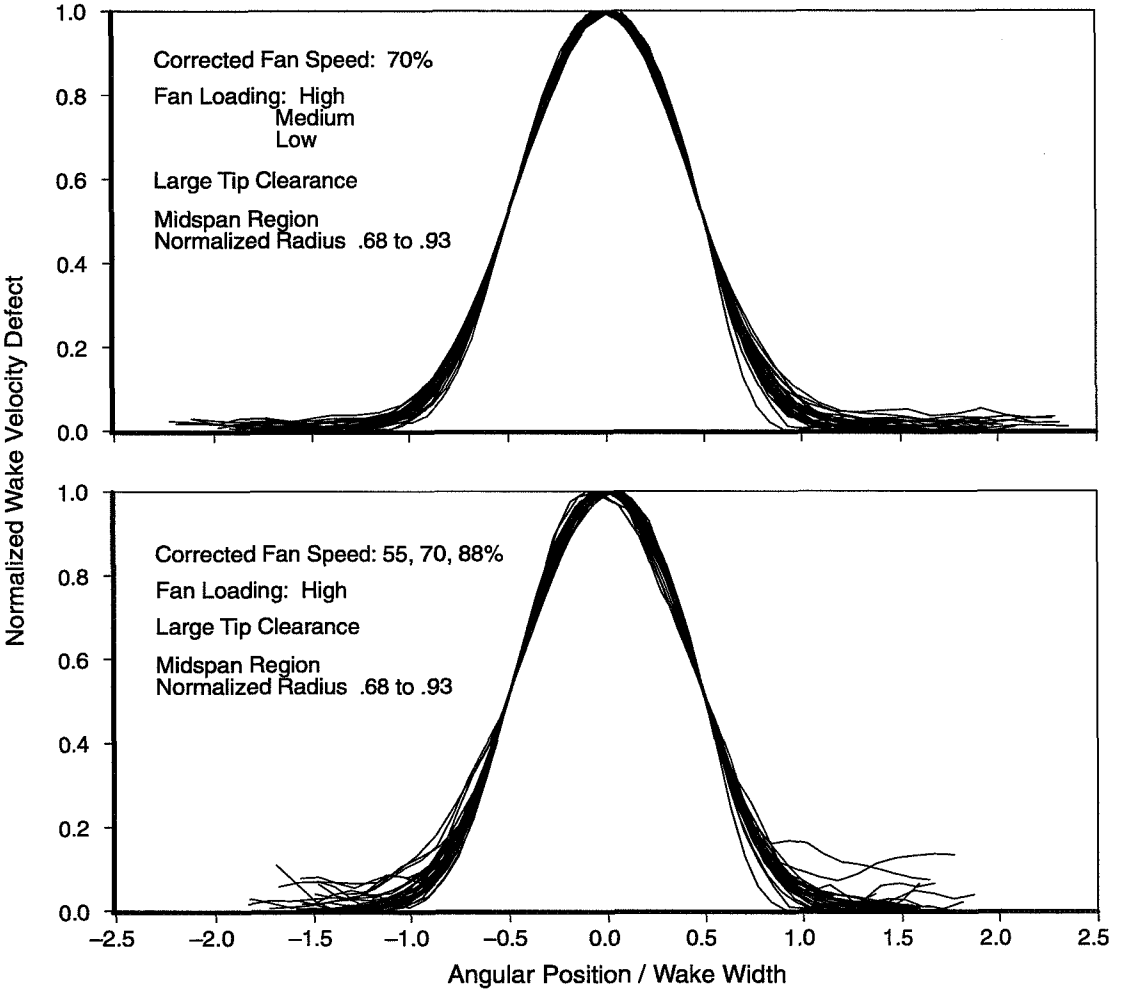

Fig. 87. Normalized Rotor Wake Velocity Defect Profiles

Profiles for the harmonic unsteady velocity components in the stationary coordinate system are shown in Fig. 88. They represent the variations resulting from averaging over the 20 rotor blade passages. The results are grouped into rows representing the three radial regions. The three columns represent the three velocity components. In all regions the wake is associated with a negative pulse-like disturbance for the streamwise component and positive pulses for the transverse and radial velocity components. The maximum disturbance velocities occur close to the wake centerline. The maximum for the radial component is offset towards the suction side of the wake for some of the locations in the tip region. The dashed lines represent the 2 locations closest to either the inner or

outer duct walls. The highest harmonic velocity variations occur close to the outer duct wall. All components but in particular the radial one are suppressed in the immediate vicinity of the walls.

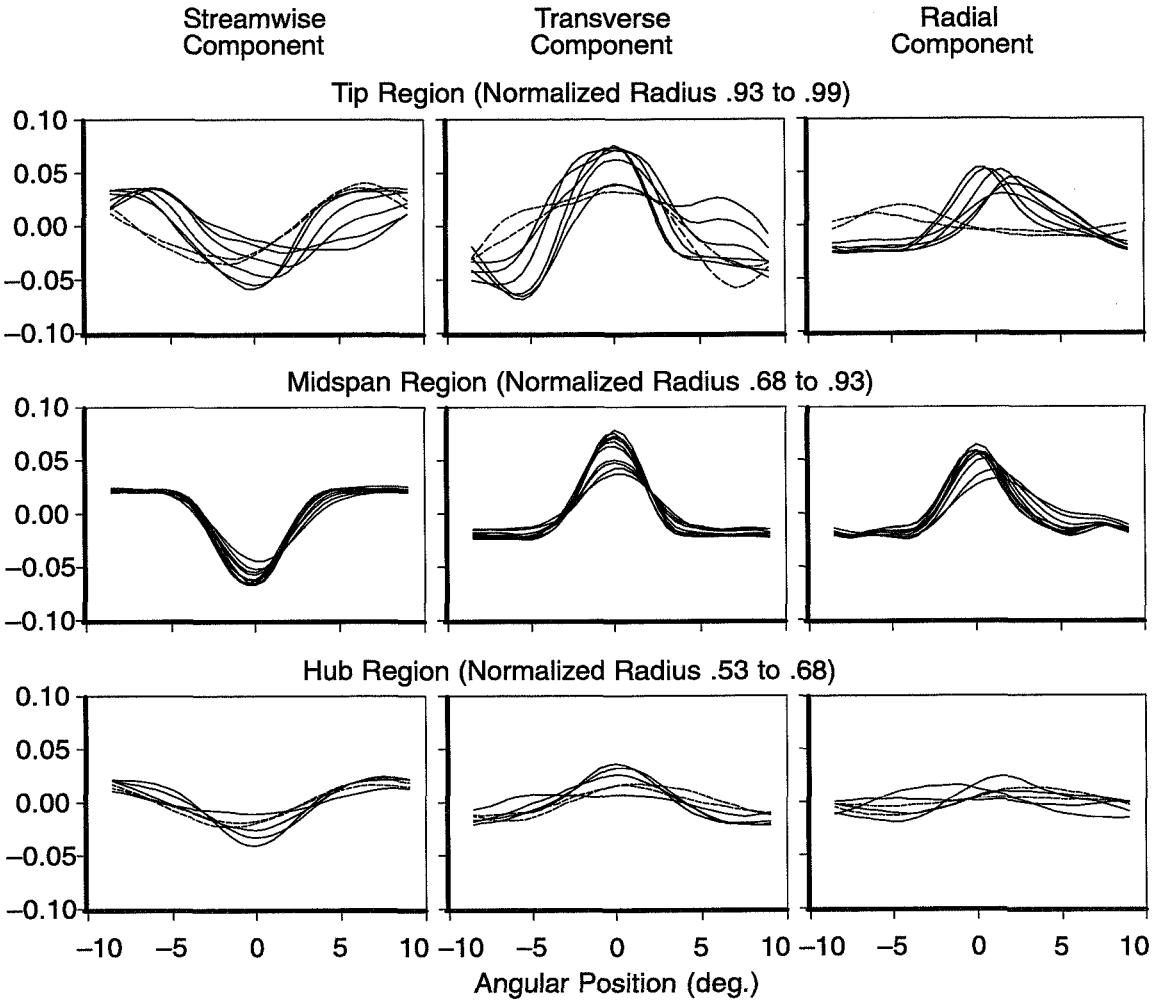

Fig. 88. Pulse-Synchronized Average Velocities Normalized with Circumferentially-Averaged Velocity in Stationary Coordinate System (Run 886 and 922)

The turbulence intensity variations corresponding to the harmonic velocity variations of Fig. 88 are depicted in Fig. 89. In general the data indicate that the average turbulence-intensities for the three components are similar in magnitude. For the midspan region the turbulence intensity profiles are nearly the same for all positions. The profiles for the transverse component in the midspan region are nearly symmetric and very similar to those reported for the streamwise component in two-dimensional wakes (references 25 and 26). The streamwise component in the rotor bound coordinate system does indeed couple very favorably with the transverse component in the stationary coordinate system. The profiles for the streamwise and the radial components exhibit significant asymmetry, with the streamwise component peaking on the suction side and the radial component on the pressure side of the wake. The highest turbulence intensities occur close to the outer wall, where the streamwise component dominates over the transverse and the radial components.

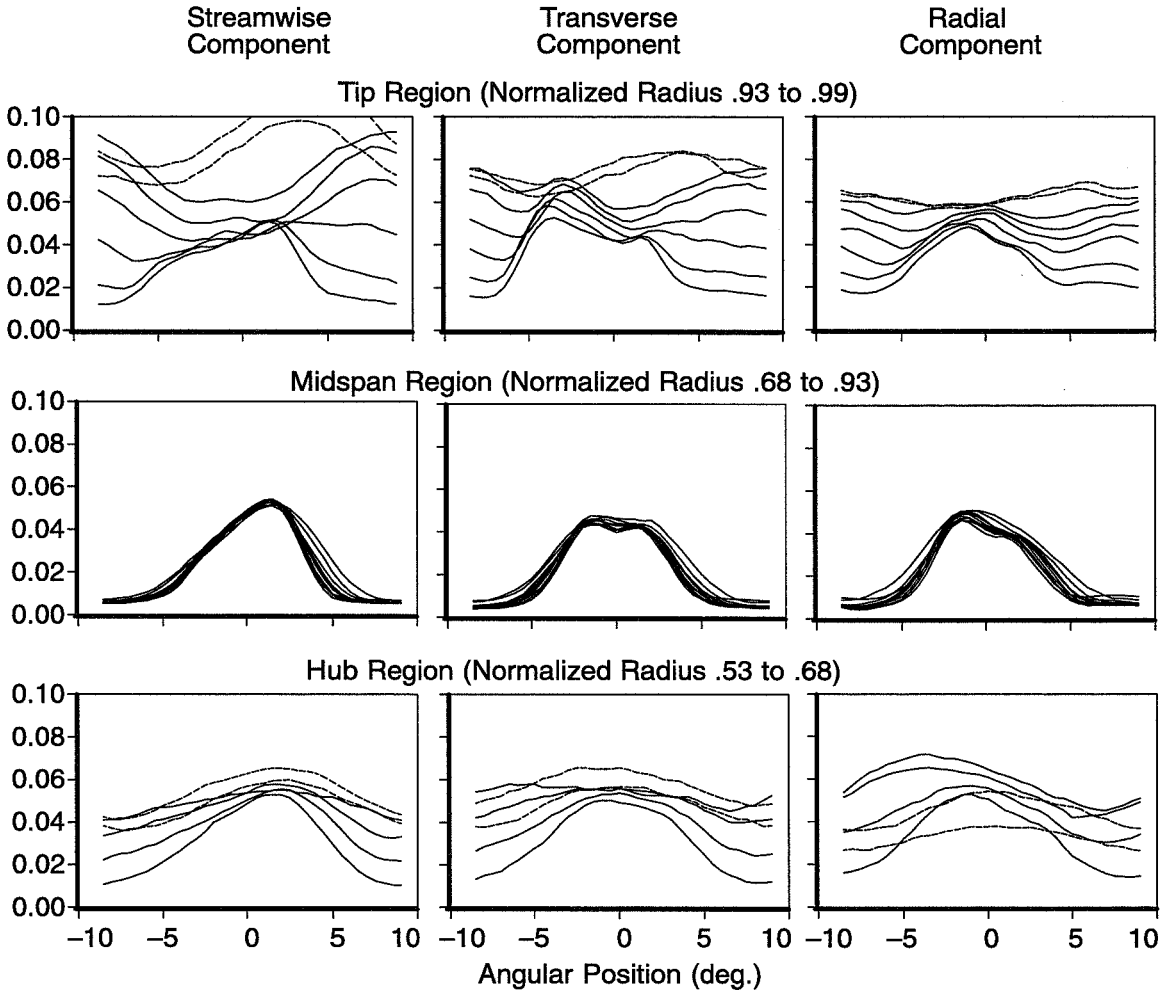

Fig. 89. Turbulence Intensities in Stationary Coordinate System Corrected Fan Speed 70%, Low Fan Loading, Large Tip Clearance (Run 886 and 922)

In two–dimensional wake models the maximum wake velocity-defect is used as the velocity scale. Wake profiles of the standard deviation of the turbulence normalized with the maximum wake velocity defect for the midspan region are shown in Fig. 90. Fig. 89 and Fig. 90 are based on the same data set. The normalization with the maximum wake velocity-defect does not collapse the data as well. The peak levels for all the turbulence components vary between 0.4 and 0.7, increasing from the tip region towards the hub. The wake data of Reference 25 indicate that for a two–dimensional airfoil wake at similar convection distances the peak levels are expected to be about 0.55 to 0.65. Based on the two-dimensional wake data one would expect the non-dimensionalized turbulence levels to increase towards the hub, because of the shorter convection distance between the rotor trailing edge and the measurement position.

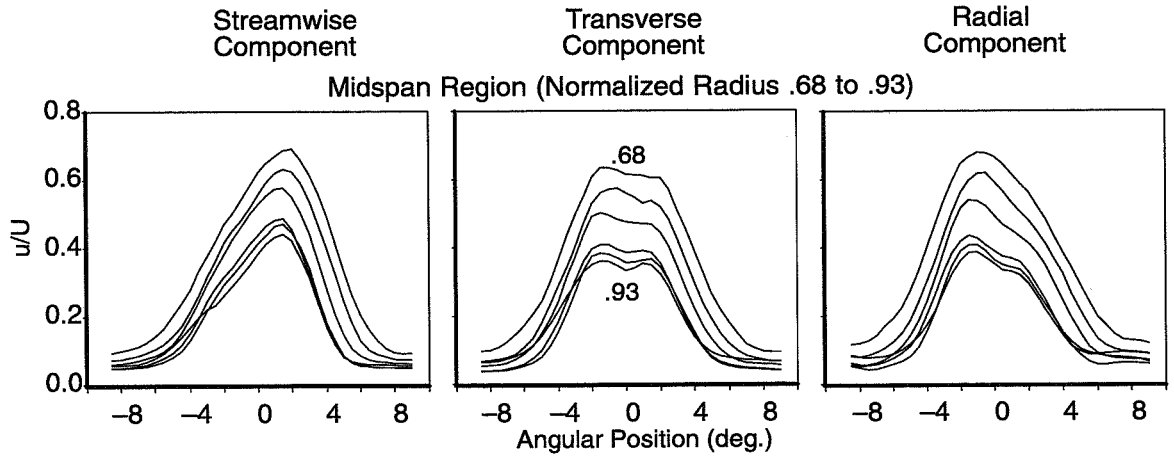

Fig. 90. Standard Deviation of Turbulence Velocity Normalized with Maximum Wake Velocity Defect, Corrected Fan Speed 70%, Low Fan Loading, Large Tip Clearance

Rotor wake parameters based on the relative velocity profiles are shown in Fig. 91 to Fig. 93. The maximum wake velocity-defect normalized with the maximum relative velocity is depicted in Fig. 91 as a function of the normalized radial position for three different fan loadings and two different tip clearances. The results are based on a corrected fan speed of 70% but are representative for all fan speeds. They indicate that in general the wake defect is not very sensitive to variations in fan loading and tip clearance. However an interesting detail is the opposite trend of the wake defect with fan loading for the hub and the tip region. With an increase in fan loading one typically expects an increase in the rotor-blade incidence angle, an increase in the rotor-blade drag coefficient and therefore an increase in the rotor-blade wake width and maximum wake-defect. This is indeed the trend exhibited by the outer half of the midspan region, but in the inner half the trend is opposite. This unusual trend is thought to be due to the following factors:

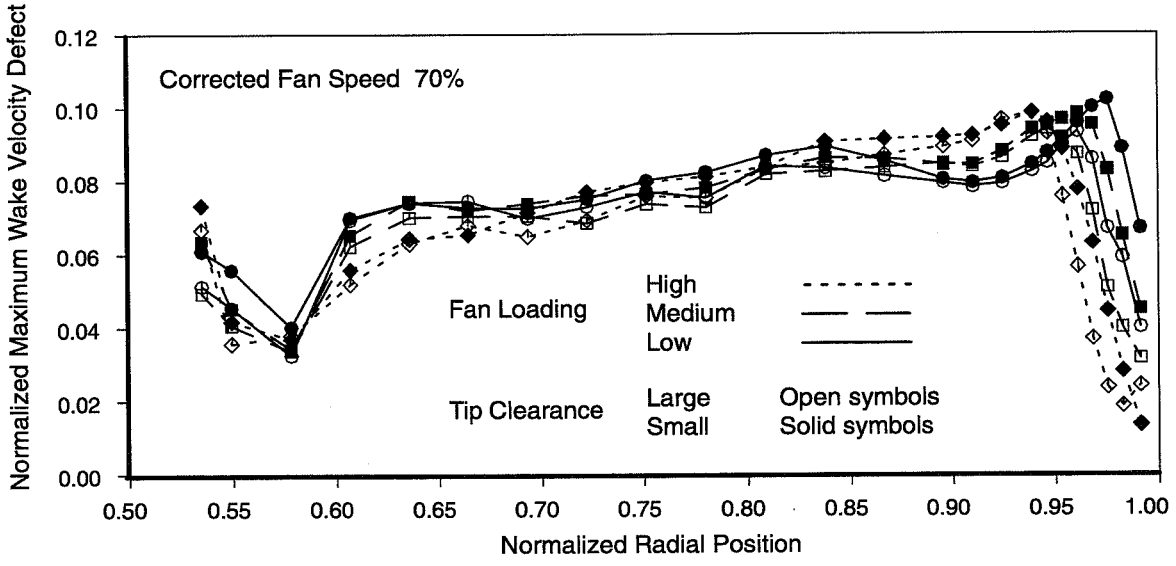

Fig. 91. Maximum Wake Velocity Defect normalized with Maximum Relative Velocity

- Increased fan loading results in higher swirl-velocities and therefore higher radial pressure-gradients downstream of the fan. This in turn will result in a smaller increase of the fan rotor pressure-rise in the hub region relative to the tip region.
- Higher fan loading increases the radial velocities, resulting in increased migration of wake material from the hub region towards the tip and increased movement of non-viscous flow segments towards the hub region.

The trends for the rotor wake-width normalized with the rotor chord are illustrated in Fig. 92 for the same conditions. The wake widths shown in this figure are based on the wake cross-section in the unwrapped cylindrical surface. A more appropriate definition would be based on the wake cross–section in a plane normal to the wake center plane. The ratio between the two is approximately equal to the cosine of the wake lean-angle. The expected trend of increasing wake width with fan loading appears in the data throughout the midspan region. The effect of tip clearance is limited to the tip region, with the wake width increasing with tip clearance.

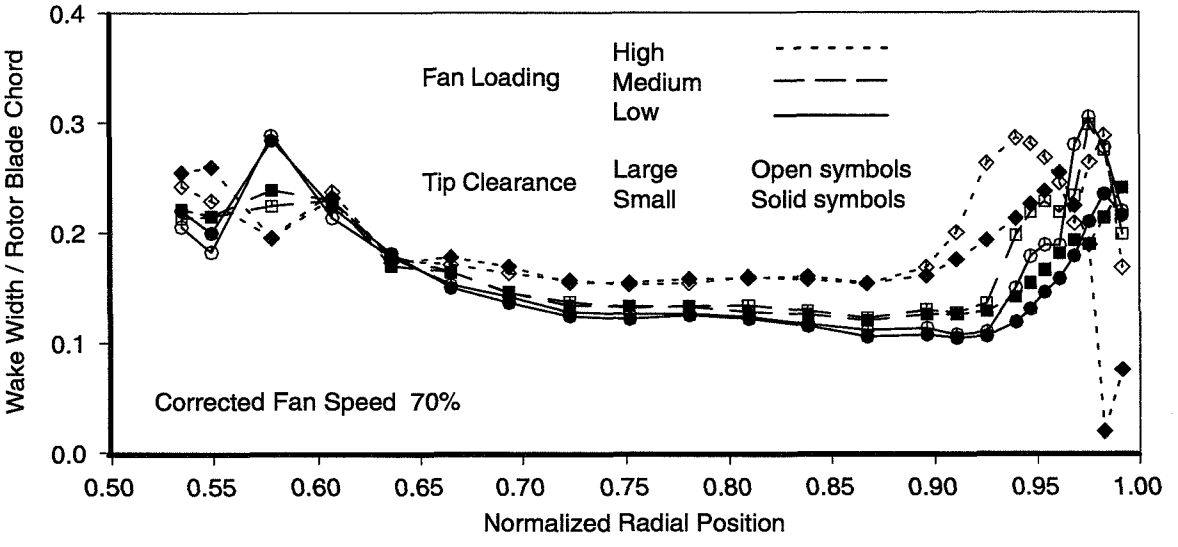

Fig. 92. Wake Width normalized with Rotor Blade Chord

The corresponding data set for the rotor drag coefficient is shown in Fig. 93. The drag coefficient has been computed by integrating the momentum defect in the relative-velocity profile over the average blade passage.

$$c_d = 2 \frac{1}{c} \int \frac{u}{U_\infty} \left[1 - \frac{u}{U_\infty} \right] dy \qquad (1)$$

with

c_d	Rotor blade drag coefficient
c	Rotor blade chord
U_∞	Maximum relative velocity in blade passage

This estimate of the drag coefficient does of course not consider any radial migration of the flow between the rotor trailing edge and the measurement location. It also becomes less reliable if the peak velocity regions between the wakes are affected by viscous flows, such as in the hub and the tip regions. The results reflect the expected trend of increased drag coefficients with higher fan loading

and with larger tip-clearance in the tip region. However the results also show the reversal of the trend with fan loading in the hub region as in the results for the maximum wake defect.

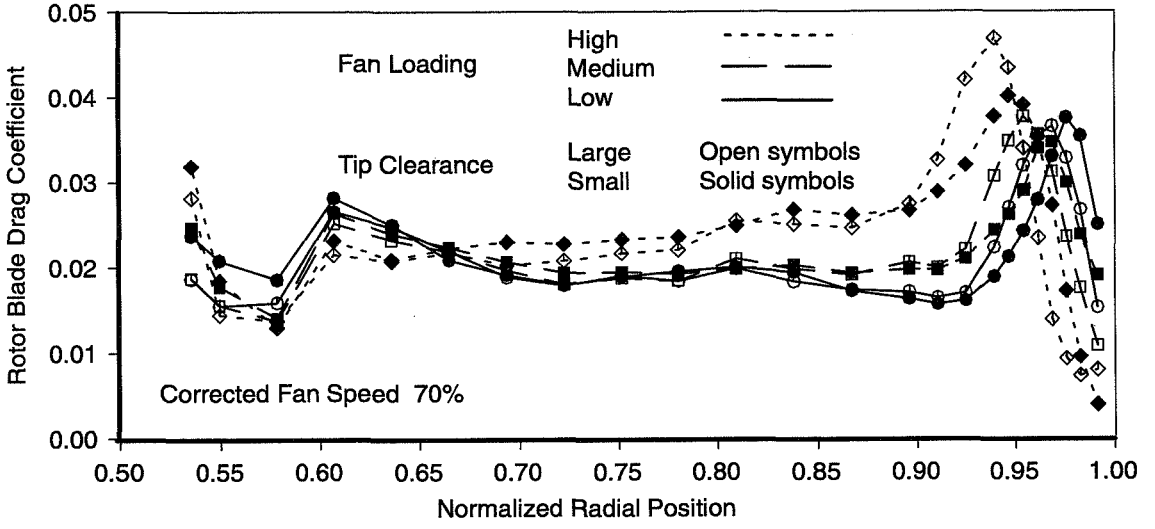

Fig. 93. Rotor Blade Drag Coefficient

Equation 3 reflects the fact that for similar wake profiles the drag coefficient is proportional to the product of the normalized maximum wake defect and the normalized wake width. Models for two–dimensional wakes typically indicate that both, the normalized wake defect as well as the normalized wake width are proportional to the square root of the drag coefficient. The data presented in Fig. 91 and Fig. 92 however indicates that the wake width is much more sensitive to changes in the drag coefficient than the maximum wake defect. Comparison of the data presented in Fig. 92 and Fig. 93 show that the effects of loading on the normalized wake width and the blade drag coefficient are very similar.

Measured and predicted wake parameters are compared in Fig. 94 and Fig. 95. The maximum wake velocity defect normalized with the maximum velocity outside of the wake is shown in Fig. 94. The wake width normalized with the rotor chord is depicted in Fig. 95. The agreement between the measured and predicted data is in general quite good, considering that some of the predictions are based on models for two-dimensional wake flows. To a large extent the good agreement is of course due to the effect that the predictions are based on the measured values for the rotor-blade drag coefficient. In general the measured data indicate that the diffusion of the wakes in the hub region is higher than what is expected based on the wake models, the wake defect is smaller and the wake width larger than the predicted values. The trend for the differences between measured and predicted wake parameters is opposite in the tip region. The only prediction that deviates unacceptably from the measured data is the the wake width based on Reference 21.

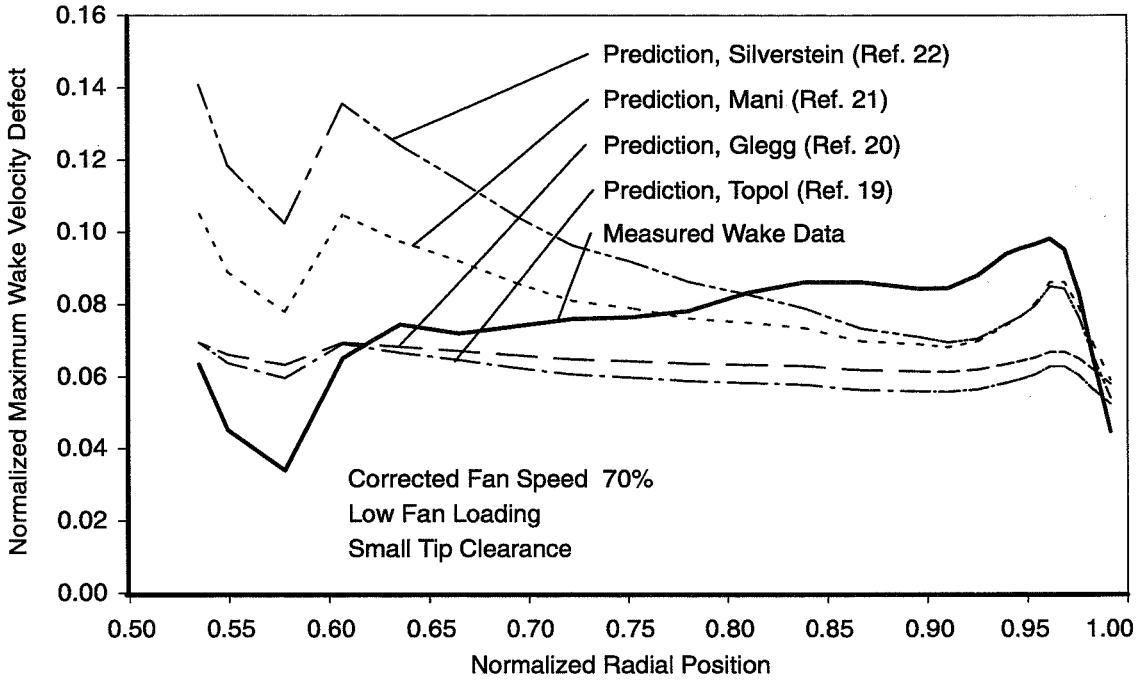

Fig. 94. Comparison of Measured and Predicted Values of Normalized Maximum Wake Velocity Defect

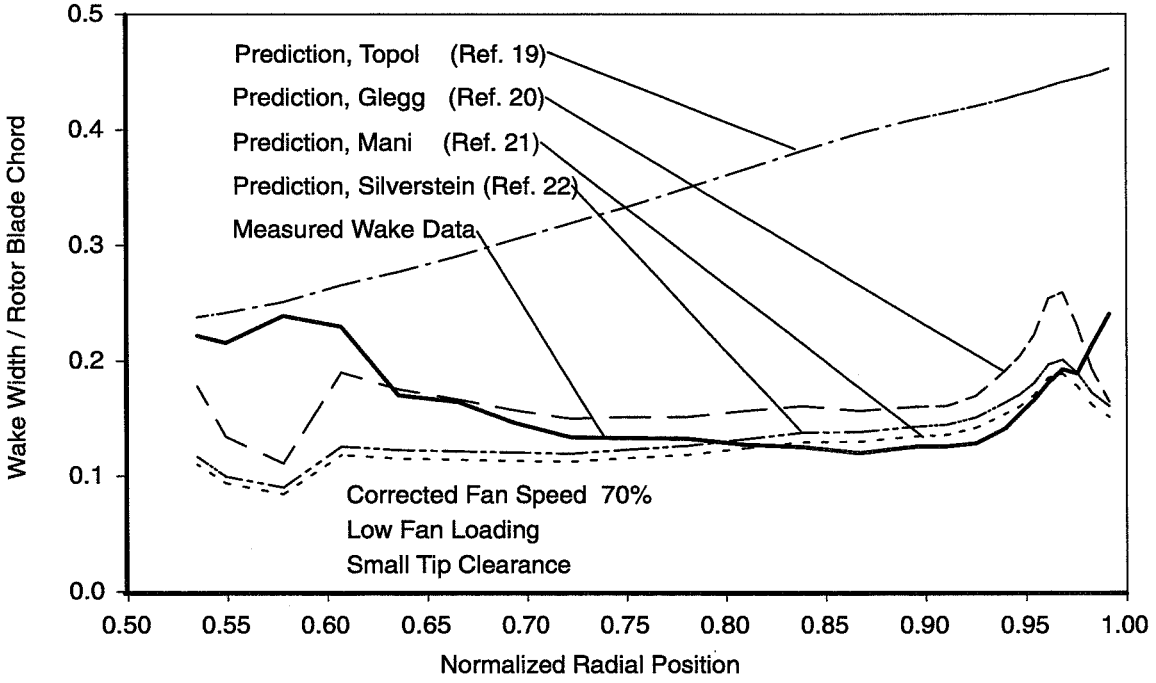

Fig. 95. Comparison of Measured and Predicted Values of Normalized Rotor Wake Width

Spectral Properties of Turbulence

The spectral distribution of the turbulence has been determined based on the recorded time series. Since we are interested in frequencies as high as the Nyquist frequency of the recorded data (50 Khz) it is not feasible to use conditional sampling of the data to obtain spectra at discrete positions relative to the rotor. The derived spectra thus represent the average spectral distribution for a flow field composed of wakes separated by clean, low-turbulence flow segments. A set of typical power spectral densities for the streamwise turbulence component is shown in Fig. 96. The spectra are grouped into the three spanwise regions and have been normalized with the local circumferential average of the mean velocity.

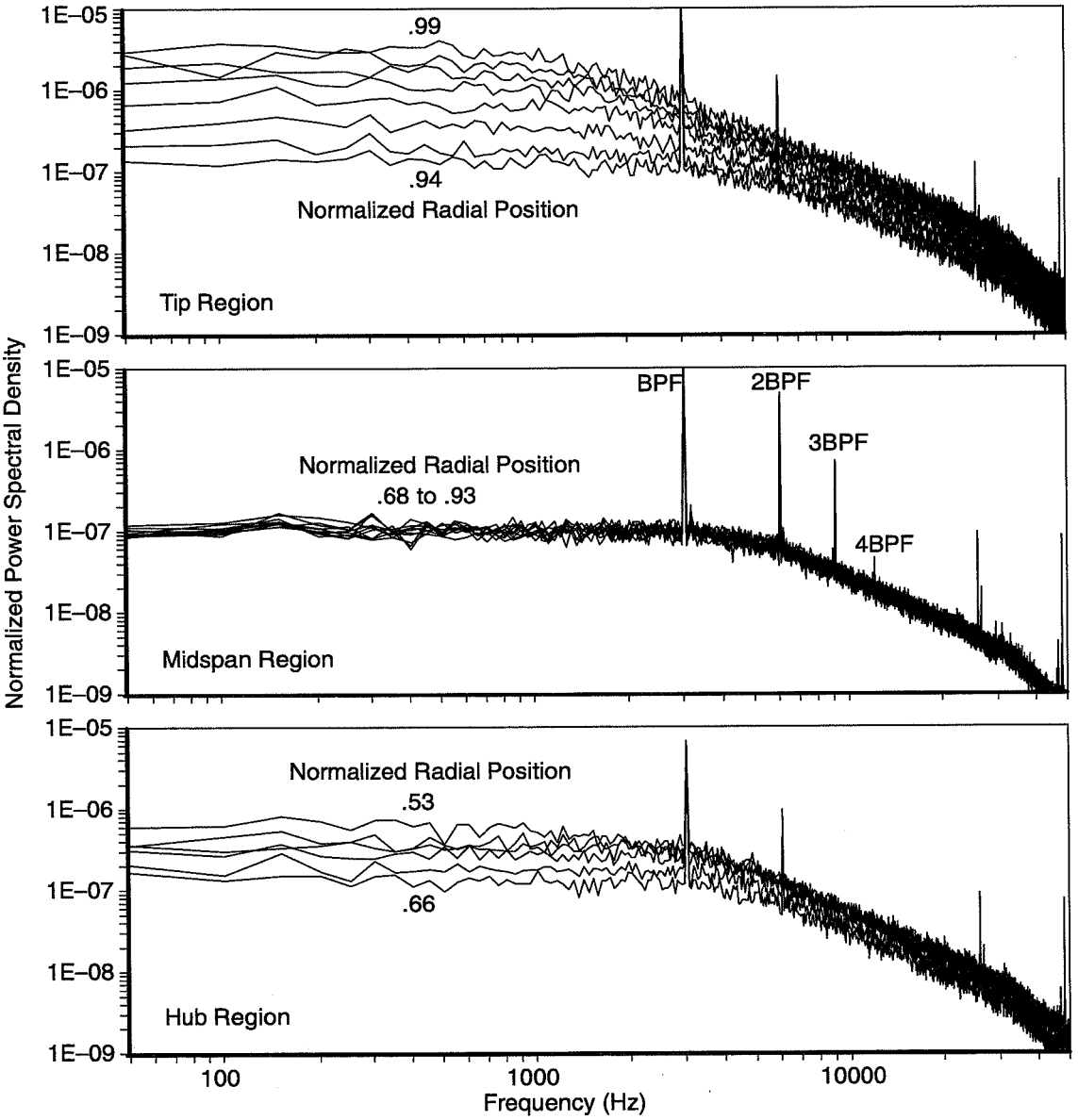

Fig. 96. Power Spectral Densities for the Streamwise Turbulence Component Normalized with Local Mean-Flow Velocity

In the tip region the spectrum level increases continuously as the observer position approaches the outer duct wall. The increase is larger in the low frequencies. In the midspan region the broadband content of the spectra collapses into a narrow band. The spectra exhibit significant tonal content at the BPF and its harmonics. The tone components beyond the fourth harmonic of the fan BPF are part of the cross-wire noise floor.

As in the data for the inlet boundary-layer turbulence, pulse-synchronized averaging has been used to extract the harmonic signal content with the fan rotational frequency as its fundamental. A common way to normalize turbulence spectra is based on using the mean flow velocity U, the turbulence variance $\overline{u^2}$ and the turbulence integral length scale.

$$PSDN_{uu}\left(f\frac{L_{ux}}{U} \right) = PSD_{uu}\left(f\frac{L_{ux}}{U} \right) \frac{1}{\overline{u^2}} = PSD_{uu}\left(f \right) \frac{U}{L_{ux}\overline{u^2}} \qquad (4)$$

with $PSDN_{uu}$ Normalized power spectral density

f Frequency (Hz)

L_{ux} Streamwise integral length scale for streamwise turbulence component

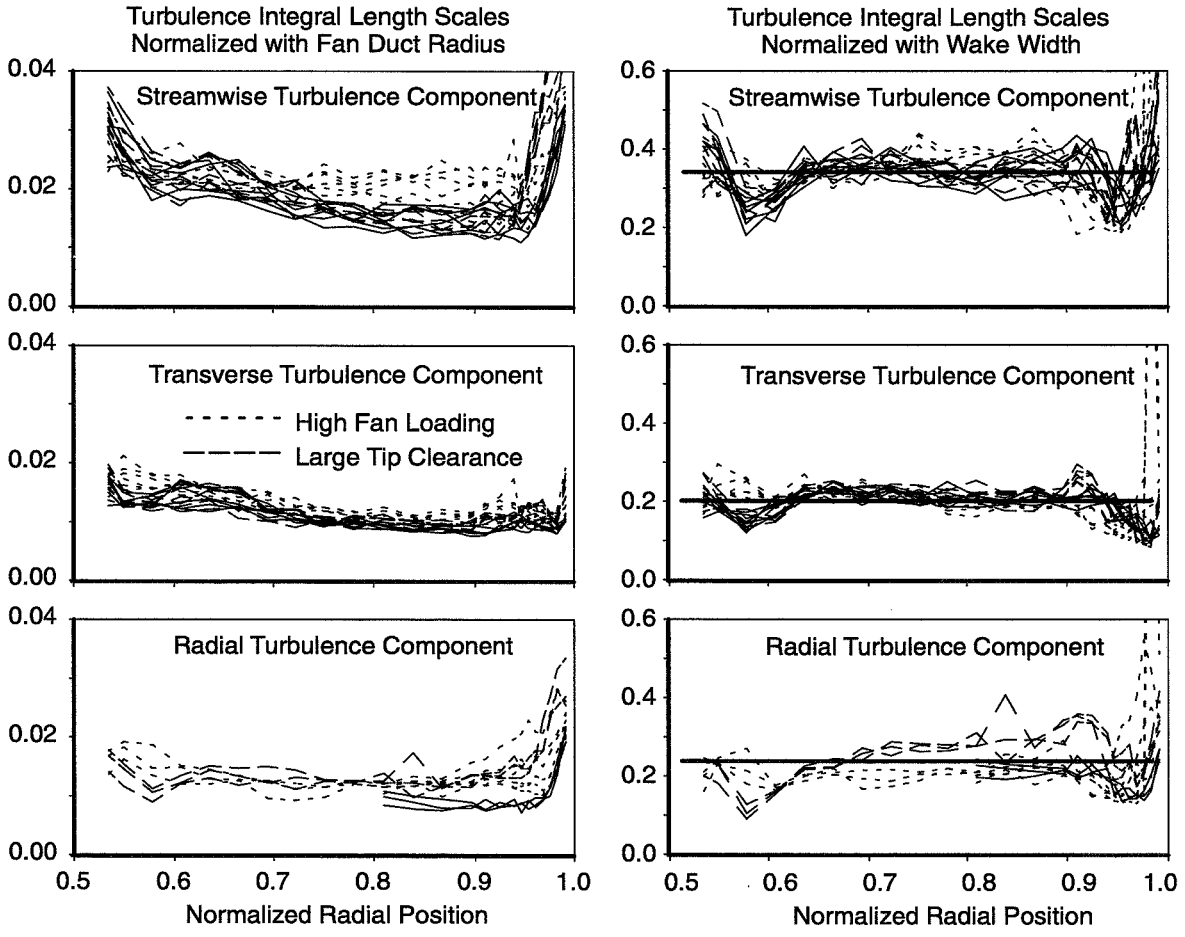

Fig. 97. Normalized Turbulence Integral Length Scales for 3 Fan Tip Speeds, 2 Tip Clearances, 3 Fan Loadings

The integral length scale can be derived either based on the integration of the correlation coefficient or with the limiting value of the power spectral density as the frequency approaches zero, see Equation 2. The latter method was selected for the data presented in Fig. 97. Because of the small bandwidth of the spectral analysis (2160 points) and the short record length (1 second), the number of averages available is relatively small (50 to 90). This resulted in significant uncertainty for the spectrum levels and caused substantial scatter in the magnitude of the integral length scales. In order to reduce this scatter and considering the flatness of the spectra at low frequencies the integral length scales have been defined based on the average of the five lowest bands of the power spectral densities.

Since the measurements with the cross-wire probes were limited to single point measurements, only the streamwise integral length scales could be determined. The scales normalized with the fan duct radius (0.22 m) are presented in the left column of Fig. 97. The data is based on three corrected fan speeds (55, 70 and 88%), the large and the small tip clearance and all three fan loadings. The data indicates some systematic trends; larger length scales with increased fan loading and larger length scales in the outer-wall region with the large tip-clearance. The data in the right column shows the same data set but normalized with the local wake-width. The data collapse is somewhat improved with this normalization. It must be remembered that close to the hub and outer duct wall the wake width is not well defined because of merging wakes and the presence of the wall boundary flows. Representative values for the streamwise integral length scales normalized with the wake width are 0.35 for the streamwise component, 0.2 for the transverse and 0.25 for the radial turbulence component. The ratio between the length scale of the streamwise turbulence component (parallel to the velocity component) and the length scales of the transverse and the radial components (normal to the velocity component) is 1.8 and 1.4. In isotropic turbulence this ratio is 2.

All the spectra of Fig. 96 normalized based on Equation 4 are shown in Fig. 98. The spectra have the characteristics of von Karman spectra with the constant low-frequency segment and the high frequency segment rolling off with an exponent of –5/3 as indicated by the straight line. The normalized frequency is the Strouhal number based on the integral length scale and the mean velocity. The high frequency tones in Fig. 98 are due to the sensor noise floor and are associated with structural resonances in the cross–wire support prongs. In Fig. 96 they appear at the same frequency at all radial positions. However in Fig. 98 they are shifted relative to each other because of the frequency normalization and therefore appear to be more prominent.

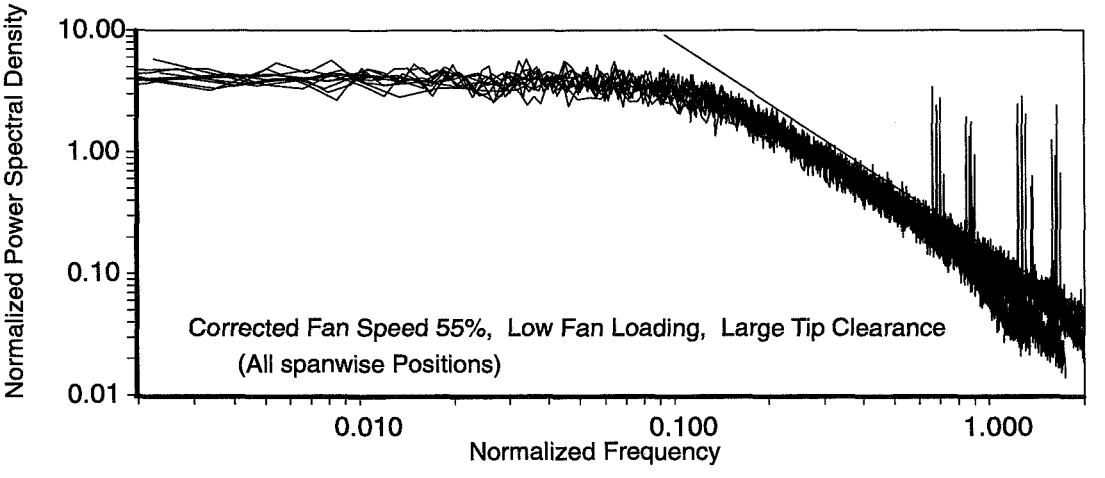

Fig. 98. Non–dimensional Power Spectral Densities of Streamwise Turbulence Component

It seems rather surprising but some of the statistical properties of this complex, highly non-homogeneous turbulence field have some similarity with those of isotropic turbulence. It has been observed earlier that the intensities of all the turbulence vector components are about of the same magnitude. Based on the 3 measured integral length scales it appears that the scale parallel to the turbulence component (L_{ux}) is about twice the size of those normal to the turbulence components (L_{vx}, L_{wx}). It was therefore decided to normalize the spectra in a fashion used for isotropic turbulence by using the variance and integral length scale of the streamwise turbulence component in the normalization of all spectra. Normalized spectra of the streamwise, transverse and radial components representative for a midspan position are compared with the von Karman spectra in Fig. 99. The equations of the one-dimensional von Karman spectra for the streamwise and the transverse turbulence components are:

$$PSDN_{uu}\left(f\frac{L_{ux}}{U}\right) = 4\left[1 + 70.7\left(f\frac{L_{ux}}{U}\right)^2\right]^{-\frac{5}{6}} \tag{5}$$

$$PSDN_{ww}\left(f\frac{L_{ux}}{U}\right) = PSD_{ww}(f)\frac{U}{L_{ux}}\frac{1}{(u^2)} = 2.\left[1. + 188.6\left(f\frac{L_{ux}}{U}\right)^2\right]\left[1. + 70.7\left(f\frac{L_{ux}}{U}\right)^2\right]^{-\frac{11}{6}} \tag{6}$$

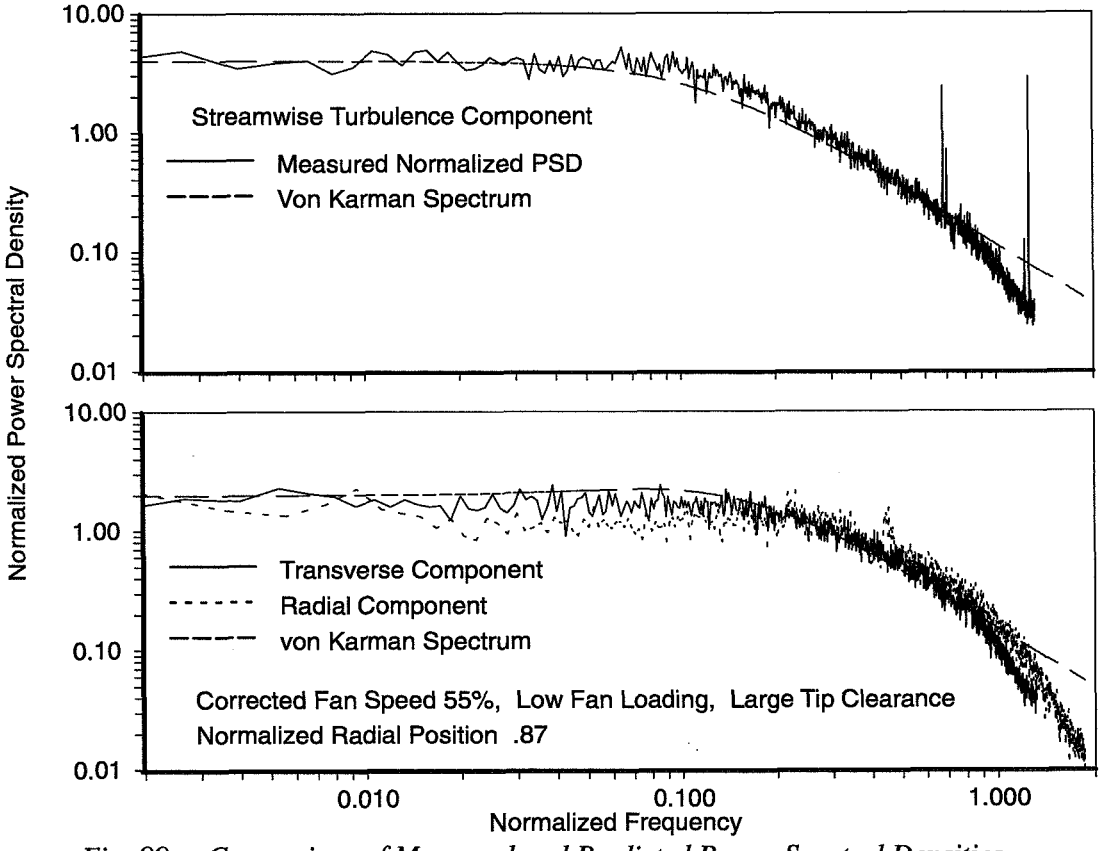

Fig. 99. Comparison of Measured and Predicted Power Spectral Densities

In general the agreement between the von Karman spectra and the normalized measured spectra is quite good. The measured spectra however roll off more rapidly at very high frequencies. This may be caused by the following:

- Signal attenuation by the anti-aliasing filter
- Limited frequency-response of the hotwire electronics
- Increased roll-off in the turbulence spectra above the upper edge of the inertial subrange

As shown in Fig. 97 the turbulence integral length scales are nearly independent of the mean flow velocity. This causes the top knee in the spectra (corner between flat spectrum segment and inertial subrange) to move to higher frequencies with increasing velocity. Similarly it may be assumed that the Kolmogoroff micro length scale is nearly independent of mean flow velocity. Since it controls the location of the lower knee in the spectra (corner between inertial subrange and steeper spectrum segment), one would expect it to move to higher frequencies with increasing velocity as well. However the steeper roll-off in the measured data seems to start at about 30 Khz independent of mean velocity. For this reason it has been concluded that it is most likely caused by the combined effect of the anti-aliasing filter and the limited frequency-response of the hotwire electronics. The contribution of this high-frequency segment of the spectra to the total power is however quite small.

Normalized power spectral densities for the three turbulence components are compared in Fig. 100. They illustrate the fact that the spectrum level of the streamwise component is higher by a factor of about 2 in the low-frequency range, below the knee and that the spectra of the transverse and the radial components are higher than that of the streamwise component in the region that may be identified as a limited inertial subrange.

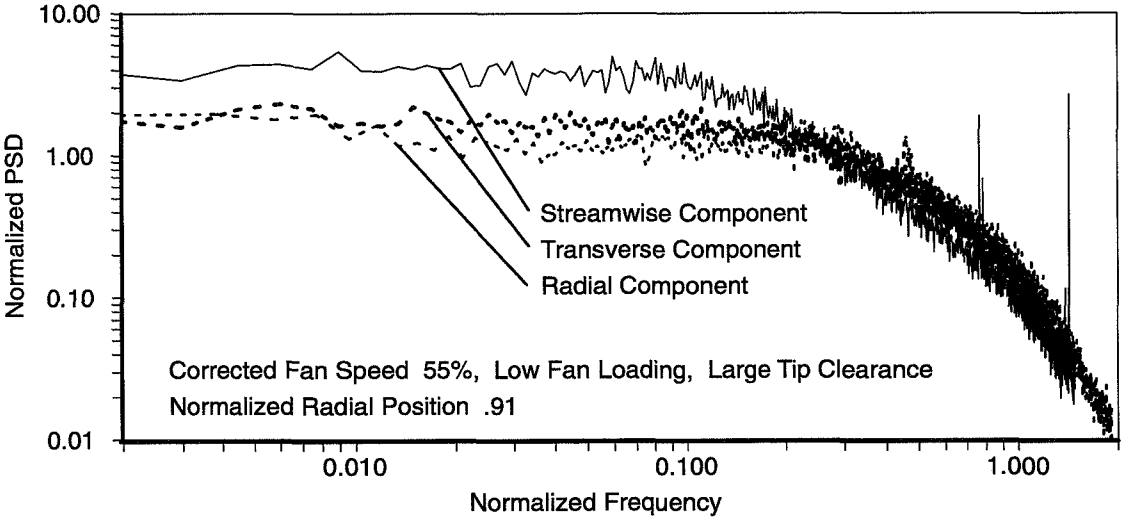

Fig. 100. Normalized Power Spectral Densities of Turbulence in Midspan Region

Normalized spectra for the three turbulence components at several radial positions are shown in Fig. 101. The results indicate that the collapse for the transverse and the radial components is not nearly as good as the one for the spectra of the streamwise component. Only the data of the midspan region are included in the comparison. The collapse of the spectra would be further degraded if data from the tip and hub wall regions would be included.

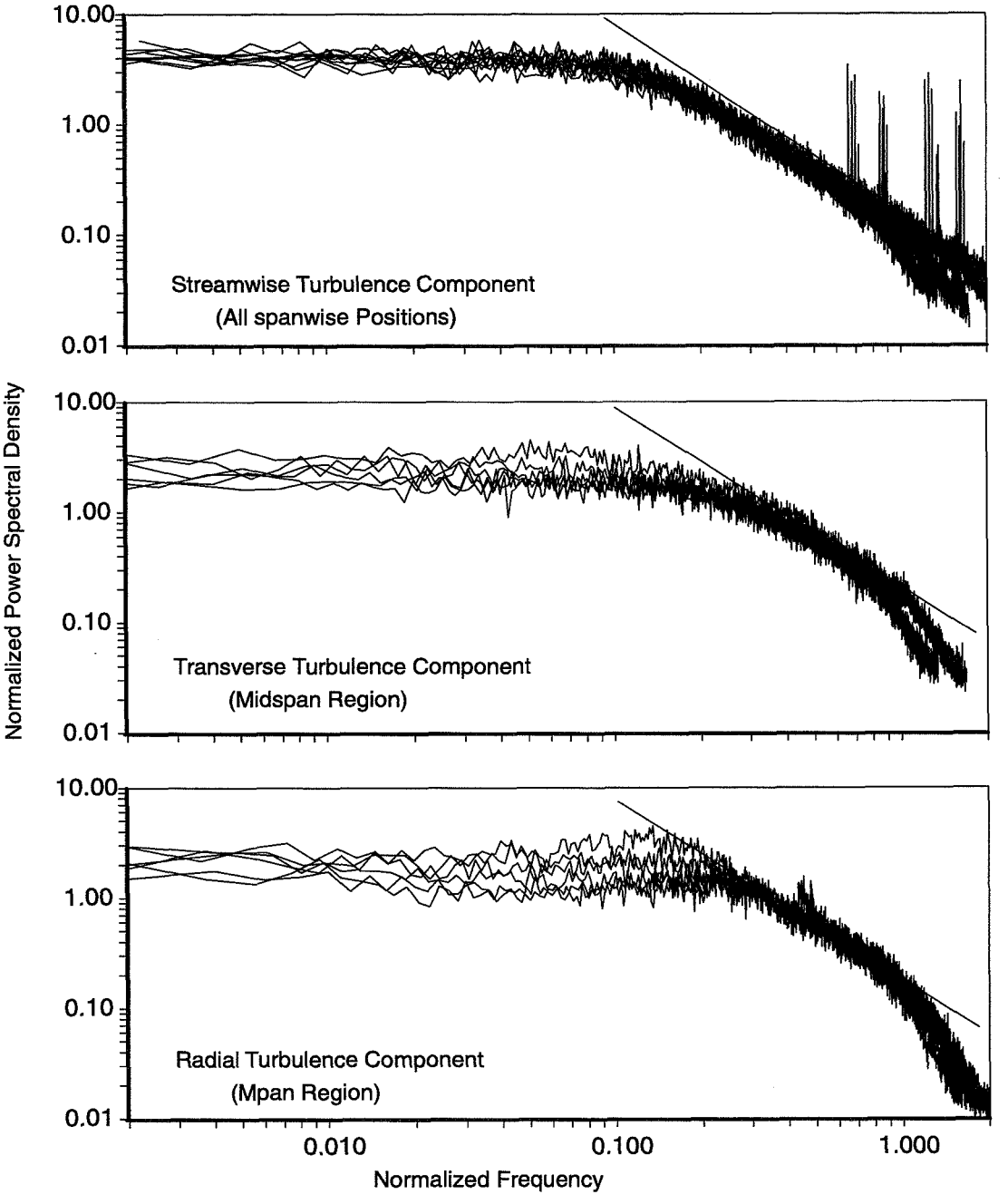

Fig. 101. Non–dimensional Power Spectral Densities of Turbulence Corrected Fan Speed 55%, Low Fan Loading, Large Tip Clearance

4.4 Far field Acoustic Measurements

Processing of sideline microphone array data

The sideline microphone array was the primary source of acoustic data. A 1600 line FFT covering the range of 0 to 25kHz was chosen to allow "buzz-saw" noise removal at frequencies as low as 50% of maximum rotor speed. This gave a minimum of 8 bins between "buzz-saw" tones which allowed the tones to be easily removed. The data system provided power spectra for each microphone, ensemble averaged over 125 samples.

The data are normalized in a number of ways to provide comparable results; this process is illustrated in Fig. 102.

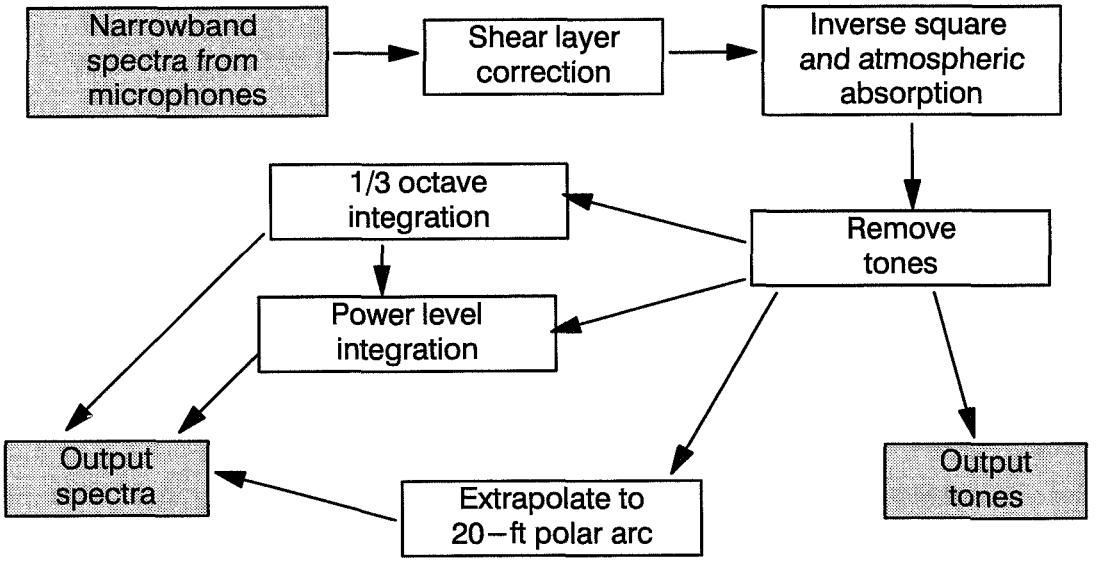

Fig. 102. Flow chart of sideline acoustic data normalization process

The sound from the fan rig propagates to the sideline microphones through the wind tunnel shear-layer (see Fig. 103, which illustrates the refraction geometry). Even at Mach 0.07, the refraction and level change is not insignificant. It is corrected using a thin shear-layer approximation due to Amiet (Ref. 27). Experience has validated the accuracy and usefulness of this approximation, in spite of the lack of frequency and directivity scattering from turbulence. In particular, at these low wind tunnel flow velocities there was no evidence of the spectral broadening that is seen at higher Mach numbers (over 0.20, approximately), at least for the 16 Hz bandwidth used in this test.

Atmospheric absorption can be significant at high frequencies, even over a short distance. The spectra were corrected using the 1995 ANSI absorption calculations (Ref 28). In the wind tunnel flow, these corrections are applied in the moving coordinate system, that is at the Doppler-shifted frequency and over the convected path length rather than the geometric one. Corrections are calculated for each narrow frequency band, before one-third octave conversion.

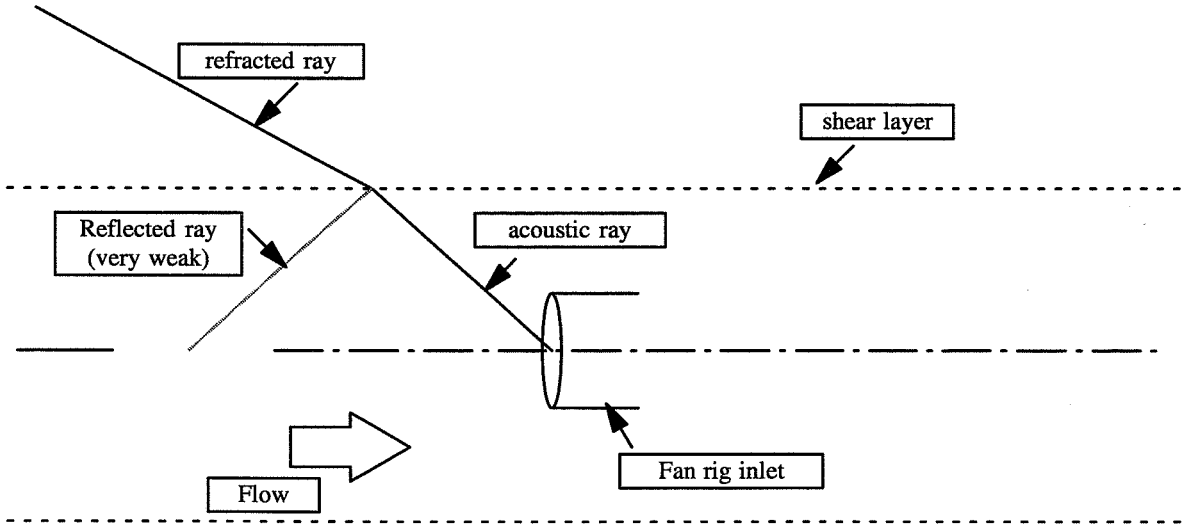

Fig. 103. Wind tunnel shear layer refraction geometry

Because this test was intended to study broadband noise, all tones were removed. This was done with a proprietary algorithm which identifies tones by estimating the second derivative of the SPL as a function of frequency, then screening these candidates to be sure they are real tones. The tone energy is removed and replaced by a linear spectral fragment level-matched to the surrounding broadband. The tone information is stored elsewhere and has not been used further.

The narrowband spectra are converted to one–third octave levels by a numerical integration using an order-3 (6-pole) Butterworth approximation to typical bandpass filters, as described in Ref 29. Little use has been made of the one-third octave data to date, but it remains available.

The most useful data so far has been the power level integration of the SPLs over angle. These power level spectra were integrated over a hemisphere assuming axisymmetric radiation, from 0 to 90 degrees directivity angle with the shield up for inlet PWL and 90 to 180 degrees with the shield down for aft-radiated PWL. The reference is 10^{-12} watts.

Test matrix

The test was originally designed with four variables – three values each of boundary-layer thickness, tip clearance, and loading, and five fan speeds. It was augmented at the mid-test workshop to include four combinations of stator count and solidity. The variables are these:

- Boundary layer thickness of zero (or as close as was possible), 50%, and 100% of the natural boundary layer in this inlet.
- Tip clearance of 0.22%, 0.41%, and 0.60% of fan radius. These are believed to span the achievable values for real engines.
- Loading of nominal (design value), slightly higher and slightly lower. The variation was roughly $\pm 10\%$ in fan pressure rise.
- Fan speeds relative to design speed were 55%, 70%, 78%, 88%, and 100%; the rotor tip relative Mach number was 1.00 at about 78% so there were two subsonic, one transonic, and two supersonic conditions.

- The stator combinations included no stators, at which condition the nozzle was adjusted to maintain the same fan conditions as in the with-stator cases so that the rotor noise sources would be the same. The reference stator condition was with 30 stators, at the design solidity. To test the effects of stator count, 15 stators of twice the chord (same design solidity) were used. Finally, a set of 60 stators was used but earlier experience precluded use of the design solidity as the small-chord stators were not strong enough. The reference stators (the same ones used for the 30-stator test conditions) were used, so the solidity was twice the design value. All were tested in the forward of two available positions, about 2.5 fan tip chords downstream of the rotor trailing edge.

Because of the augmented test matrix (extra stator conditions), it was no longer possible to test all combinations of the (now five) variables, so a reduced matrix was tested. This reduced matrix is illustrated in Fig. 104. Basically, only the extreme values of boundary layer thickness, tip clearance, and loading were tested, at all five fan speeds. The four stator arrangements were selected from a matrix of 19 possibilities (including the no-stator case). In addition to these, for the 30–stator case only, certain intermediate value combinations were added to enable a fractional factorial expansion. It was intended that this might be used to fit a quadratic analysis of variance (ANOVA), assuming higher-order interactions to be small. In the event, the 2-level (linear) test matrix indicated that there were several components of broadband noise each of which had different sensitivities to the test variables, so the quadratic ANOVA for that case would be somewhat meaningless. (In fact it might well have been useful for optimization, if this were a real engine.)

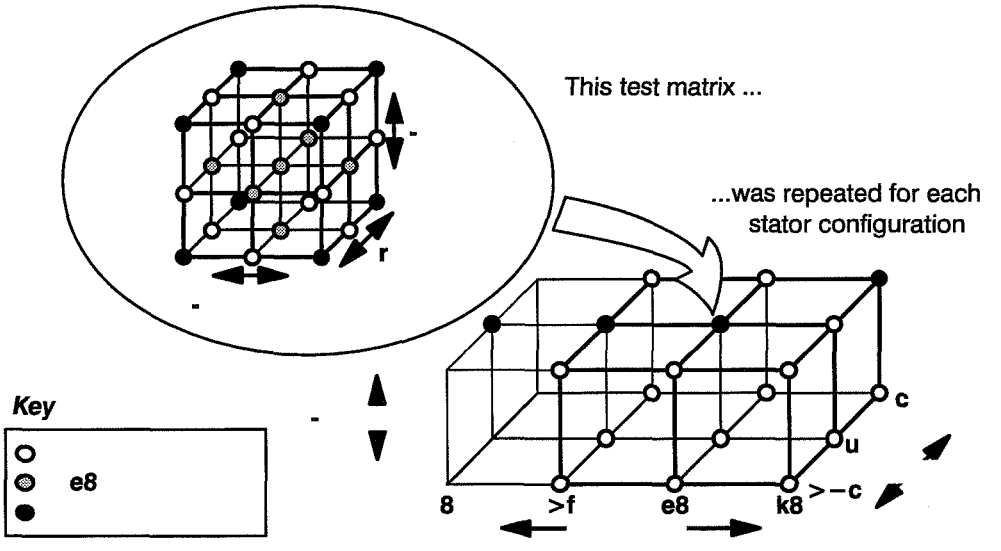

Fig. 104. Test matrix, showing fraction of the full factorial expansion tested

The results, in particular the forward- and aft-radiated power level spectra, were then manipulated to extract sub-component levels as described below. These sub-component levels remain a function of fan speed, loading, tip clearance, and sometimes blade count. ANOVA has been used in many cases to extract the mean value (averaged over tip clearance and loading), plus the linear main and interaction effects of these variables, all as functions of fan speed and possibly stator count.

Selected results – far-field

The principal data shown here are the sideline (far-field) microphone data, in the form of estimated inlet and aft-duct radiated sound power levels re: 10^{-12} watts. These are 1600-point Hanning-windowed narrowband spectra, 0–25kHz, of the broadband component. In some cases, a tone–like spike can be seen at multiples of the blade passage frequency; these are presumed to be tone haystacking that was too wide to be detected by the tone–removal algorithm. In most if not all such cases a much higher tone of narrower width has been removed. No further attempt has been made to identify and remove these spikes.

These data are presented in 8 plots, Fig. 105 – Fig. 112. These plots summarize the range of configurations tested. These figures are not suitable for detailed interpretation, but do serve to illustrate general trends. The power level spectra are shown for all four stator variations, at the 5 fan speeds, for low and high loading in each figure. The figures cover inlet- or aft-radiated power at large or small tip clearance with or without boundary-layer, under the following conditions:

- Smallest tip clearance, full boundary-layer
- Smallest tip clearance, no boundary-layer
- Largest tip clearance, full boundary-layer
- Largest tip clearance, no boundary-layer

There are two plots on each page, at low and high loading. Each plot compares narrowband spectra for various fan exit guide vane sets (including rotor-alone). In virtually all cases the spectra at high frequencies are ordered according to the number of stators at any given fan speed (the more stators, the more noise). The one exception is at the highest fan speed at high loading, where the 30- and 60- stator cases are virtually identical. Other plot formats, such as one-third octave spectra or comparisons of loading, boundary layer, or tip clearance effects are possible but would make this report excessively long. They can be generated if there is a need, however.

Only the extreme values of the three principal variables (boundary-layer thickness, fan loading, and fan tip clearance) are shown in these plots. For the single case of 30 medium-chord stators (the most realistic case, at least for broadband noise) there are other data at all combinations of two intermediate and one extreme value plus the central point with all three intermediate values. These additional data are available on request.

These same data are presented in Appendix 3 in 32 plots which are suitable for detailed comparison and interpretation.

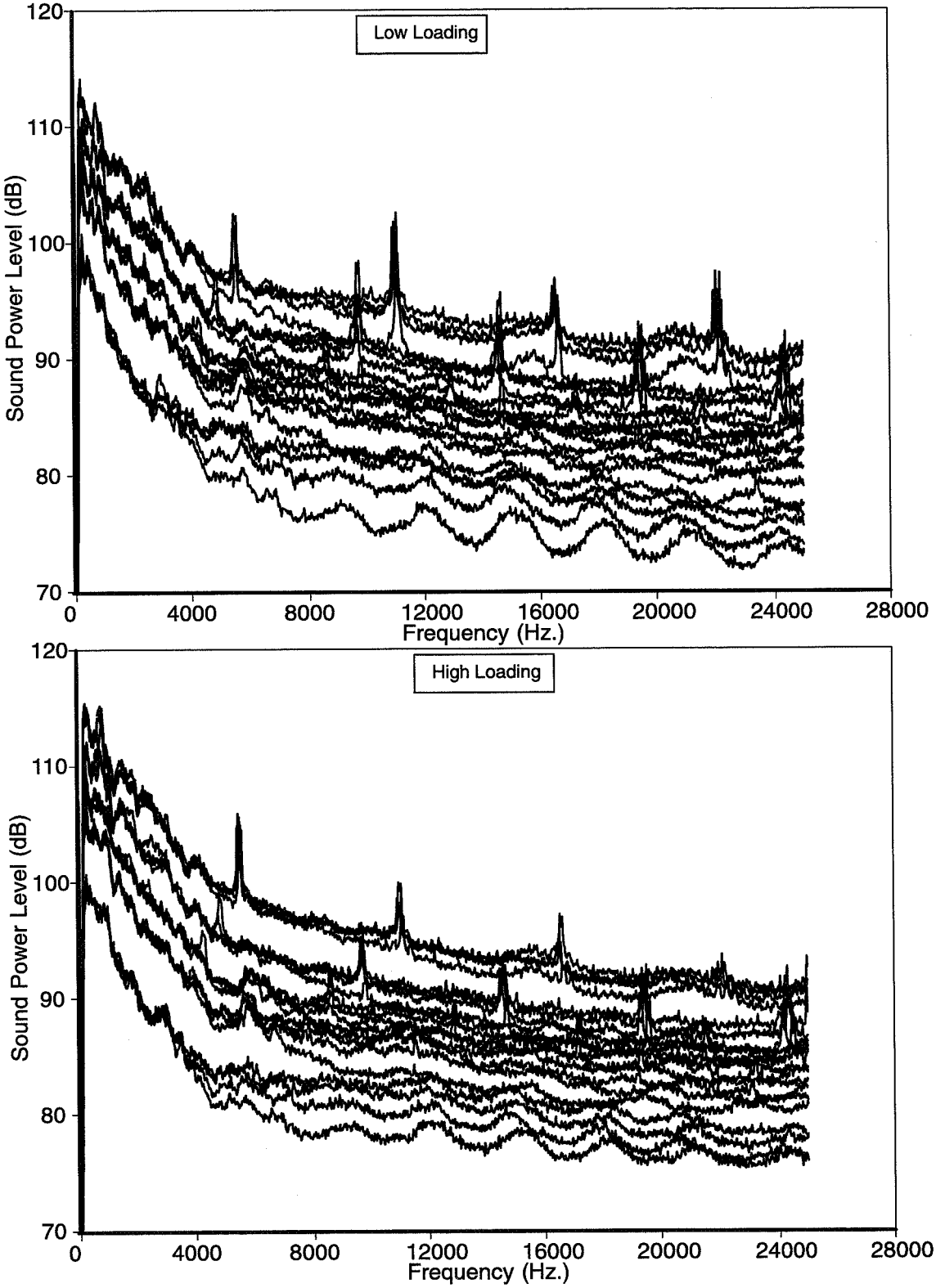

Fig. 105. Inlet–radiated power level spectra, small tip clearance, full boundary layer

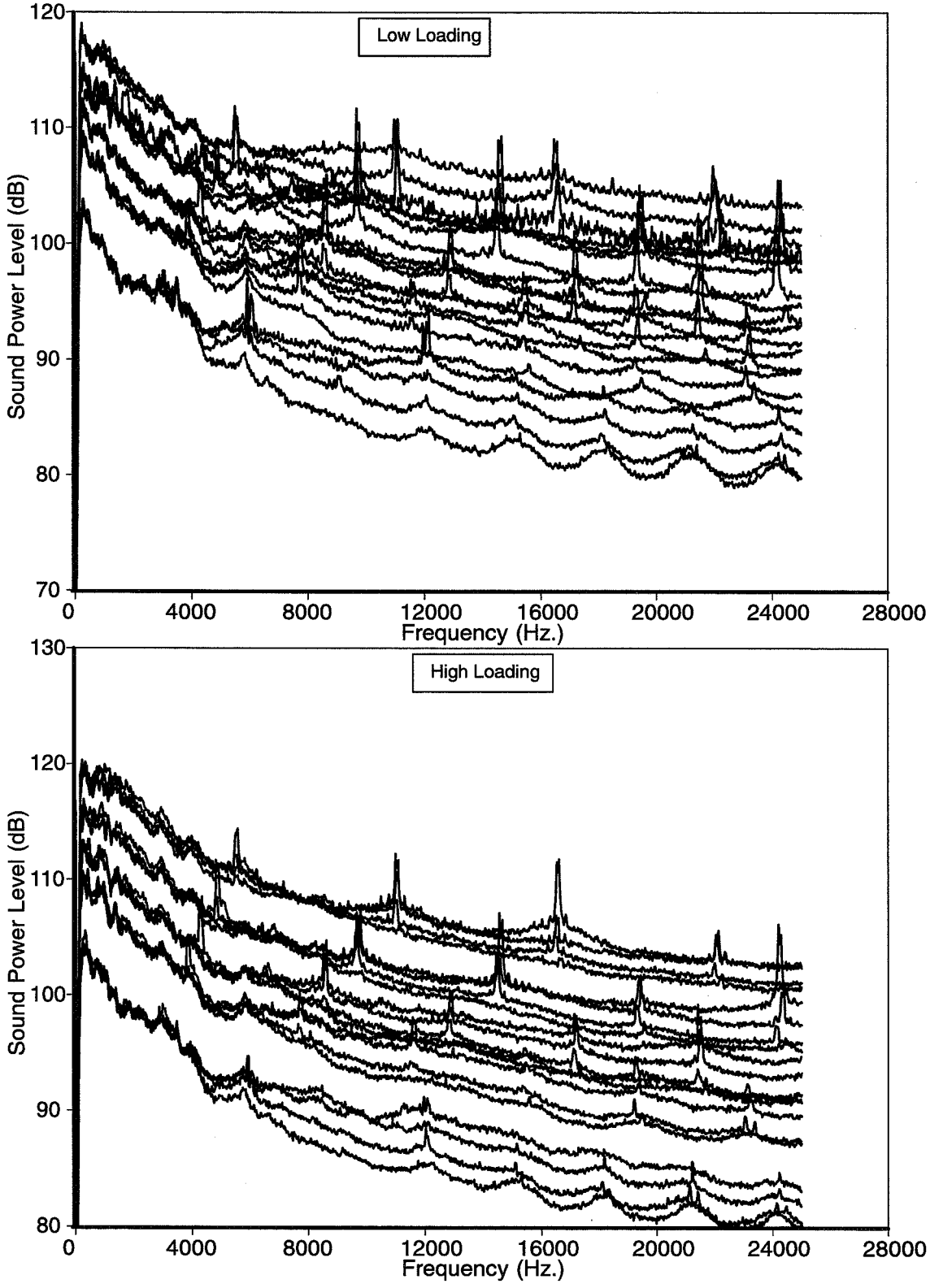

Fig. 106. Aft–radiated power level spectra, small tip clearance, full boundary layer

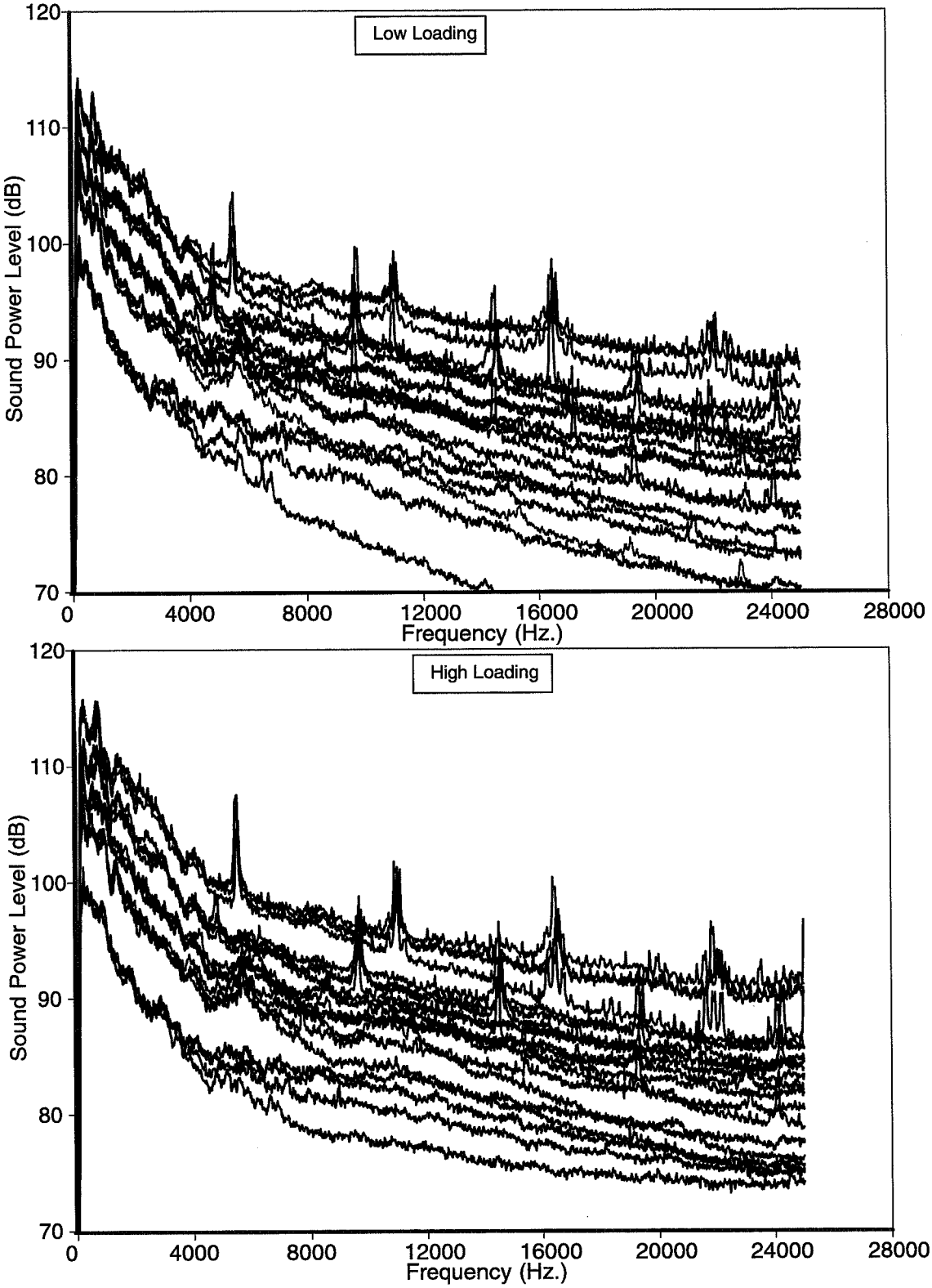

Fig. 107. Inlet–radiated power level spectra, small tip clearance, no boundary layer

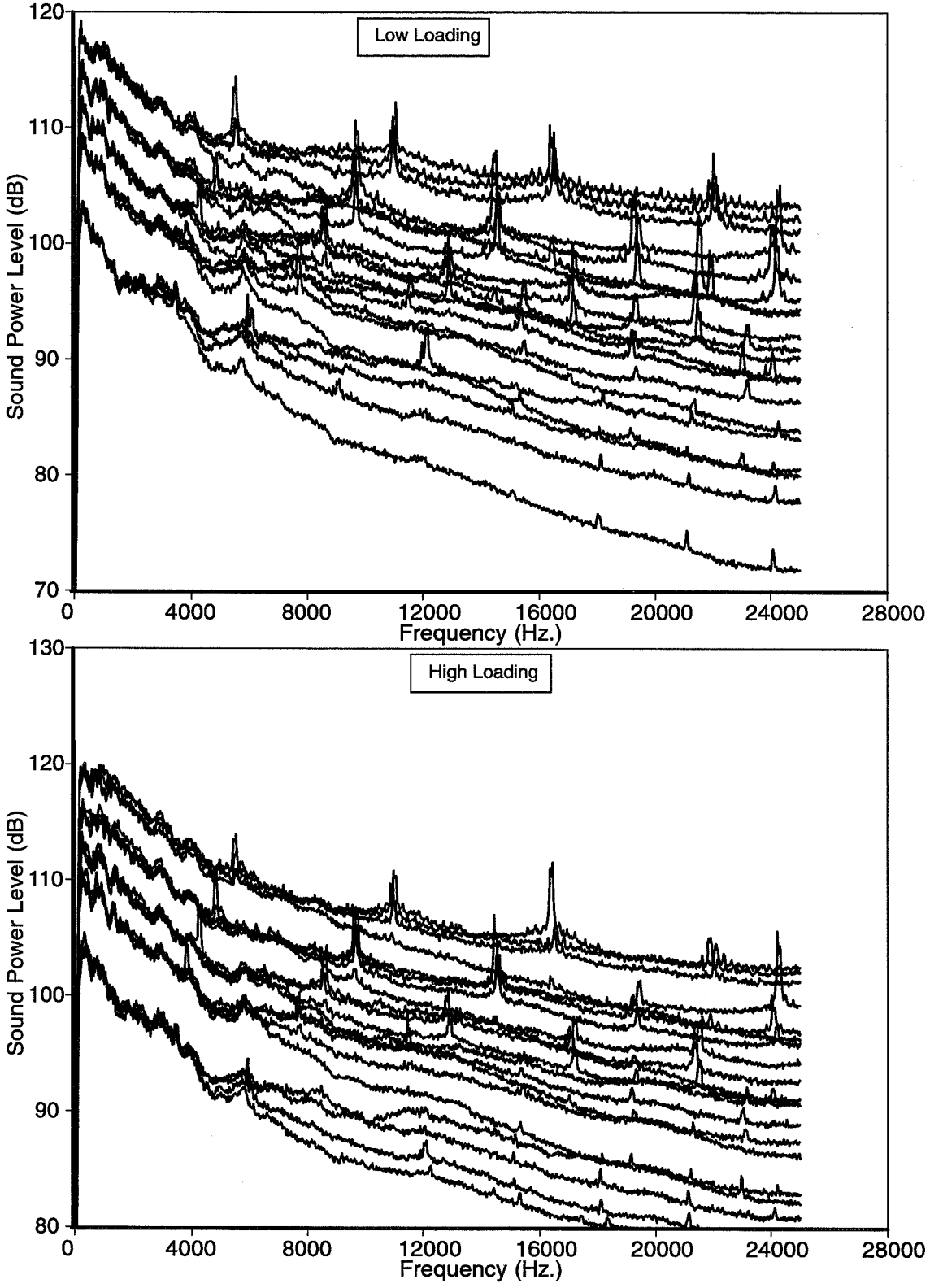

Fig. 108. Aft–radiated power level spectra, small tip clearance, no boundary layer

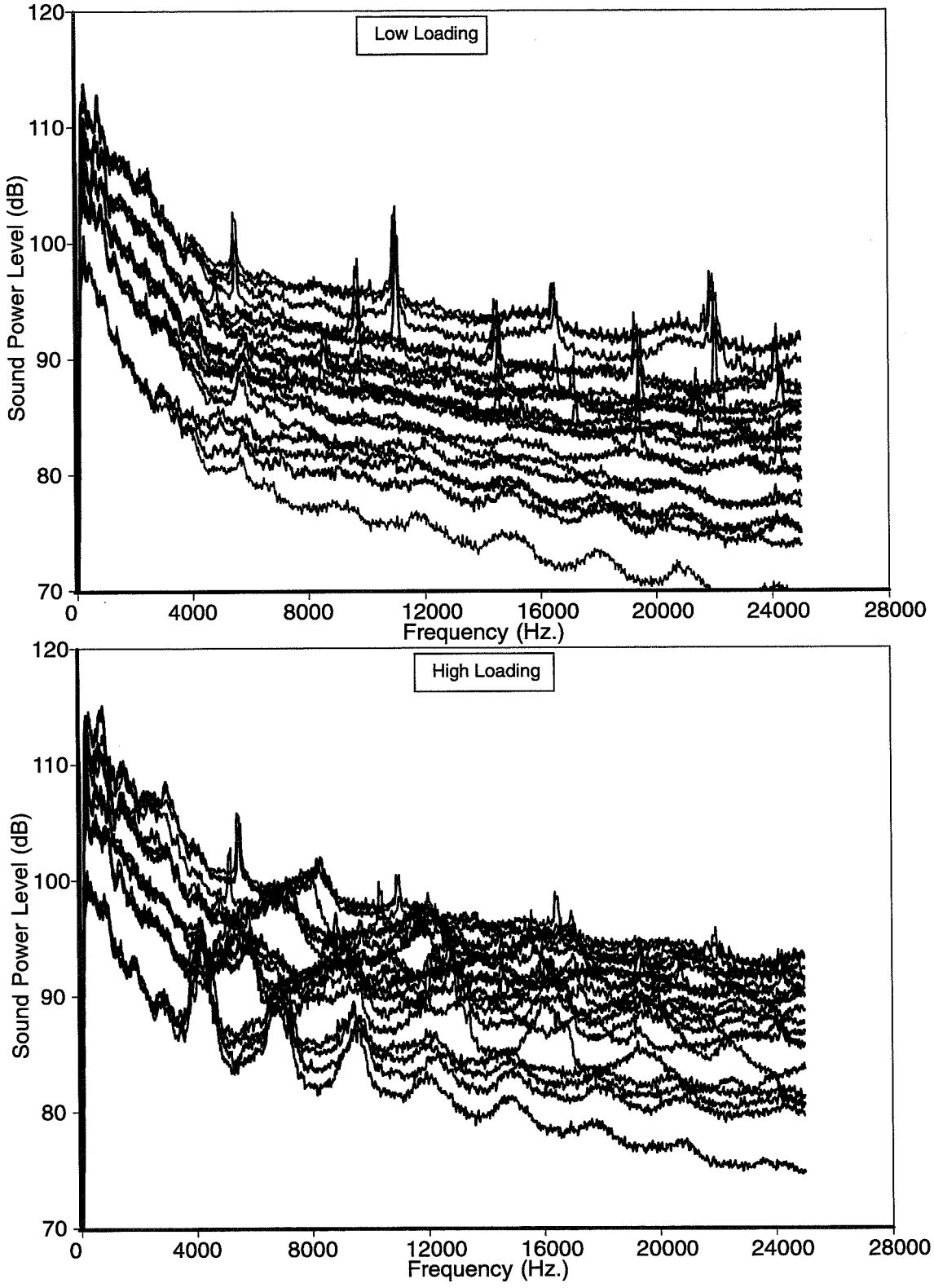

Fig. 109. Inlet–radiated power level spectra, large tip clearance, full boundary layer

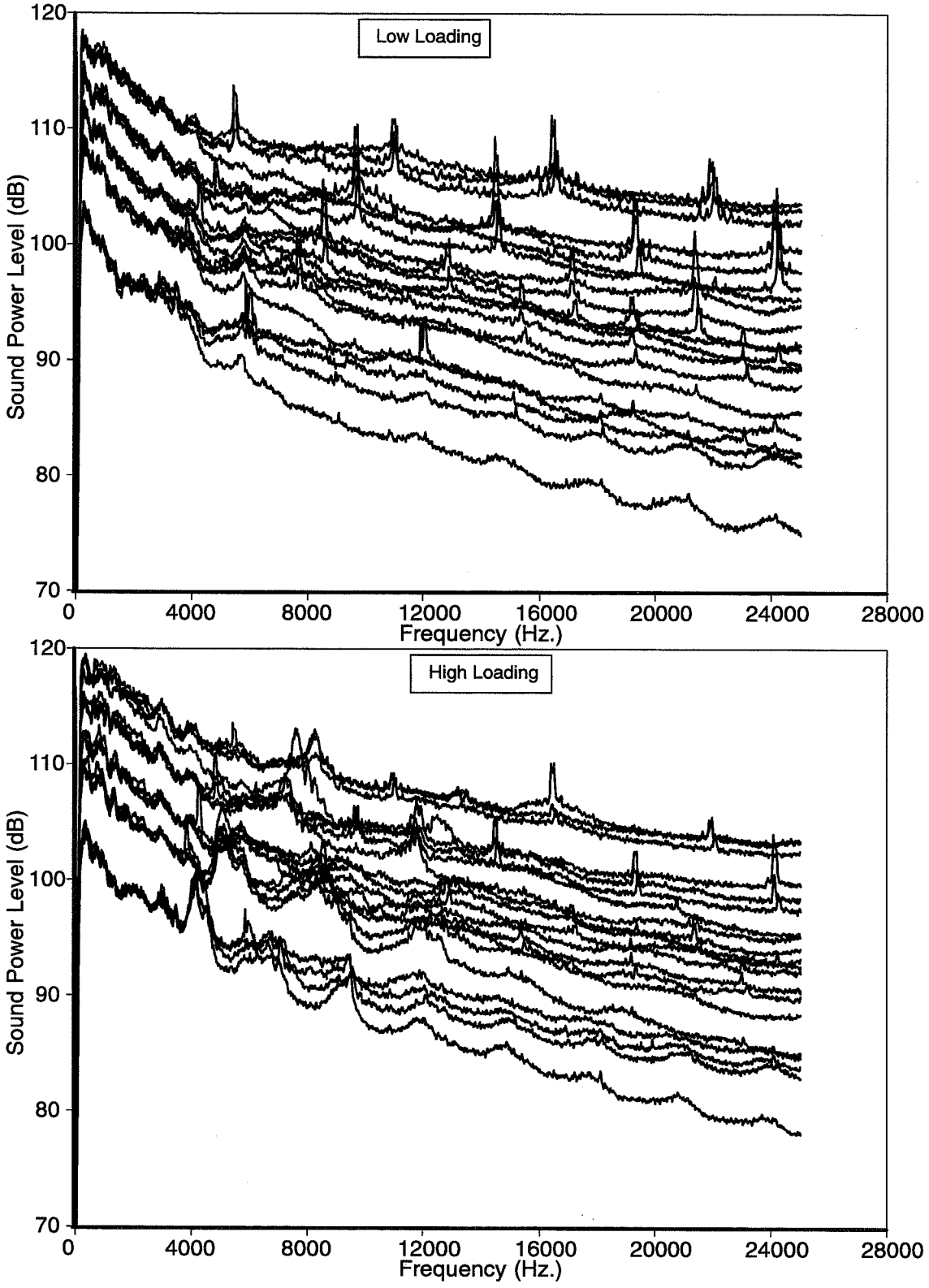

Fig. 110. Aft–radiated power level spectra, large tip clearance, full boundary layer

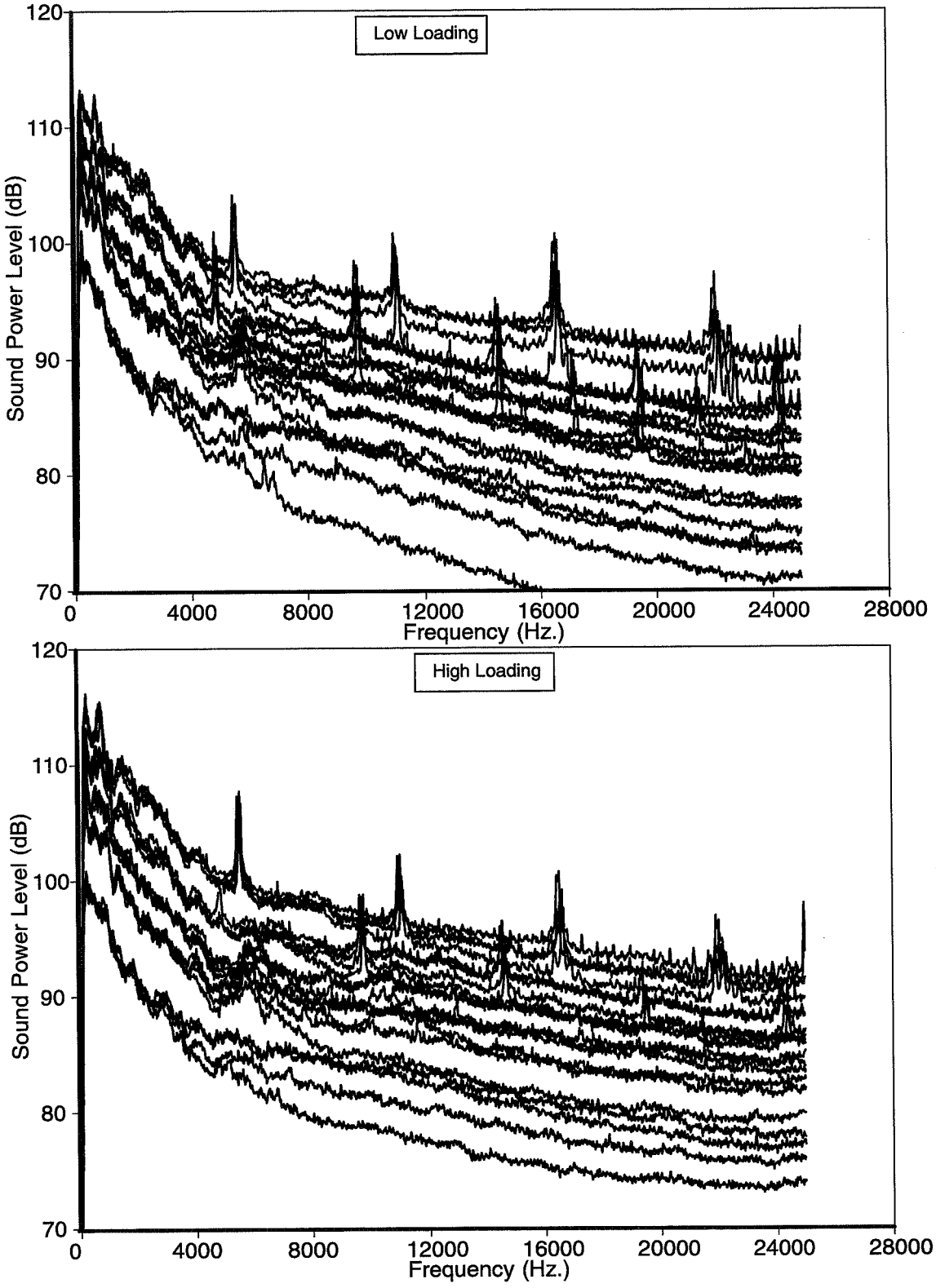

Fig. 111. Inlet–radiated power level spectra, large tip clearance, no boundary layer

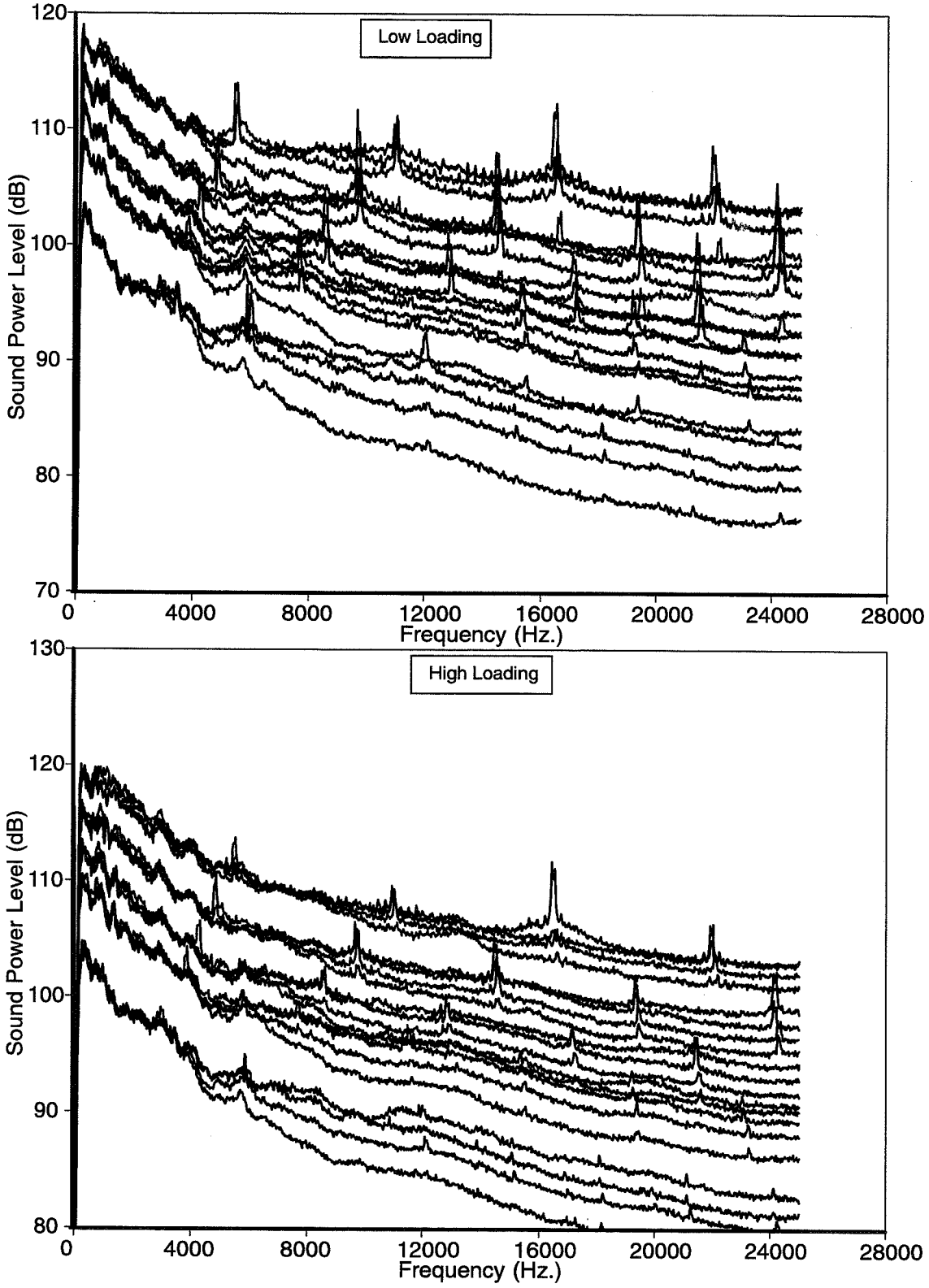

Fig. 112. Aft–radiated power level spectra, large tip clearance, no boundary layer

4.5 In-Duct Acoustic Measurements

In-duct microphone signal processing

Signal processing for the in duct microphones is illustrated in Fig. 113. The cross–spectrum of each channel with respect to channel 1 is recorded in the data system; 16 examples are recorded but no averaging takes place initially. These data are used to produce two outputs, the duct wall pressure spectrum and the modal distribution spectrum, as illustrated in Fig. 113.

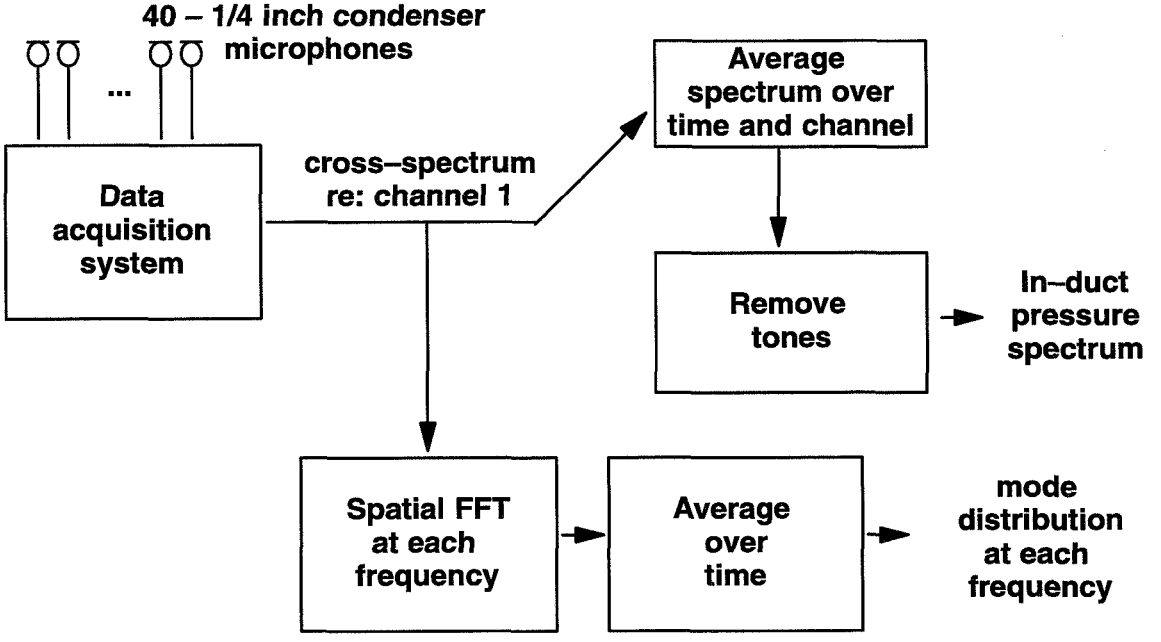

Fig. 113. Mode measurement data reduction process

The duct wall pressure spectrum is an ensemble average over microphones and time of the PSDs. The PSD is obtained by squaring the complex magnitude of each cross-spectrum and dividing by the first one, which is the channel 1 autospectrum. Tones are removed as in the far field case. This provides a power-averaged estimate of the wall pressure broadband spectrum, but does not estimate the power level in the duct. Some attempts have been made to extract such an estimate using the modal information, but to do so requires knowledge of the radial as well as circumferential mode amplitudes. A uniform-power (equipartition) assumption was tried, but the results were not satisfactory and it was not pursued.

The mode analysis used here is more fully described elsewhere (Ref. 10). It provides an estimate of the circumferential wavenumber spectrum at each frequency, i.e. the SPL is a function of both frequency and mode order. These estimates are ensemble averaged over the 16 samples so the scatter in broadband noise is reduced somewhat, but is still not insubstantial at around 1 dB rms.

Available data

Because of the time required to acquire in-duct data, it was not practical to make these measurements for both inlet and aft-duct arrays at all conditions. Flow time for a single measurement was about the same as that for far field data. In order to maximize the number of conditions in the available test time, it was decided to take inlet duct data at 70% and 88% fan speed, and aft duct (actually,

between the stators and rotor when stators were installed) data at 55%, 78%, and 100%. Consequently, there are no data for both arrays at the same fan speeds, but there are both subsonic and supersonic tip-speed data for both arrays.

Selected results – wall pressure spectra

The duct-wall acoustic pressure spectra look generally similar in shape to the far field data above 2–5kHz. The far field spectra show a rapid rise in level with decreasing frequency below that point. The beginning of the low-frequency rise varies depending on the particular test condition. The duct-wall average sound pressure level is typically 10 to 20 dB greater than the far-field power level. An example is shown in Fig. 114, comparing the far field power level with the duct-wall average pressure spectrum less 15dB. In this case (no stators, high loading, small tip clearance, full boundary-layer) it is readily seen that the difference between duct-wall pressure and far field sound power is a function of fan speed. Note also there are a few "humps" in the in-duct spectrum that do not appear in the far field. The origin of these differences has not yet been fully explored. In the aft duct the low-frequency level continues to rise at low frequencies in the duct, though not so steeply as in the far field. It is speculated that this is due to duct-wall turbulence on the microphones, although it is also possible that strut noise is propagating up the duct.

For a similar case with stators (but no boundary layer), illustrated by Fig. 115, the appearance is similar, even though the duct microphones are upstream of the stators and hence their comparison with the aft-radiated far field spectrum is questionable, at least so far as stator–originated noise is concerned. Note that the very lowest frequency levels match those of Fig. 114, but above 1–2kHz the levels are higher and the spectrum is more flat. This supports the notion that there is an in-duct source of low-frequency pressure fluctuations that is not a fan-generated acoustic source.

As these data are broadly similar to the far field sound power spectra, except for the above-mentioned low frequency differences, they are not shown in further detail here. The same sub-component analysis was done with both data sets; further examples are shown in the next section.

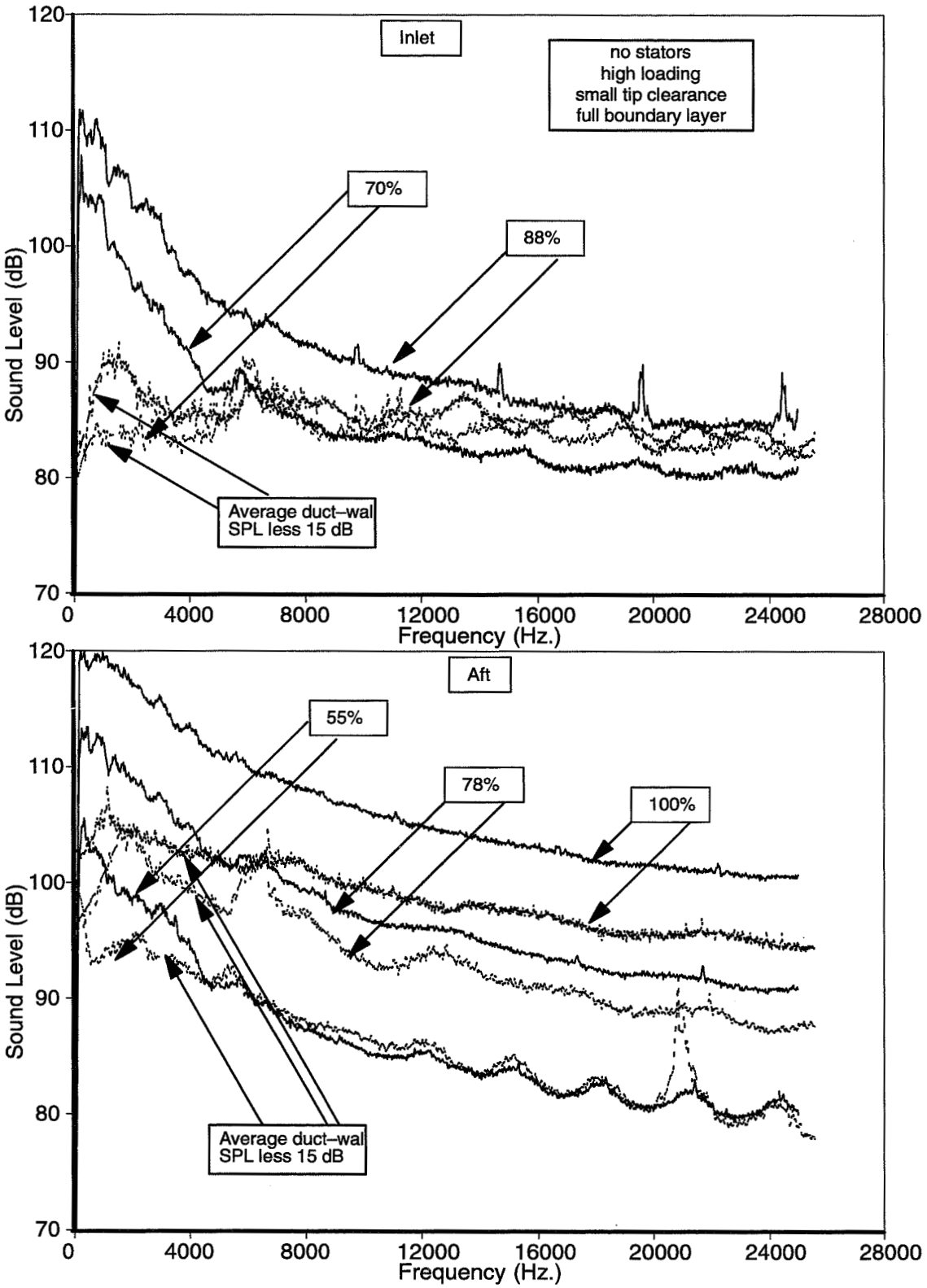

Fig. 114. Comparison of far field sound power with average duct wall pressure spectra

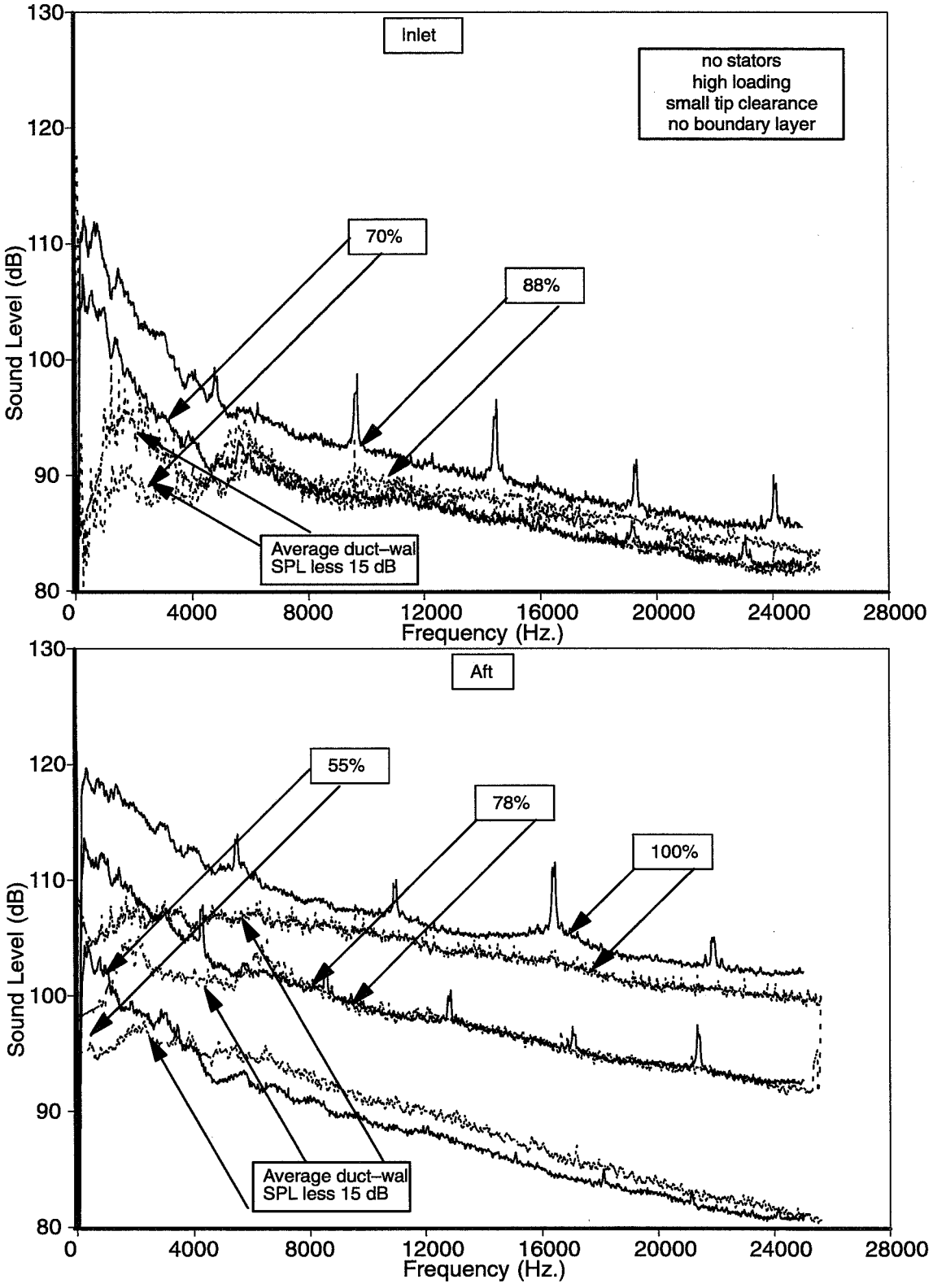

Fig. 115. Comparison of far field sound power with average duct wall pressure spectra

Selected results – modes

The inlet array used 40 microphones covering a half circle, which gave a resolution (bin spacing) of two spinning orders with the discrete Fourier transform beamforming used here. This is the array illustrated in Fig. 26. Alias-free results are available up to spinning orders of ± 40 which is not cut on below a frequency a little over twice the blade-passage frequency, about 8kHz. Above that frequency, aliasing of cut-on modes must be tolerated; fortunately in this test the modal structure could be sensibly interpreted in that region. The aliasing is illustrated in Fig. 116, where a region of spinning order/frequency space is indicated which is unambiguous below the 8kHz frequency.

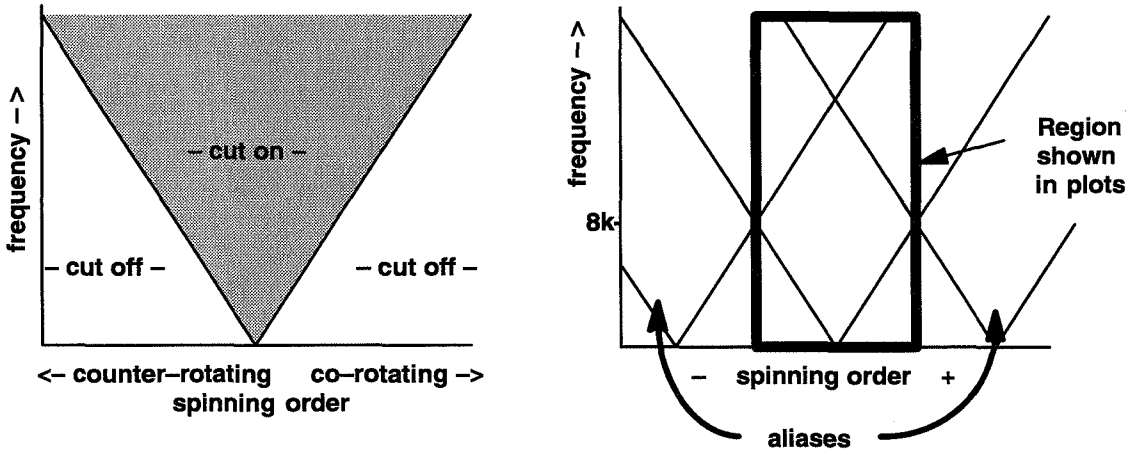

Fig. 116. Acoustic cuton and aliasing for inlet array

All the results shown here are presented as color maps of SPL on the mode–frequency space illustrated above. All are shown with the same color scale to facilitate comparisons.

A typical example of an inlet modal distribution is shown in Fig. 117. The boundary between cut-off and cut-on modes is clearly visible, as is a bias towards co-rotating modes in the sound pressure. Because of this bias, the aliasing above 8kHz is also clear and fairly easily interpreted. The rotor-stator interaction tones are visible as bright spots at the expected spinning orders, m = –10, 10, 30, ..., for blade passage frequency, 2BPF, 3BPF, etc.; BPF is about 4kHz. The rotor-locked field is cut off at this tip speed, and hence is not seen. Note that the tones are associated with elevated levels at all modes; this is due to the modal signal/noise ratio being limited by variations in frequency response and position of the sensors. A horizontal slice of the plot taken near 3 BPF is shown in Fig. 118 to illustrate this effect; note that the interaction mode clears the background by at least 30 dB.

At supersonic tip speed, as shown in Fig. 119, the fan tones are stronger because the rotor-locked field is cut on. The rotor shaft harmonic tones ("buzzsaw" tones) are also apparent, clearly delineating a line near the co-rotating cuton edge. The underlying broadband however remains visible even without tone extraction. It is apparent that the broadband noise, while still predominantly co-rotating, has a preferred cuton ratio that is not unity – in fact, the strongest broadband noise is in spinning orders about half the maximum cut on value. This observation provides some qualitative assurance that the high levels are not simply an artifact of the lower axial group velocity of near-cutoff modes, and do in fact represent a preferred modal organization.

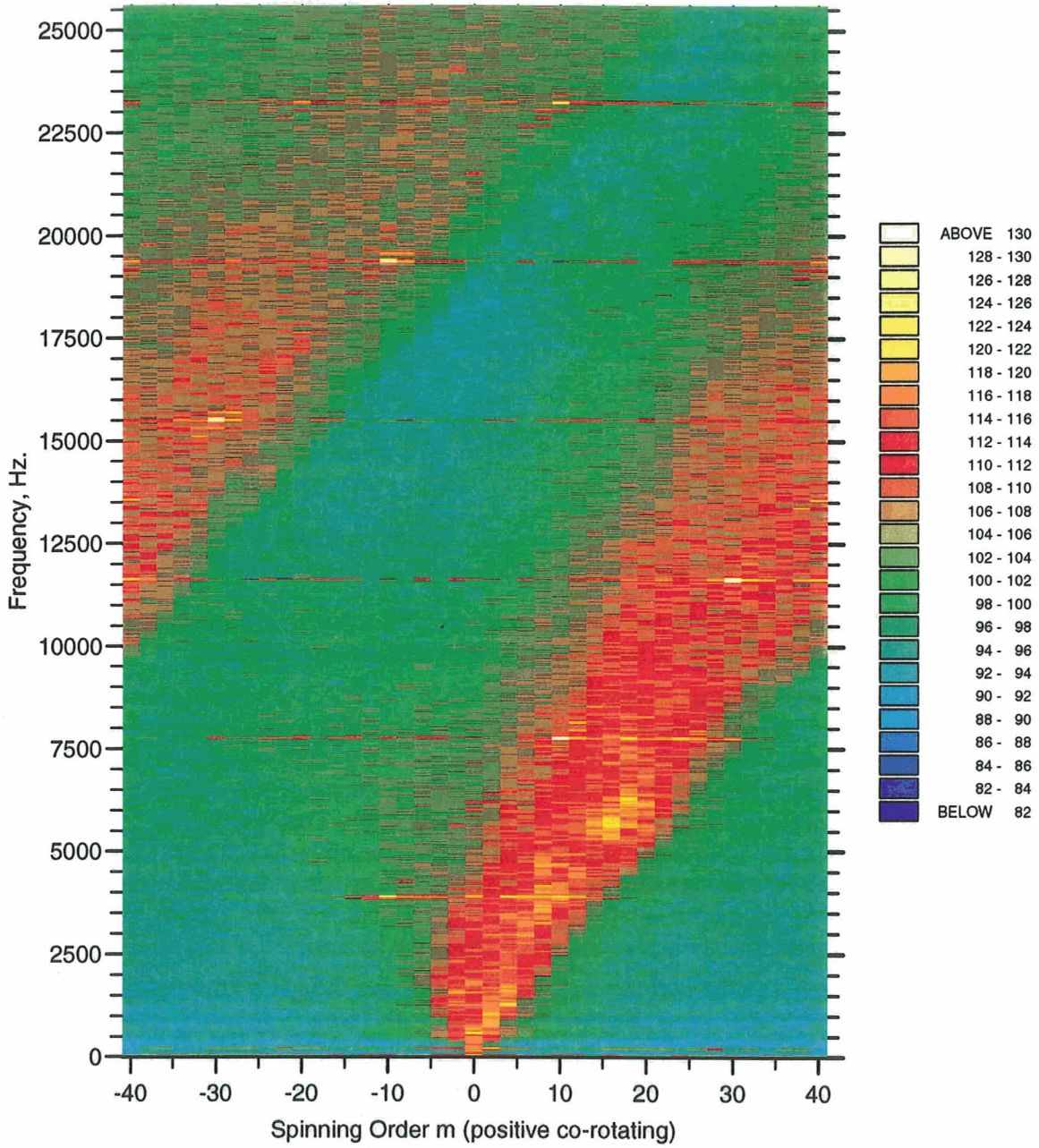

Fig. 117. Typical inlet modes, subsonic tip speed.

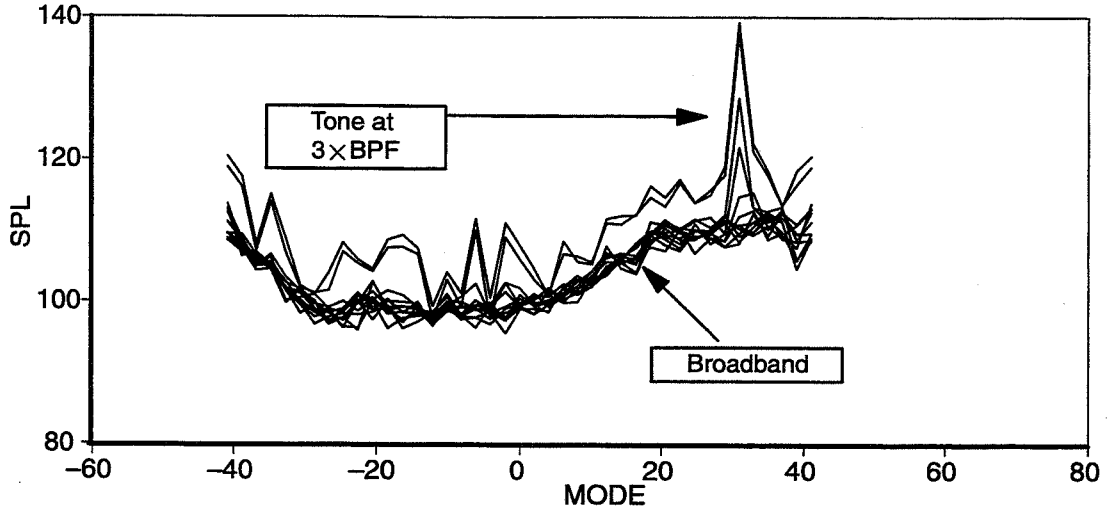

Fig. 118. Modal spectrum at several frequencies near 3BPF (11600Hz)

The above mode plots were for a configuration with 30 stators, and as will be shown were probably dominated by stator-generated noise. A much simpler case is shown in Fig. 120, where there are no stators and the boundary layer has been removed by suction. Here the concentration of power in co-rotating modes close to cutoff is evident, with very low levels in the counter-rotating direction. This is contrasted with the results in Fig. 121 which is the same condition except that the boundary layer is present. Here it can be seen that the boundary-layer related noise (the excess over that in Fig. 120) appears to be more widely distributed across all propagating modes.

A typical result in the aft duct is shown in Fig. 122. This is for 30 stators again, though the direct rotor-stator tone modes are not seen except possibly at BPF. The rotor interactions with stator second harmonic (especially spinning orders –20 at 2BPF and +20 at 4BPF) are more visible. Very clear however is the rotor-locked field. Since it is acoustically cut off, this is presumably due to the rotor wakes impinging on the microphone array. Note the asymmetric mode cutoff boundaries due to swirl in this section of the duct, between the fan and the stators. Note also that fairly high levels are seen in modes that are cut off. These are presumably due to the highly turbulent flow field near the wall. This is borne out by Fig. 123, which is the same condition except for an increased tip clearance and thus wall turbulence intensity. An increase in non-acoustic level is seen, particularly at the lower frequencies. Although as yet untried, it is speculated that an improvement in signal-to-noise can be effected by using the non-propagating mode levels to estimate this wall pressure and subtracting it from all modes.

It should be noted that this data is still upstream of the stators. It would be desirable in any future tests of this nature to acquire data downstream of the stators also, which was not possible in the present test due to physical bulk of the microphones chosen. Of particular interest is the downstream-propagating stator noise, whose modal structure remains unmeasured.

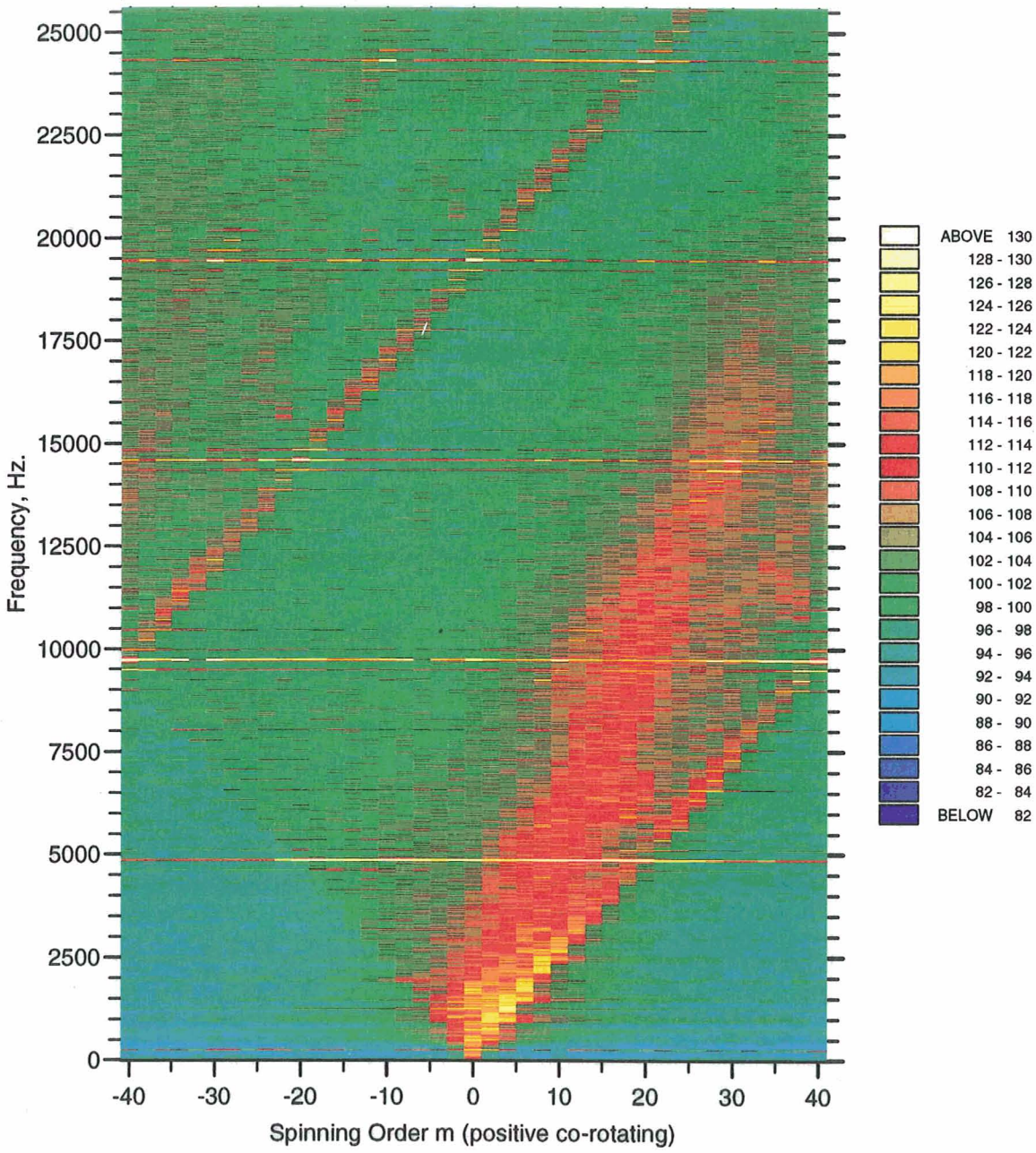

Fig. 119. Typical inlet modes, supersonic tip speed.

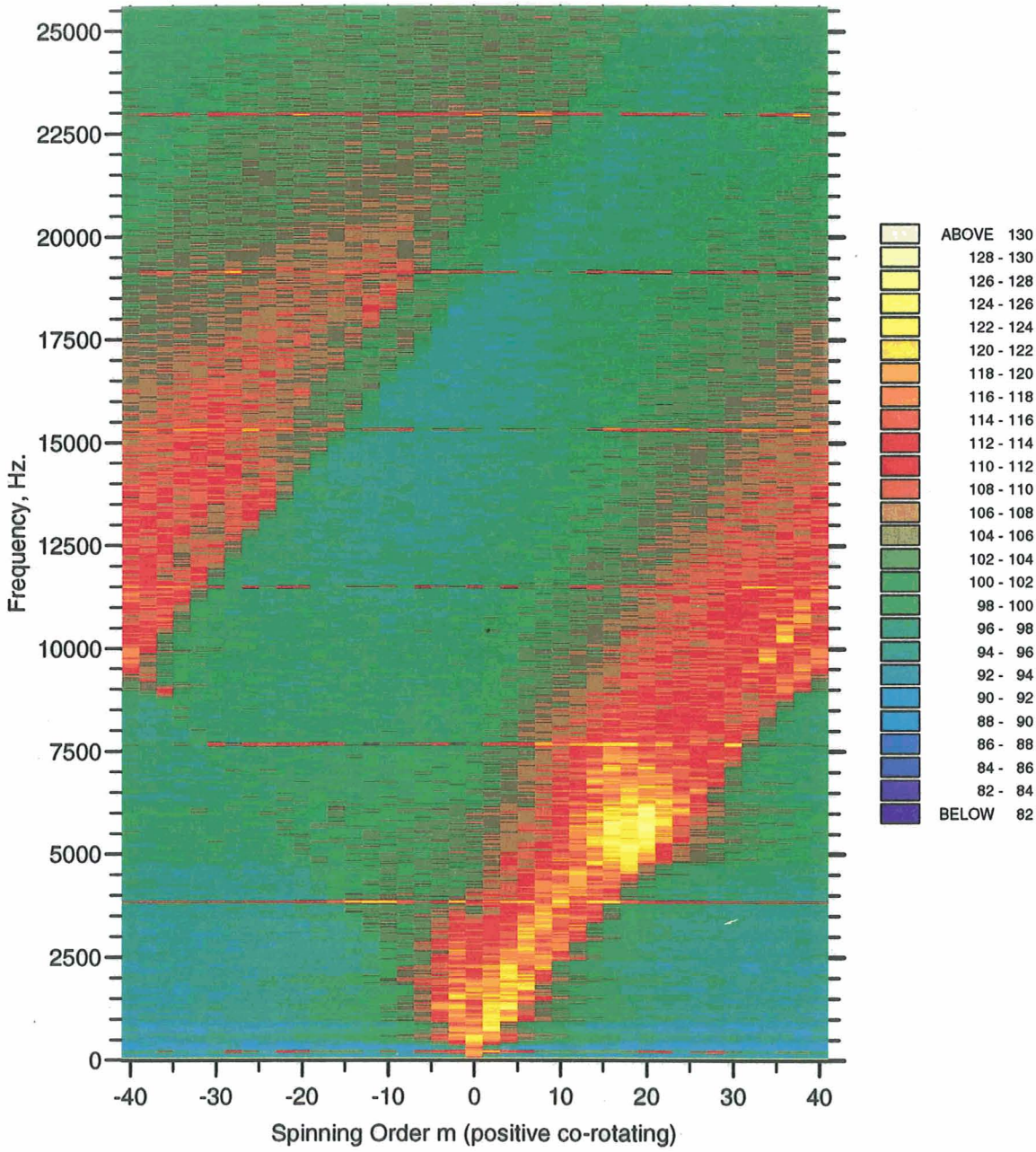

Fig. 120. Inlet modes, rotor alone, no boundary layer.

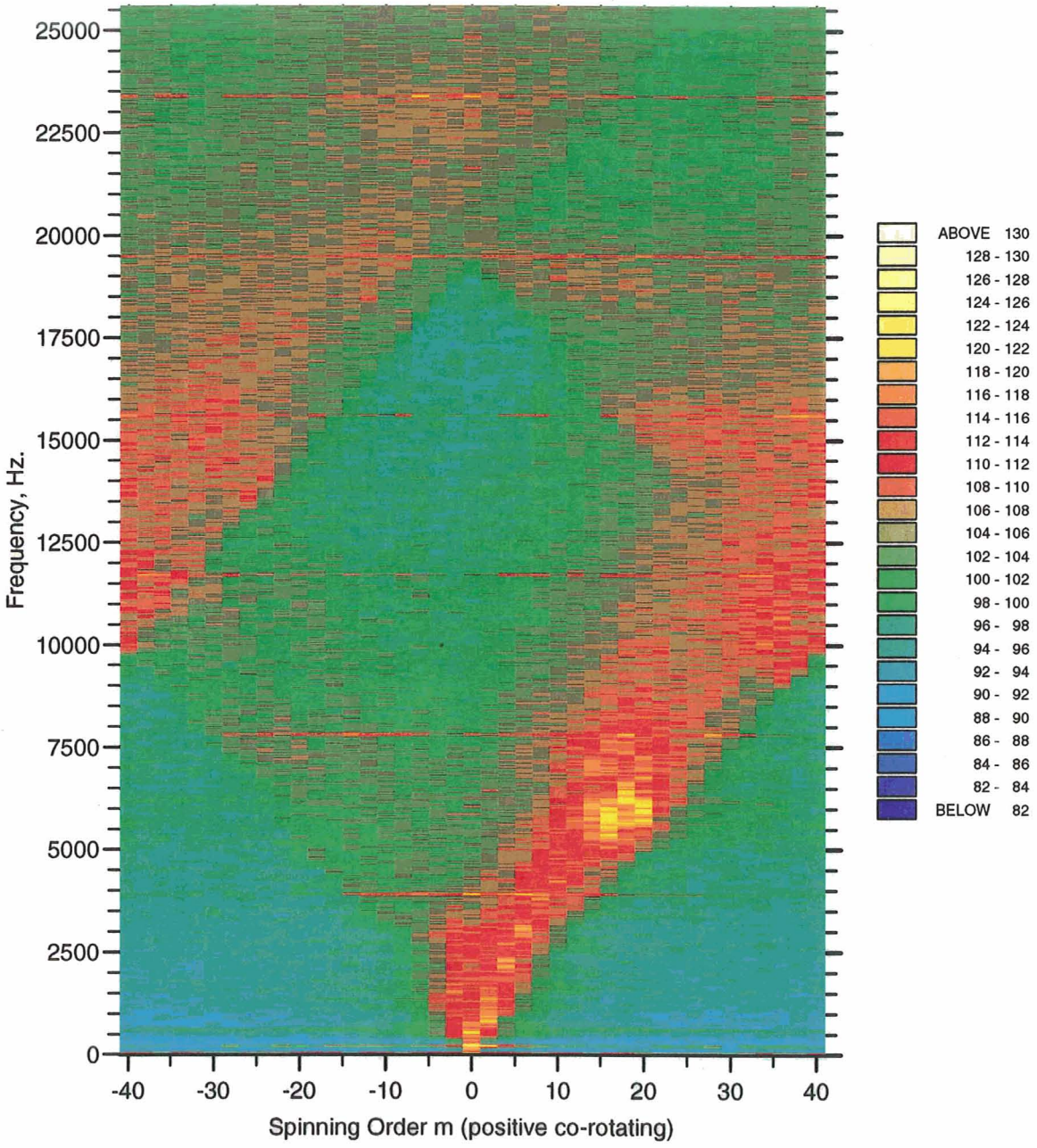

Fig. 121. Inlet modes, rotor alone with boundary layer.

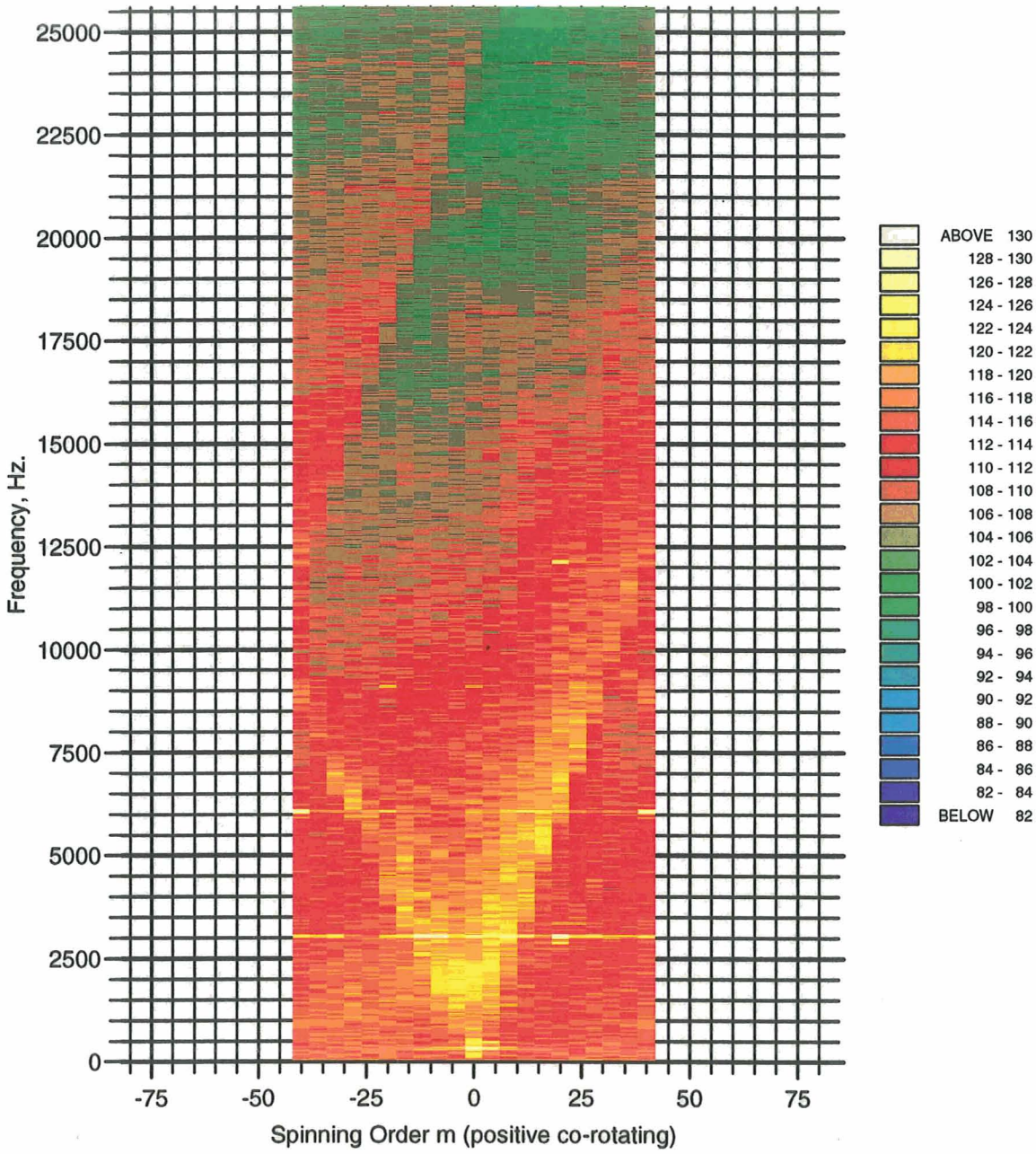

Fig. 122. Typical aft duct modes, subsonic tip speed.

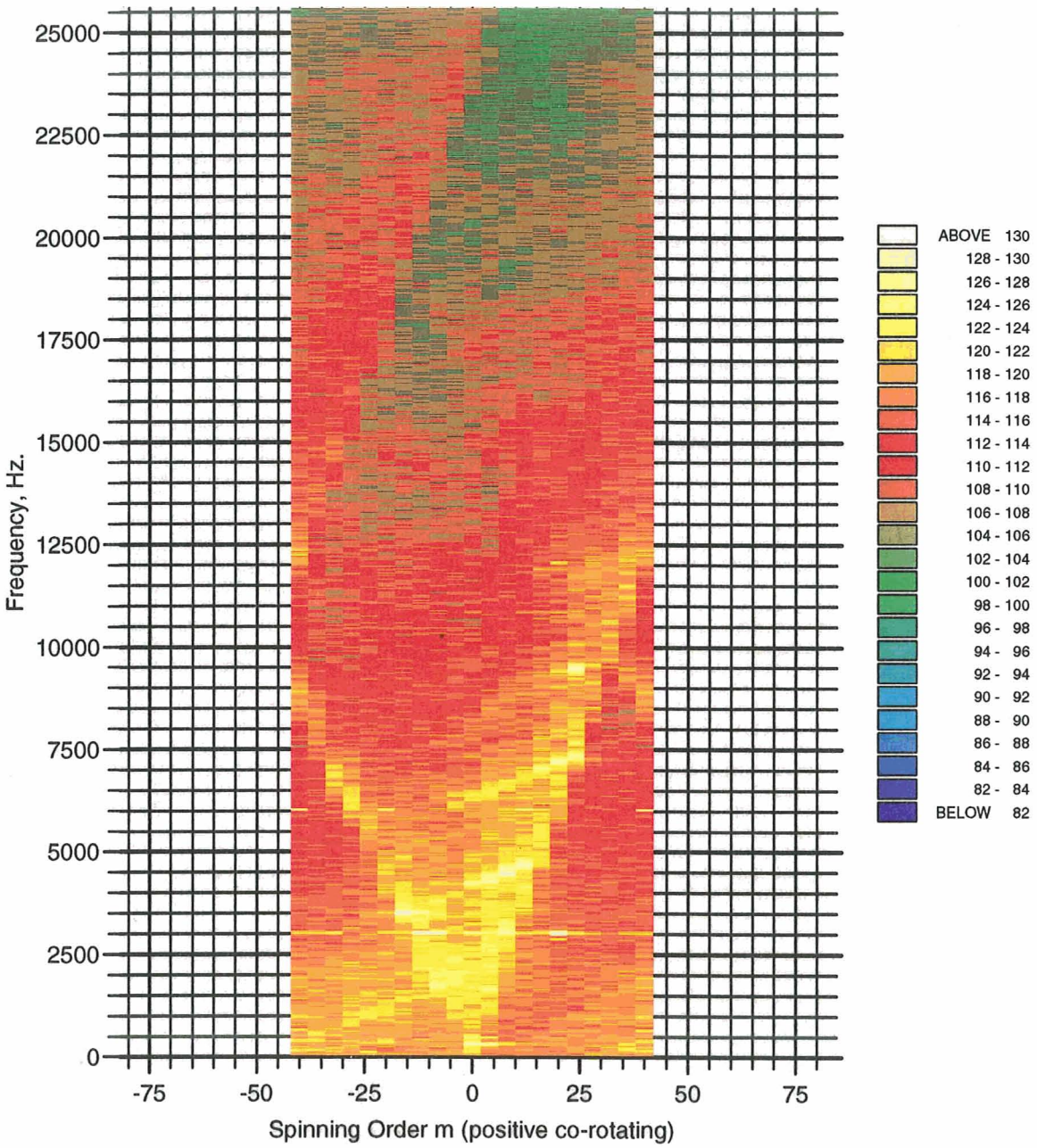

Fig. 123. Aft duct modes, large tip clearance.

4.6 Sub-component Noise Results

To further understand the results from this test, a sub-component analysis was undertaken. Prior to the test, a list was made of possible noise sources (Fig. 124). Initially it was anticipated that the rotor interaction with the turbulent boundary layer would be the predominant noise source mechanism. As the study has so far indicated, however, only the stator trailing edge noise is insignificant, and there is yet another source which can become dominant under certain conditions.

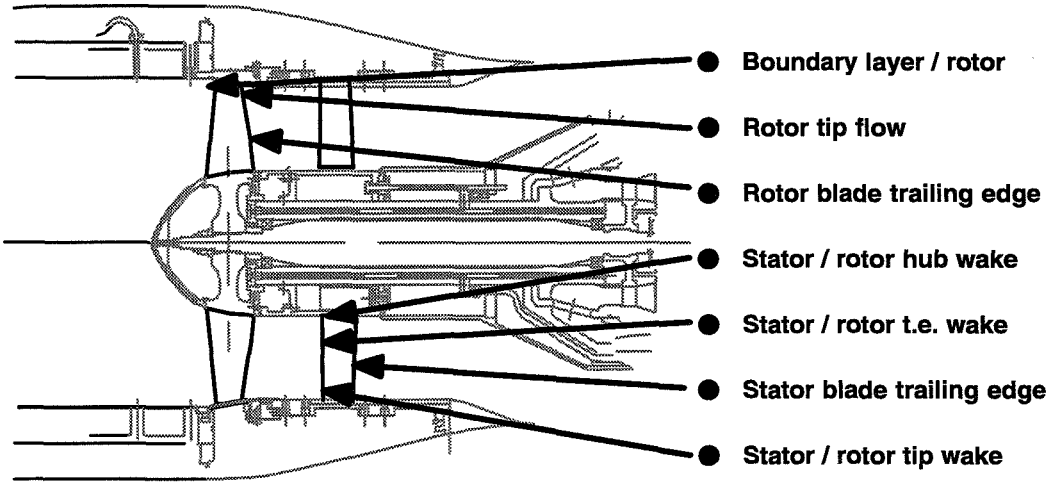

Fig. 124. Pre–test list of potential noise mechanisms

The three major components are rotor noise, boundary-layer noise, and stator noise. These sub-components are extracted by the process illustrated in Fig. 125. To get an idea of their relative levels, the radiated sound power level spectra of each are shown in Fig. 126. These spectra are averaged over variations in tip clearance and fan loading, and are presented here at low speeds, 70% rpm for inlet-radiated and 55% for aft-radiated noise. Results of the same analysis done on in-duct wall average sound pressure level is shown in Fig. 127. (These power settings were chosen to facilitate this comparison, as in–duct data is not available for inlet and aft ducts at the same fan speed.) Note that the "aft" stator noise in the in-duct case is actually measured upstream of the stators and downstream of the rotor in the duct, and hence cannot be easily compared to the aft-radiated spectrum.

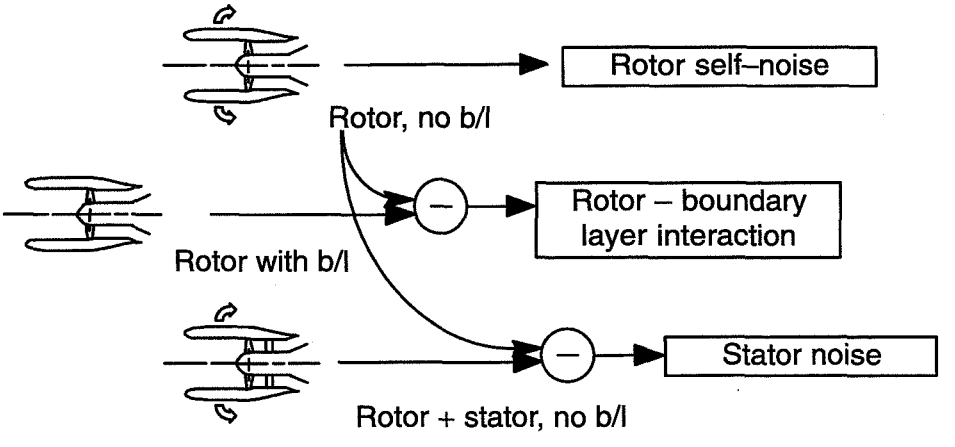

Fig. 125. Sub–component spectral extraction process

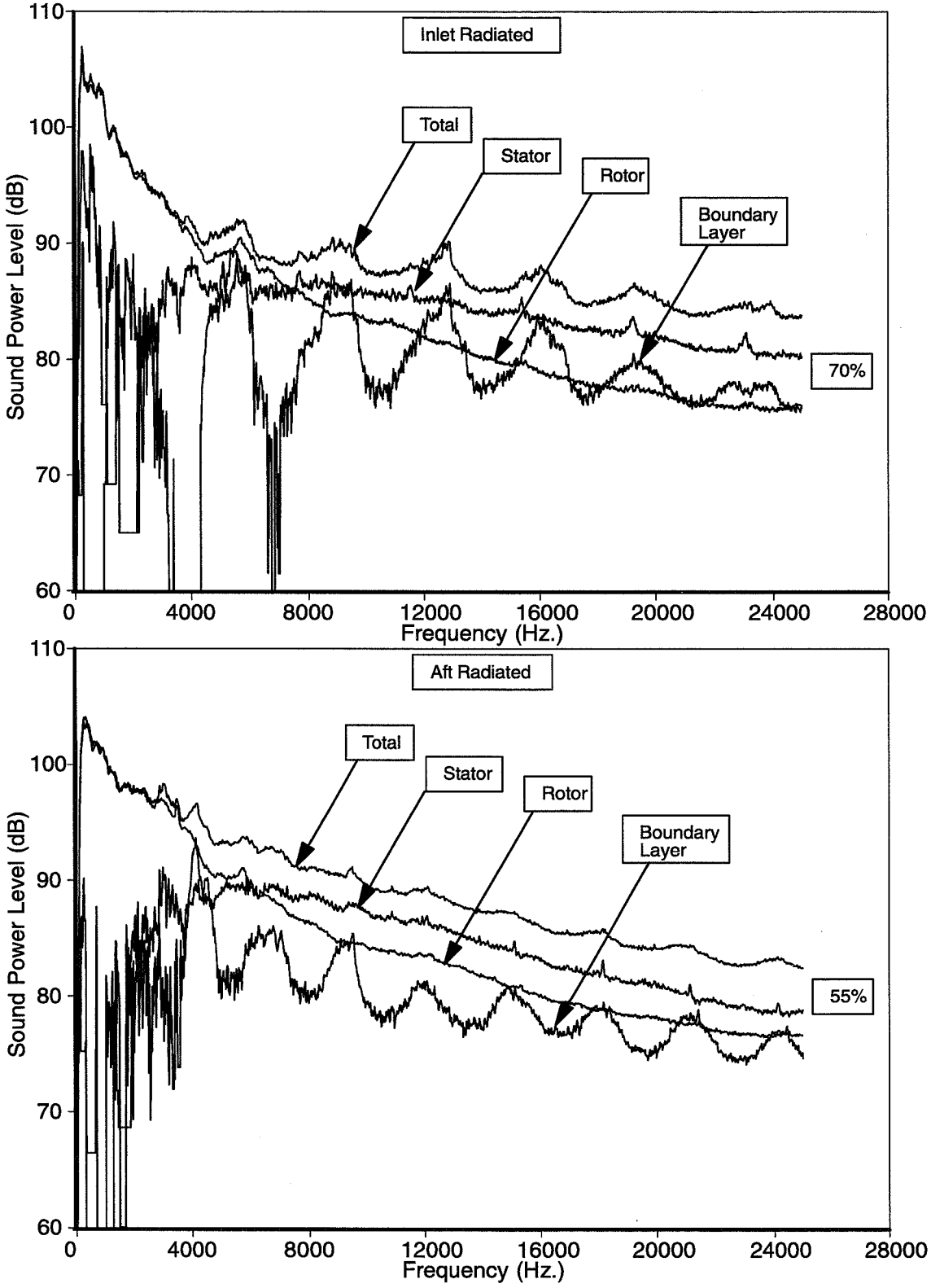

Fig. 126. Sub–component spectra, radiated power, averaged over loading and tip clearance

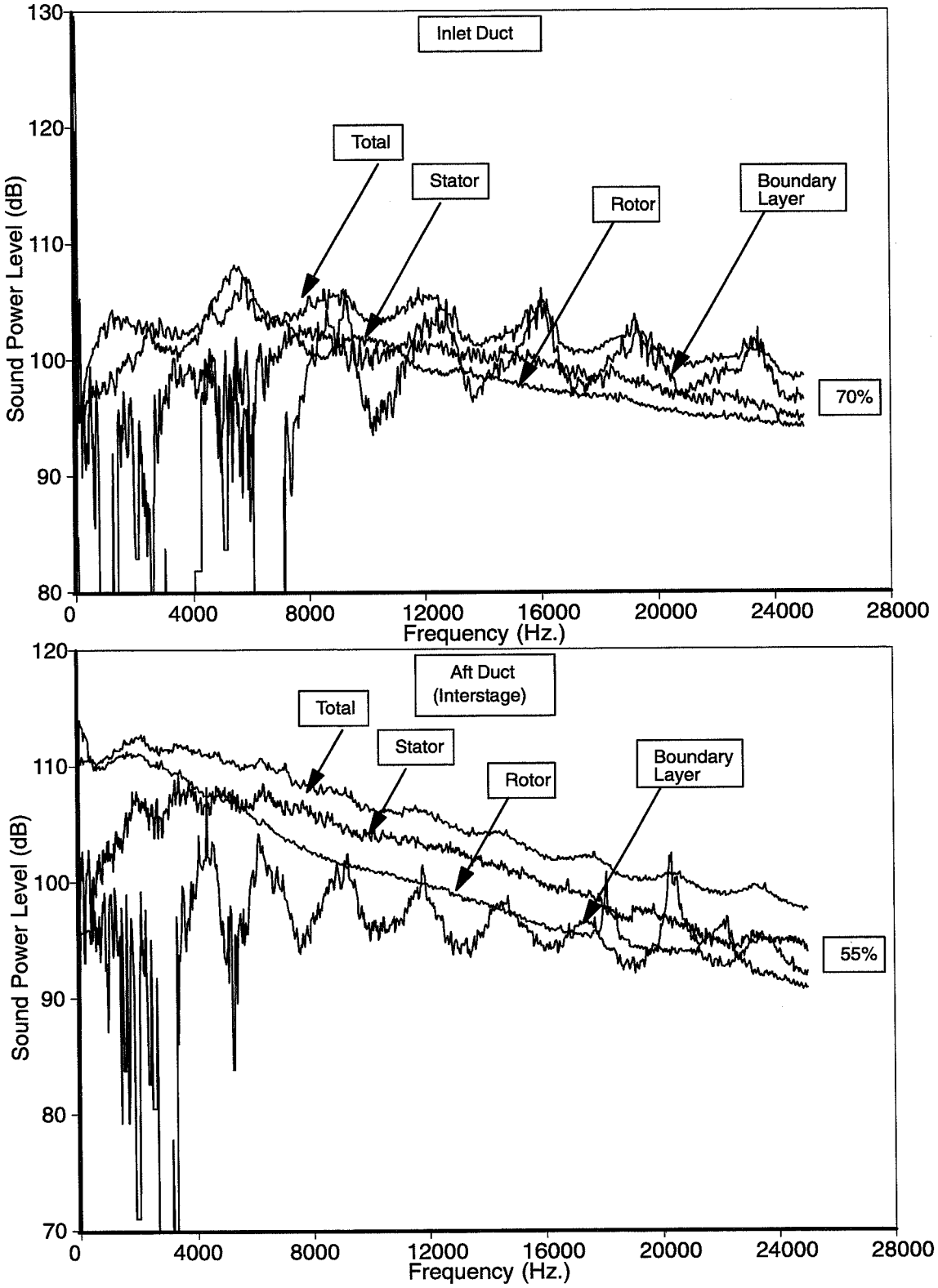

Fig. 127. Sub–component spectra, in–duct SPL, averaged over loading and tip clearance

Rotor self–noise

The rotor self-noise is the noise measured in the rotor-alone configuration with no boundary layer. It is the only component not derived by subtracting two measurements; consequently it includes any other (non–fan) noise sources as possible confounding influences. In the far-field data shown in Fig. 128 the rig noise floor (probably due to exhaust flow impinging on the support structure) is clearly dominant at low frequencies – note how the spectra for different tip clearances merge, leaving only a dependance on loading and consequently exhaust velocity.

Fig. 129 shows the same results for data taken inside the duct. These spectra show no such merging, suggesting that the exhaust noise is not dominant inside the duct, in either the inlet or the aft duct. However, even in this case it is seen that the self-noise peaks at substantially lower frequencies than the other broadband noise components. This difference suggests that there may be another noise source. It remains unclear what this source might be, or even whether it exists (see below for a speculation however).

The OASPL dependance on fan speed is illustrated in Fig. 130. Here the OASPL is calculated above 5kHz, where the low-frequency noise floor is presumably not significant. A quick calculation shows that the level follows approximately a sixth-power law in velocity, suggesting that this noise mechanism is a dipole source. Note that the OASPL is more sensitive to loading than tip clearance. This suggests that tip noise if present is at least not dominant. However, a close study of the spectra (Fig. 128, Fig. 129) shows that at very high frequencies the effect of tip clearance does become large. This does not show up in the OASPL which is dominated by mid-frequency energy around 5–10 kHz, but may influence PNL especially for very large engines.

A modal distribution has already been shown in Fig. 120 for this source. The duct pressure is seen to be concentrated in modes within 20 spinning orders of the co-rotating cuton boundary.

It is speculated that there may be as many as three different source mechanisms here. Glegg has modelled the rotor trailing-edge noise (due to boundary layer turbulence shedding off the trailing edge) with fairly good results (Ref. 30). This mechanism might be expected to show some dependance on loading, but not on tip clearance. The tip flows may also be noise sources, in two ways. There is some turbulent boundary layer flowing from the pressure side of the blade to the suction side through the tip clearance region. This may be the source of any residual tip clearance sensitivity at high frequencies. It also appears (Ref. 31) that there is a tip vortex shedding off the tip leading edge which may strike the pressure side of the neighboring blade in the cascade near its trailing edge. Because the turbulence scale in the vortex may be larger than in the blade boundary layers, it is speculated that this is the source of low-frequency rotor self-noise. All of these possibilities are however unproven. Further study is needed to arrive at an understanding of this noise source sufficient to guide design decisions.

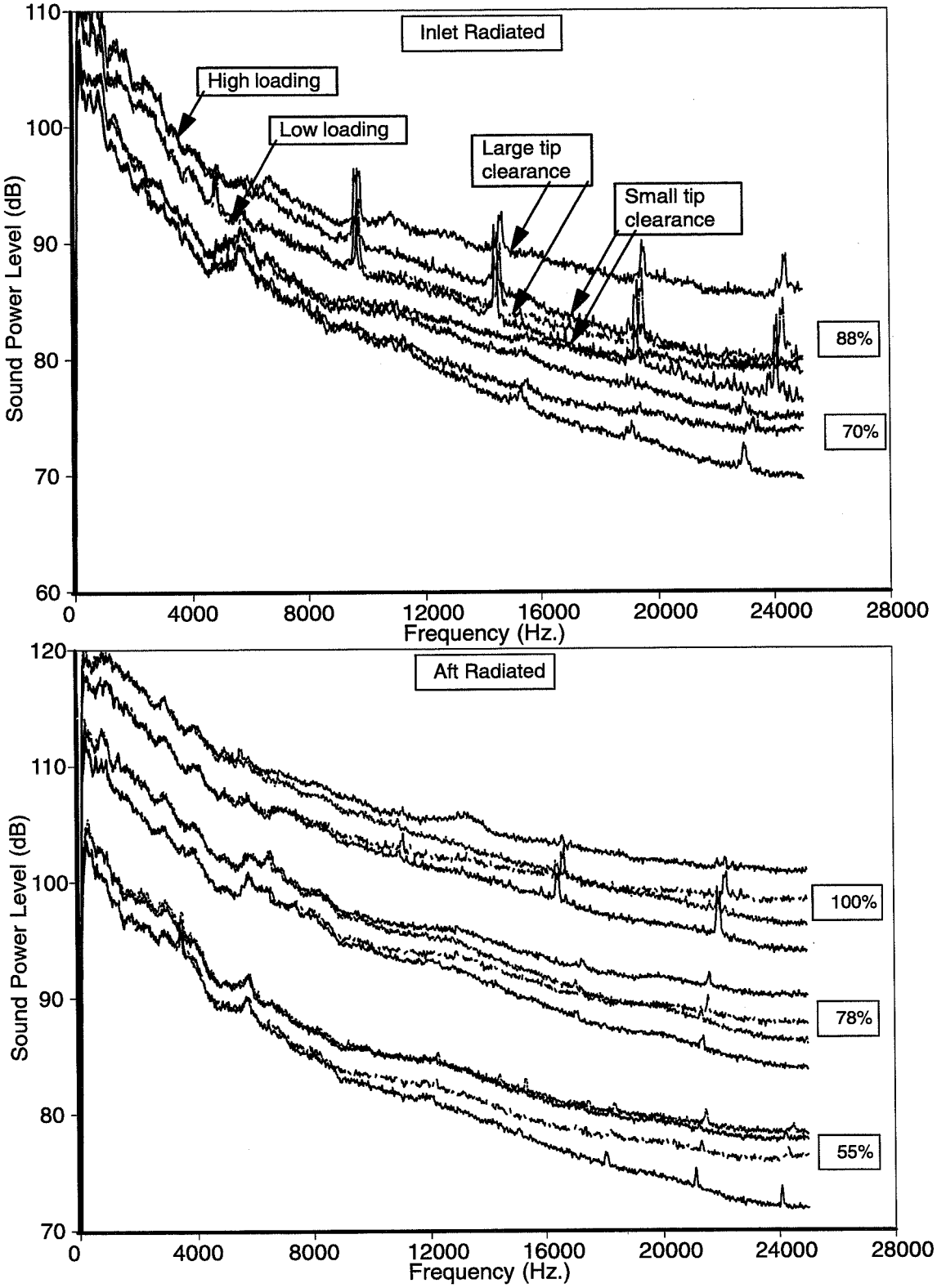

Fig. 128. Spectra of rotor–alone noise; far-field sound power

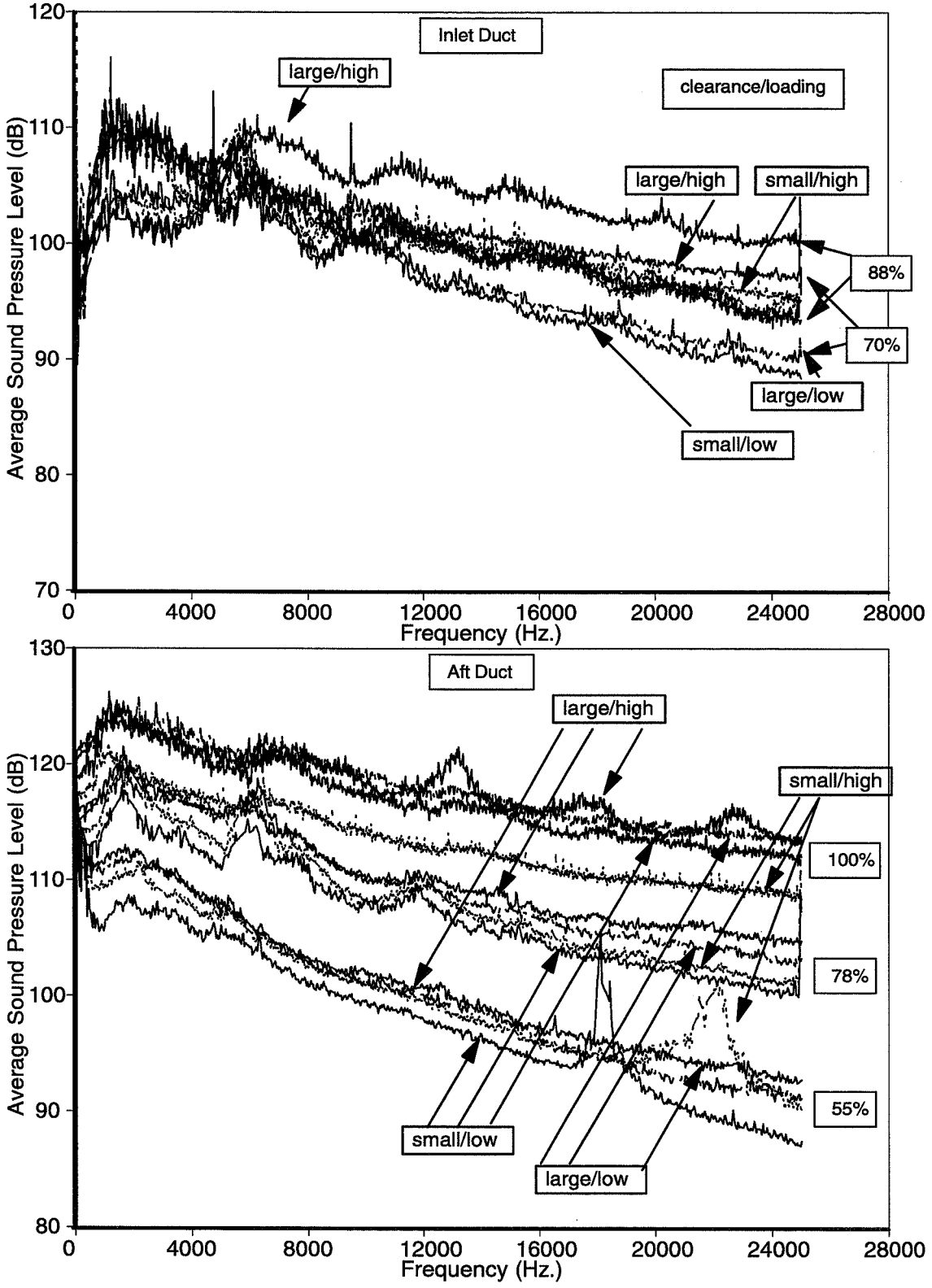

Fig. 129. Spectra of rotor–alone noise; duct wall average sound pressure

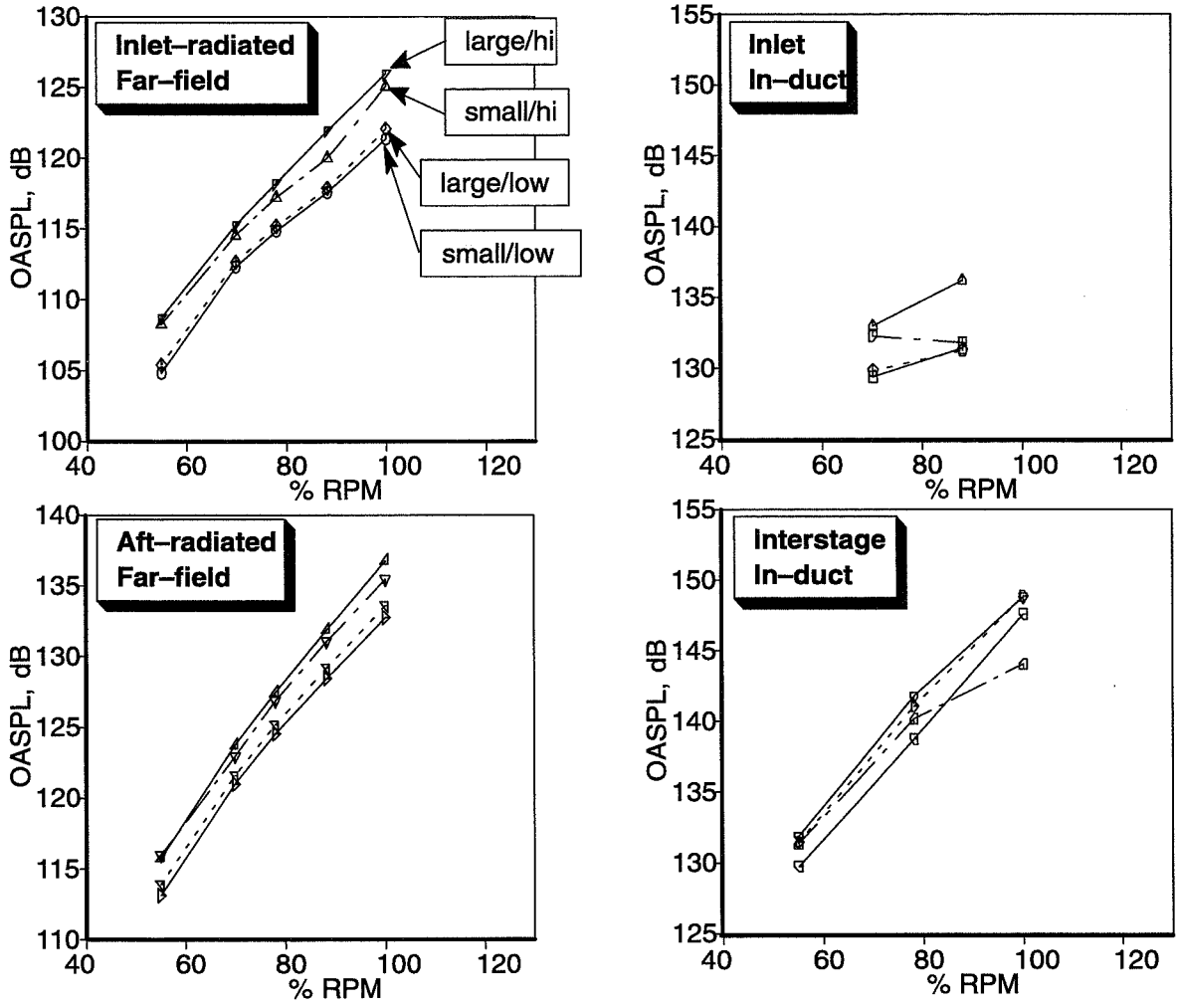

Fig. 130. Rotor–alone OASPL (5–25kHz) versus fan speed. The notations indicate tip clearance and fan loading variations.

Rotor interaction with inlet boundary layer

The boundary-layer interaction noise is estimated by subtracting the rotor-alone noise without boundary layer from that of the same condition with full boundary layer. Assuming that the boundary layer does not affect either the generation or the propagation of rotor self-noise, what is left must be due to the rotor interacting with the boundary-layer turbulence. It is certainly possible that this assumption is not true; for example if there is significant tip clearance flow whose character is influenced by boundary-layer thickness then there will be some error due to tip noise sources.

Typical spectra for far-field sound power spectra of this component are shown in Fig. 131, the corresponding in-duct average wall pressure spectra are in Fig. 132. The most striking feature of this source is the spectral humps. Except for the high loading/high tip-clearance case (a special case – see discussion below), these humps are centered at the blade passage frequency and its harmonics. They are not related to spectral broadening of the fan tones, as can be seen in Fig. 133 which shows a typical spectrum fragment before the tone was removed. This feature is equally clear in the in-duct

data. Presumably this is due to the axial length scale of the boundary-layer turbulence – a long length scale, such as occurs when atmospheric turbulence is ingested into an engine in static testing, would generate something more like a tone, while very short length scales must generate uncorrelated fluctuations with a wideband flat spectrum.

The OASPL sensitivity of this source with RPM is shown in Fig. 134. A rough estimate shows it to be closer to a fourth power of tip speed, and to never exceed the sixth power. It is expected from the available theories that this is a dipole source. Mani has explored the possibility that at high frequencies there is a dominant quadrupole noise due to the turbulence interacting with the rotor potential field. The measured low sensitivity to tip speed does not appear to support this argument however.

There is a strong sensitivity to tip clearance in this source at the two clearances tested, even (at least in the far field data) at low loading. The larger tip clearance is believed to be slightly larger (by geometric scaling) than is typical of modern large turbofan engines, but it exhibits a substantial reduction of this noise in the far-field spectra. This is not observed in the in-duct data; no explanation is offered for this difference at present. It may or may not be relevant that this clearance corresponds approximately to the boundary layer momentum thickness. The smaller clearance is believed to be (by geometric scaling) approximately typical of or smaller than the clearance in modern engines. Clearly more variety of tip clearances in the range of expected typical engine values should be tested to identify the sensitivity of this source.

The OASPL is virtually independent of fan loading, at least for the small tip-clearance case, as was also seen in the spectra above. This is consistent with the fluctuating-lift dipole theory, and is in contrast to the rotor-alone noise which exhibited a greater sensitivity to loading than tip clearance.

Comparing Fig. 120 and Fig. 121, rotor-alone mode plots without and with boundary layer, it is seen that the difference seems to be widely distributed over the propagating modes, which is a feature consistent with Glegg's predictions. It would be desirable to subtract the mode plots to look at this more closely but this has yet to be done.

Rotor interaction with rotating disturbance

Looking again at the spectra of Fig. 131 and Fig. 132, it is seen that the spectrum is different in the large tip-clearance, high loading case. The level is significantly higher, the humps are more ragged, and they are not centered on the blade passage harmonic series. The mode plot, Fig. 135, is even more striking. These humps are seen to be highly structured in the mode–frequency plane.

This pattern is consistent with the rotor interacting with a non-uniformity that is rotating in the same direction as the fan but at a slower speed. Based on Fig. 135, it is estimated that the nonuniformity is of high order, 30 to 60 lobes per revolution, and is rotating at something like 1/3 of the fan speed. This is not what is usually referred to as rotating stall, which would be expected to have only a few lobes and would severely affect the fan performance; there is nothing especially unusual about the fan performance under these conditions. This phenomenon has only been seen in the high loading, large tip-clearance condition with thick boundary layer.

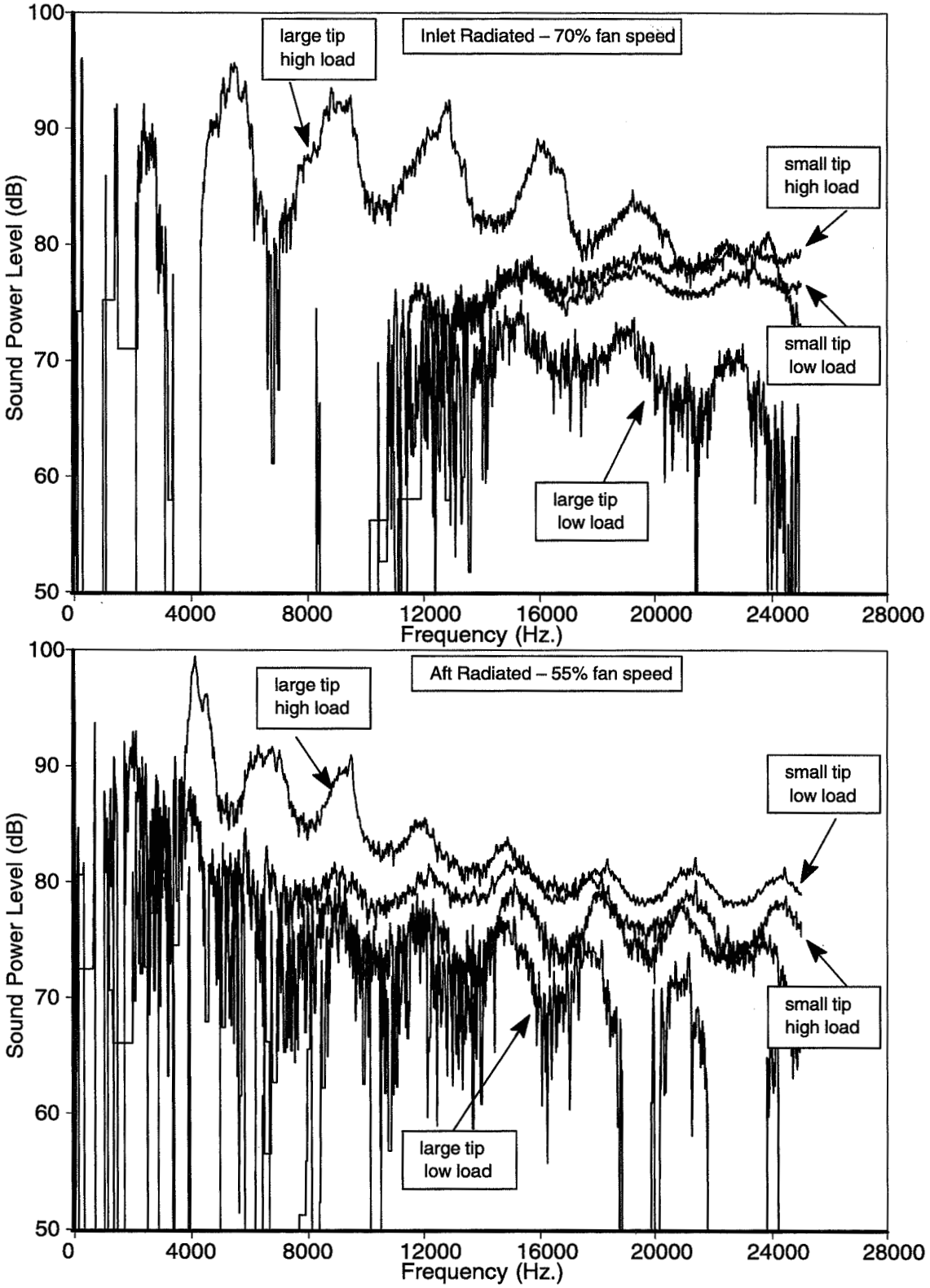

Fig. 131. Net boundary layer noise, far–field sound power spectra

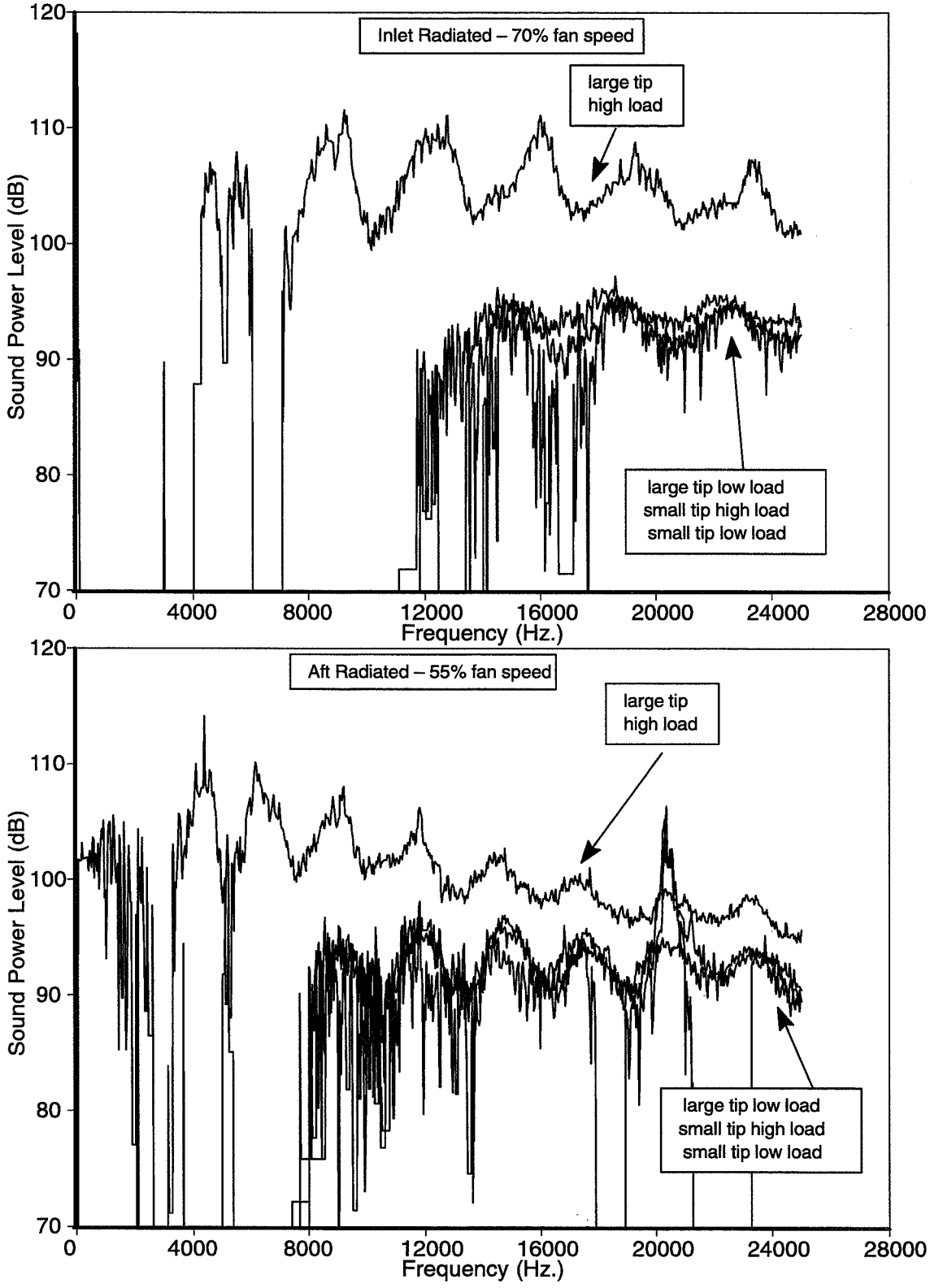

Fig. 132. Net boundary layer noise, in–duct average wall spectra

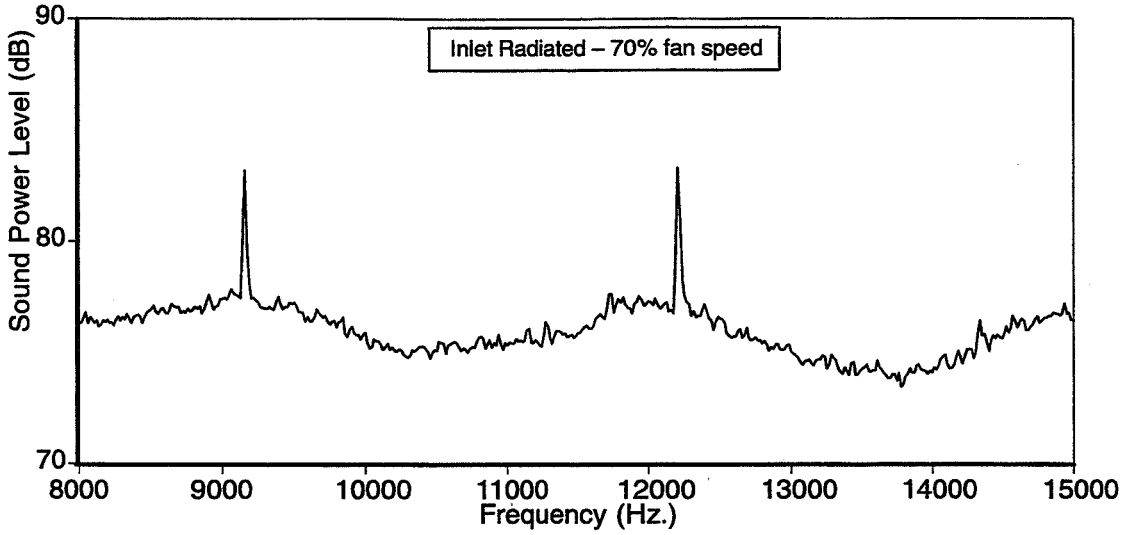

Fig. 133. Spectrum before tone removal, showing hump at 2BPF with second harmonic tone

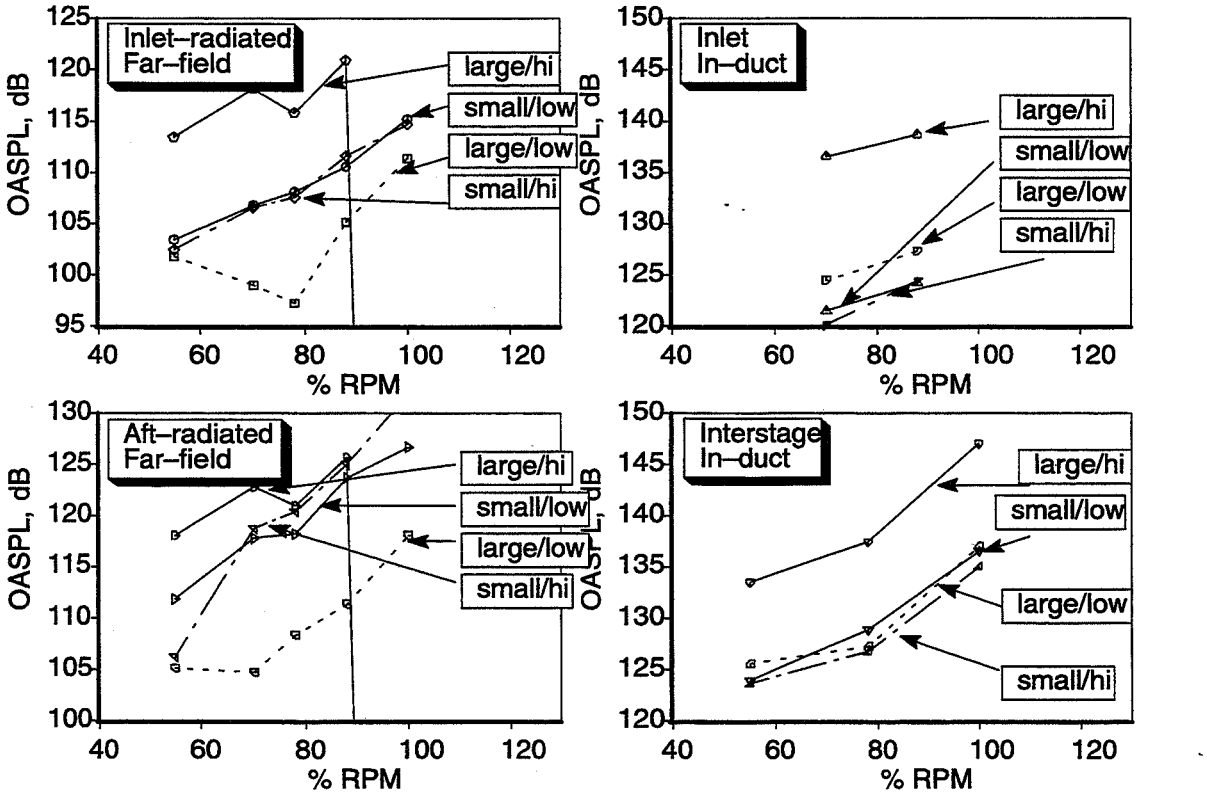

Fig. 134. Net boundary layer noise versus fan speed. The notations indicate tip clearance and fan loading.

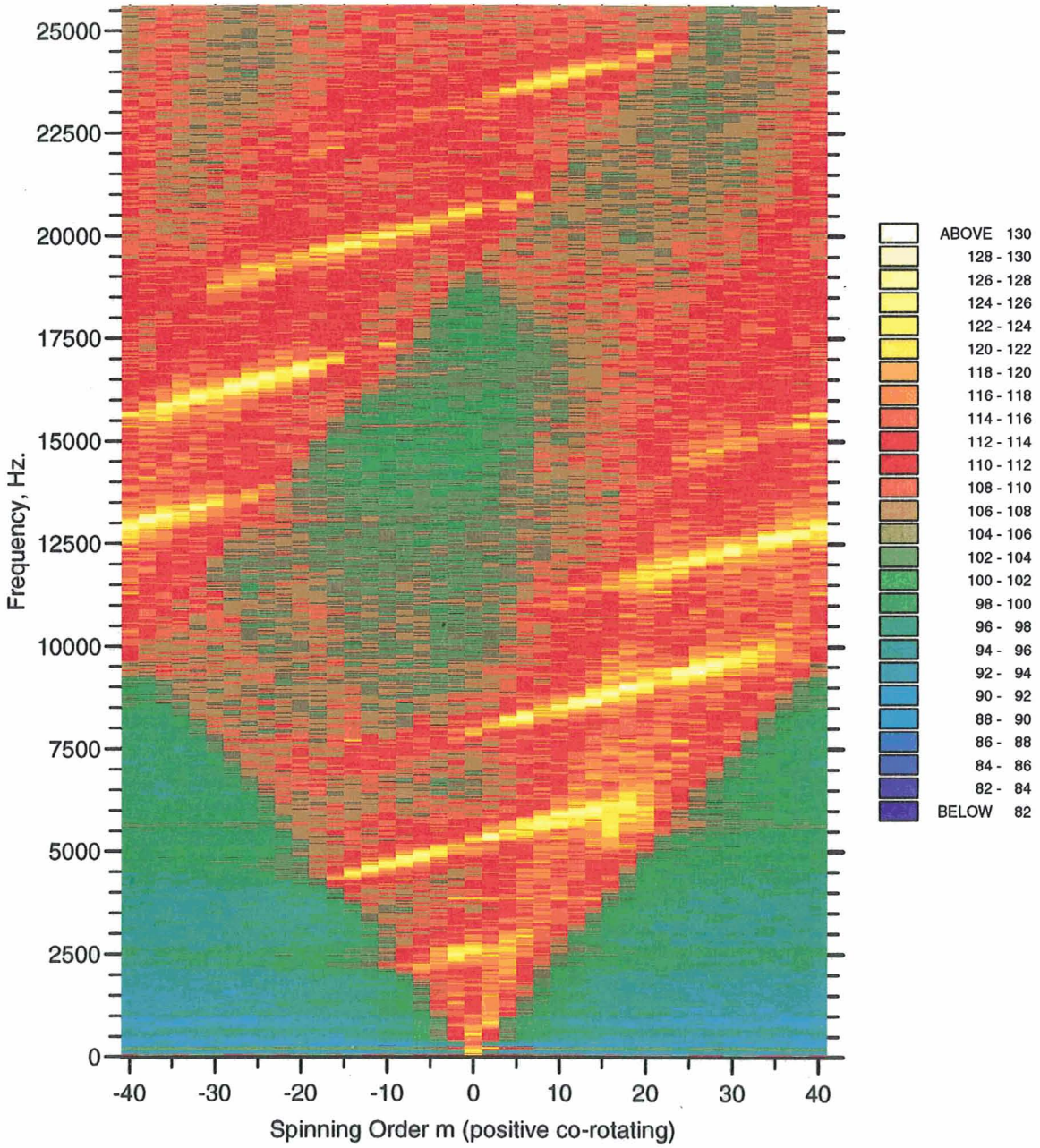

Fig. 135. Inlet modes, rotating non-uniformity souce.

Stator interaction with rotor wake turbulence

Net stator noise is estimated by subtracting total noise without stators from the noise for an identical fan condition with stators installed. Forward-radiated stator noise thus has been transmitted through the rotor which will have an unknown effect on the level and modal distribution. Unfortunately it was not practical to measure both inlet and aft-duct modes for the same condition, so there is no measured assessment of the effect of transmission through the rotor. Similarly, the aft–radiated calculation is only valid under the assumption that the aft-radiated rotor noise is not significantly affected by transmission through the stator row, or the change in swirl in the duct downstream of the stators. Note also that the aft in-duct measurements were made between the rotor and stator rows, so no mode measurements were made of the aft-radiating stator noise. Nevertheless, the resulting estimates show some clear and consistent trends and are thought to be valuable.

Both the far-field and in-duct spectra show a broad, smooth spectrum with a single peak in the general vicinity of 1 or 2 times blade passage frequency. The levels are only slightly sensitive to tip clearance and loading – see Fig. 136 for a typical example. All four combinations are shown and the maximum variation is about 3dB. This small sensitivity has not yet been examined in any detail.

Looking at spectra averaged over loading and tip-clearance variations (Fig. 137) the effect of stator count can be seen at several fan speeds. At least for high frequencies and at moderate fan speeds, the noise power increases nearly linearly with number of stators. This appears to be the case even at low frequencies when comparing 15- and 30-stator results. However with decreasing frequency the spectra for 60 stators fall off sooner and more rapidly than the 15- and 30-stator spectra. It is speculated that this is due to the greater solidity (twice the design value used with 30 and 15 stators) of the stator set. Certainly more data on a wider variety of stator configurations is needed to clarify how stator count and solidity interact to affect stator noise. Some unanswered questions include: Does the solidity effect increase at even higher solidities? How is the peak frequency related to chord and spacing? Are these effects predicted by the fluctuating-lift models under development by other researchers?

The OASPL trends with RPM are shown separately for low frequencies (Fig. 138) and high frequencies (Fig. 139) because of the different behavior described above. It is seen that the aft-radiated noise power increases with fan speed, at a rate approximating the sixth power. The in-duct results between the fan and stators (labeled "interstage") suggest that the forward-radiated noise also follows this rule; however the inlet data, both radiated and in-duct, follow a flatter and less smooth trend. It is speculated that this is a result of rotor blade row transmission effects, especially the presence of shocks at supersonic tip speeds.

Modal data for stator noise are shown in Fig. 140, a configuration chosen to be dominated by stator noise. Fig. 141 shows the same configuration without the stators, to confirm this. These results again show a predominance of co-rotating modes. This is consistent with a blade-normal dipole in the forward-radiating direction, and would be expected to also pass through the rotor more easily. Qualitatively there appears to be little difference between the modal distributions before and after the rotor, although the lack of comparisons at the same RPM clouds the issue. Unfortunately there is no data available on mode distributions downstream of the stators; if the blade radiation is like the cardioid (as speculated for rotor trailing-edge noise) then the downstream mode distribution might show a counter-rotating preference.

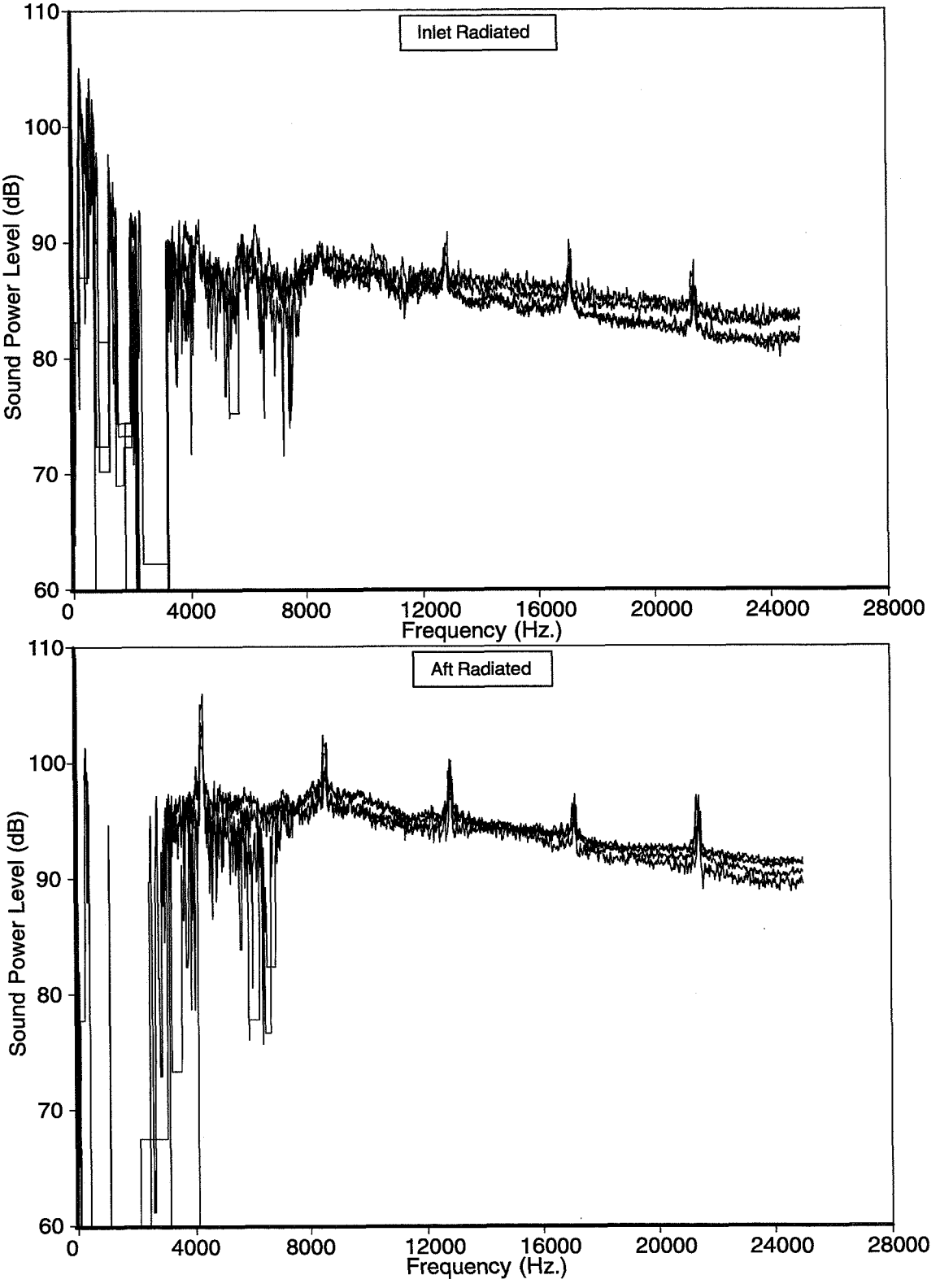

Fig. 136. Net stator noise; 78% rpm, 30 stators, 4 combinations of tip clearance and loading

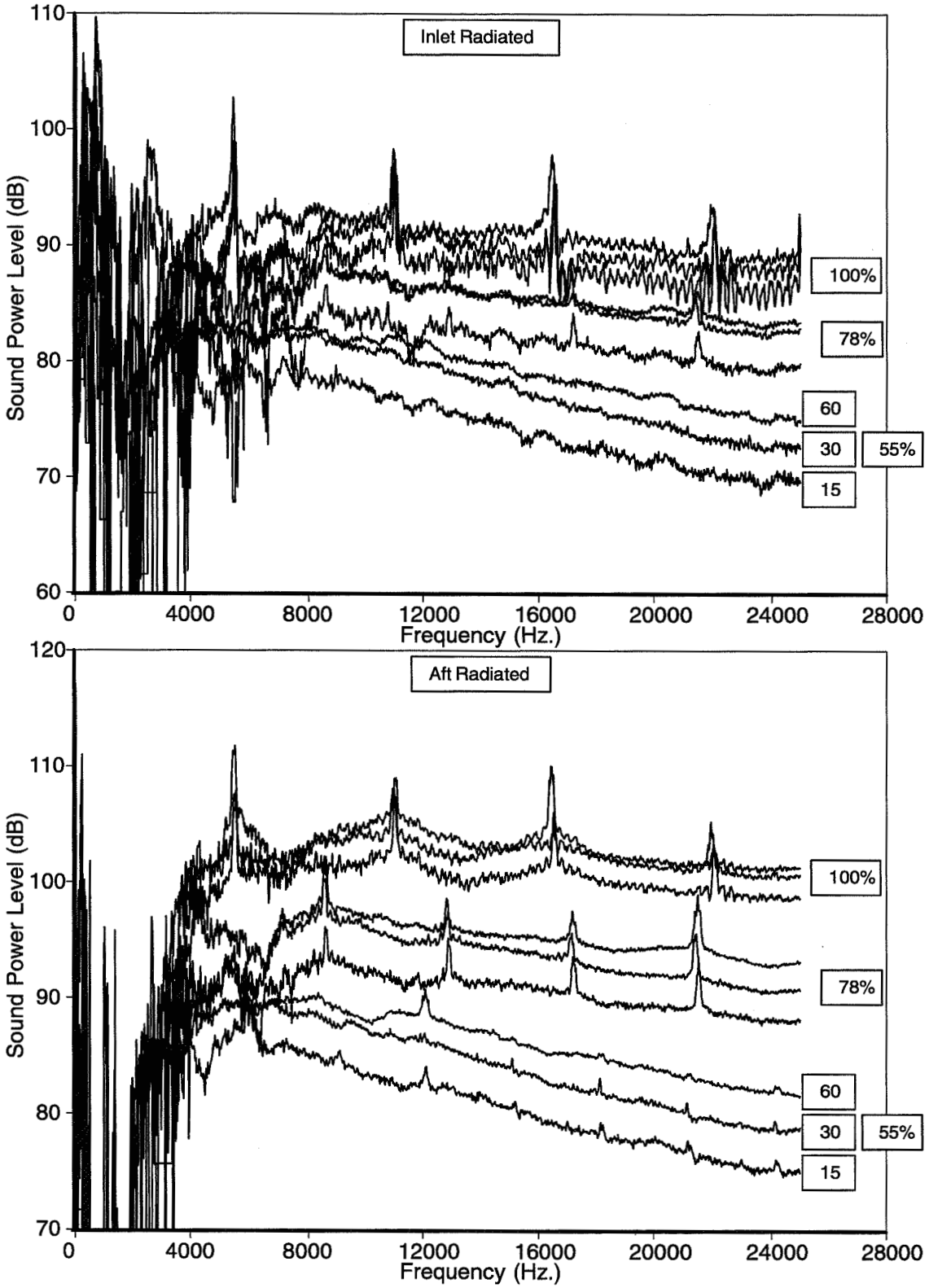

Fig. 137. Net stator noise at several fan speeds, showing 15, 30, and 60 stator levels

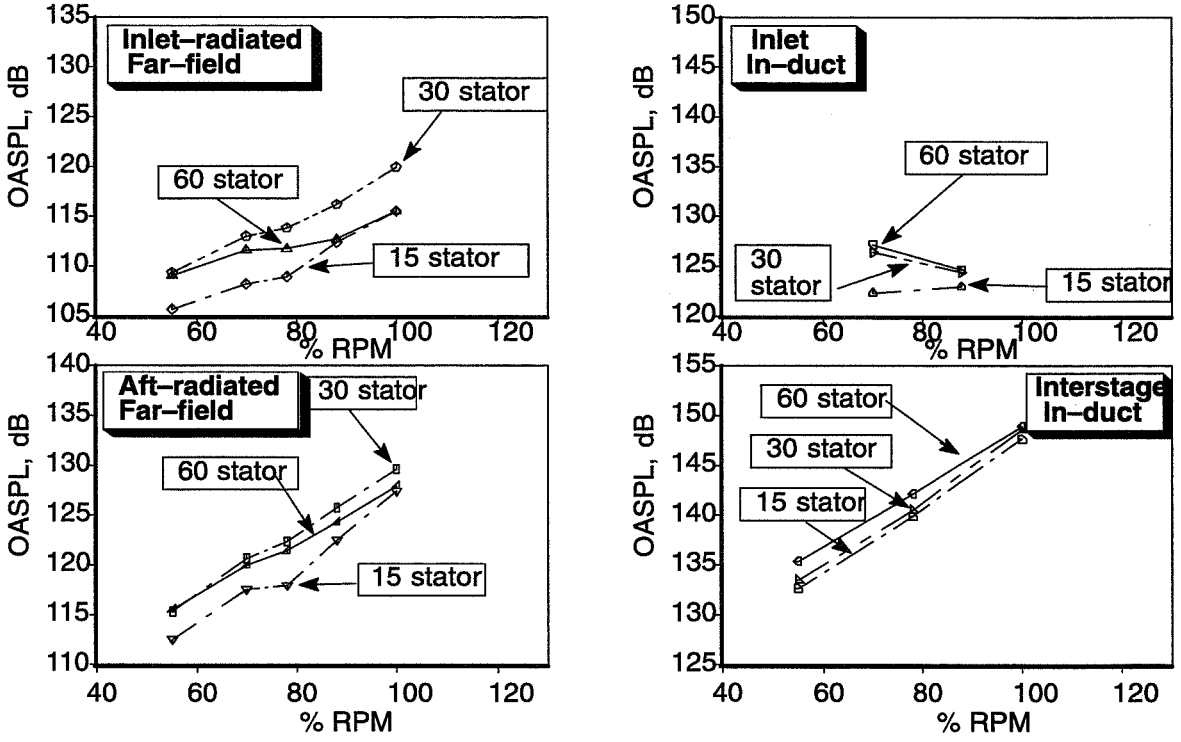

Fig. 138. Net stator noise, OASPL as a function of fan speed, 2k–10kHz

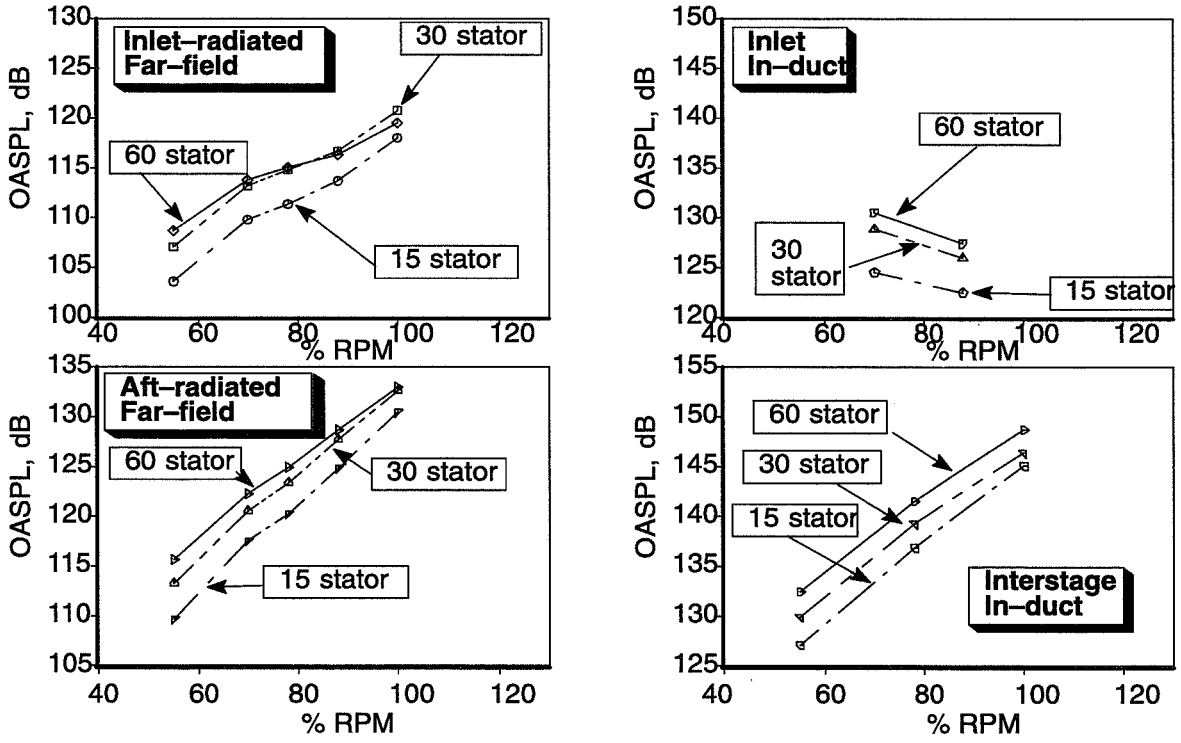

Fig. 139. Net stator noise, OASPL as a function of fan speed, 10k–25kHz

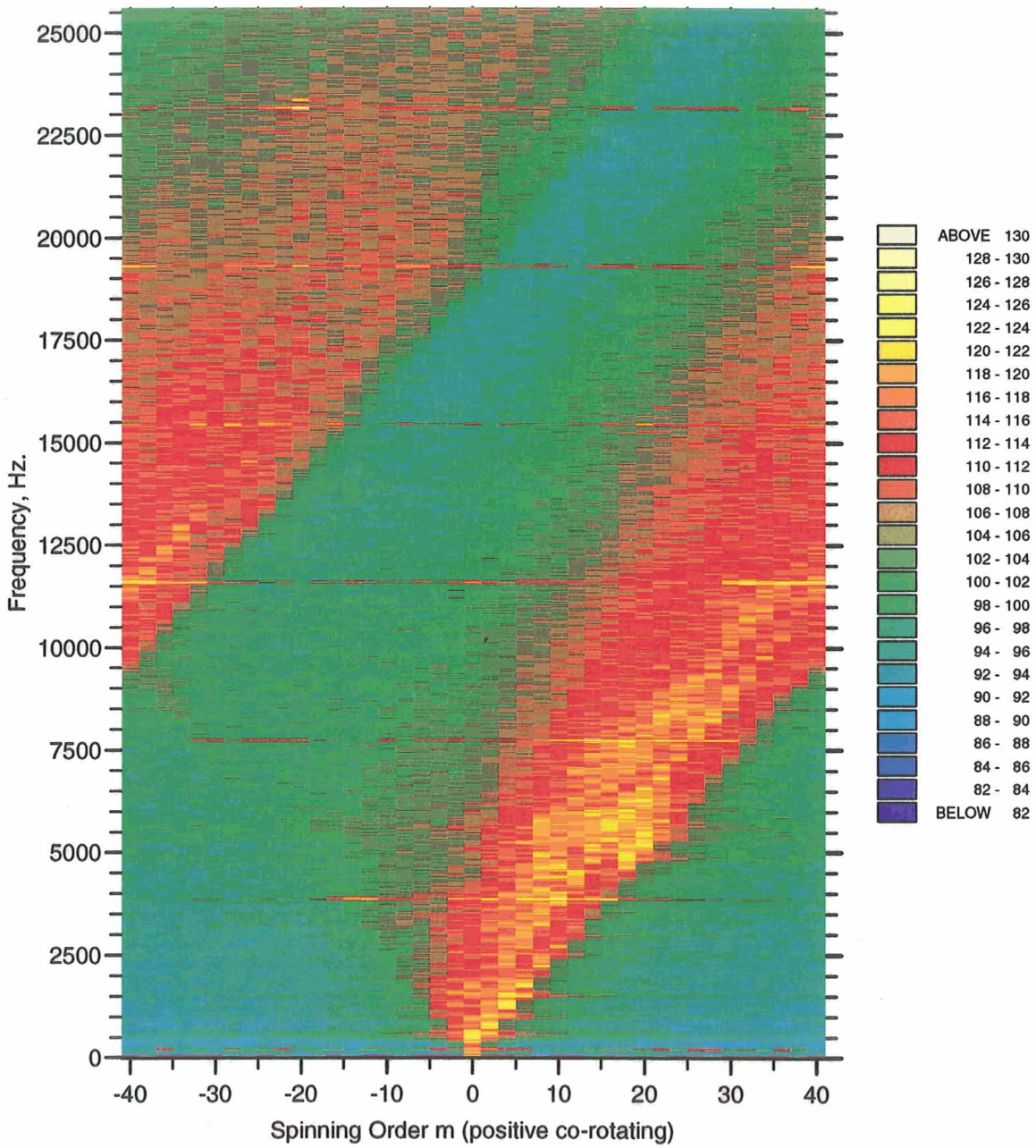

Fig. 140. Inlet modes, maximum stator noise.

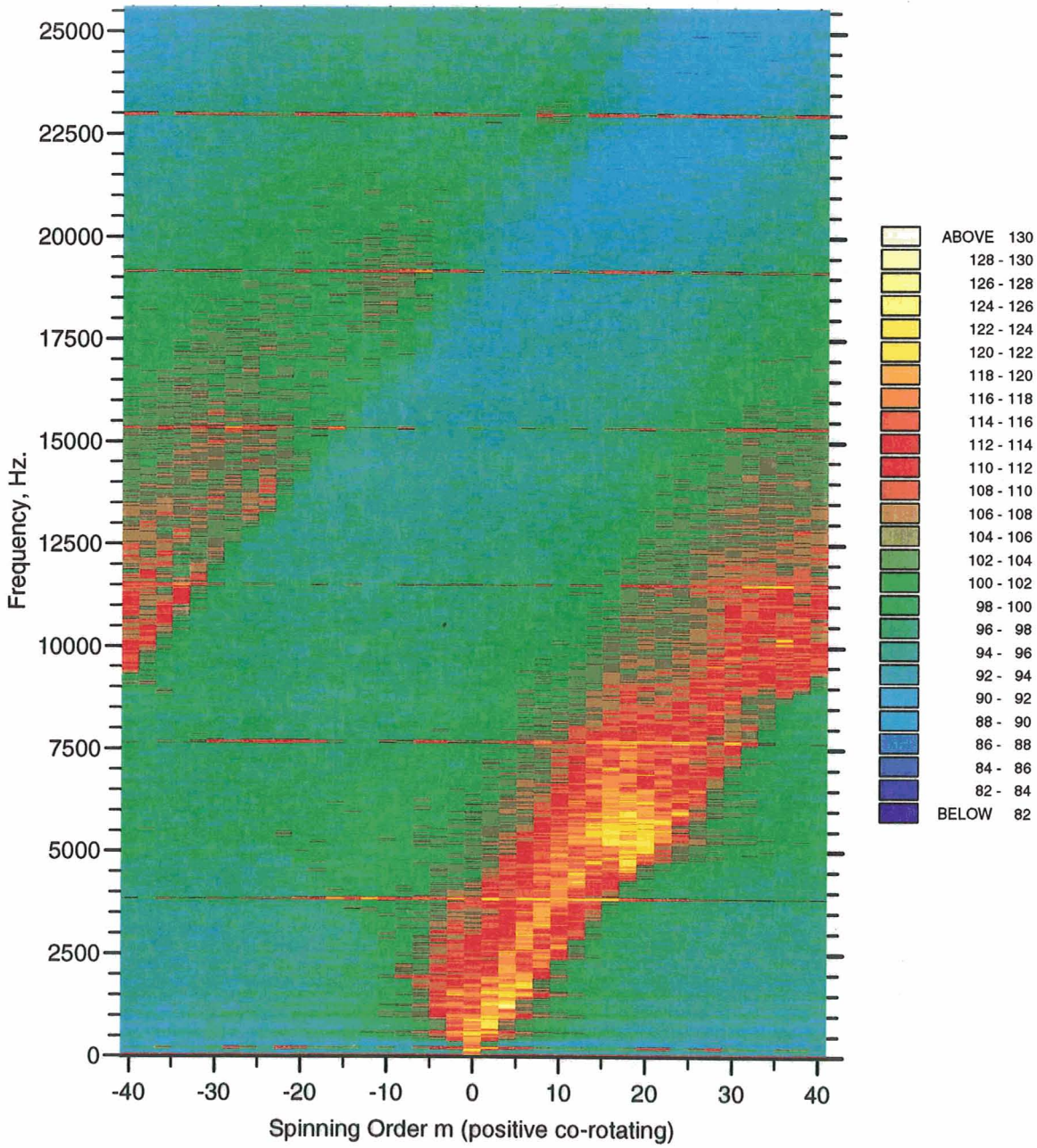

Fig. 141. Inlet modes, no stators, otherwise same as Fig. H.

4.7 Rubstrip Unsteady Pressure Measurements

The analysis of the rubstrip surface pressure data has been limited to a minimum. First, the data set was never considered to be one of the key sets of test information and second, the quality of the data was limited by the transducers used. An attempt has been made to correct for the limited frequency response of the transducers. Unfortunately things are further complicated by the very high unsteady pressure levels especially near the leading edge of the fan rotor at high corrected fan speeds. It is fair to assume that the dynamic response effects due to the cavity behind the protective screen depend on the unsteady pressure levels and the corrective terms were derived only for very low level. In general it can be said that the results look quite plausible at subsonic fan tip speeds (low pressure levels) but become less coherent at transonic and supersonic tip speeds.

The data has been normalized in the following fashion:

- The pressures are normalized with standard-day ambient pressure at sea level
- Axial and circumferential position are normalized with the axial fan tip chord.
- The presented data only include the ac component of the signal. The dc pressure rise through the blade row is not shown.

Changes in fan tip clearance have a unique effect on this data set. The tip clearance is changed by moving the fan rotor axially within its rubstrip. The change from small to large tip clearance requires an axial displacement of the rotor by about 12 percent of the axial rotor chord. This causes the axial position of the transducers relative to the rotor to change between conditions of different tip clearance and makes it difficult to compare such conditions. The variation of the tip clearance is achieved by putting shims of different thickness behind the rotor. A change in the rotor tip clearance therefore requires the removal of the fan rotor. The torque loads between the rotor and the shaft are transmitted by 32 equispaced splines. Between the conditions of the small and the large tip clearance the rotor angular position relative to the shaft was accidently changed by one spline (11.25 degrees). This change in the angular position of the blades relative to the pulse has not been corrected in the presented data.

Contour plots of the normalized pulse-synchronized pressures are shown in Fig. 142. Since the variations between blade passages are relatively small the data presentation is limited to slightly more than 3 blade passages. The results are based on conditions with full inlet boundary layer, the small tip clearance and low fan loading. The three segments of the figure represent different corrected fan speeds (55, 70 and 88%). The direction of rotation of the rotor is from right to left and the axial mean-flow direction is from the bottom to the top of the figure. The approximate position of the rotor chord is estimated based on the pressure distribution at the lowest corrected fan speed (55%) and then applied to the higher fan speed conditions. The data provides the following observations:

- In subsonic tip-speed conditions the rotor blade location is well defined by the sharp pressure drop from the pressure to the suction surface of the rotor blades.
- At subsonic fan tip-speeds the rotor-bound pressure field decays rapidly forward of the fan rotor
- At supersonic tip-speeds a shock-wave appears near the leading edge of the blades. It extends part–way into the blade passage and forward into the inlet
- At supersonic tip-speeds the unsteady pressure levels become very high. The pressure patterns become more jagged, less continuous and must be considered less reliable.

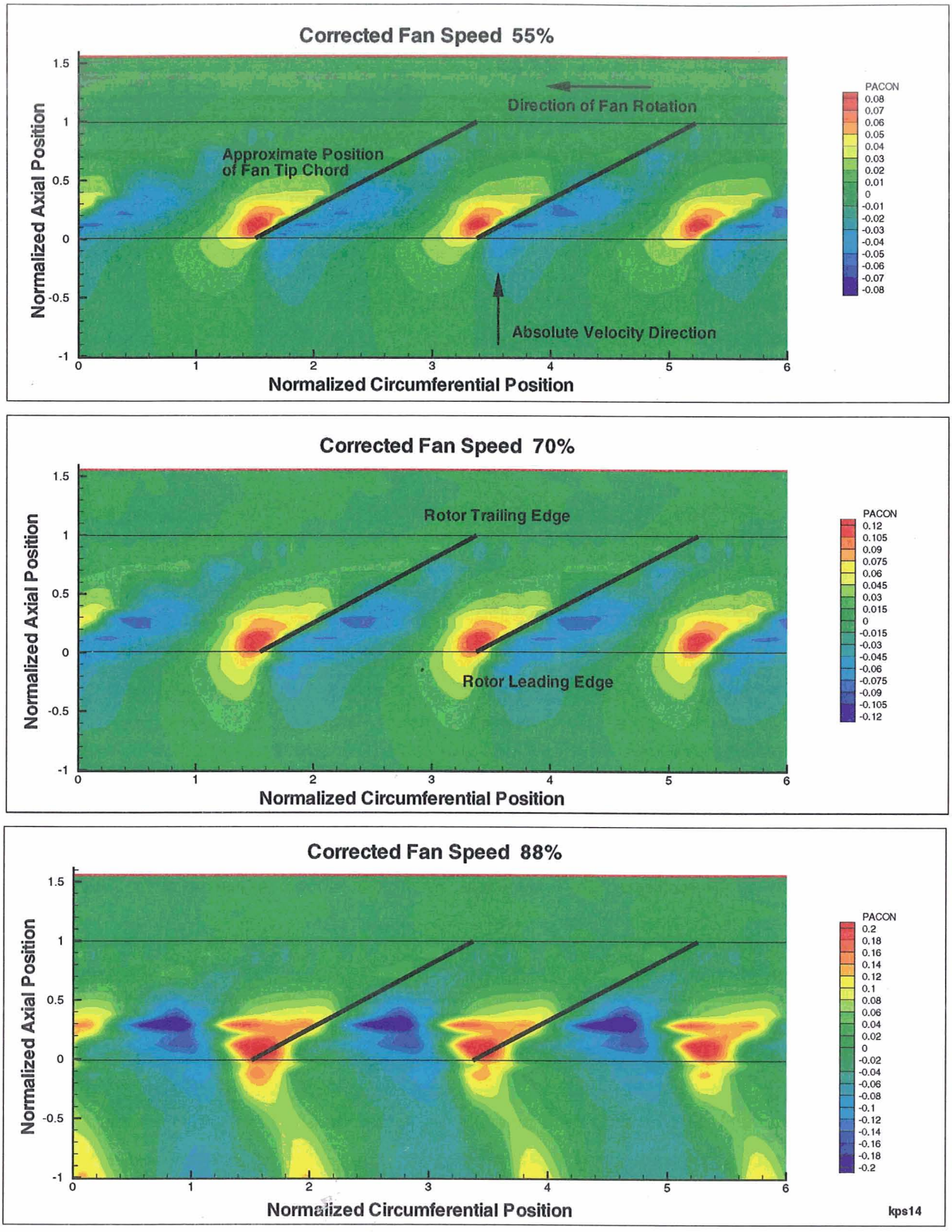

Figure 142 Normalized Pulse Synchronized Surface Pressures on Rubstrip Small Tip Clearance, Full Inlet Boundary Layer Low Fan Loading (Runs 891, 894, 895)

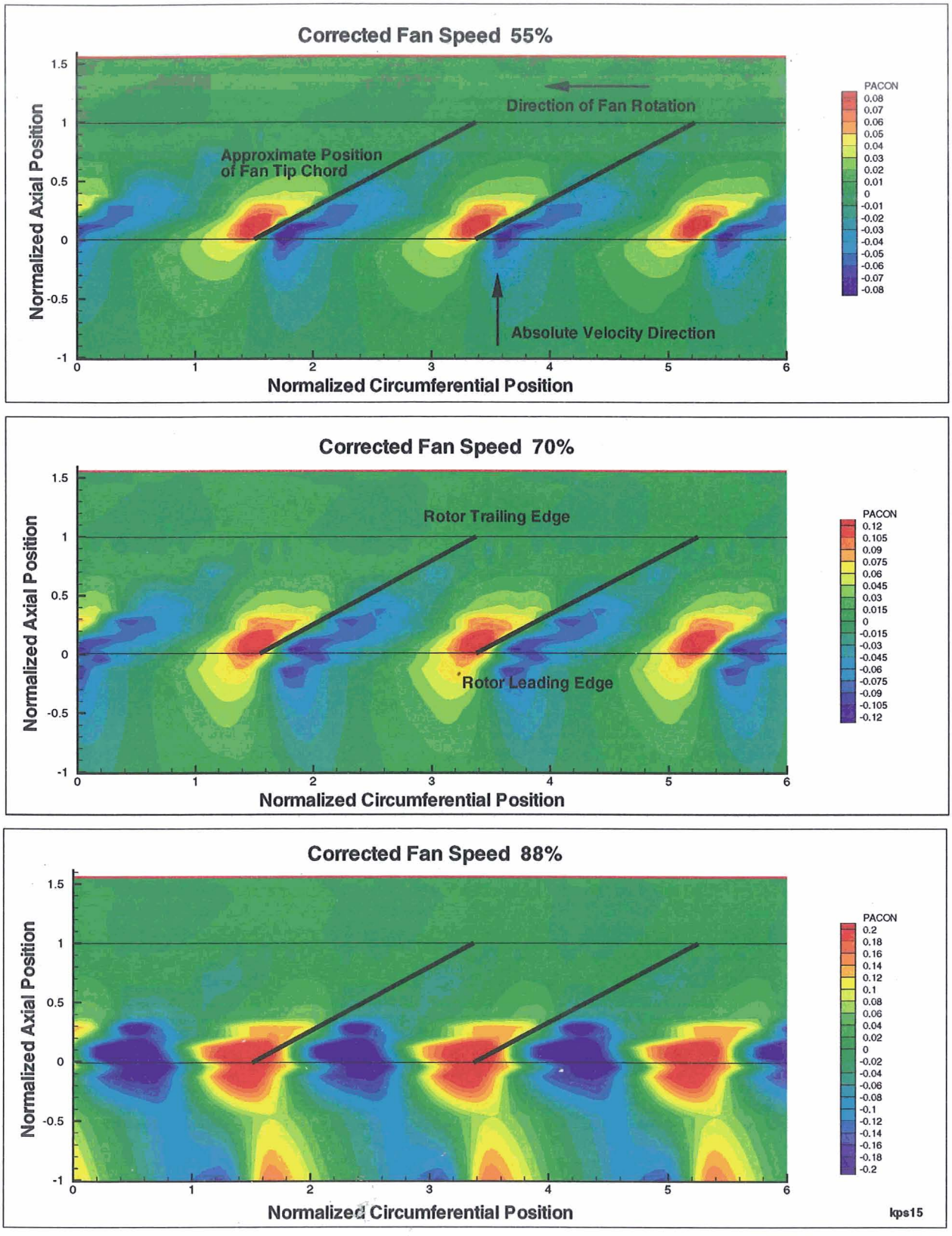

Figure 143 Normalized Pulse Synchronized Surface Pressures on Rubstrip Small Tip Clearance, Full Inlet Boundary Layer High Fan Loading (Runs 892, 893, 896)

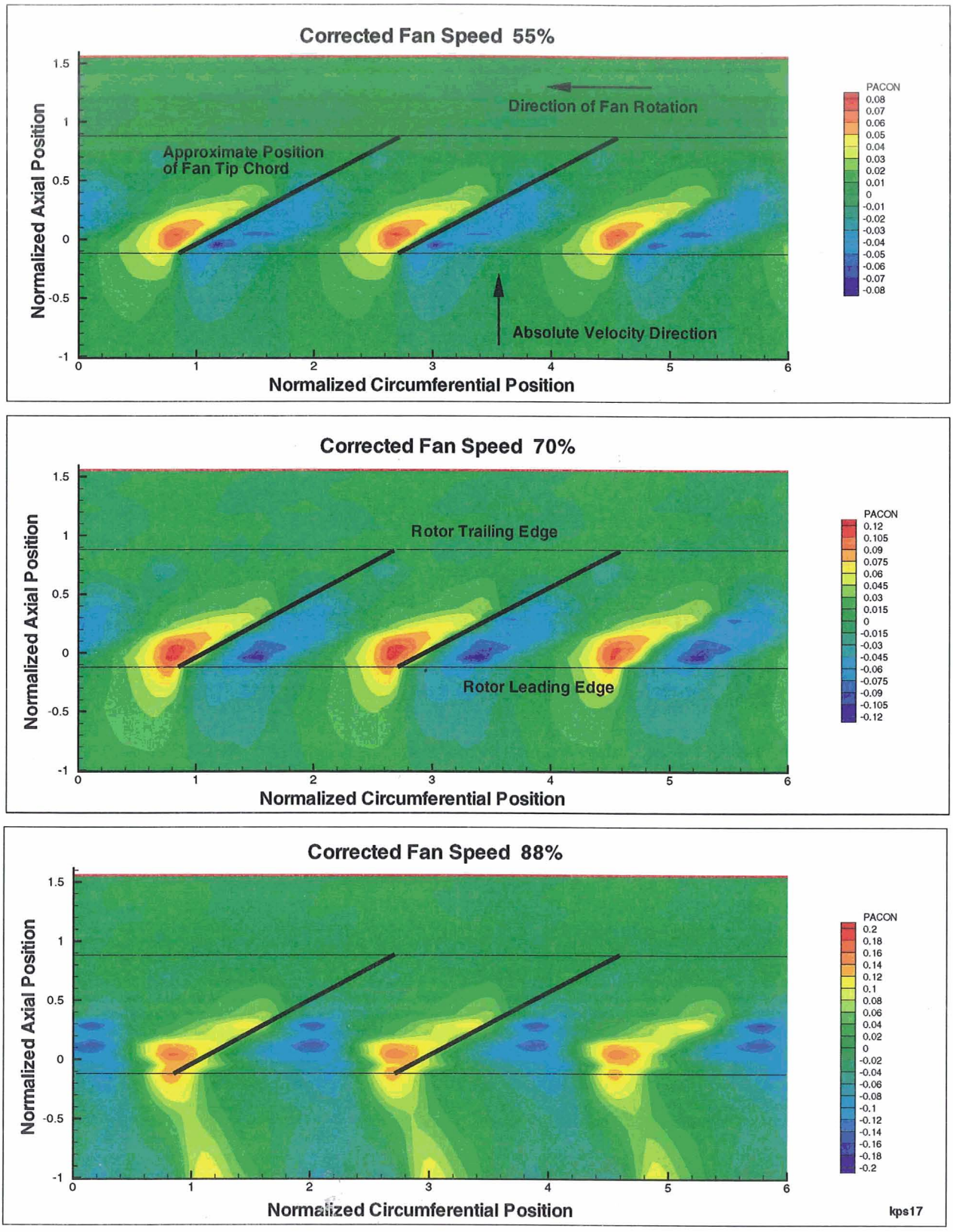

Figure 144 Normalized Pulse Synchronized Surface Pressures on Rubstrip Large Tip Clearance, Full Inlet Boundary Layer Low Fan Loading (Runs 883, 886, 887)

- The decrease of the strength of the shock-wave upstream of the rotor is expected; however its subsequent increase towards the forward most transducer of the array is considered to be another indication of transducer problems at high unsteady pressure levels.
- The chordwise variation of the pressures along the pressure side of the blades is larger than along the suction side. This is due to the fact that the dc component of the pressure is not included in the results.

The same results for the high fan loading conditions are displayed Fig. 143. They indicate that the loading increase is associated with an increased pressure differential across the rotor blade in the leading edge region. In the supersonic tip speed condition the bow shock is separated further from the leading-edge and its strength increased.

Results for conditions with the large tip clearance are shown in Fig. 144. The results clearly reflect the fact that the rotor has moved upstream relative to the sensor array and its clock position on the shaft has been changed. When compared with the results for the small tip clearance shown in Fig. 142 they indicate lower positive and negative peak values.

Pulse-synchronized pressures at three different axial stations and three different fan speeds are shown Fig. 145. The two upper windows represent measurements close to the fan leading edge. The region of sharp decrease in pressure with increasing angular position for the subsonic fan tip speed condition (70%) defines the position of the blade leading edge. The sharp increase in pressure just to the left of the leading-edge position is associated with the leading-edge shock.

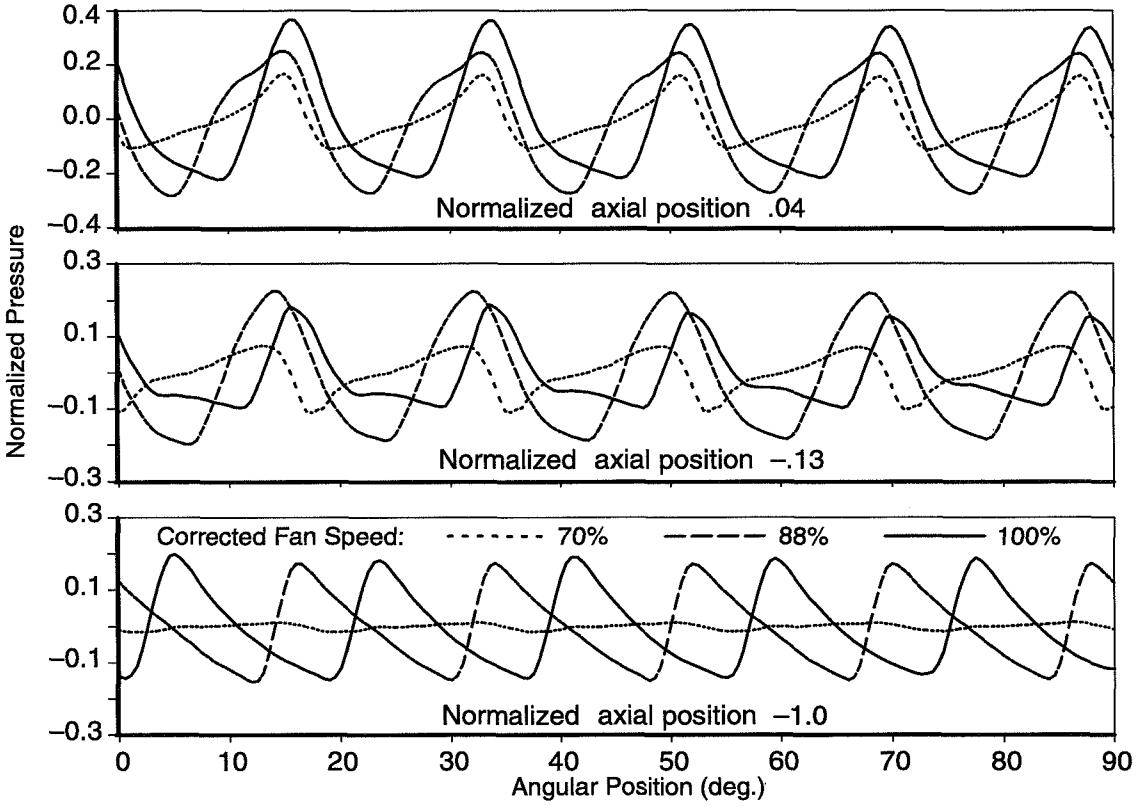

Fig. 145. Effect of Corrected Fan Speed on Normalized Rubstrip Surface Pressures High Fan Loading, Small Fan Tip Clearance, No Inlet Boundary Layer

The bottom window of Fig. 145 presents the corresponding pressure signatures at an axial position one axial chord length upstream of the fan leading edge. The results demonstrate the difference in propagation between subsonic and supersonic fan tip speed conditions.

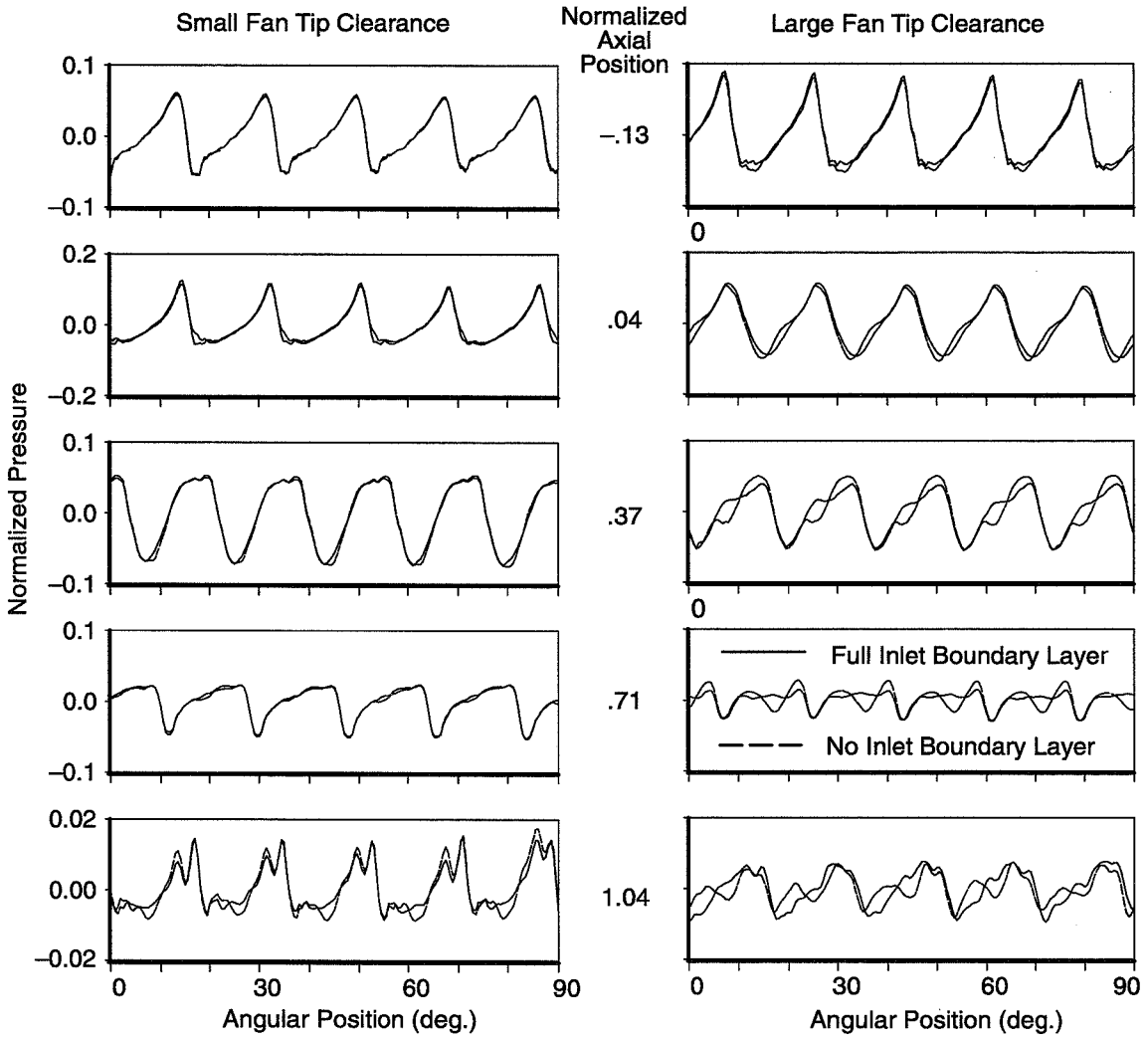

Fig. 146. Effect of Inlet Boundary Layer and Fan Tip Clearance on Rubstrip Surface Pressures, Corrected Fan Speed 70%, Low Fan Loading

Effects of the inlet boundary layer and the fan tip clearance on the rubstrip surface pressures are shown in Fig. 146. The figure shows the pulse-synchronized pressures at five axial positions, from the leading edge to the trailing edge. The two columns represent data for the small and the large fan tip clearance. The data presented in Fig. 146 is based on a subsonic fan tip-speed and therefore the pressure field decays very rapidly upstream of the rotor. In the pressure signals the location of the blades is characterized by the steep drop in the pressure from the pressure to the suction surface. At a given transducer the arrival of the pressure side precedes the suction side, therefore the passing of a rotor blade is indicated by a steep decrease in pressure with increasing angular position. In the case of the small fan tip clearance (left column of Fig. 146) the differences between the two inlet boundary-layer conditions are negligible within the blade passage. In the data for the large tip clear-

ance however there exist consistent differences. A second low-pressure area appears part-way across the blade passage in the data without inlet boundary layer. This disturbance of the pressure profile appears close to the suction side of the passage at the upstream chordwise positions and migrates towards the pressure side with increasing chordwise position. Since it primarily appears in conditions with high tip clearance and no inlet boundary layer, it may be associated with the rotor tip flows driven by the tip-gap pressure differential (Reference 31). It is fair to assume that such flow features would become better observable in a situation without inlet boundary layer.

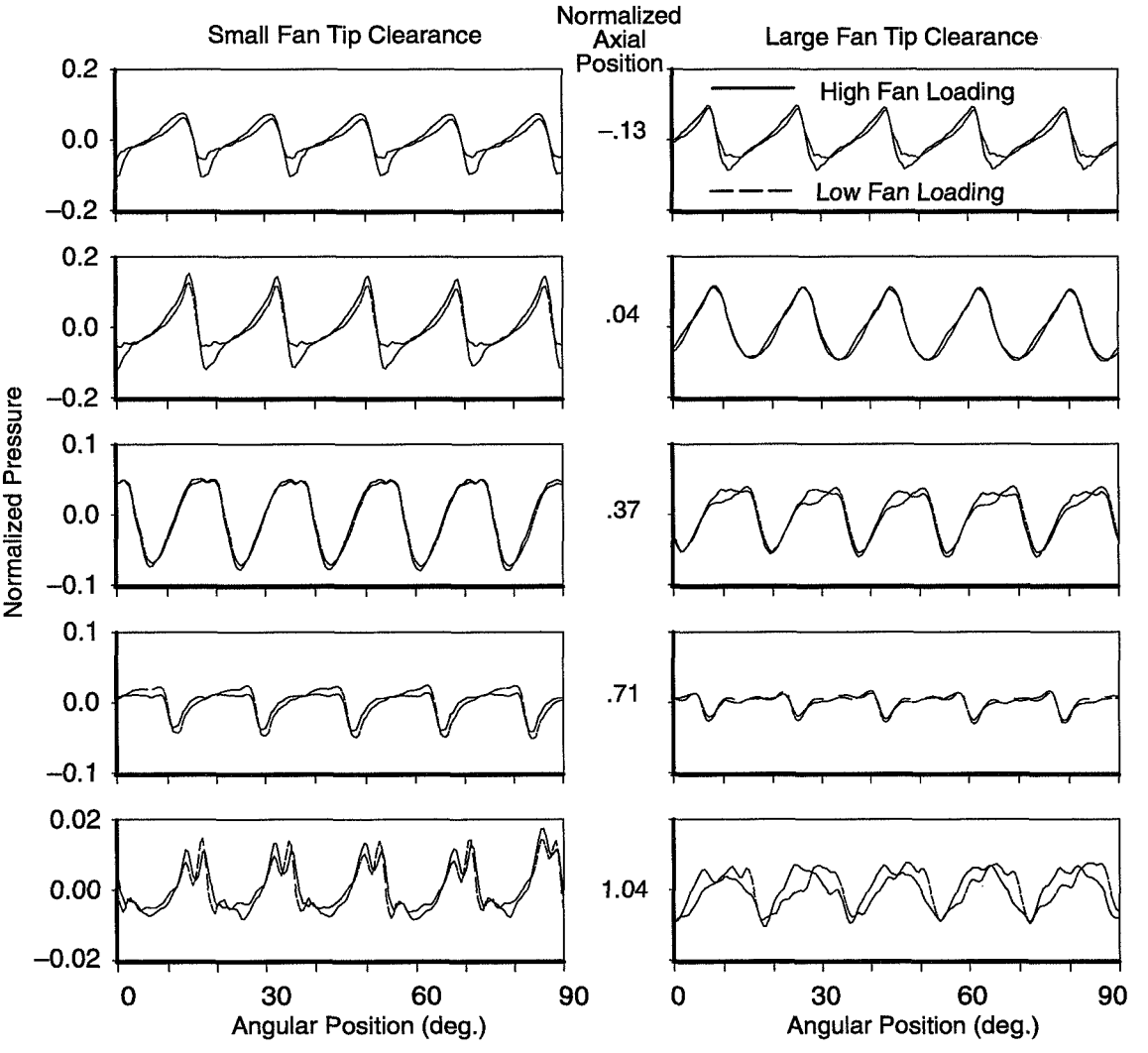

Fig. 147. Effect of Fan Loading and Fan Tip Clearance on Rubstrip Surface Pressures; Corrected Fan Speed 70%, Full Inlet Boundary Layer

Pressure signatures for different fan loading and fan tip clearances are compared in Fig. 147. Fan loading seems to primarily affect the fan leading-edge region, where the pressure differential across the blade increases with fan loading.

5 Conclusions

This section summarizes the conclusions reached in analysis of the test data.

Facility Noise-Floor Levels

- Background noise levels from the LSAF free-jet are well below the fan broadband levels and therefore do not contaminate the fan noise signature.
- Fan-noise measurements in the far field at frequencies below 4 kHz are contaminated by the noise generated by the fan exhaust impinging on the fan-rig strut.

Inlet boundary-layer turbulence measurements:

- The characteristics of the inlet boundary-layer turbulence are similar to those of a flat plate boundary layer.
- The favorable pressure gradients in the inlet, in particular close to the fan face, are the probable cause for the differences in the mean-velocity profiles, the turbulence intensity profiles and the streamwise integral length-scale distributions between the measured data and the flat plate data in zero pressure gradient.
- Boundary-layer suction provided near zero percent of the full boundary layer thickness for the maximum suction conditions.
- Significant noise floors which usually contaminate the cross-wire signals at high velocities can be minimized by proper sensor modifications and extraction of the pulse-synchronized average signal.

Fan duct unsteady flow measurements:

- At the axial position of the stators the dominating features of the unsteady flow are the streamwise velocity deficit and the related secondary flows in the rotor wakes.
- The highest turbulence intensities occur in a region close to the outer wall. The radial extent of this region is strongly affected by fan tip clearance.
- The lowest turbulence intensities occur in the midspan region because of the clean flow between the wakes.
- The turbulence in the hub wall region increases as fan loading is reduced
- In spite of the complexity of the rotor wakes they exhibit remarkable similarities with two–dimensional wakes.
- Von Karman spectra provide good approximations for the spectral distributions of the turbulence velocities.

Acoustic levels

- Significant fan broadband noise comes from at least three separate mechanisms.
- Rotor self-noise is significant even with clean inflow and no boundary layer
- Rotor tip clearance affects rotor self-noise
- The interaction of the rotor with inlet boundary-layer turbulence is a significant source.
- Interaction noise of the rotor with the inlet boundary layer is strongly affected by rotor tip clearance.

- High level noise can be generated by a high-order unsteady nonuniformity rotating at a fraction of the fan speed, at least when tip clearance and loading are both large.
- Stator-generated noise is the loudest of the significant sources, at least on this rig.
- Stator noise is significantly affected by propagation through the fan.

Aerothermal measurements and analysis

- Stator and rotor incidence are significantly impacted by loading.
- Stator incidence is not influenced by inlet boundary-layer size.
- Stator tip incidence is significantly impacted by clearance changes.
- Rotor tip incidence is significantly impacted by inlet boundary-layer size.
- Data analysis with accurate radial mixing is necessary for an accurate stator leading edge solution.
- Accurate data analysis requires good measurements for use with blockage calculation.
- Accurate data analysis requires well-calibrated rotor exit rake instrumentation.

6 Recommendations

This test, like most tests, has introduced as many questions as it answered. It also helped identify some things that could be improved in future tests. Based on these considerations, the following recommendations are made for future work:

- This data set was always intended to provide the basis for validation tests of noise mechanism models originated by other researchers. It has also introduced some new mechanisms not previously modeled at all. It is recommended that further model development work be done, and that data from the present data set be made available as part of that effort. This would include further analysis of the data from this test, for example calculation of the sub-component noise mode distributions, as needed to assist model development.

- In future tests with the 18 inch Boeing fan rig the low frequency noise floor needs to be reduced. A study of the extraneous rig noise sources (not reported here) has indicated that 5 to 7 dB reduction in low–frequency noise is readily achievable.

- In future testing, mode data should be acquired downstream of the stators as well as in the inlet and between the rotor and stators as was done here. Mode data should be taken for all arrays at every condition, also – this has become more practical since the test due to data system improvements.

- There has been some question of how broadly applicable these results are. To answer this question, a similar test should be done including back–to–back comparisons with a different fan. It is recommended that such a fan be significantly different and be designed to the best modern standards to better reflect current practice among engine vendors.

- The test matrix did not include enough stator variations to separate the effects of number and solidity of the stators, nor to identify any rotor–stator spacing effects. A further test is recommended to assess these effects.

- The so-called "rotating instability" noise, seen only at high loading, thick boundary layer, and large tip clearance conditions, is clearly a serious problem if it occurs. While there is no evidence that it is present in modern engines, it is recommended that it be assessed in sufficient detail to provide design guidelines adequate to avoid it in future designs. This noise also has limited the confidence with which many conclusions can be drawn from the present test, especially the sensitivity of other sources to these variables. It is recommended that an extension of the present test be done to fill in the test matrix with more intermediate values of tip clearance and loading.

- Rotor self–noise was found to be sensitive to tip clearance, suggesting the possibility of another noise mechanism. To sort this out, measurements of the flow in the tip region are needed, along with acoustic measurements; test data with little or no tip clearance are also needed to separate tip noise from rotor noise. These measurements should preferably be done with no boundary layer to remove the masking of that noise source.

- Unsteady flow measurements similar to the ones made during this test should be acquired at several axial positions relative to the rotor to better document the axial evolution of the rotor wakes.

7 References

1. Law, C. H., Puterbaugh, S. L., "A Computer Program For Axial Compressor Design (UD0300M)," *Air Force Wright Aeronautical Laboratories*, AFWAL–TR–82–2074, September, 1982.

2. Allen, R. M. and Reed, D. H., "Development of the Boeing Low-Speed Aeroacoustic Facility (LSAF)," AIAA Paper DGLR/AIAA–92—02–030, 1992.

3. Scharpf, D. F., "The Design and Evaluation of a Splitter Plane for Half-Span Model Testing in an Open-Jet Wind Tunnel," *First Joint CEAS/AIAA Aeroacoustics Conference (16th AIAA Aeroacoustics Conference)*, June 12–15 1995, Munich, Germany, Paper # CEAS/AIAA–95–153, pp. 1039 – 1047.

4. Dougherty, R. P., Scharpf, D. F., and Underbrink, J. R., "Test Report Boeing/NASA Ames Flap-Edge Noise Test:Phased-Array Development," NASA CDCR 21–000, Feb 16, 1995.

5. Underbrink, J. R., and Dougherty, R. P., "Array Design for Non-Intrusive Measurement of Noise Sources," Noise–Con 96, Seattle, WA, Sept. 29–Oct. 2, 1996.

6. Ross, R., "Spectral Broadening Effects in Open Wind Tunnels in Relation to Noise Assessment," AIAA Journal, Volume **19**(5), May, 1981.

7. Ahuja, K. K., Tanna, H. K., and Tester, B. J., "An Experimental Study of Transmission, Reflection and Scattering of Sound in a Free Jet Flight Simulation Facility and Comparison with Theory," Journal of Sound and Vibration,Volume **75**(1), 1981.

8. McGinley, C., private communication, July 1994.

9. Quazi, Azizul H. "Array Beam Response in the Presence of Amplitude and Phase Fluctuations," J. Acous. Soc. Am. 72(1) July 1982 pp171–180.

10. Joppa, Paul, "Duct Mode Measurement of Fan Broadband Noise," *Proceedings of 1996 National Conference on Noise Control Engineering*, pp 127–132, Institute of Noise Control Engineering.

11. Ganz, Ulrich, "Multi–Modal Directivities of Fan Tone Noise," *Proceedings of 1996 National Conference on Noise Control Engineering*, pp 139–144, Institute of Noise Control Engineering.

12. Medlock, A., "Multistage Compressor Test Data Analysis Computer Program (PERCH)," *Air Force Wright Aeronautical Laboratories*, AFWAL–TR–83–2053, July, 1983.

13. Klebanoff, P.S., "Characteristics of Turbulence in a Boundary Layer with Zero Pressure Gradient," NACA TN 3178, July 1954.

14. Bradshaw, P., "The Turbulence Structure of Equilibrium Boundary Layers," J. Fluid. Mech. (1967), vol. 29, Part 4, pp. 625–645.

15. Grant, G.L., "The large eddies of turbulent motion," J. Fluid. Mech. (1958), vol. 4, pp. 149.

16. Schubauer, G.B. and Klebanoff, P.S., "Investigation of the separation of the turbulent boundary layer," NACA Report 1030, 1951.

17. Favre A., Gaviglio, J. and Dumas, R., "Further space–time correlations of velocity in a turbulent boundary layer," J. Fluid. Mech. (1958), vol. 3, pp. 344

18. Kovasznay L.S., et al, "Large–scale motion in the intermittent region of a turbulent boundary layer," J. Fluid. Mech. (1970), vol. 41, Part 2, pp. 283–325.

19. Spalart P.R., "Direct simulation of a turbulent boundary layer up to Re = 1410," J. Fluid. Mech. (1988), vol. 187, pp. 61–98.

20. Majiggi, R.K., Gliebe, P.R., "Development of a Rotor Wake / Vortex Model," NASA–CR–174849, June 1984.

21. Topol D. A. and Philbrick D. A.,"Fan Noise Prediction System Development: Wake Model Improvements and Code Evaluations," NASA Contract NAS3–25952 (Task 10), April 1993.

22. Glegg, S. A. L., "Broadband Noise from Ducted Prop Fans," AIAA 93–4402, Oct. 1993.

23. Gliebe, P. R., Ho P. Y., Mani R., "UHB Engine Fan Broadband Noise Reduction Study," NASA–CR 198357, June 1995.

24. Silverstein, A., Katzoff, S., Bullivant, W. K., "Downwash and Wake behind Plain and Flapped Airfoils," NACA Report 651, 1939.

25. I. Wygnanski, F. Champagne, B. Marasli, "On the large–scale structures in two–dimensional small–deficit, turbulent wakes," J. Fluid. Mech. (1986), vol. 168, pp. 31–71.

26. J. O. Hinze, *Turbulence*, McGraw–Hill, 1975.

27. Amiet, Roy K.,"Correction of Open Jet Wind Tunnel Measurements for Shear Layer Refraction," AIAA paper 75–532, 1975.

28. ANSI S1.26–1995, "Method for Calculation of the Absorption of Sound by the Atmosphere," Am. Nat. Standards Inst., 1995.

29. ANSI S1.11–1986, "Specification for Octave–Band and Fractional–Octave–Band Analog and Digital Filters," Am. Nat. Standards Inst., 1986.

30. Glegg, Stewart A. L. and Cyrille Jochault, "Broadband Self Noise from a Ducted Fan," AIAA paper 97–1612, May 1997.

31. J. G. Moore and J. Moore, "CFD Calculations for the Boeing Fan," Turbomachinery Research Group report no. JM/97–3, Mechanical Engineering Dept, Virginia Polytechnic Institute, July 1997.

8 Tables

8.1 Data Sets available for Hotwire Measurements in Fan Duct

The numbers shown in the table indicate the Run during which the data set was acquired followed by the number of test points

Tip Clearance (mm)	Inlet Boundary Layer (%)	Corrected Fan Speed (%)	Streamwise + Transverse Turbulence Component			Streamwise + Radial Turbulence Component		
			Fan Loading			Fan Loading		
			Low (17k)	Medium (19.7k)	High (24k)	Low (17k)	Medium (19.7k)	High (24k)
.46	100.	55.	900/24	901/24	902/24	891/14		892/14
		70.	905/24	904/24	903/24	894/14		893/14
		88.	926/24	927/24	928/24	895/14		896/14
		100.	931/24	930/24	929/24	898/14 899/14		
.46	.0	55.	906/14 907/14	908/14	909/14			
		70.	912/14	911/14	910/14			
		88.	913/14	914/14	915/14			
		100.						
1.27	100.	55.	861/24 917/24	862/24 918/24	863/24 919/24	883/24		884/24
		70.	866/24 922/24	865/24 921/24	864/24 920/24	886/24		885/24
		88.	923/24 880/24	924/24	925/24	887/24		888/24
		100.				890/24		889/24
1.27	.0	55.	867/12	868/12	869/12			
		70.	872/12	871/12	870/12			
		88.	873/12	874/12	875/12			
		100.	878/12	877/12	876/12			

8.2 Radial Positions for Hotwire Measurements in Fan Duct

Fan duct outer radius: 21.97 cm
Fan duct inner radius: 11.43 cm

Testpoint	radial position (cm)	normalized radial pos.	radial region
1	21.78	.991	tip
2	21.59	.983	tip
3	21.43	.975	tip
4	21.27	.968	tip
5	21.12	.961	tip
6	20.96	.954	tip
7	20.80	.947	tip
8	20.64	.939	tip
9	20.32	.925	midspan
10	20.00	.910	midspan
11	19.69	.896	midspan
12	19.05	.867	midspan
13	18.42	.838	midspan
14	17.78	.809	midspan
15	17.15	.780	midspan
16	16.51	.751	midspan
17	15.88	.723	midspan
18	15.24	.694	midspan
19	14.61	.665	hub
20	13.97	.636	hub
21	13.34	.607	hub
22	12.70	.578	hub
23	12.07	.549	hub
24	11.75	.535	hub

9 Nomenclature

b	constant used in sound power as a function of exhaust Mach number
c	Rotor blade chord
c_d	Rotor blade drag coefficient
D	Diameter
f	Frequency
L_{ux}	Streamwise integral length scale of velocity component u
M_{jet}	Fan rig exhaust jet Mach number
n	Exponent for sound power as a function of Mach number
St	Strouhal number
$U_{exhaust}$	Fan rig exhaust velocity
U	1
U_∞	Maximum relative velocity in blade passage
$\overline{u^2}$	

Symbols

δ	LSAF shear layer thickness
δ	)
Δf	spectral bandwidth
λ	Wavelength

Abbreviations

LSAF	Low-Speed Aeroacoustic Facility
$PSD_{uu}(f)$	Power spectral density of velocity component u at frequency f
SPL	Sound Pressure Level
OASPL	Overall SPL
BPF	Blade Passage Frequency
PNL	Percieved Noise Level

10 Appendices

10.1 Appendix 1 – Test History

The test occurred in three segments, as described below. The second and third segments were each able to benefit from improvements made after studying the previous results; thus each segment effectively replaced the previous one. (In the following notes, all dates are in 1995.)

- The initial test included:
  1. Feb 7, Runs 1 to 12
     Background noise checks for tunnel noise and boundary-layer suction noise
  2. Elliptical mirror scans of the rig in operation, looking for extraneous noise sources
  3. Feb 10, Runs 59 to 100
     Boundary-layer calibration (see section 2.3); note that these data were used throughout the rest of the test.
  4. A set of azimuthal sideline array scans every 10 degrees (see section 3.5); note that a lack of azimuthal variation was confirmed, and no further use was made of this array.
  5. In-duct and sideline data for the rotor-alone case at the intermediate tip clearance, at 8 different rpms. This set was with all combinations of three boundary layers and three fan loadings, and included inlet and aft-duct modal data.
  6. A set of cross-correlation data among selected sideline mics.
  7. Feb 22, Runs 240 to 316
     A set of fan performance rake data
- At this point, testing was suspended for about three weeks. During this interval, the nozzle was modified to allow greater fan pressure ratios to be achieved, software problems were fixed, the method of averaging mode data was changed to reduce an emphasis on correlated modes (see Ref. 10 for details), three small cavities in the rubstrip were plugged, and mechanical damping of the fan rig support structure was increased to reduce spurious noises. The following data was then acquired at the nominal tip clearance:
  1. March 20, Runs 318 to 323
     New nozzle positions were found which duplicated the pressure ratios of the previous test segment (rotor-alone)
  2. March 20 to March 21, Runs 324 to 359
     Hot wire unsteady flows in the inlet
  3. March 22 to March 23, Runs 360 to 403
     Hot wire unsteady flows in the fan duct at a position near where the leading edge of the smallest stators would have been (rotor-alone)
  4. More elliptic mirror scans (rotor-alone)
  5. March 24 to March 27, Runs 405 to 466:
     A set of fan performance rake data was taken after sixty narrow fan exit guide

vanes (design solidity) were installed, and new nozzle settings were chosen to produce the same rotor mass flows as before.

6 March 28
It was observed that pressure fluctuations at the most upstream positions in the inlet were higher than those at locations further downstream. This was thought to indicate local separation of the laminar boundary layer. An inlet boundary-layer trip strip was installed 31.8 mm upstream of the throat.

7 March 29 to March 30, Run 467 t0 581:
In-duct and sideline data with and without fan exit guide vanes, at 5 different rpms. This set was taken with all combinations of three boundary layers and three fan loadings, but included modal data in the inlet only.

8 March 31, Runs 582 to 684:
Same as Runs 467 to 581 but without stators

- The test was again suspended for about 3 weeks, during which time a mid-test workshop was held with all the NASA study participants to review the data and to adjust plans for the final test segment. It was agreed at the workshop that higher fan loadings should be studied, the phased-array acoustic telescope should be tried to help identify possible non-fan noise sources, and that the number of fan exit guide vanes should be varied. There was some feeling that the effect of tip clearance was not likely to be significant, though we ultimately elected to include it in the study. The following data were collected:

  1 April 19, Runs 685 to 716:
  New operating lines were established, with the lowest one corresponding to the previous high one, a middle line close to the design point, and a higher line just below the onset of the characteristic rotating-stall noise spectrum (at the intermediate tip clearance). Phased-array acoustic telescope data was collected at several frequencies and array positions.

  2 April 24 to April 25, Runs 717 to 810:
  Rotor-alone acoustic data at high and low values of tip clearance, loading, and boundary layer, at 5 rpms; mode data in fan duct for 3 rpms and inlet for 2 rpms. Run 759 is the first data set with the small rotor tip clearance.

  3 April 26, Runs 811 to 860:
  Fan performance rake data, rotor-alone, at high and low values of tip clearance, loading, and boundary layer

  4 April 27, Runs 861 to 935:
  Hot wire data in fan duct (rotor-alone), at two to three loadings, two tip clearances, two boundary-layer thicknesses for four rpms

  5 May 2, Runs 936 to 1000:
  Thirty medium-chord fan exit guide vanes (design solidity) were installed and nozzle settings were selected to match the fan flows of the rotor-alone case. Fan performance rake data with the 30 medium-chord fan exit guide vanes, at five rpms and a set of conditions that represent a fractional factorial subset of the 27 possible combinations of loading, tip clearance, and boundary layer. This set was intended to allow calculation of quadratic main effects and first-order interactions

of the variables. It included as a subset all the extreme-value combinations (as in items 3, 4, 9, and 10).

6 May 3 to May 4, Runs 1001 to 1166:
Acoustic data with the 30 medium-chord fan exit guide vanes, at the above fractional factorial set of conditions, at five rpms; mode data in fan duct for three rpms and inlet for two.

7 May 5, Runs 1167 to 1248:
Acoustic data with 60 medium-chord fan exit guide vanes (twice the design solidity, necessitated by the failure of the narrow-chord vanes in the previous segment of the test), at the extreme-value combinations of tip clearance, loading, and boundary layer, at five rpms; mode data in fan duct for three rpms and inlet for two.

8 May 6, Runs 1249 to 1320:
Acoustic data with 15 wide-chord fan exit guide vanes (design solidity), at the extreme-value combinations of tip clearance, loading, and boundary layer, at five rpms; mode data in fan duct for three rpms and inlet for two.

10.2 Appendix 2 Data Analysis of Hotwire Rotor Wake Meassurements

It is the purpose of this appendix to describe in more detail the data analysis process for the hotwire measurements downstream of the rotor. The analysis process is composed of two segments. The output of the first segment provides simultaneous time histories for the local velocity, the flow angle and the synchronizing pulse. The duration of these time histories is one second and they are based on a sampling rate of 100 kilosamples per second. This appendix is concerned with the second segment of the analysis that makes use of these time histories.

The mean flow downstream of the rotor is not axial, because of the angular momentum imparted on the flow by the rotor. It enters the stators at an angle of about 30 degrees relative to the fan axis. This angle varies with radial position as well as with fan loading. It is desirable to minimize the offset between the center of the angular calibration range of the cross–wire sensors and the average mean flow angle in order to prevent the flow conditions from exceeding the calibration range. The calibration range of the cross–wires is typically centered around their axis of symmetry where their sensitivity to flow angle variations is highest. For these reasons the sensors were installed with their axis of symmetry offset by 30 degrees relative to the fan axis. This offset angle was kept the same for all radial positions.

The raw time histories are of limited direct use because the sampling is not synchronized with the rotor. In order to separate the periodic and random signal components the signals are resampled at a rate of 720 points per rotor revolution. The resampling is achieved by linear interpolation of the velocity and flow angle time histories at temporal values derived based on adjacent pulses in the pulse time history. Each data point of the resampled time history therefore corresponds to a particular position of the rotor and can be associated with an angular position in the rotor frame. In the first step of the averaging process the average velocity and flow angle are determined for each one of the 720 points covering one rotor rotation. This is achieved by decomposing the instantaneous velocity (U) into components parallel and normal to the probe axis (PA) and averaging them over all rotations, see Fig. 148. This provides the local mean flow velocity U_a and flow angle α_a at the 720 angu-

lar positions relative to the rotor. A mean flow velocity U_{aa} and flow angle α_{aa} characteristic for the particular radial position and operating condition is then determined by averaging the components of U_a over all angular positions.

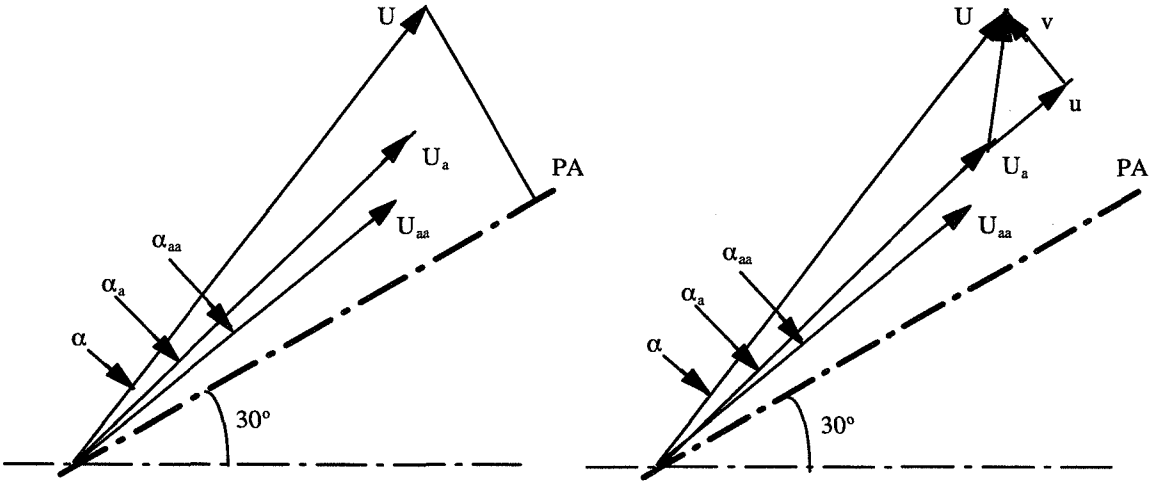

a. Average Velocity Components

b. Random velocity Components

Fig. 148. Analysis of Rotor Wake Velocity Field

The random velocity field is determined by subtracting the local mean velocity U_a from the instantaneous velocity U and by decomposing the resulting velocity vector into components parallel and normal to the mean velocity U_{aa}. This provides the instantaneous values of the streamwise (u) and the transverse (v) random velocity components. The mean square value of these random velocity components is derived by summing over the number of rotor rotations available in each data set. The root mean square values of these velocities normalized with the mean velocity U_{aa} then provide the local turbulence intensities. The mean square values resulting from averaging over all rotations and all angular positions then provide after appropriate normalization the circumferentially averaged turbulence intensity.

Velocity components in the rotor bound coordinate system are computed based on a simple transform using the local wheel speed of the rotor. The local mean relative velocity and the circumferentially averaged relative velocity are computed based on their counterparts in the stationary coordinate system. The turbulence intensities in the rotor bound system are derived by computing the instantaneous velocity vectors in this system and then determining their statistical properties as in the stationary system.

Further averaging is done to determine the average wake parameters. The data points representing one full rotor rotation are broken down into 20 equi–sized blade passages. Averages are then formed based on these 20 data sets to represent the average blade passage. The minimum relative velocity is used to locate the center of the rotor wake and the data is reordered such that the wake center coincides with the center of the blade passage

10.3 Appendix 3
Sound power spectra, far–field

On the following pages, spectra of estimated sound power radiated to the far field are shown. These spectra are produced as described in Section 4.4. They are the same plots as summarized in that section, but have been separated so that only one stator configuration appears on each plot. There are four sections of eight plots each, the sections containing rotor–alone, 15 stator, 30 stator, and 60 stator data. Within each section the order is slightly different than before; the reader is cautioned to read the captions carefully for this reason. Each plot contains five spectra at the five different fan speeds tested; the higher levels are invariably associated with higher fan speeds and are easily identified.

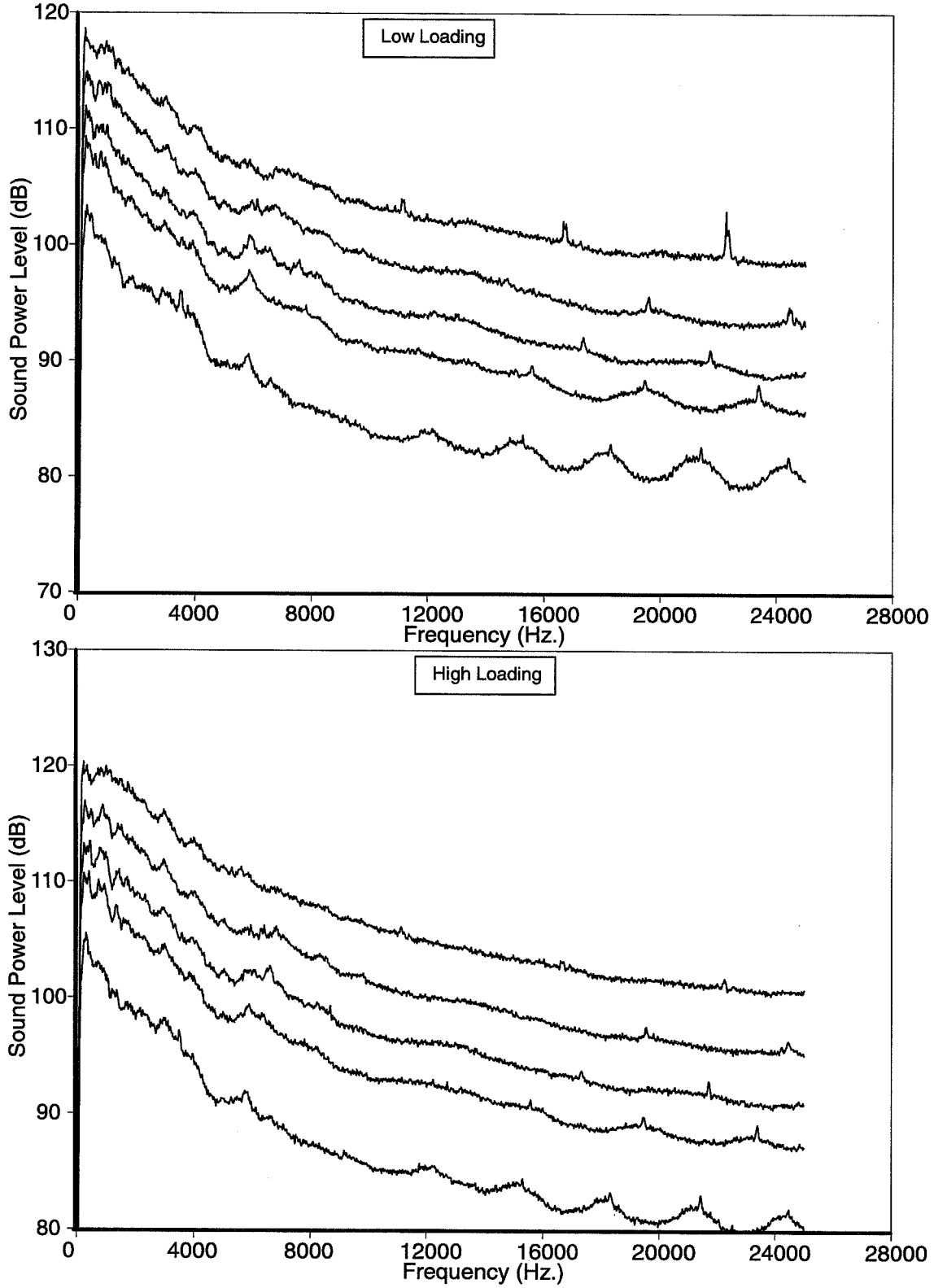

Fig. 149. Aft–radiated power level spectra; rotor–alone, small tip clearance, full boundary layer

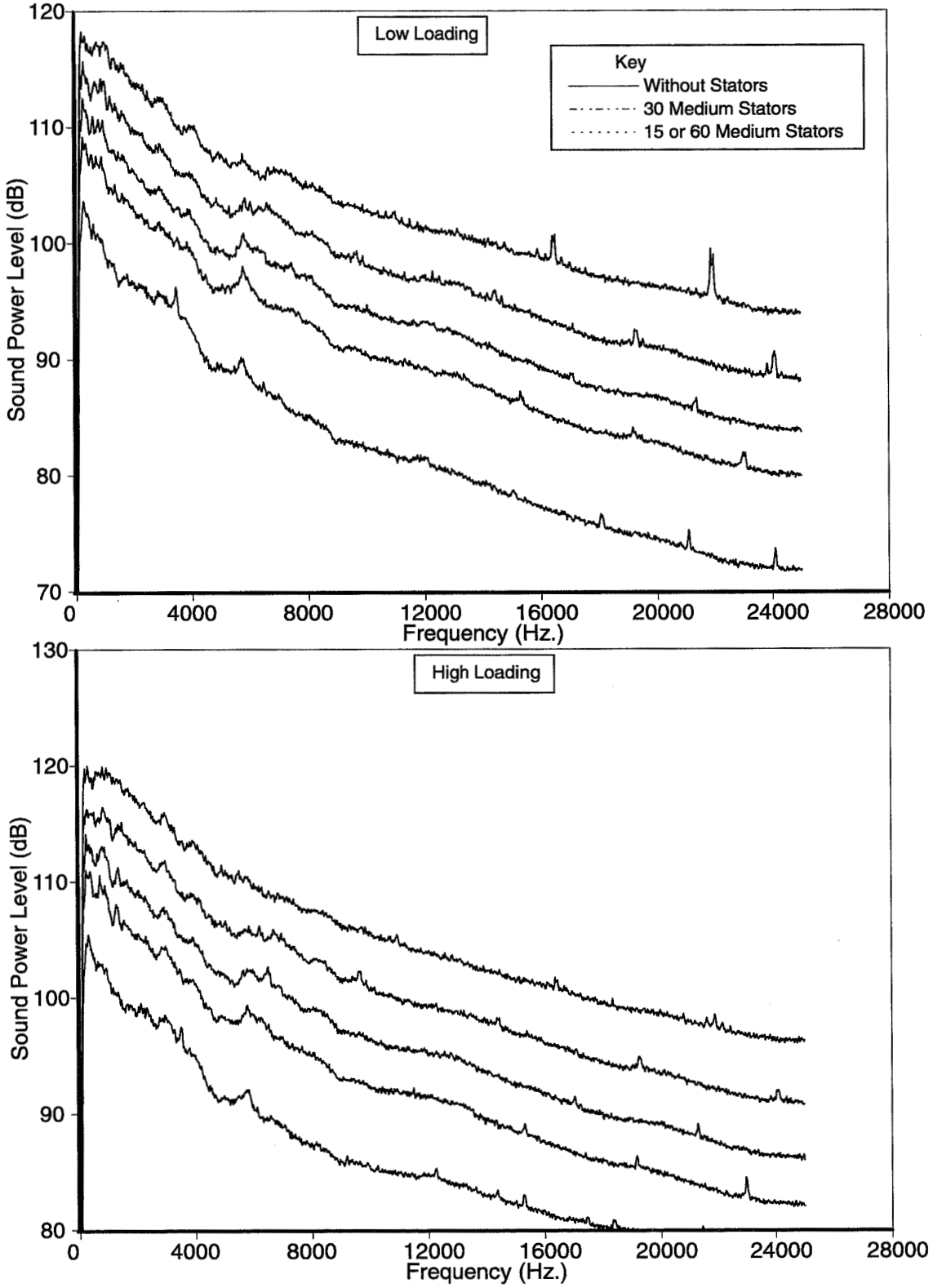

Fig. 150. Aft–radiated power level spectra; rotor–alone, small tip clearance, zero boundary layer

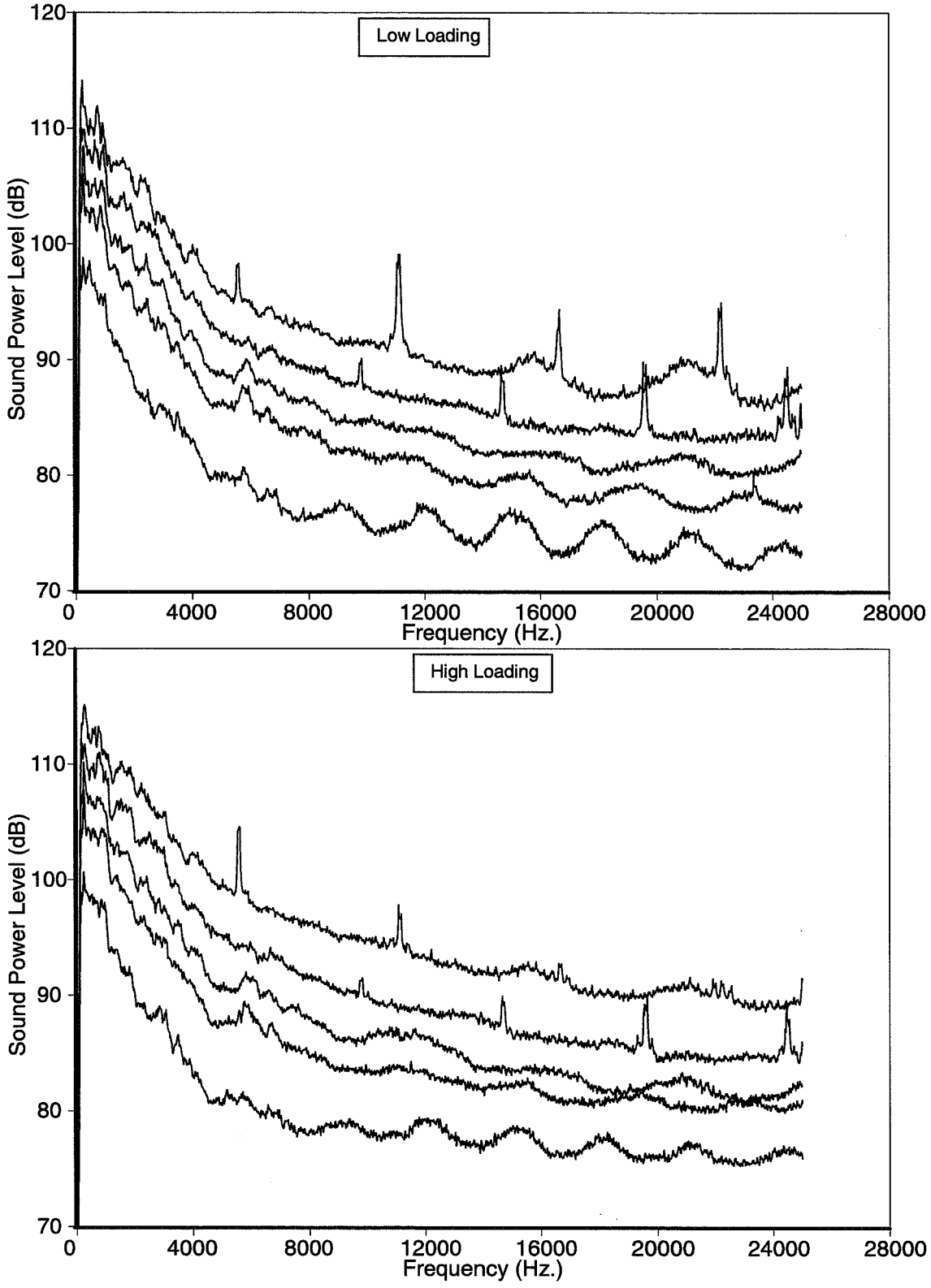

Fig. 151. Inlet–radiated power level spectra; rotor–alone, small tip clearance, full boundary layer

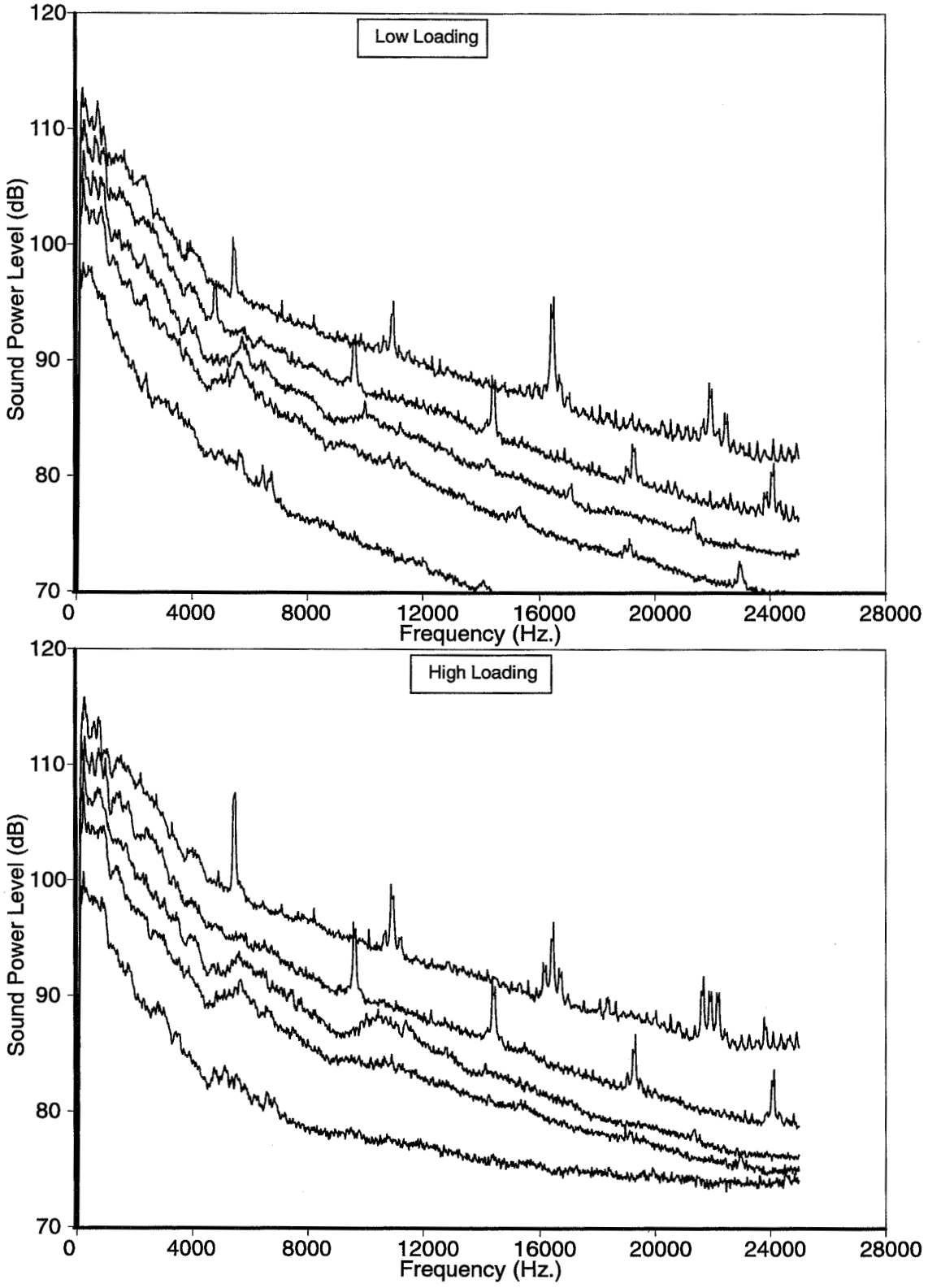

Fig. 152. Inlet–radiated power level spectra; rotor–alone, small tip clearance, zero boundary layer

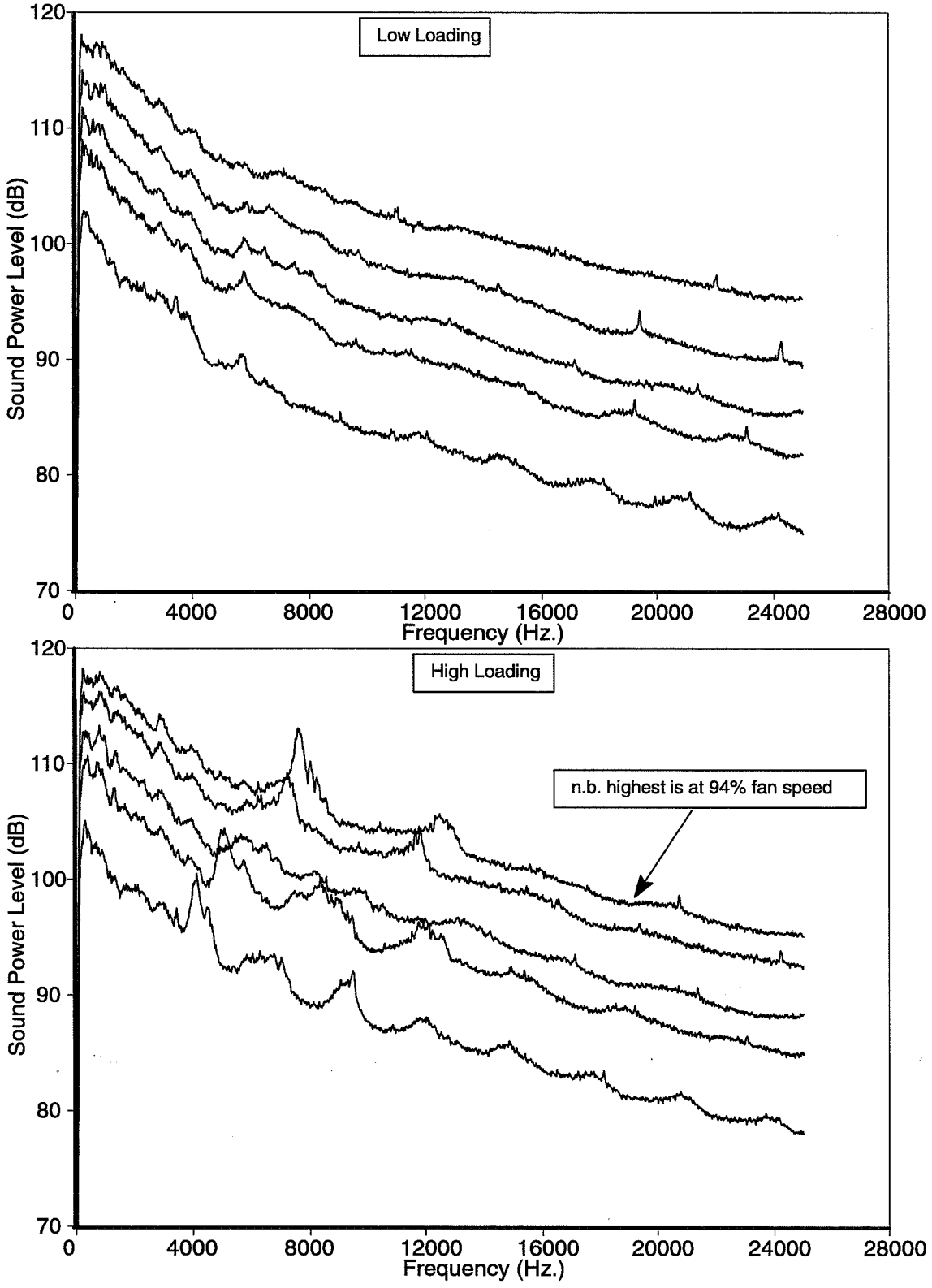

Fig. 153. Aft–radiated power level spectra; rotor–alone, large tip clearance, full boundary layer

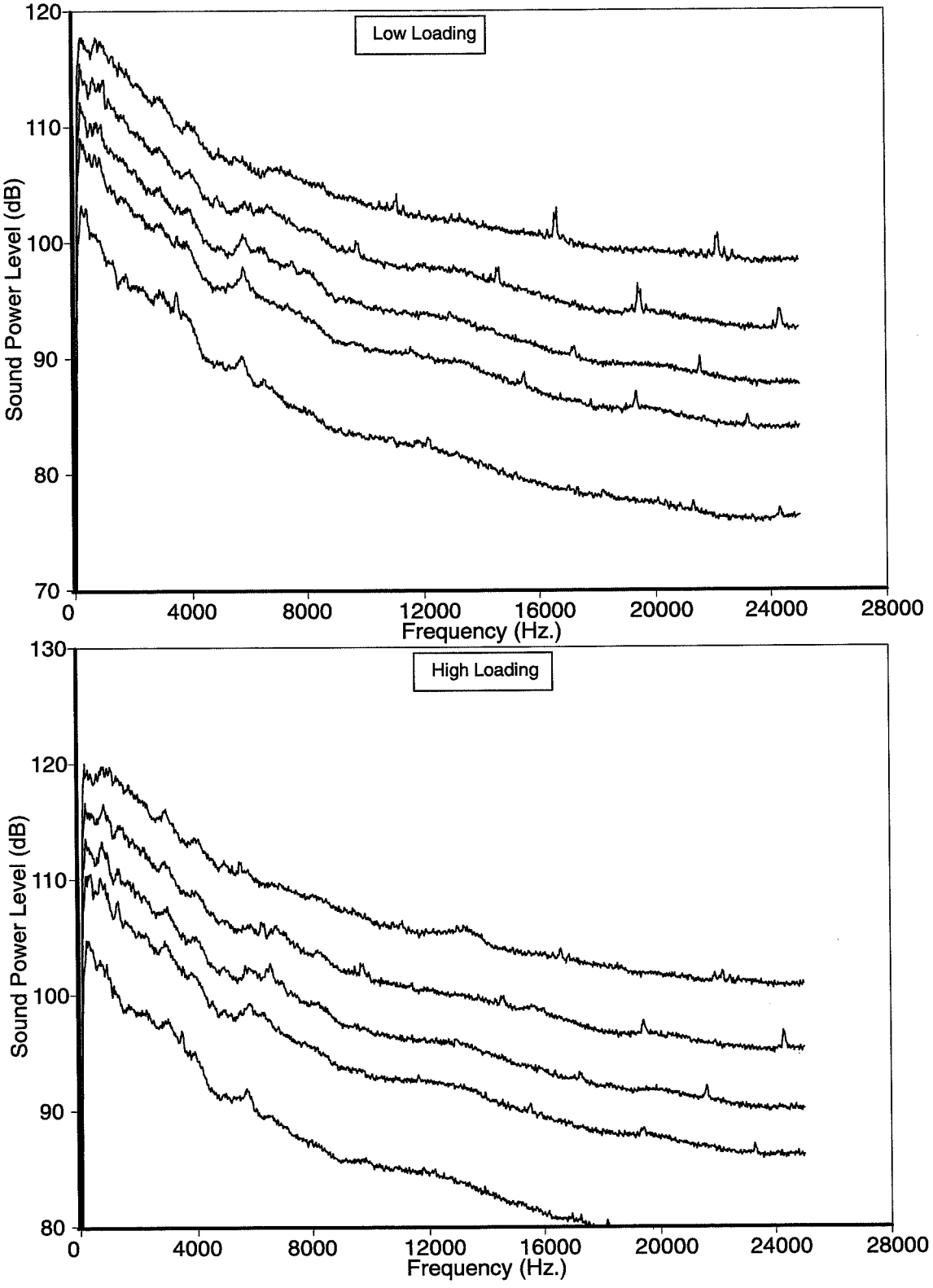

Fig. 154. Aft–radiated power level spectra; rotor–alone, large tip clearance, zero boundary layer

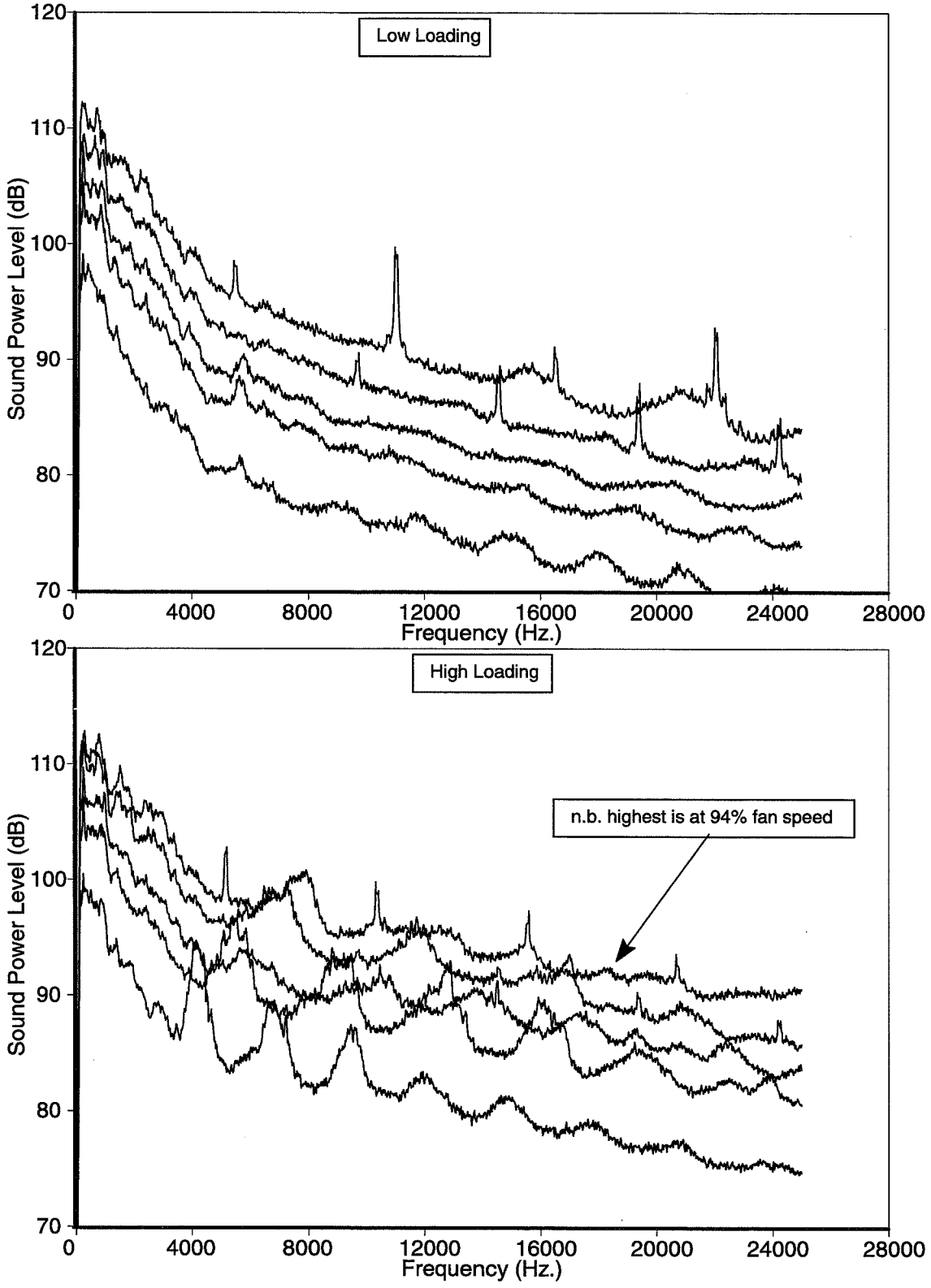

Fig. 155. Inlet–radiated power level spectra; rotor–alone, large tip clearance, full boundary layer

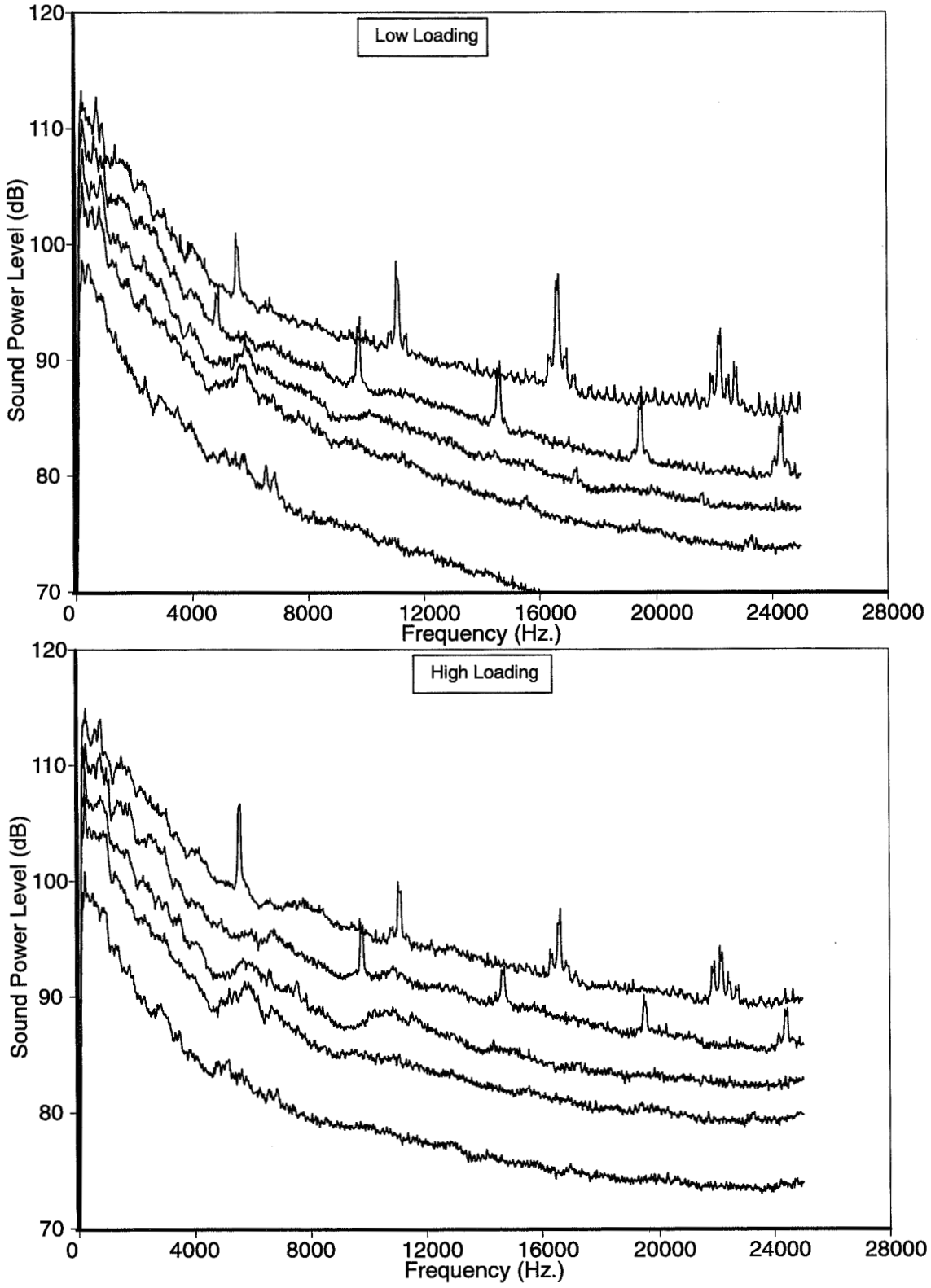

Fig. 156. Inlet–radiated power level spectra; rotor–alone, large tip clearance, zero boundary layer

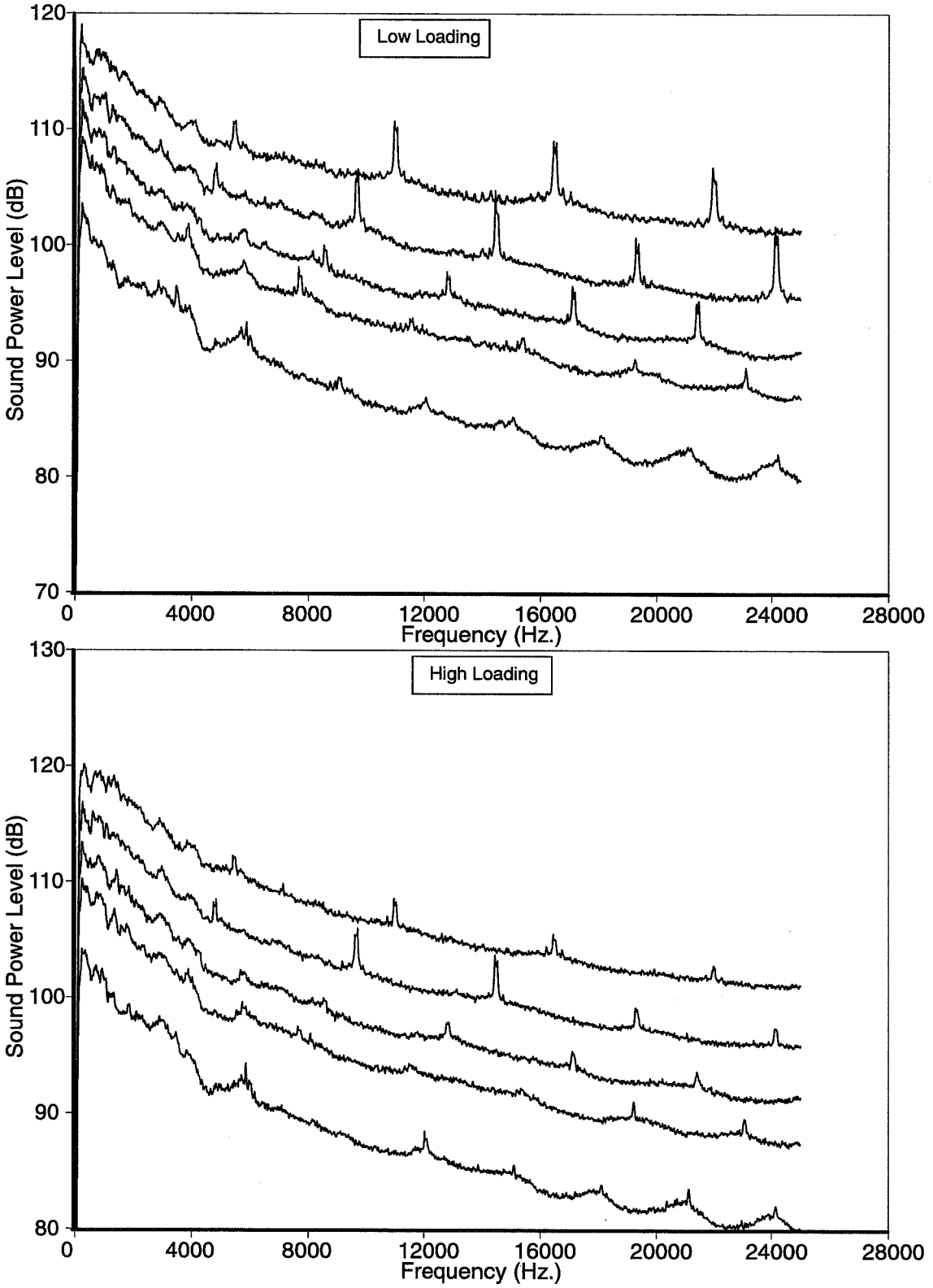

Fig. 157. Aft–radiated power level spectra; fifteen stators, small tip clearance, full boundary layer

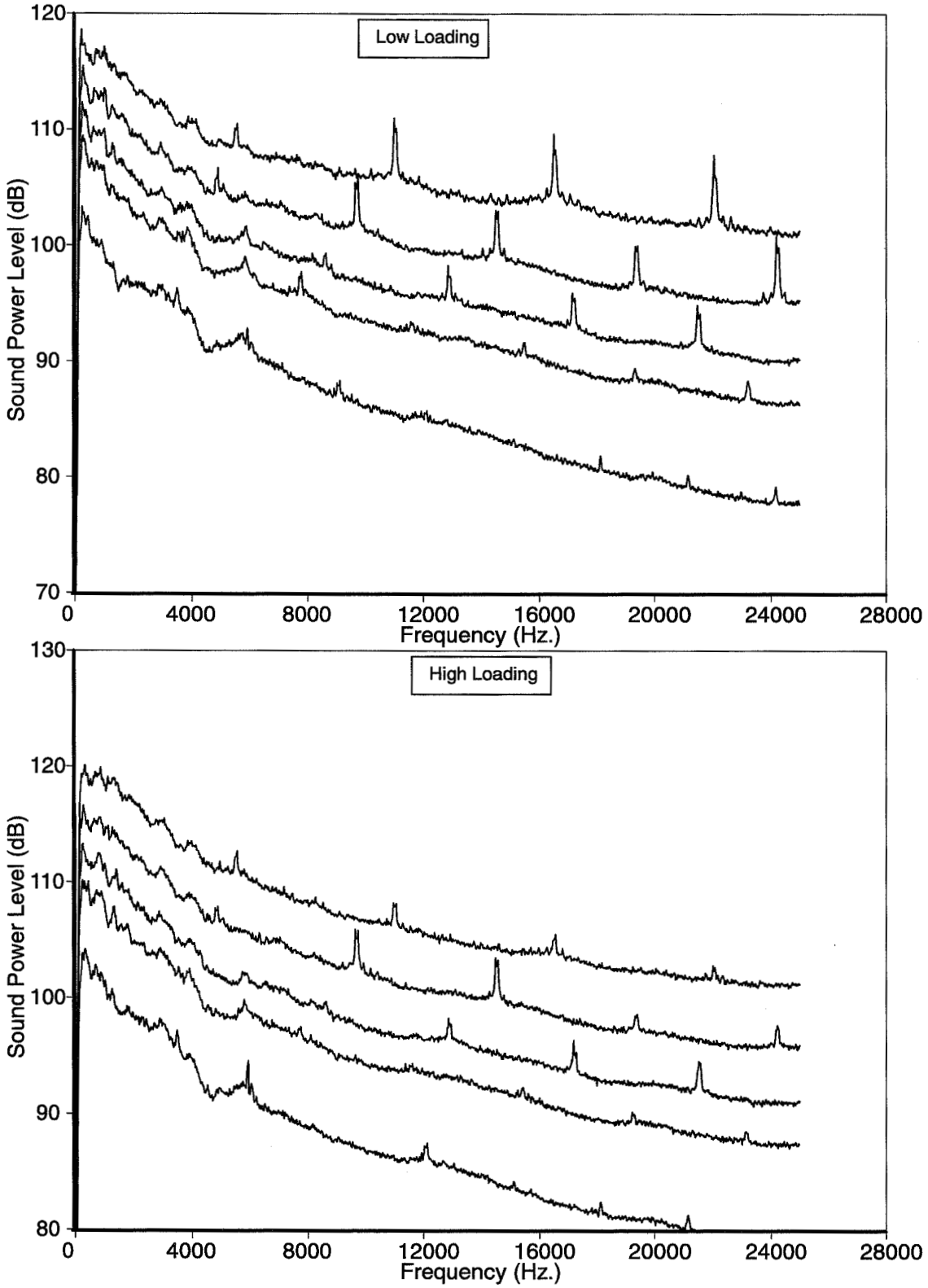

Fig. 158. Aft–radiated power level spectra; fifteen stators, small tip clearance, zero boundary layer

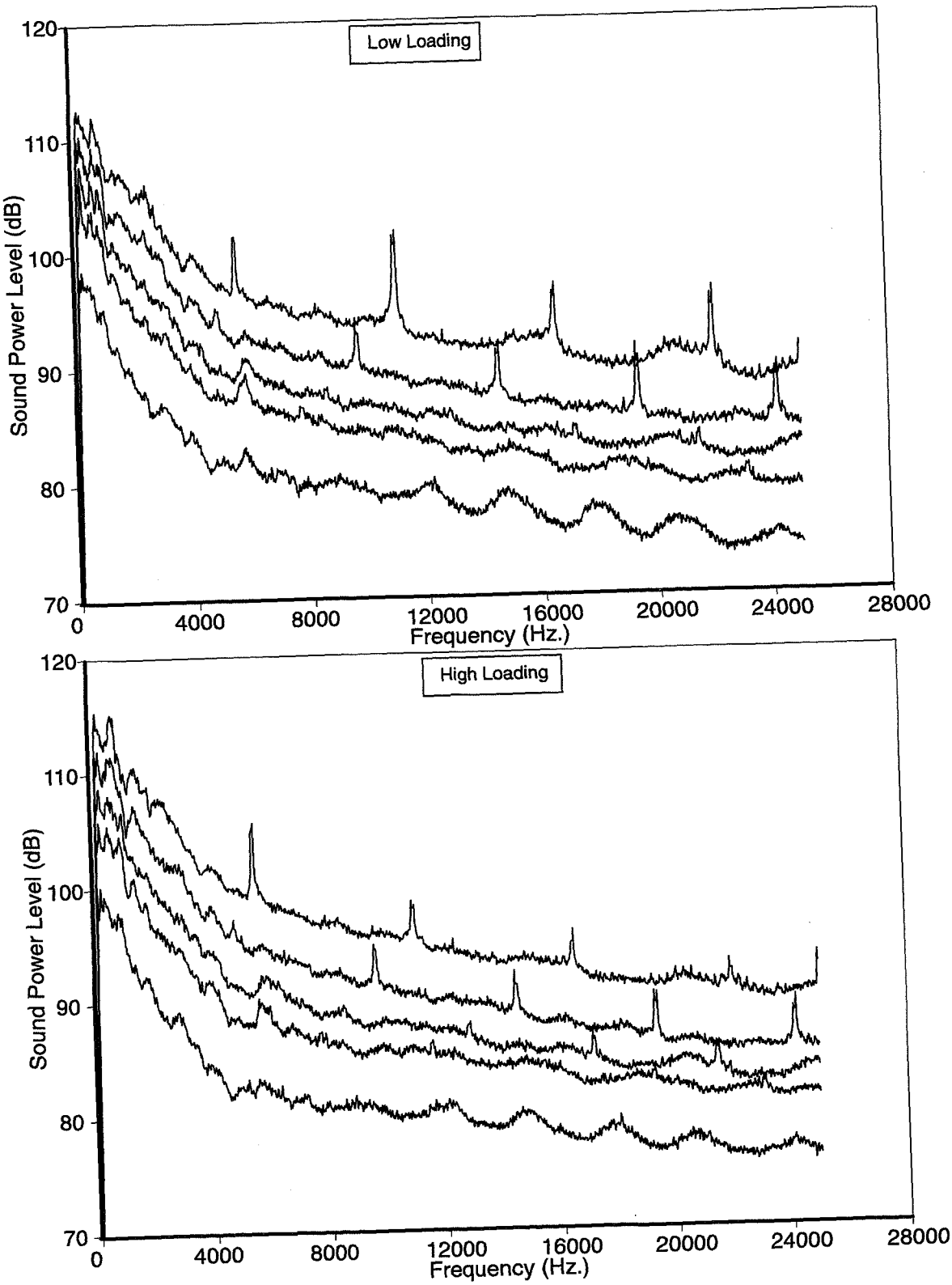

Fig. 159. Inlet–radiated power level spectra; fifteen stators, small tip clearance, full boundary layer

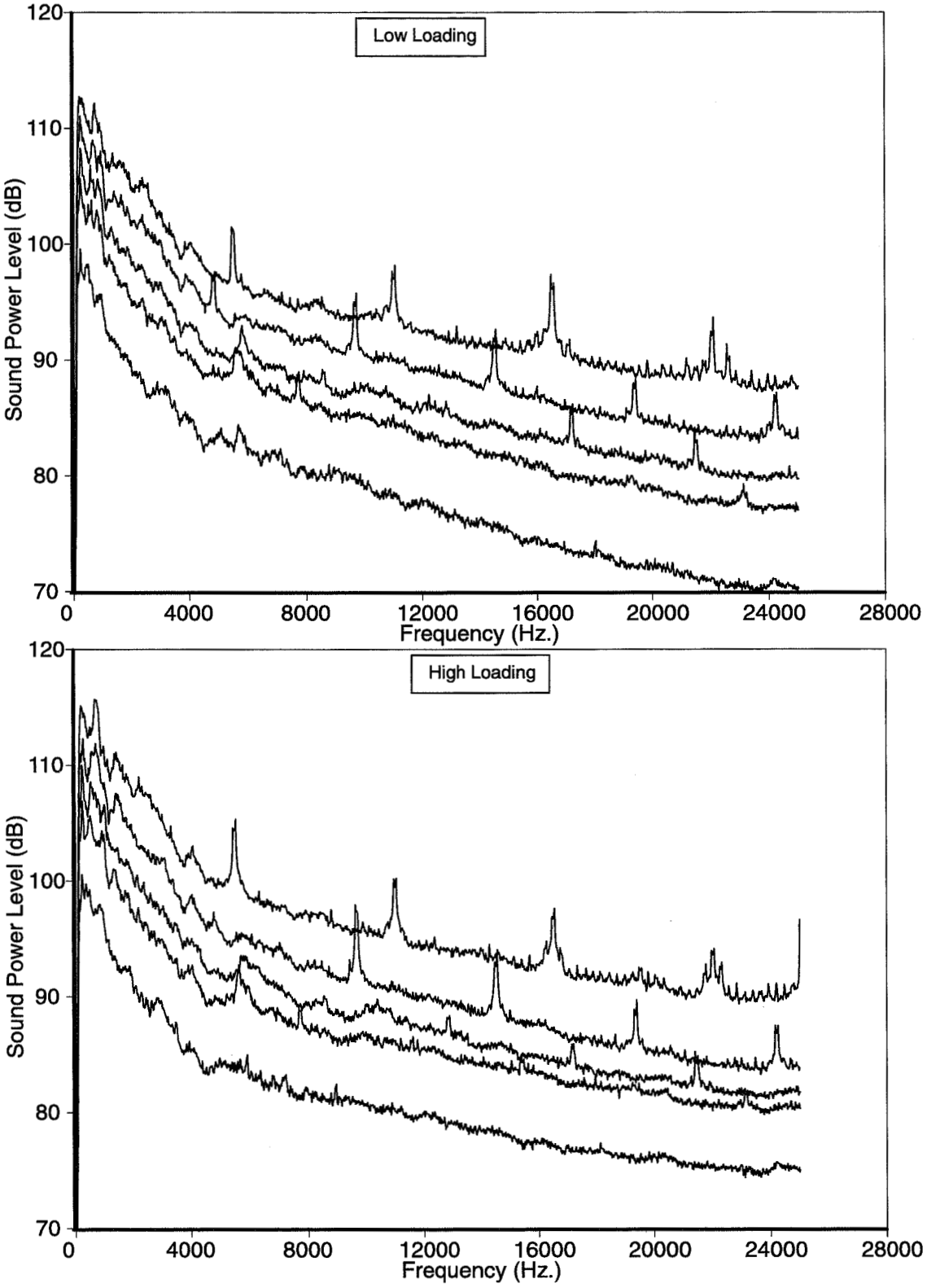

Fig. 160. Inlet–radiated power level spectra; fifteen stators, small tip clearance, zero boundary layer

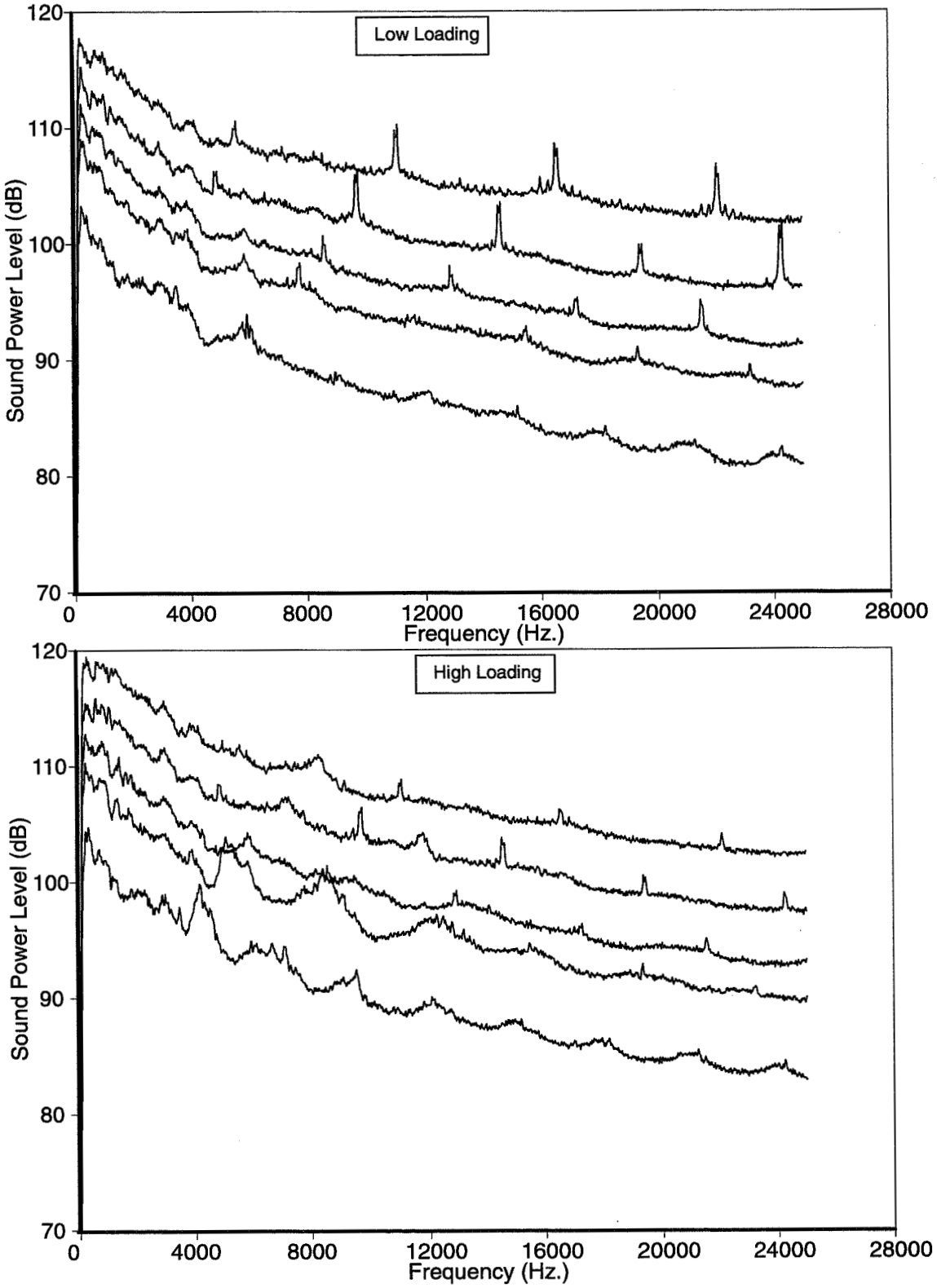

Fig. 161. Aft–radiated power level spectra; fifteen stators, large tip clearance, full boundary layer

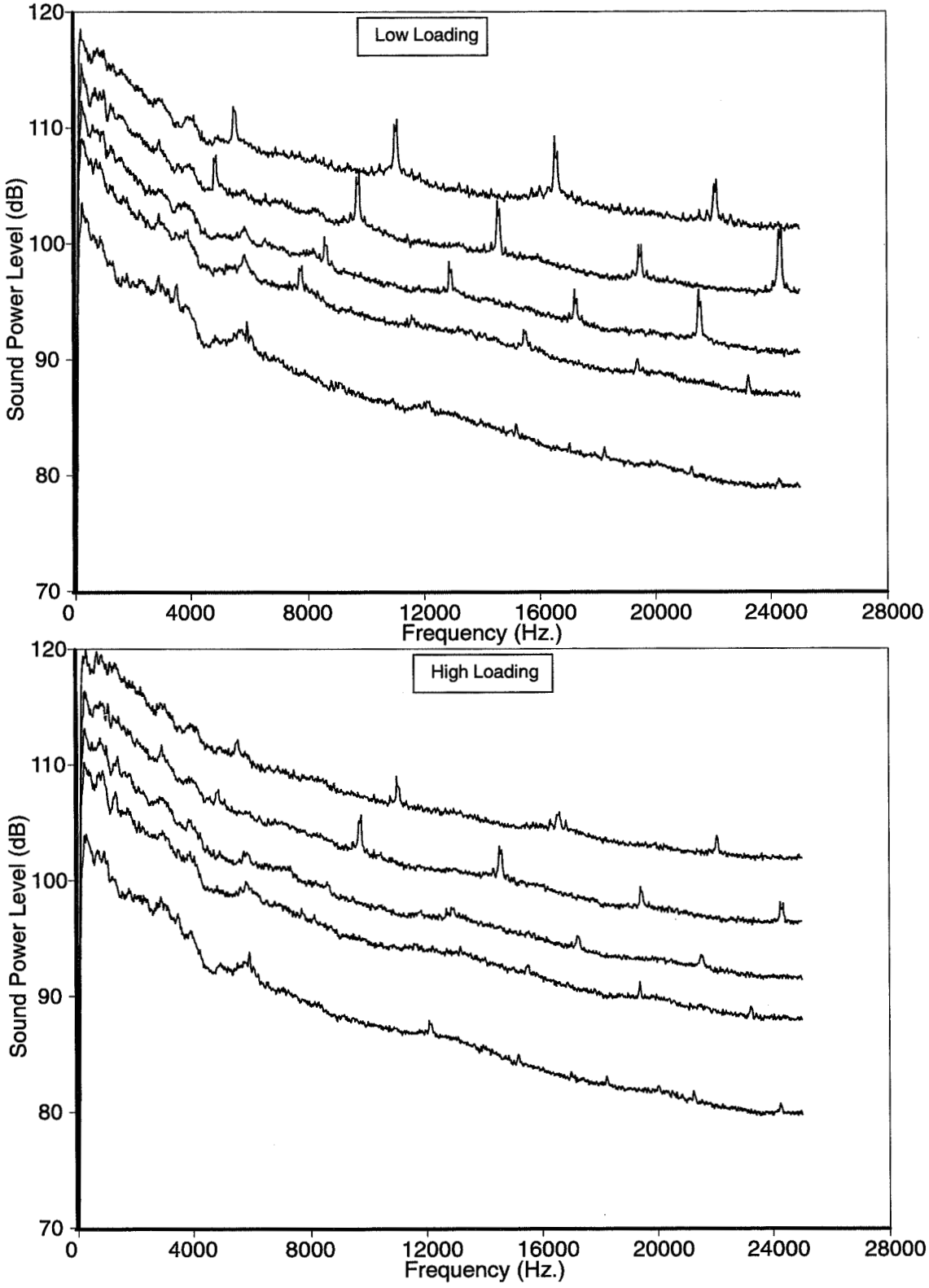

Fig. 162. Aft–radiated power level spectra; fifteen stators, large tip clearance, zero boundary layer

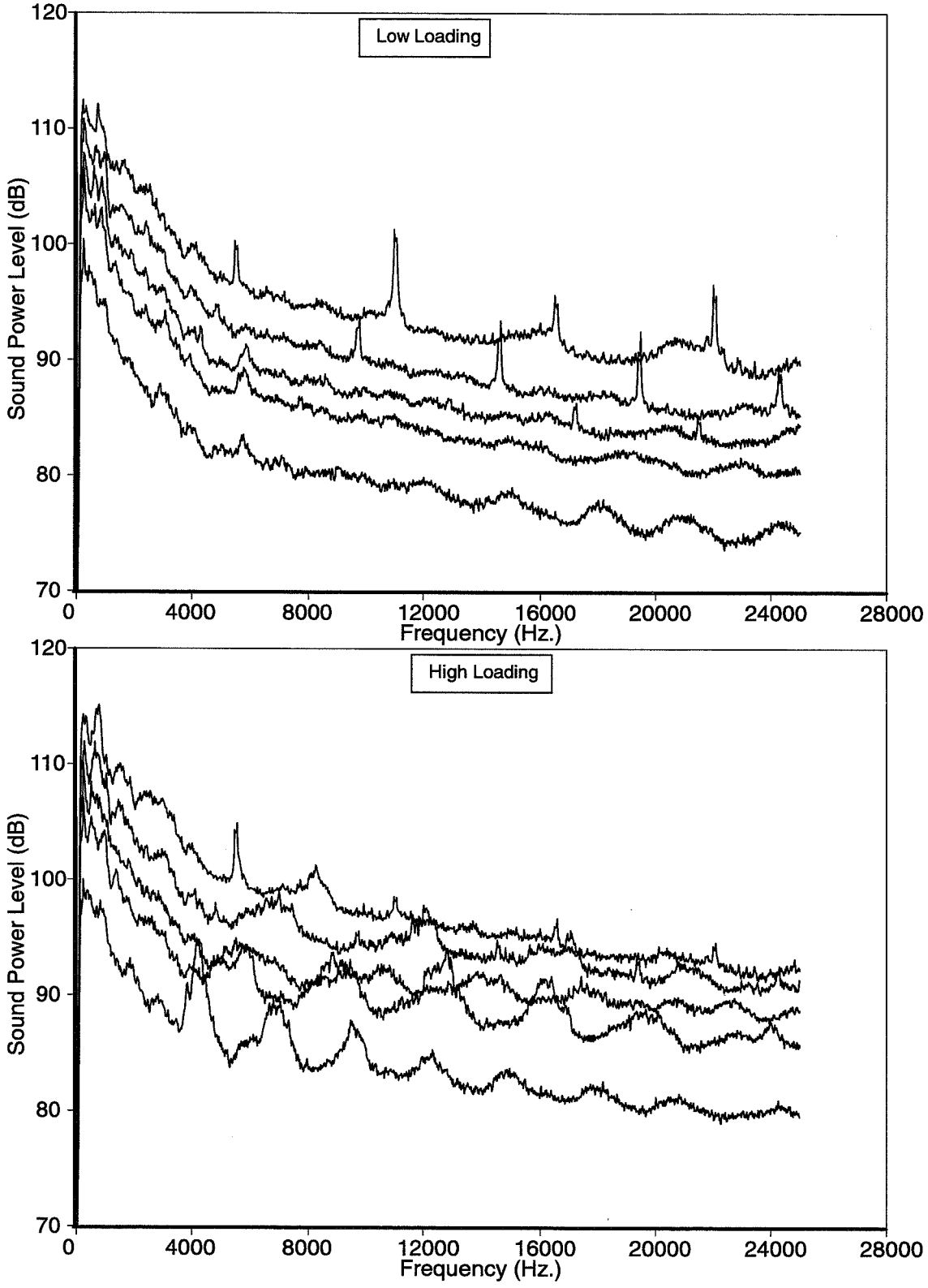

Fig. 163. Inlet–radiated power level spectra; fifteen stators, large tip clearance, full boundary layer

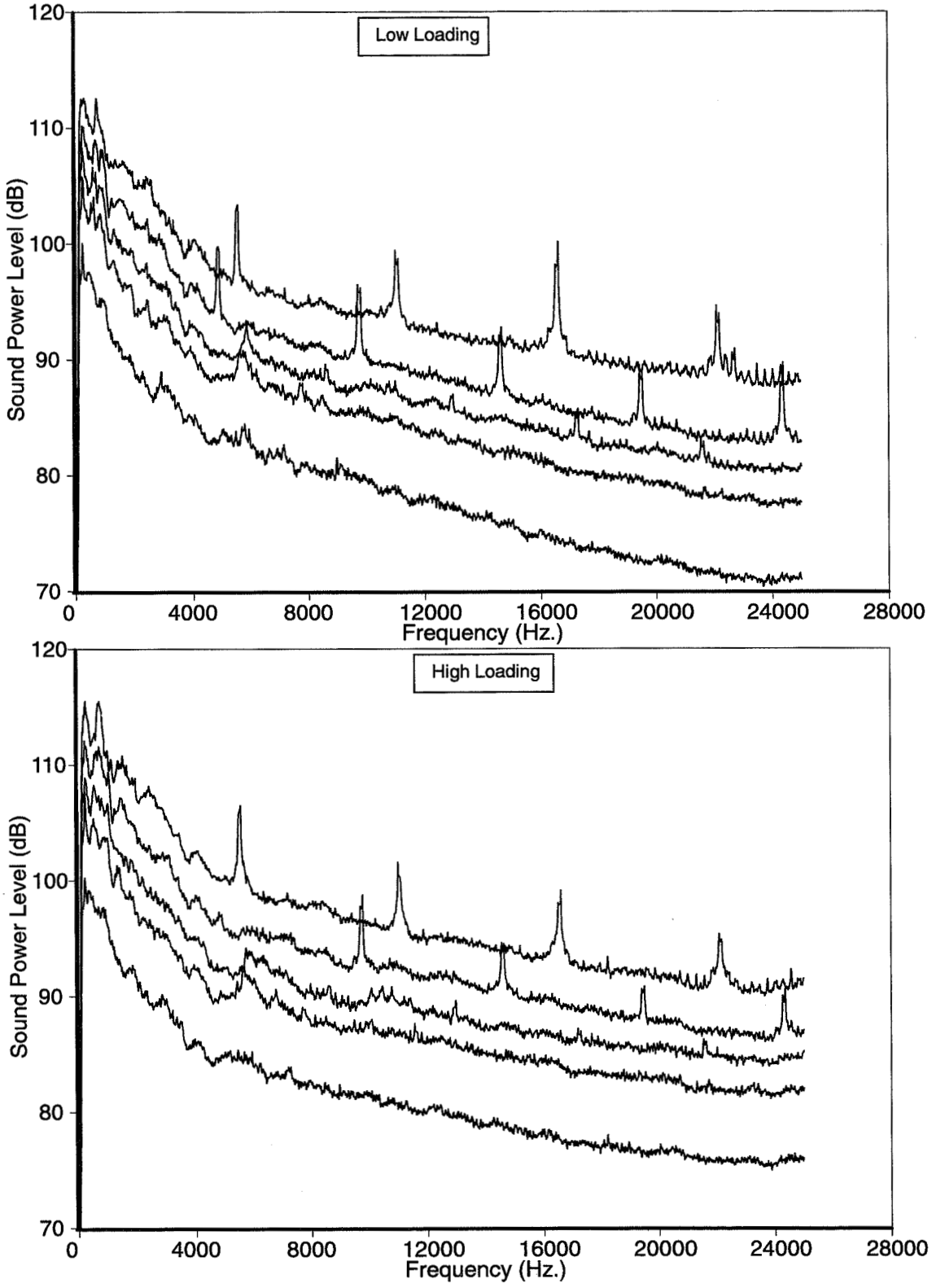

Fig. 164. Inlet–radiated power level spectra; fifteen stators, large tip clearance, zero boundary layer

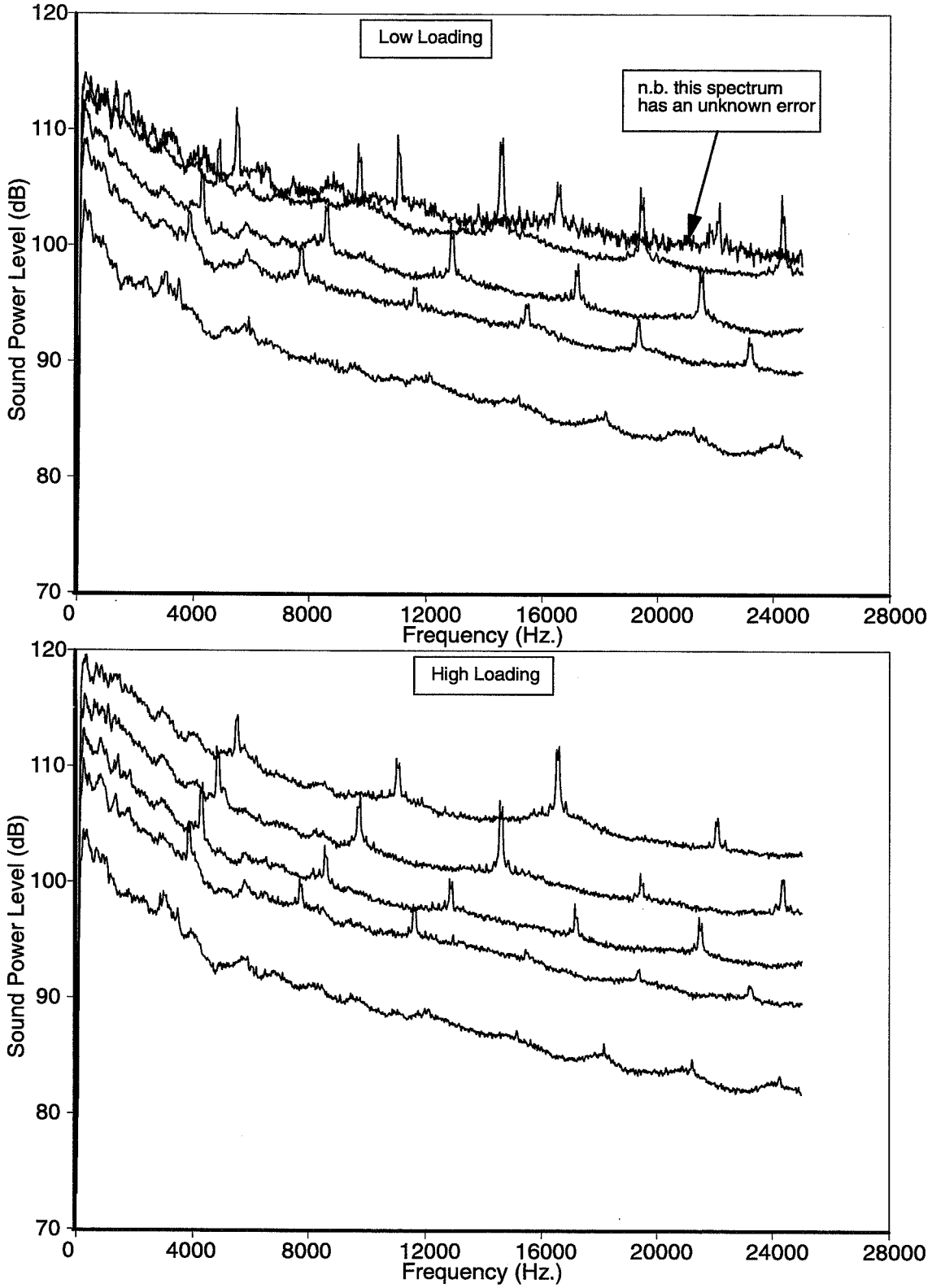

Fig. 165. Aft–radiated power level spectra; thirty stators, small tip clearance, full boundary layer

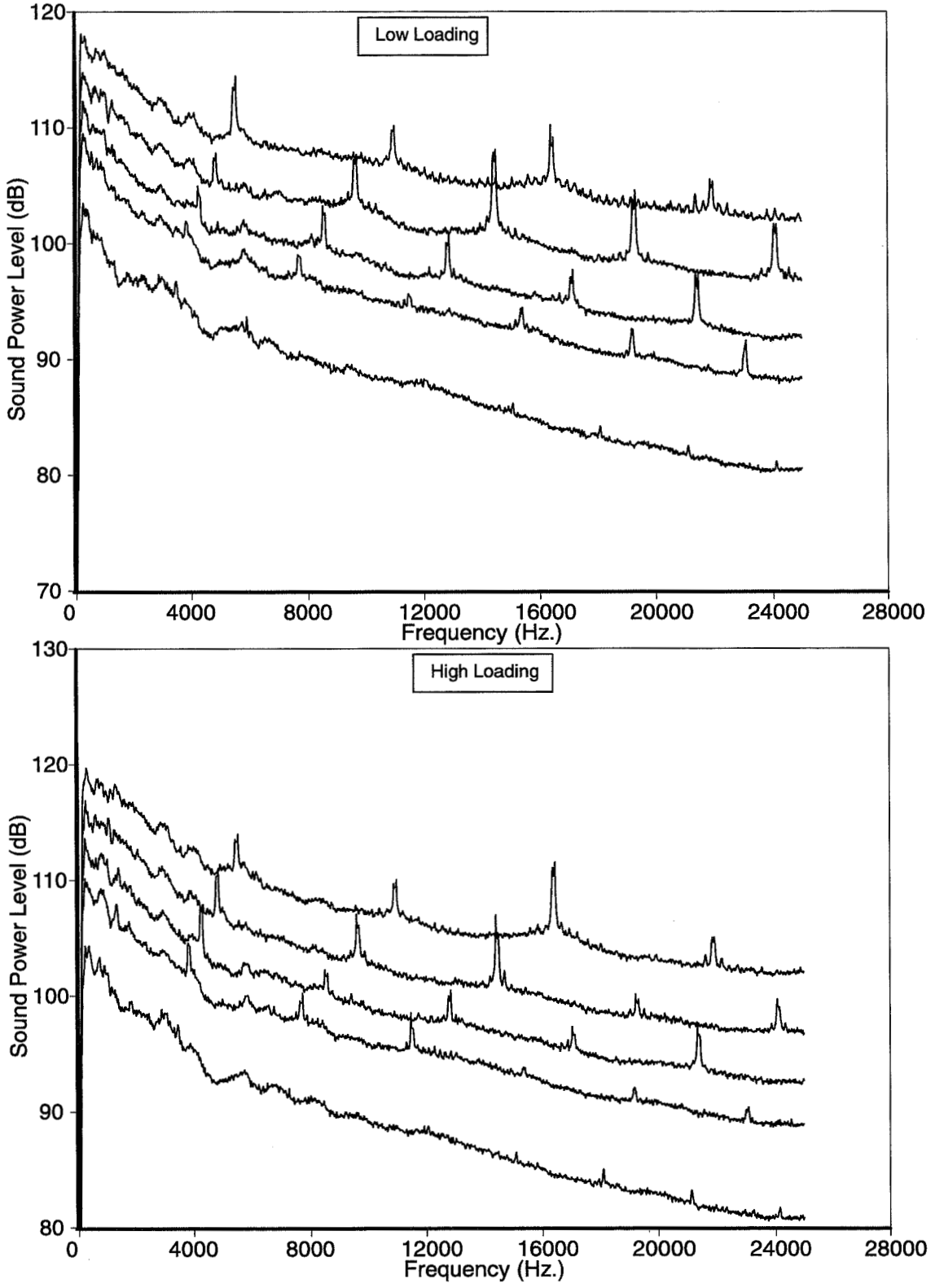

Fig. 166. Aft–radiated power level spectra; thirty stators, small tip clearance, zero boundary layer

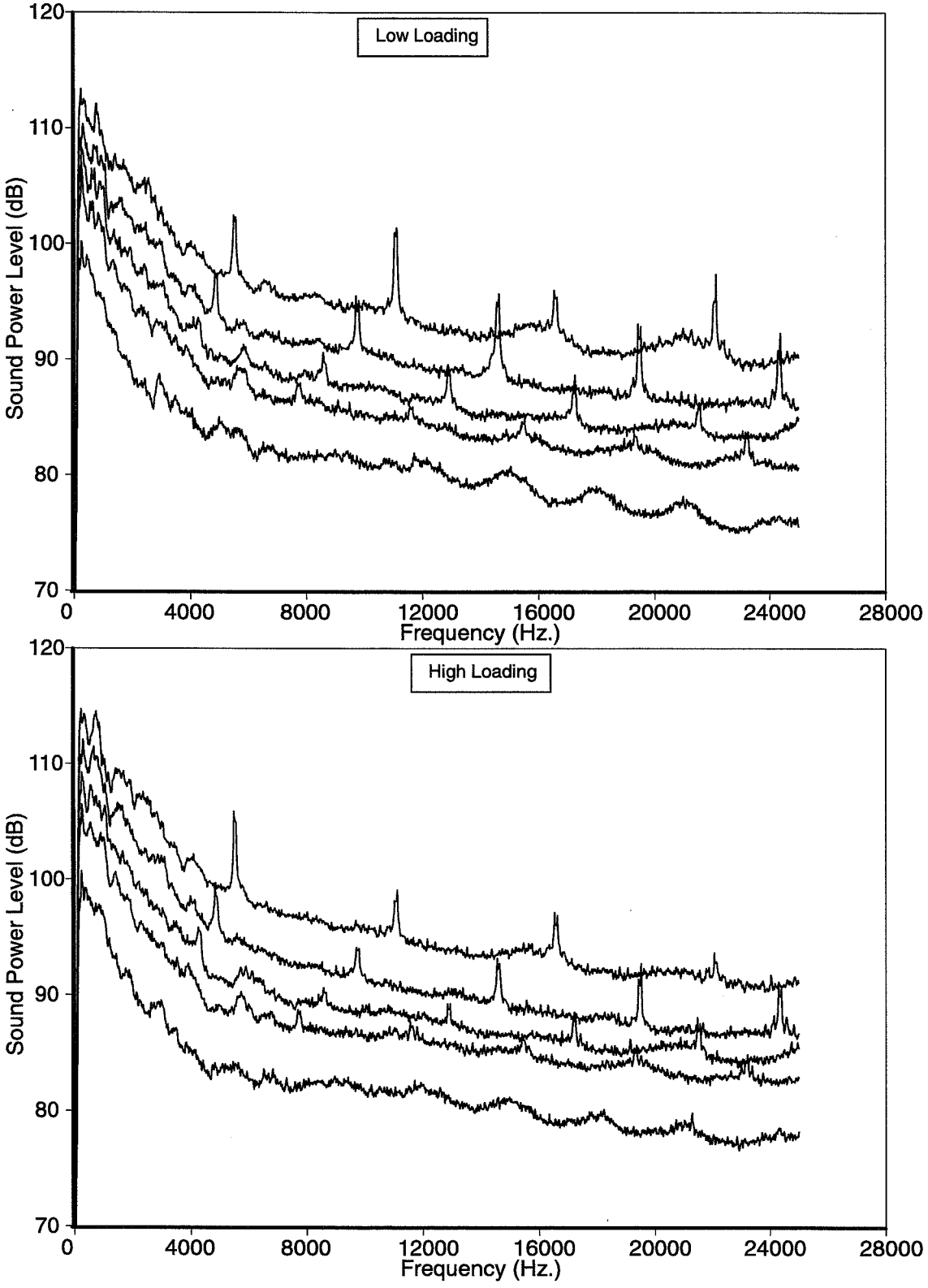

Fig. 167. Inlet–radiated power level spectra; thirty stators, small tip clearance, full boundary layer

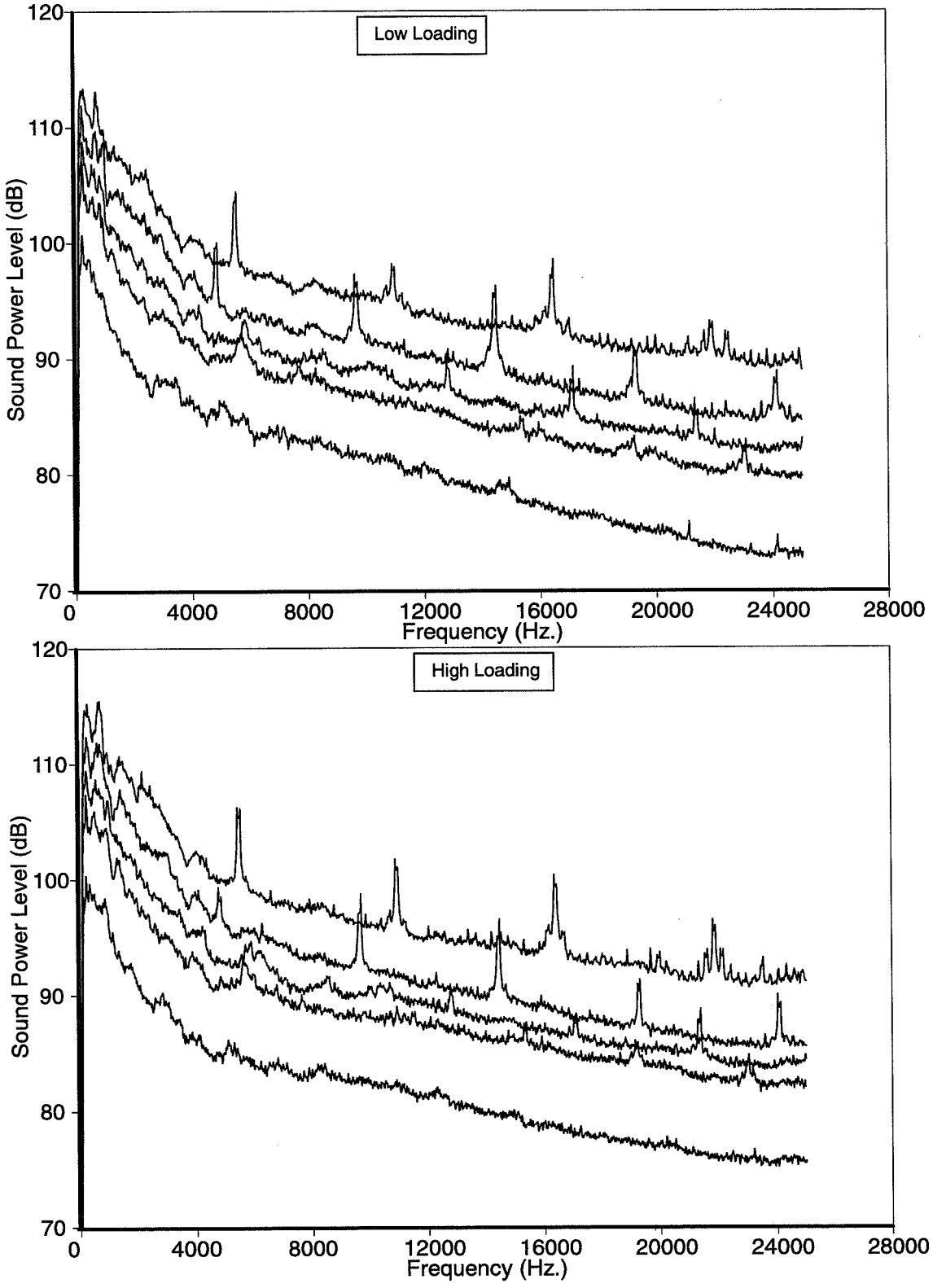

Fig. 168. Inlet–radiated power level spectra; thirty stators, small tip clearance, zero boundary layer

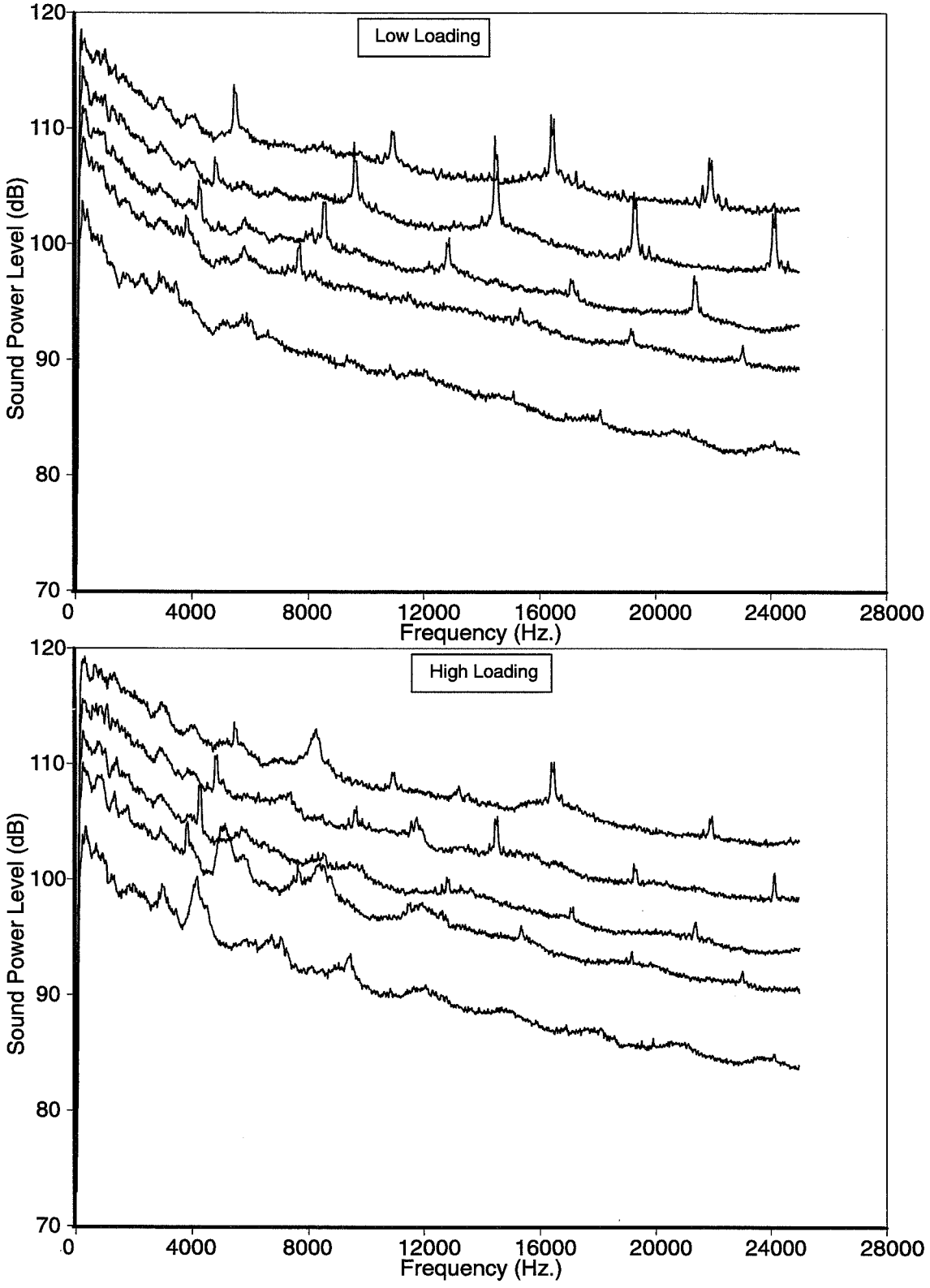

Fig. 169. Aft–radiated power level spectra; thirty stators, large tip clearance, full boundary layer

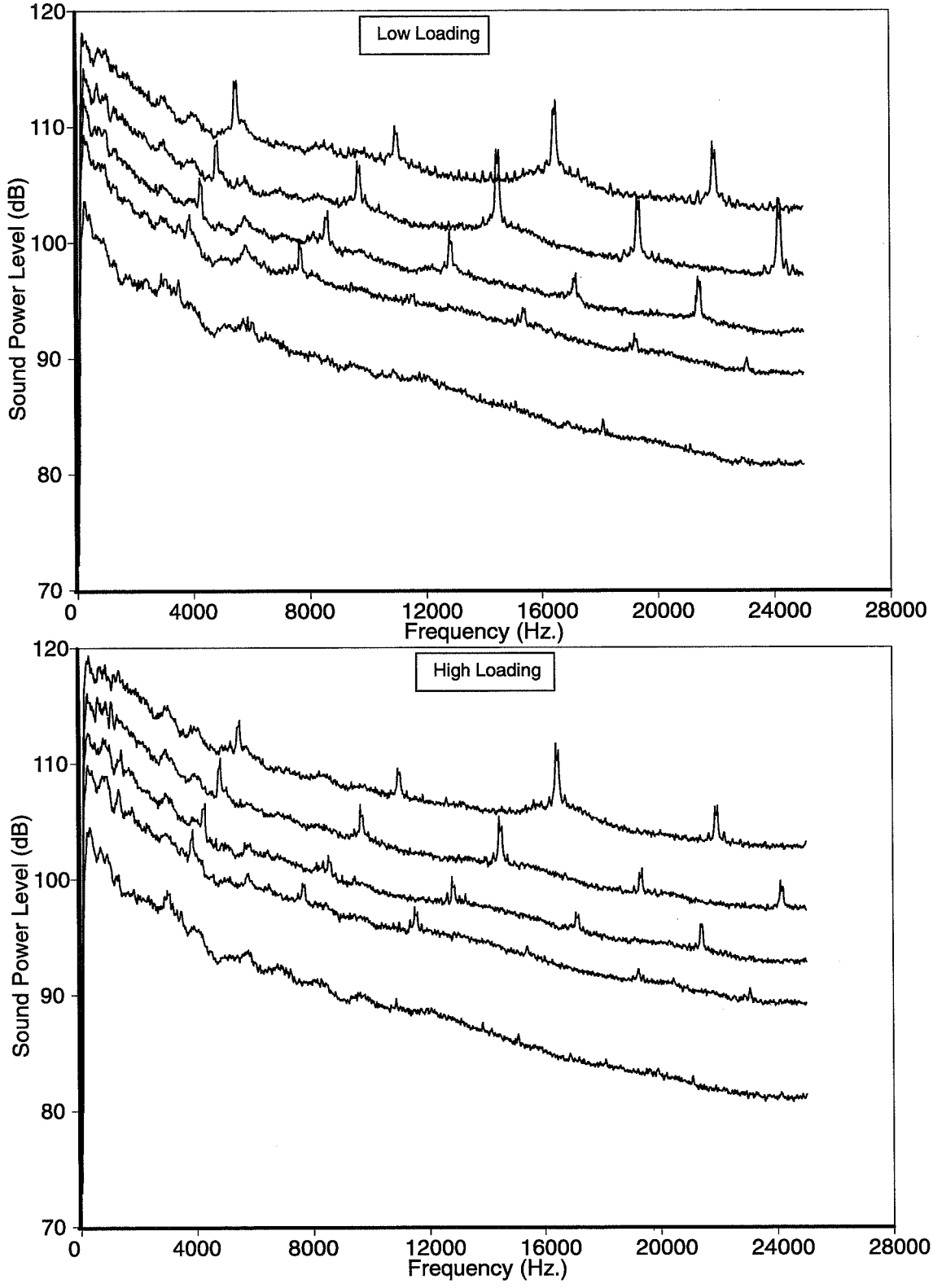

Fig. 170. Aft–radiated power level spectra; thirty stators, large tip clearance, zero boundary layer

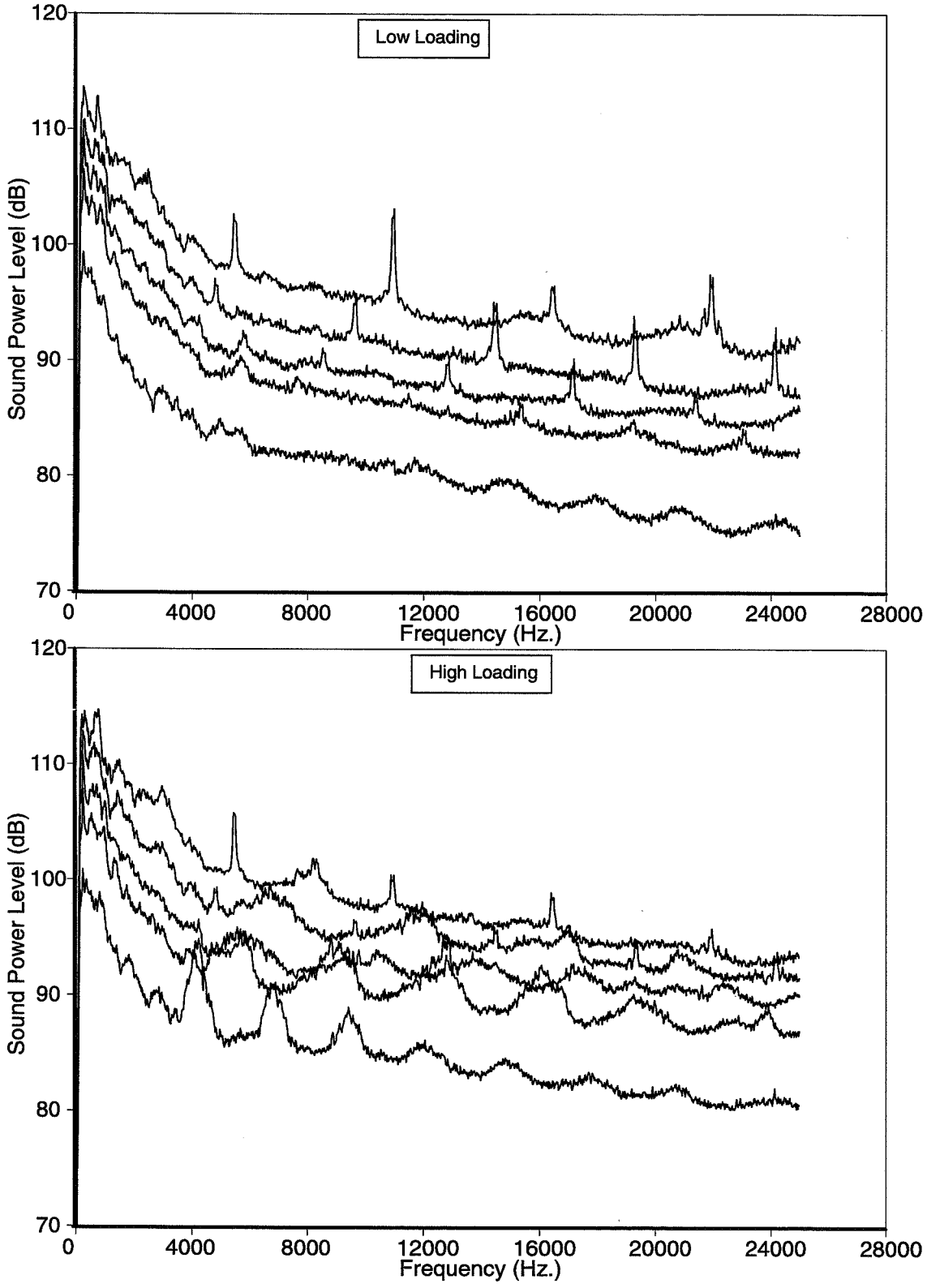

Fig. 171. Inlet–radiated power level spectra; thirty stators, large tip clearance, full boundary layer

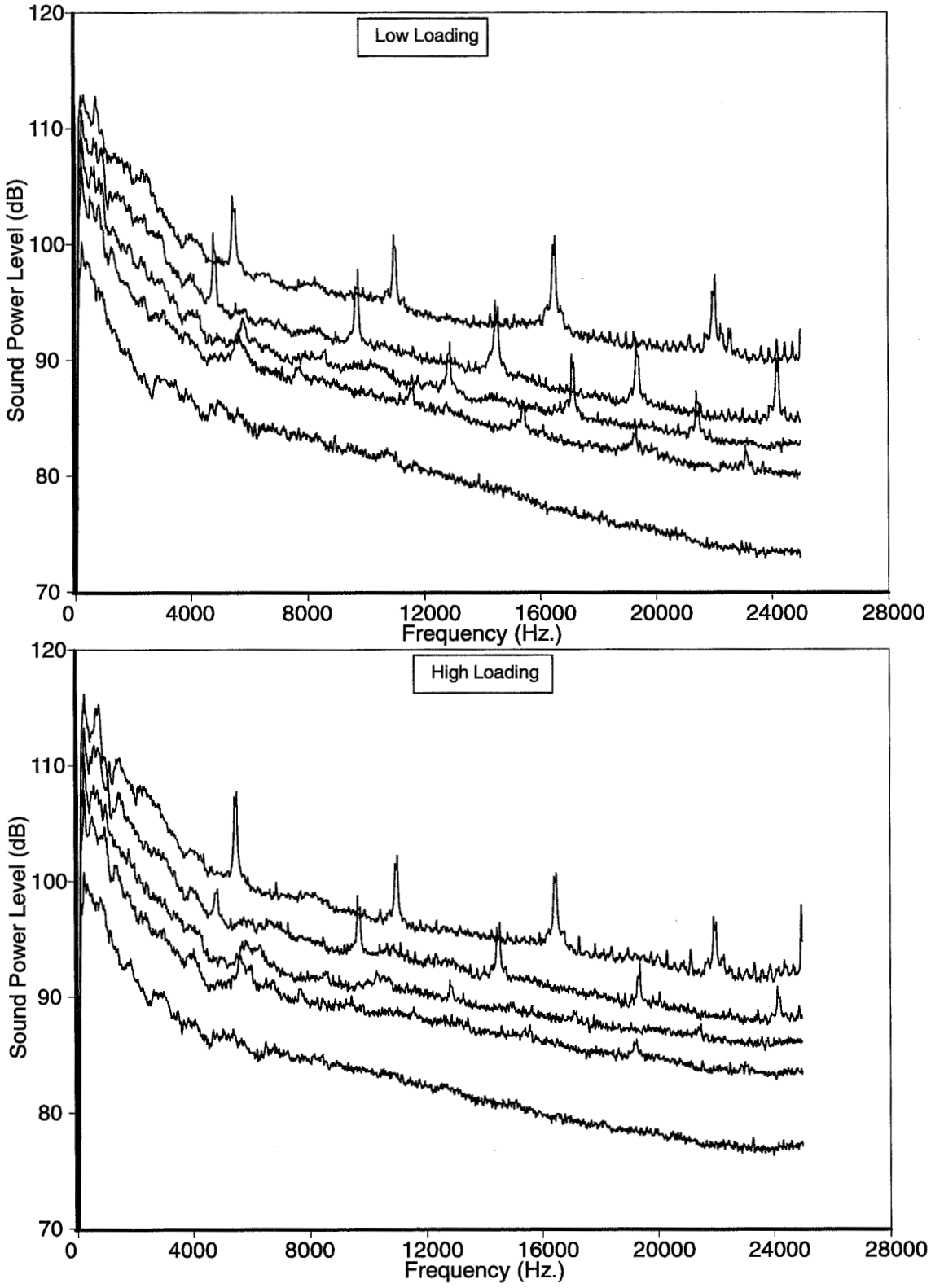

Fig. 172. Inlet–radiated power level spectra; thirty stators, large tip clearance, zero boundary layer

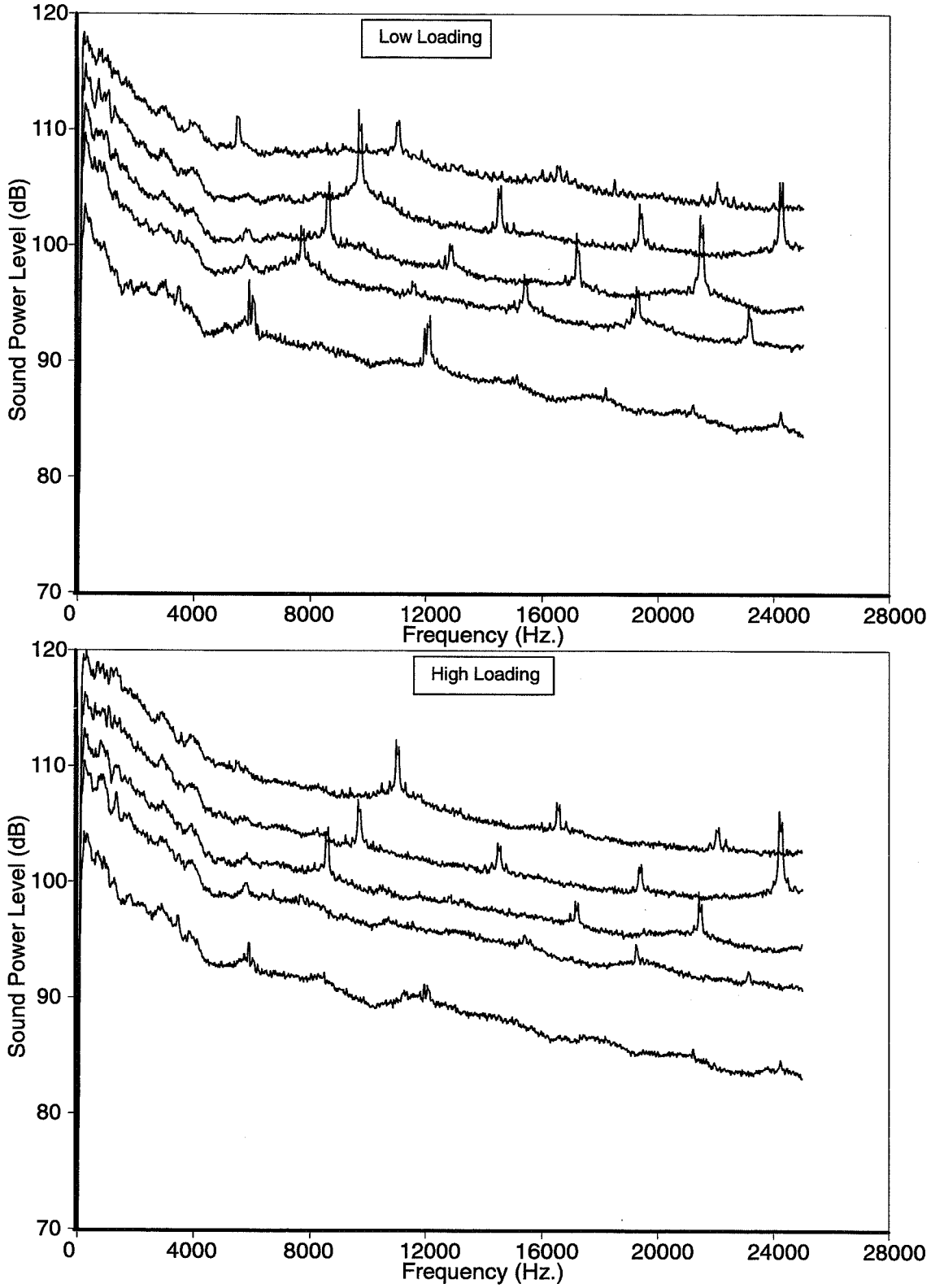

Fig. 173. Aft–radiated power level spectra; sixty stators, small tip clearance, full boundary layer

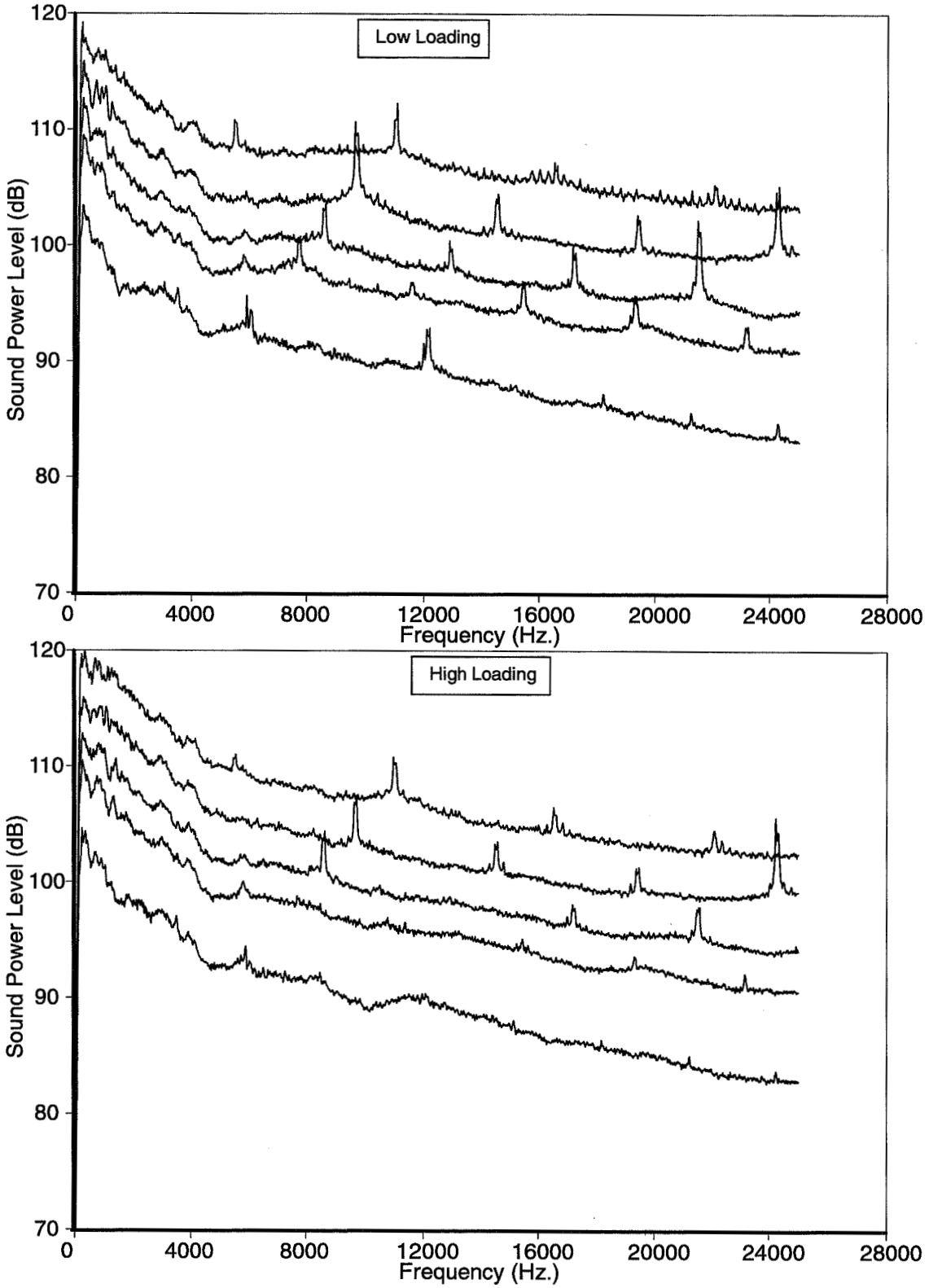

Fig. 174. Aft–radiated power level spectra; sixty stators, small tip clearance, zero boundary layer

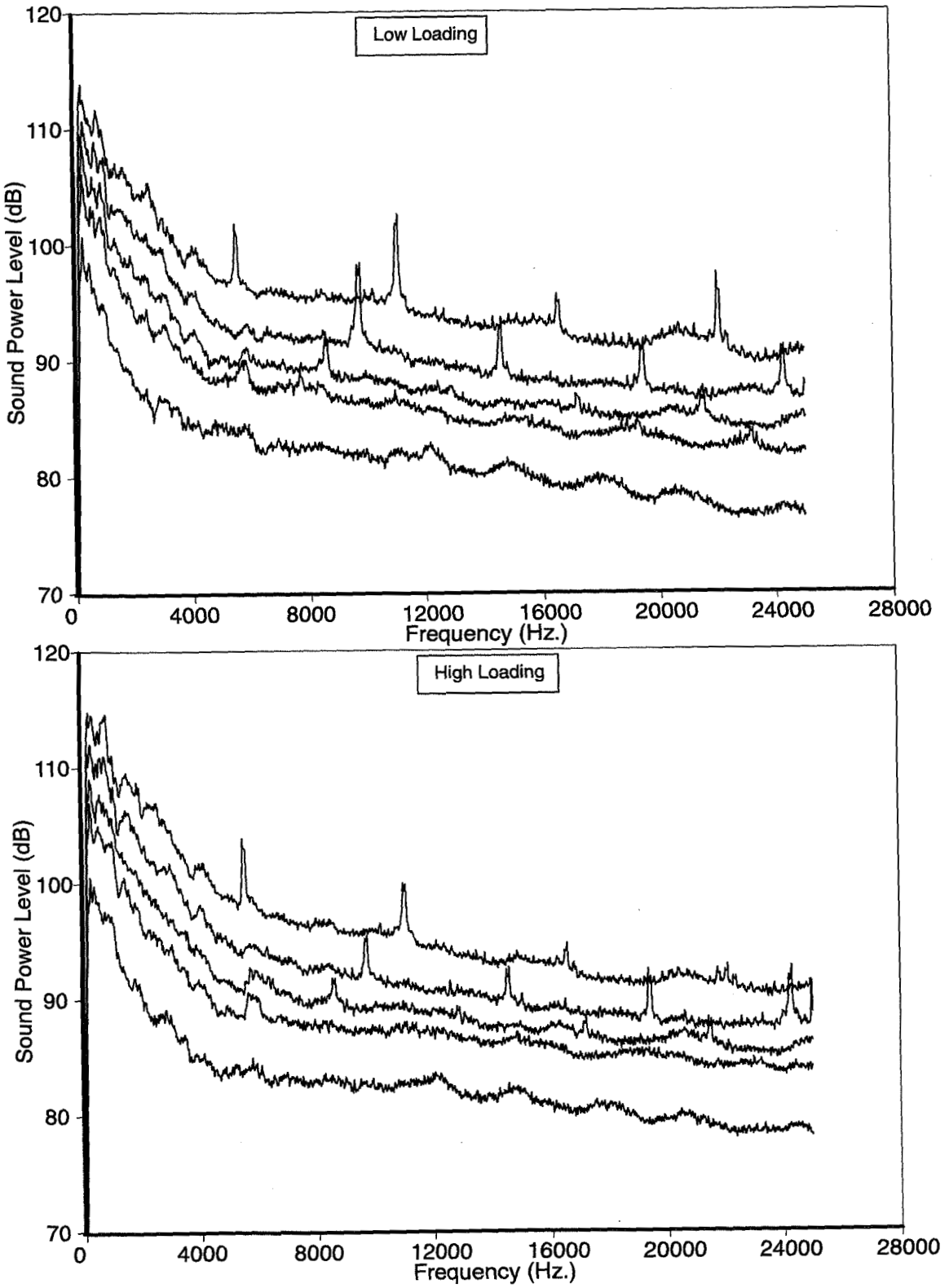

Fig. 175. Inlet–radiated power level spectra; sixty stators, small tip clearance, full boundary layer

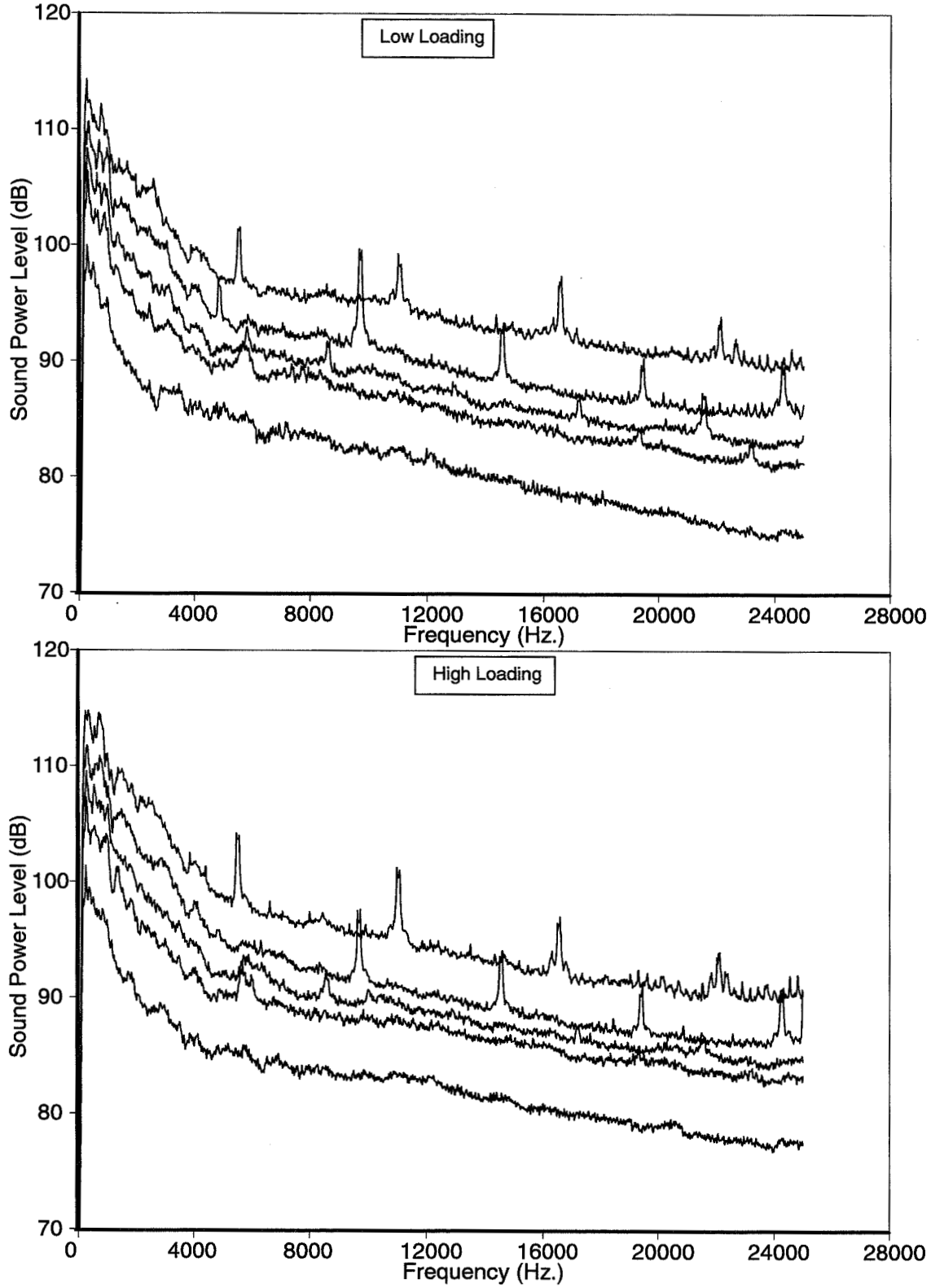

Fig. 176. Inlet–radiated power level spectra; sixty stators, small tip clearance, zero boundary layer

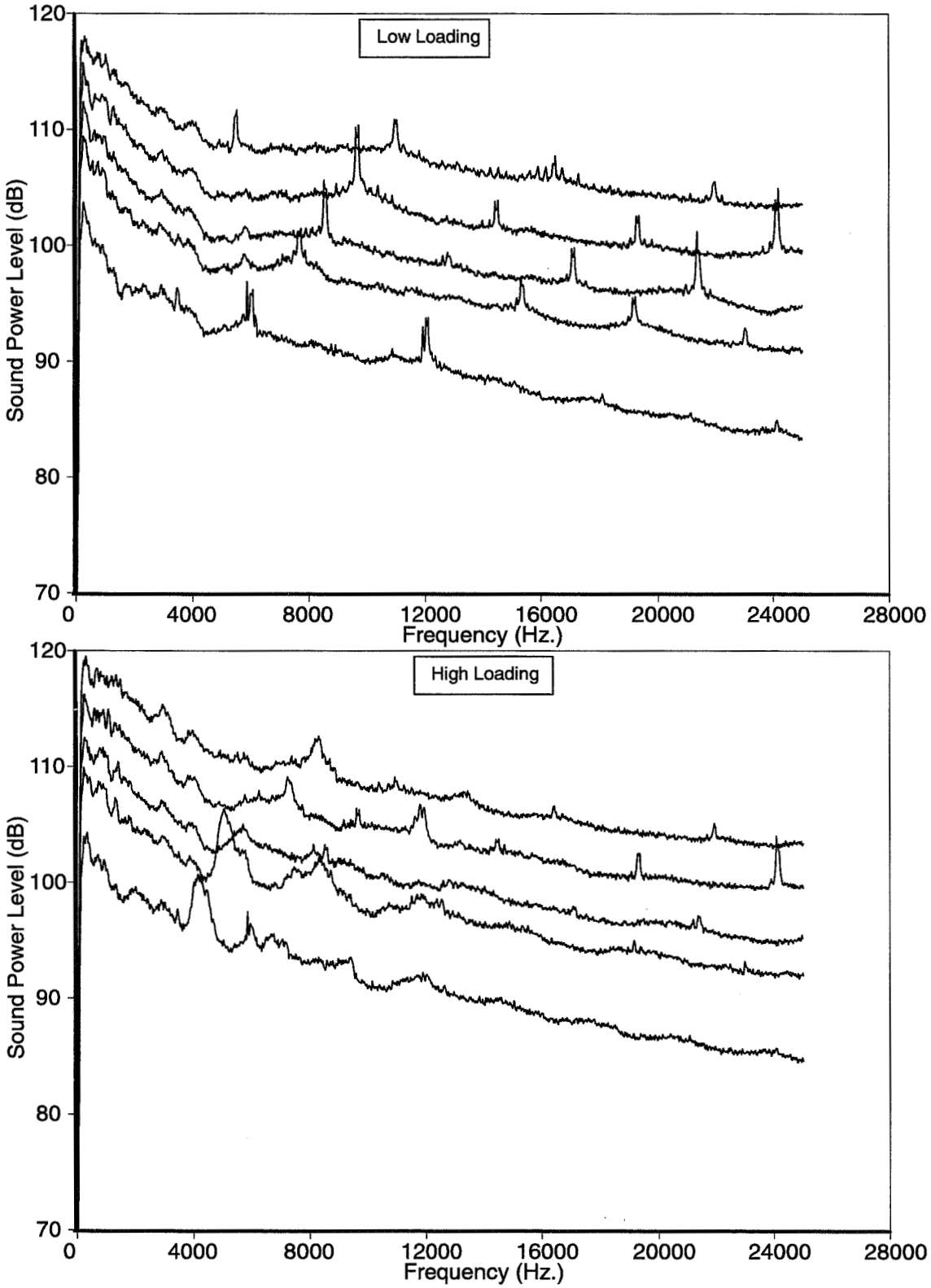

Fig. 177. Aft–radiated power level spectra; sixty stators, large tip clearance, full boundary layer

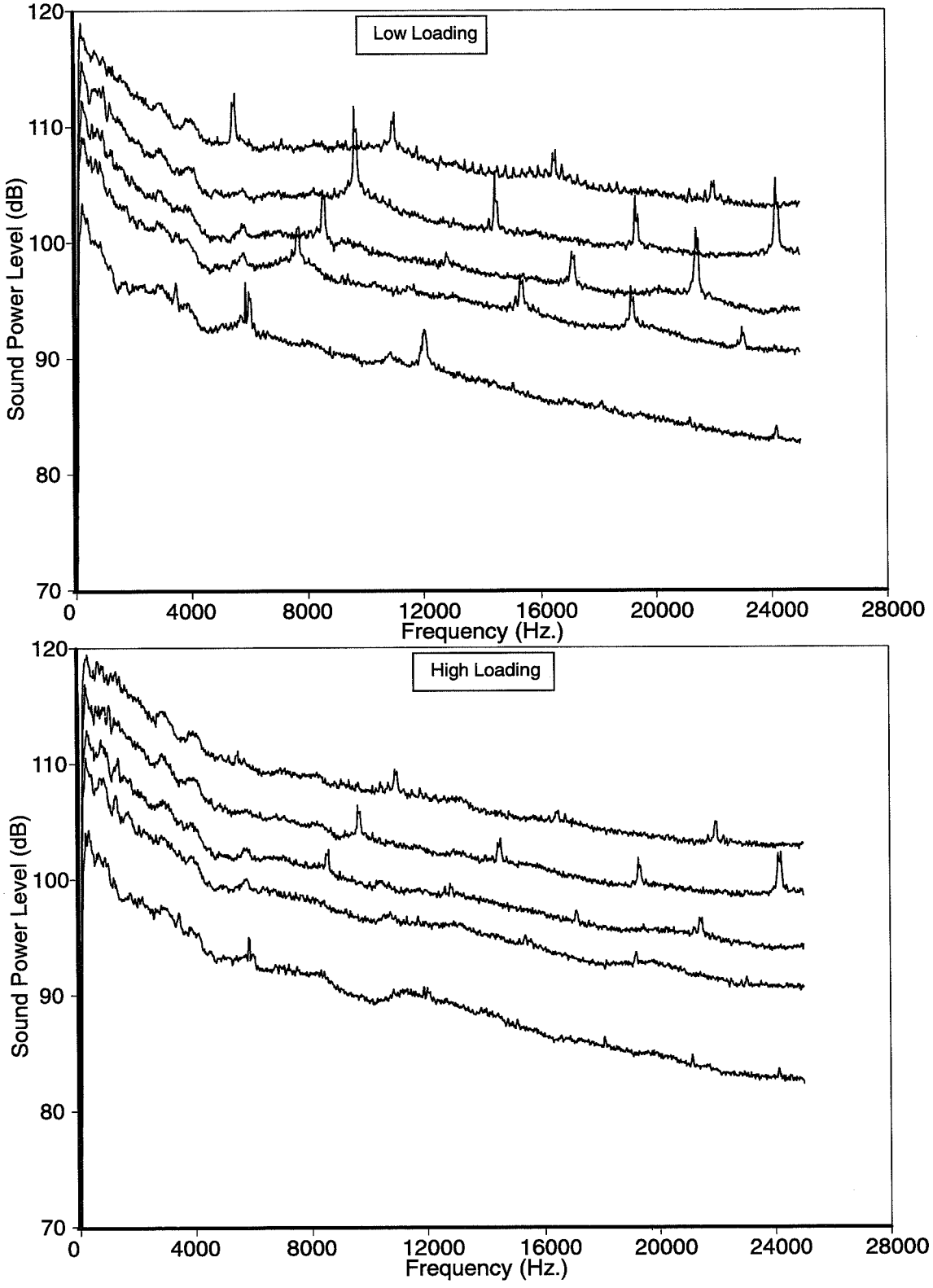

Fig. 178. Aft–radiated power level spectra; sixty stators, large tip clearance, zero boundary layer

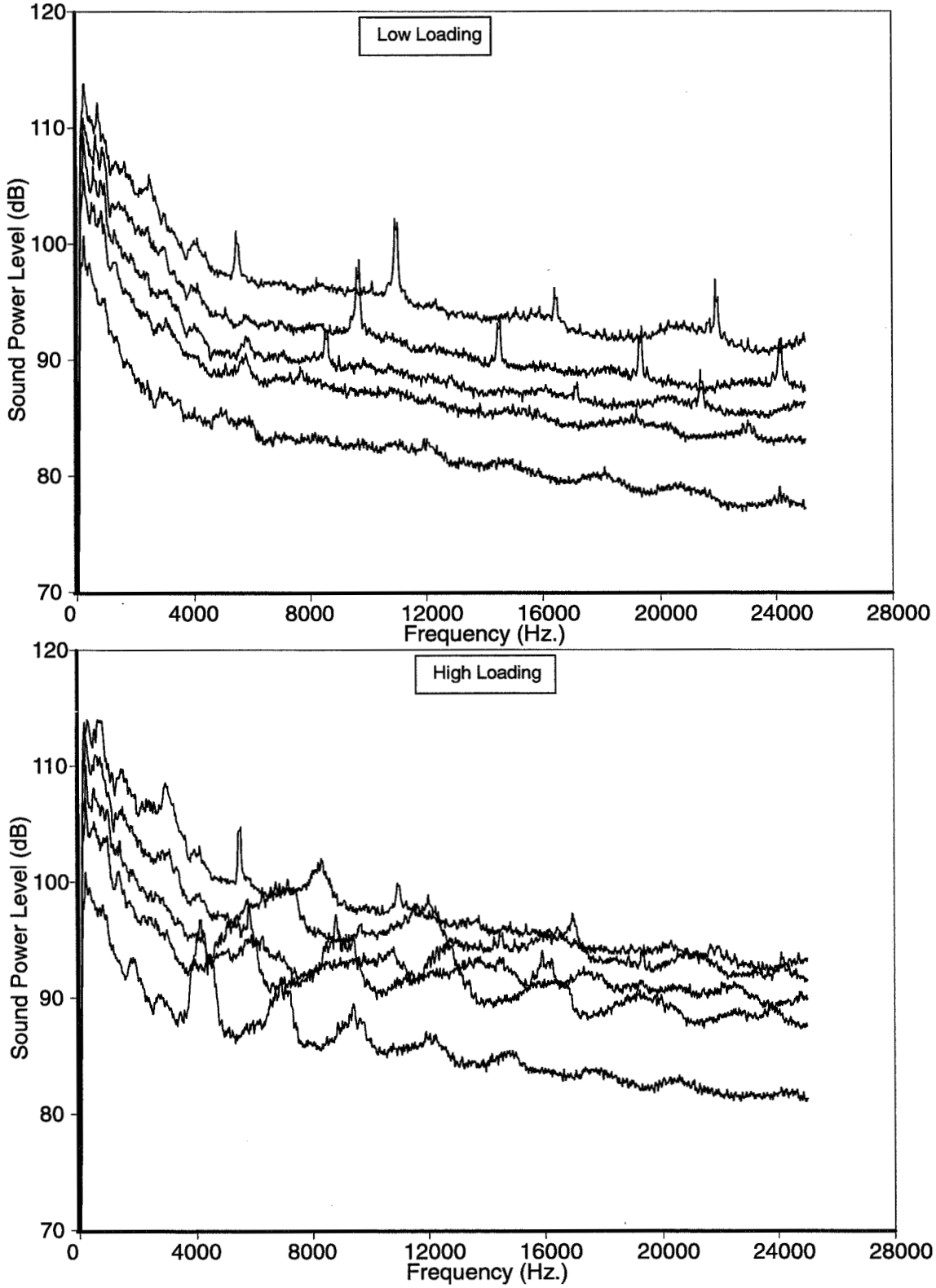

Fig. 179. Inlet–radiated power level spectra; sixty stators, large tip clearance, full boundary layer

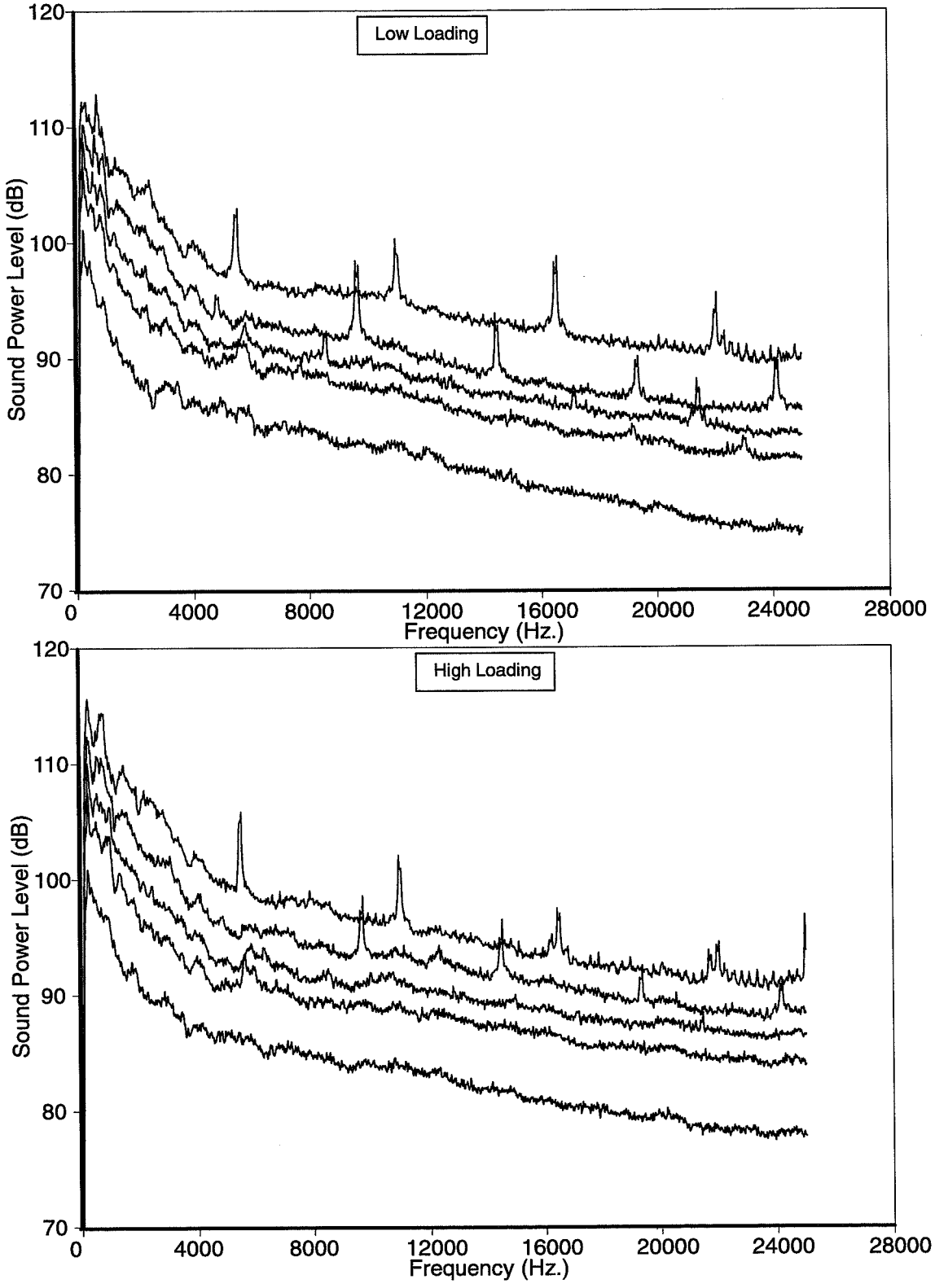

Fig. 180. Inlet–radiated power level spectra; sixty stators, large tip clearance, zero boundary layer

REPORT DOCUMENTATION PAGE

Form Approved
OMB No. 0704-0188

1. AGENCY USE ONLY (Leave blank)	2. REPORT DATE	3. REPORT TYPE AND DATES COVERED
	September 1998	Contractor Report

4. TITLE AND SUBTITLE
Boeing 18-Inch Fan Rig Broadband Noise Test

5. FUNDING NUMBERS
WU 538-03-11-01
NAS1-20090, Task 4

6. AUTHOR(S)
Ulrich W. Ganz, Paul D. Joppa, Timothy J. Patten, and Daniel F. Scharpf

7. PERFORMING ORGANIZATION NAME(S) AND ADDRESS(ES)
Boeing Commercial Airplane Group
P.O. Box 3707
Seattle, WA 98124

8. PERFORMING ORGANIZATION REPORT NUMBER

9. SPONSORING / MONITORING AGENCY NAME(S) AND ADDRESS(ES)
National Aeronautics and Space Administration
Langley Research Center
Hampton, VA 23681-2199

10. SPONSORING / MONITORING AGENCY REPORT NUMBER
NASA/CR-1998-208704

11. SUPPLEMENTARY NOTES
Langley Technical Monitor - Joe W. Posey

12a. DISTRIBUTION / AVAILABILITY STATEMENT
Unclassified - Unlimited
Subject Category 71
Distribution: Nonstandard
Availability: NASA CASI (301) 621-0390

12b. DISTRIBUTION CODE

13. ABSTRACT (Maximum 200 words)

The purposes of the subject test were to identify and quantify the mechanisms by which fan broadband noise is produced, and to assess the validity of such theoretical models of those mechanisms as may be available. The test was conducted with the Boeing 18-inch fan rig in the Boeing Low-Speed Aeroacoustic Facility (LSAF). The rig was designed to be particularly clean and geometrically simple to facilitate theoretical modeling and to minimize sources of interferring noise. The inlet is cylindrical and is equipped with a boundary layer suction system. The fan is typical of modern high-by-pass ratio designs ,but is capable of operating with or without fan exit guide vanes (stators), and there is only a single flow stream. Fan loading and tip clearance are adjustable. Instrumentation included measurements of fan performance, the unsteady flow field incident on the fan and stators, and far-field and in-duct acoustic fields. The acoustic results were manipulated to estimate the noise generated by different sources. Significant fan broadband noise was found to come from the rotor self-noise as measured with clean inflow and no boundary layer. The rotor tip clearance affected rotor self-noise somewhat. The interaction of the rotor with inlet boundary layer turbulence is also a significant source, and is strongly affected by rotor tip clearance. High level noise can be generated by a high-order nonuniformity rotating at a fraction of the fan speed, at least when tip clearance and loading are both large. Stator-generated noise is the loudest of the significant sources, by a small margin, at least on this rig. Stator noise is significantly affected by propagation through the fan.

14. SUBJECT TERMS
Ducted Fan Noise, Broadband Fan Noise and Turbomachinery Noise

15. NUMBER OF PAGES
205

16. PRICE CODE
A10

17. SECURITY CLASSIFICATION OF REPORT	18. SECURITY CLASSIFICATION OF THIS PAGE	19. SECURITY CLASSIFICATION OF ABSTRACT	20. LIMITATION OF ABSTRACT
Unclassified	Unclassified	Unclassified	